Polysaccharides for Bitumen Extraction, Environmental Decontamination and Cell Culture

by

Natun Dasgupta

A thesis

presented to the University of Waterloo

in fulfillment of the

thesis requirement for the degree of

Doctor of Philosophy

in

Chemistry

Waterloo, Ontario, Canada, 2022

Examining Committee Membership

The following served on the Examining Committee for this thesis. The decision of the Examining Committee is by majority vote.

External Examiner	Yue Zhao Professor Chemistry Université de Sherbrooke
Supervisor	Mario Gauthier Professor Emeritus Chemistry
Internal Member	Jean Duhamel Professor Chemistry
Internal Member	Scott Taylor Professor Chemistry
Internal-external Member	Tizazu Mekonnen Assistant Professor Chemical Engineering

AUTHOR'S DECLARATION

This thesis consists of material which I authored or co-authored: see Statement of Contributions included in the thesis. This is a true copy of the thesis, including any required final revisions, as accepted by my examiners.

I understand that my thesis may be made electronically available to the public.

Statement of Contributions

Chapter 2 of this thesis, entitled "Synthesis of Thermoresponsive Starch Nanoparticles Grafted with Poly(di(ethylene glycol) Methyl Ether Methacrylate)", was developed by myself and my supervisor, Prof. Mario Gauthier. Dr. Vo Thu An Nguyen guided me initially with RAFT polymerization using starch-based RAFT agents. Oliver Wang (co-op student, Summer 2018) initiated the characterization of xanthation reactions under my guidance. I completed all the remaining experimental work, characterization and analysis, and wrote the chapter with regular consultation with my supervisor.

Chapter 3, entitled "Thermoresponsive Starch Nanoparticles for the Extraction of Bitumen from Oil Sands", was developed by myself and my supervisor, Prof. Mario Gauthier. Jasmine Zhang from Prof. Jean Duhamel's group determined the oil and fines content in the Imperial Oil oil sands (IOos) and Athabasca Sand Bank oil sands (SBos) samples, and did some UV-visible spectroscopy characterization. I completed all the remaining experimental work, characterization and oil extractions, and wrote the chapter with frequent consultation with my supervisor.

Chapter 4, entitled "Starch-stabilized Iron Nanoparticles for the Photocatalytic Degradation of Methylene Blue", was developed by myself and my supervisor, Prof. Mario Gauthier. Milind Nayak (co-op student, Fall 2019) assisted me with the UV-visible spectroscopy characterization of the materials and the total organic content analysis of the samples. I completed all the remaining experimental work, characterization and analysis, and wrote the chapter with frequent consultation with my supervisor.

Chapter 5, entitled “Chitosan Grafted with Thermoresponsive Poly(di(ethylene glycol) Methyl Ether Methacrylate) for Cell Culture”, was developed by myself, my supervisor, Prof. Mario Gauthier, and Prof. Maud Gorbet in the Systems Design Engineering Department. Prof. Maud Gorbet and her student, Duo Sun, handled the growth of cells on the modified and unmodified chitosan films. I completed all the remaining experimental work, characterization, analysis, and wrote the chapter with frequent consultation with Prof. Mario Gauthier and Prof. Maud Gorbet.

Abstract

Polysaccharides are polymeric carbohydrates with long chains of monosaccharide units linked by glycosidic bonds. Some of the most prevalent polysaccharides in nature include starch and chitin. For the work reported in this thesis, amylopectin was used either in nanoparticle (fragmented) or cooked forms, while chitin was used in its deacetylated (chitosan) form. The work focuses on developing synthetic techniques to chemically modify starch and chitosan for bitumen extraction, dye degradation, and cell growth and extraction.

Starch nanoparticles (SNPs) were modified with carbon disulfide in the presence of NaOH to form xanthated SNPs, which were reacted with methyl-2-bromopropionate to form novel starch-based RAFT (reversible addition-fragmentation chain transfer) macroinitiators with different degrees of substitution (DS). The starch-based RAFT agents were then used to graft thermoresponsive poly(di(ethylene glycol) methyl ether methacrylate) ($PMEO_2MA$) onto the SNPs. RAFT polymerization was found to be an efficient method for the synthesis of thermoresponsive polymer-grafted SNPs, providing straightforward control over the number and length of grafted $PMEO_2MA$ segments, as well as the hydrophilic-lipophilic balance (HLB) of the nanoparticles in solution.

Temperature-dependent solubility of the $PMEO_2MA$-grafted SNPs was observed, as the SNPs were amphiphilic above their lower critical aggregation temperature (LCAT), forming micellar aggregates dispersed in water that were useful to extract bitumen from the sand and silt components in oil sands. The optimal SNP-*g*-$PMEO_2MA$ composition, structure, and concentration were determined through cycles of bitumen extraction. The addition of 0.5 M NaCl

was shown to minimize the interference of fines with the extraction process, increasing the bitumen extraction efficiency to ~80% under optimal conditions.

In another application, starch was used to stabilize iron nanoparticles serving in the Fenton reaction. The photocatalytic Fenton reaction uses hydrogen peroxide and Fe^{2+} under relatively acidic conditions (pH 2-3) to produce hydroxyl radicals as strong oxidant. The low pH, used partly to maintain solubility of the iron catalyst, is problematic because it leads to the generation of large volumes of decontaminated, yet very acidic water. Cooked starch, being hydrophilic, was investigated as a colloidal stabilizer for iron (Fe^{2+}/Fe^{3+}) oxide nanoparticles. The photocatalytic Fenton reaction, investigated at a pH significantly higher than usual (pH 4), enabled the efficient degradation of methylene blue. It was shown that the starch-stabilized catalysts could be reused in several degradation cycles, thereby providing an environment-friendly and cost-effective method to degrade residual dyes in water.

$PMEO_2MA$ chains were also grown from chitosan films modified with RAFT-active sites of the same type used for the SNPs, thus making the chitosan films thermoresponsive. The length of the grafted $PMEO_2MA$ chains was controlled by varying the degree of substitution (DS) of the chitosan-based RAFT agent and the amount of monomer added in the grafting reaction, as determined by gel permeation chromatography (GPC) analysis of the chains cleaved from the chitosan substrates. The growth of cells on the films, and their detachment at low temperatures were confirmed in cell growth studies combined with fluorescence microscopy.

The reported results demonstrate that the hydroxyl groups of amylopectin starch and chitosan can be utilized to obtain novel materials useful in different application areas.

Acknowledgements

I would like to express my appreciation for my supervisor, Professor Mario Gauthier, who has been encouraging and extremely supportive while guiding me through my Ph.D. research. It would not have been possible to accomplish this research without his valuable experience and teachings.

I would like to thank my supervisory committee members Prof. Jean Duhamel, Prof. Scott Taylor, Prof. Tizazu Mekonnen, and my external examiner, Prof. Yue Zhao, for their valuable contributions.

I would like to thank Prof. Maud Gorbet and her co-op student, Duo Sun, for conducting the cell culture experiments in their lab.

I would like to thank Joanne Fernandez for being an elder sister to me and an extremely supportive lab mate. Her baked goods were often uplifting for the mood during difficult times. I am also grateful to Oliver Wang and Milind Nayak. Oliver has been very kind, understanding, and helpful to my research during his time in the lab. Milind was a very hard-working and proactive co-op student in the laboratory, which allowed us to learn from one another.

I would also like to thank my coworkers at the University of Waterloo for their friendship and association: Dr. Deepak Vishnu, Dr. An Nguyen, Dr. Mosa Alsehli, Dr. Janine Thoma, Dr. Damin Kim, Jasmine Zhang, Liying Wang, Victoria Hisko, Ala Alturk, Basma Mahi, Paul Dymond, Sanjay Patel, Abdullah Ba-Salem, and all other current and past associates from the Gauthier and Duhamel laboratories.

I am forever grateful to my parents, Sarbani Dasgupta and Anup Dasgupta, for their unconditional love, support, and for always having faith in my life choices. I would not be able to pursue my education in Canada without the efforts and vision of my father. My mother and I are pillars of support for each other, and I hope to follow in her footsteps of moral and kindness.

There are friends, there is family, and there are friends that become family. I would like to express my gratitude to such friends, whose association was critical to my Ph.D. work at the University of Waterloo.

Shan Priyan – I am grateful to have a friend like you. I have cherished our times since we were roommates. You have been very understanding and have always shown up for me whenever I needed help, whether it was driving me somewhere, ACL injury, or helping me move places. Thank you for believing in me and being part of The Roll Joint. I will always admire the good times I have spent with you, and I look forward to more memories with you in the future.

Saif Fazal Mahamood – Thanks for being my friend and roommate during some of my most difficult times. My time in Waterloo would have been incomplete without you, together we have made great friends with a community of people that will be cherished forever. We have hustled through university life together, and I hope that we never let go of that attitude. I don't think that I have enjoyed playing FIFA with anyone as much as you, and I hope to continue doing so 40 years from now. We are not in the same city anymore, but I hope you know that I will always be there for you, as I will never forget your contributions to my life.

Rafay Sohail – I never expected us to become such good friends. During some of my most difficult moments, you have been a breath of fresh air. The memories we have built on our

trips will last a lifetime. I miss playing football and FIFA with you; 2016-2017 was one of the most enjoyable moments of my life. I appreciate you coming to see Shan and me from Markham nearly every week, and I hope that we can continue to make beautiful memories as a trio.

Amogh Sohoni – We are friends, but I consider you like my brother. Thanks for all the memorable trips that we have done together. Hikes will never be the same without Rafay and yourself. I hope that we always stay in touch regardless of where we are.

Susmita Bose – I have been grateful to have you as a friend in Waterloo. Thanks for making such delicious food with love. The COVID-19 pandemic has been a difficult time for all of us, but your presence helped me cope with that period. I wish you the very best in life, and myself opportunities to experience more of your delicious cooking.

Rachana Sai, Udit Mondal, and Zubain Sayed: Thanks to you all for being always kind and caring. You three are among my oldest friends in Canada, and I couldn't be any more grateful to have you in my life. Zubain, I look forward to making more Euro trips with you.

Vinay Guthal and Saad Qazi: You two are some of the most loveable people in my life. I cannot express enough gratitude to know you both. The kindness and empathy that I have seen in both of you help me become a better person every day. You both give to others wholeheartedly, and I hope that you continue doing so.

Kiran Keswani and Manreet Kaur: Thank you Kiran for all the long phone conversations during good and not-so-good times. I hope we continue being supportive of each other regardless of where we are located. Thank you Manreet for always being supportive. I am happy that we

could still maintain our friendship, even being miles apart. I hope that you are proud of yourself, because I am.

Raqibul Hayder and Shivani Hegde: Raqib (Dada), thanks for being an elder brother and for guiding me through my difficult times. I love our conversations, and hopefully we get to work again together in the future. Thank you Shivani for being such a good human being. Being around you, I have learned a few things about empathy. Please continue to be yourself and keep spreading kindness wherever you go.

I would also like to thank friends from the Boyz Group, Graduate House, the Bhangra Group, the Avalon Group, and my Bengali friends that I made during my time at Waterloo.

Last but not the least, I would like to thank the Natural Sciences and Engineering Research Council (NSERC) and Ecosynthetix for their financial support.

Dedication

I am dedicating this dissertation to the loving memory of my grandmother, Pratima Gupta (1947-2016). My grandmother loved me wholeheartedly and made my childhood memorable. I wish she were here to witness my graduation; may Krishna guide her soul to heavenly abode. I would also want to dedicate it to my mother, Sarbani Dasgupta, for her immeasurable sacrifices in raising me to be an educated, but above all, a good human being.

"Persistence refines the miserable

piece of carbon in you into

the purest form of diamond"

-Anonymous

Table of Contents

List of Figures

List of Tables

List of Schemes

List of Abbreviations

ACS	American Chemical Society
ANOVA	Analysis of variance
A_o	Absorbance at time t = 0
AOP	Advanced oxidation processes
A_t	Absorbance at time t
ATR-FTIR	Attenuated total reflectance-Fourier-transform infrared spectroscopy
ATRP	Atom transfer radical polymerization
b	Block
CAN	Ceric ammonium nitrate
Chito	Chitosan
CHWE	Clark hot water extraction
C_o	Concentration at time t = 0
C_t	Concentration at time t
d	Day(s)
DLS	Dynamic light scattering
DMEM	Dulbecco's modified Eagle's medium
DMF	N,N-Dimethylformamide
DMSO	Dimethyl sulfoxide
DS	Degree of substitution

DSC	Differential scanning calorimetry
DVB	Divinylbenzene
ECS	Expanded corn starch
FBS	Fetal bovine serum
FTIR	Fourier-transform infrared
g	Graft, grafted
GPC	Gel permeation chromatography
GPy	Glucopyranose
h	Hour(s)
HCEC	Human corneal epithelial cells
HEA	2-Hydroxyethyl acrylate
HLB	Hydrophilic-lipophilic balance
HPLC	High-performance liquid chromatography
Ioos	Imperial Oil oil sands
KM	Keratinocyte medium
LAM	Less activated monomers
LCAT	Lower critical aggregation temperature
LCST	Lower critical solution temperature
M	Molar
MAM	More activated monomers

MB	Methylene blue
MEO_2MA	Di(ethylene glycol) methyl ether methacrylate
min	Minute(s)
M_n	Number-average molecular weight
Mt^n/L	Transition metal species in oxidation state n, with ligand L
M_w	Weight-average molecular weight
MWCO	Molecular weight cut-off
NMP	Nitroxide-mediated polymerization
NMR	Nuclear magnetic resonance
NNPAM	N-*n*-propylacrylamide
PAMs	Polyacrylamide(s)
PANI	Polyaniline
PDI	Polydispersity index
PEG	Poly(ethylene glycol)
PGMA	Poly(glycidyl methacrylate)
PHEA	Poly(2-hydroxyethyl acrylate)
$P_m•/ P_n•$	Polymeric radical
PMDETA	N,N,N′,N″,N″-Pentamethyldiethylenetriamine
$PMEO_2MA$	Poly(di(ethylene glycol) methyl ether methacrylate)
PMMA	Poly(methyl methacrylate)

PNIPAM	Poly(N-isopropylacrylamide)
PNNPAM	Poly(N-*n*-propylacrylamide)
POEGMA	Poly(oligo(ethylene glycol) methacrylate)
PVAc	Poly(vinyl acetate)
R·	Alkyl radical
RAFT	Reversible addition-fragmentation chain transfer
RBF	Round-bottom flask
RDRP	Reversible deactivation radical polymerization
RI	Refractive index
RO_2·	Alkyl peroxide radical
s	Second(s)
SAGD	Steam-assisted gravity-drainage
Sbos	Alberta Innovate Technology Futures Sample Bank oil sands
SI	Swelling index
SNPs	Starch nanoparticles
St	Starch
tcp	Tissue culture plate
TCPS	Tissue culture plate surface
TEM	Transmission electron microscopy
TEMPO	4-Hydroxy-2,2,6,6-tetramethylpiperidin-1-oxyl

THF	Tetrahydrofuran
TOC	Total organic carbon
UCST	Upper critical solution temperature
wt%	Weight percent
X_n	Number-average degree of polymerization
XRD	X-ray diffraction
ΔG_{mix}	Gibbs free energy of mixing
ΔH_{mix}	Enthalpy of mixing
ΔS_{mix}	Entropy of mixing
λ	Wavelength
θ_c	Contact Angle

Chapter 1

Foreword, Background and Literature Review

1.1 Opening Remarks

Starch is a renewable, biodegradable material and the most common carbohydrate in human diet, but it also has multiple non-food applications. For example, it is currently used as a filler in petrochemical-based materials to generate plastics with enhanced biodegradability.[1] Starch is added to yarns to improve their mechanical strength and resistance to moisture.[2] It also serves in the soap industry, to produce skin-friendly biodegradable detergents.[3] Due to the presence of hydroxyl groups in its glucopyranose (Gpy) units, starch is hydrophilic and can be modified by conducting reactions in water for the development of new starch-based products.

Chitosan is another polysaccharide derived from naturally occurring chitin, the second most abundant polysaccharide,[4] through partial deacetylation. Chitosan has several industrial and biomedical applications in areas such as food products, pharmaceuticals, packaging, cosmetics, textiles, and agriculture.[5] It is non-toxic, biodegradable, biocompatible, and has antimicrobial properties.[6] Its main drawback is that at physiological pH, it is insoluble; it can be dispersed in dilute acidic solutions, which limits somewhat its potential applications, but it has nevertheless remarkable film-forming properties. These films are transparent and have good mechanical properties; thus chitosan-based composites are now being utilized for packaging.[7] Chitosan has hydroxyl groups like starch, but also highly reactive amino groups that may be exploited to make a range of new products.

1.2 Research Objectives and Thesis Outline

The common objective of the projects described in this thesis was to modify two common polysaccharides, namely starch and chitosan, for specific applications. Unmodified starch has been used widely as a colloidal stabilizer in the formation of complexes with metallic salt nanoparticles in solution. Thermoresponsive polymers are also of interest for various applications. The combination of polysaccharides with thermoresponsive polymers should lead to unique properties, combined with high biocompatibility and biodegradability. Some of these materials have been used, among others, in biomedical applications such as gene delivery and tissue engineering.[8] "Living" radical polymerization methods, also known as reversible-deactivation radical polymerization (RDRP) techniques, have been mainly employed to synthesize thermoresponsive polymers.

The thesis consists of six chapters. Following this brief foreword, a literature review is presented which provides background information subdivided into sections on starch, chitosan, thermoresponsive polymers, and their modification in relation with applications. The synthesis of thermoresponsive starch nanoparticles (SNPs) by grafting with poly(di(ethylene glycol) methyl ether methacrylate) ($PMEO_2MA$) is described in Chapter 2. The synthetic methods developed provide easy control over the characteristics of the grafted SNPs (number and length of grafted $PMEO_2MA$ segments), and therefore over the hydrophilic-lipophilic balance (HLB) of the nanoparticles. The application of these modified SNPs in the extraction of bitumen from tar sands on a laboratory scale was explored in Chapter 3. These amphiphilic nanoparticles

provide a sustainable alternate method for the treatment of oil sands. The preparation and the use of starch-stabilized iron (Fe^{2+}/Fe^{3+}) oxide nanoparticle complexes as catalyst systems for Fenton reactions is investigated in Chapter 4. The hydrophilicity of starch allowed the formation of colloidally stable iron oxide nanoparticles in aqueous solutions, enabling Fenton reactions to degrade methylene blue at pH values closer to neutrality. Chapter 5 concerns the development of thermoresponsive chitosan films grafted with $PMEO_2MA$, and their application in cell culture. Thermoresponsive chitosan allowed the cells to grow at physiological temperature, to be released at temperatures below the lower critical solution temperature (LCST) of the modified thermoresponsive chitosan.

This thesis is concluded in Chapter 6 with a general overview of the results obtained, concluding remarks drawn from the results, a summary of original contributions to knowledge, and suggestions for future work.

In agreement with the University of Waterloo thesis guidelines, Chapters 2–5 are written in the format of individual manuscripts to be submitted for publication in scientific journals. Each chapter includes an abstract, an introductory section providing background related to the topic explored, detailed experimental methods, the discussion of results, and conclusions.

1.3 Background Information

Polysaccharides have sparked a lot of interest in recent decades as biodegradable polymers in a variety of applications. These biomaterials are essentially polymeric carbohydrates,

consisting mainly of monosaccharide units connected through glycosidic linkages. The resulting chains can be linear or branched, depending on the linking mode of the building blocks. Polysaccharides are widespread in plants, bacteria, algae, fungi, and animals.[9] Structural polysaccharides like chitin and cellulose serve as scaffold materials in crustaceans and plants, respectively, while starch is used for energy storage in plants.[10] In turn, humans use starch as an energy source and store excess energy as glycogen, a material chemically similar to starch but with a more densely branched structure.[11] In nature, bacterial polysaccharides can also engulf bacteria to form biofilms causing dental plaque and metal corrosion, or serve as support for the growth and the propagation of disease-causing pathogens.[9]

One of the most pressing eco-technological issues is the treatment of plastic waste.[12] Polysaccharides can serve as substitutes for some petroleum-based products, allowing the development of more sustainable and environmentally friendly products due to their ability to be degraded by microorganisms and enzymes.[13] Plasticized starch products are an interesting option to achieve this, in that they are entirely biodegradable materials containing more than 40% starch, with the balance made up of biodegradable additives. Their mechanical properties can be comparable to polypropylene and other popular plastics. These materials are currently used in food processing and by food services. Starch has been investigated extensively to prepare biodegradable plastics, but other notable plastics derived from polysaccharides include cellulose acetate, chitosan, and soy-based plastics.[12] Polysaccharides are also essential for applications in the pharmaceutical industry.[14] For example, starch is a precursor in the synthesis of cyclodextrins

serving as complexing agents,[15] and cellulose has been used for drug delivery.[16] Another option being explored is the addition of starch as a filler in synthetic petroleum-based plastics, to facilitate their disintegration.[17] This is because starch degradation generates pores in starch-resin blends, which can accelerate the slow degradation of synthetic plastics.[17] Chitosan can be modified to create mucoadhesive polymers for the treatment of gastrointestinal infections.[18] Other applications of chitosan include treating lead and mercury poisoning,[19] as coagulating agents,[20] and in drug delivery.[18] Polysaccharides are therefore not only valuable food ingredients, but also have many other uses. While research is ongoing to scale-up laboratory processes, many of these materials are already marketed by the industry and are being mass-produced. Polysaccharides thus provide cost-effective and environmentally safe long-term solutions for various applications.

1.4 Starch

Plants generate and store starch as a long-term energy source. Starch is made up of two main polymers, amylose and amylopectin, and is a natural, biodegradable material. Amylose is a mostly linear polysaccharide that accounts for 15–35% of plant starch granules.[1] It is made up of D-anhydroglucose units linked together by α-(1,4) glycosidic linkages (Figure 1-1). Amylopectin, unlike amylose, has a branched structure with a backbone made up of α-(1,4) glycosidic linkages, and about 5% of α-(1,6) linked branches (Figure 1-1). Amylose-rich starch typically has a molecular weight of 10^5–10^6 g/mol, while the molecular weight of amylopectin-

rich starch can reach over 10^7 g/mol.[21] Starch can be isolated from rice, oat, peas, wheat, tapioca, potatoes, corn, and other plants.[1] In year 2000, starch production was about 48 million tons per year.[22] This shows that starch is of interest to the industry and academia for high-value applications.

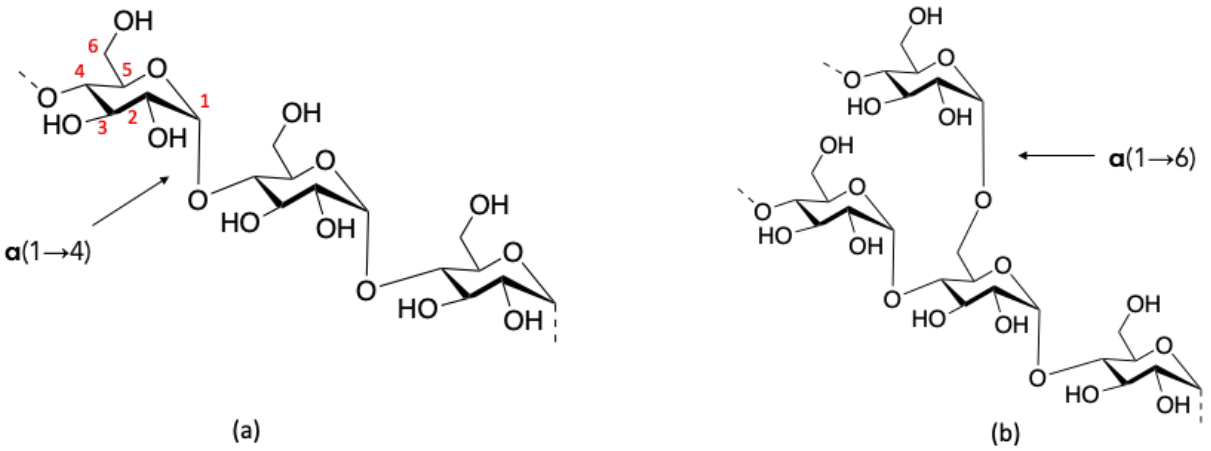

Figure 1-1: Chemical structure of a) amylose and b) amylopectin. The carbon atoms in the GPy unit of amylose are numbered from 1–6.

Starch granules consist of concentric alternating amorphous and semi-crystalline growth rings, as determined by X-ray diffraction (XRD) and microscopy, and shown in Figure 1-2. The granules (a) include growth rings (100–500 nm) (b), made up of blocklets (d) comprising alternating amorphous and crystalline lamellae (c), containing glucose units (0.3–0.5 nm) in

amylopectin (g) and amylose chains (h).[23] The amorphous core of the starch granules consists mostly of amylose in non-waxy starches, and disordered amylopectin surrounds the amylose in a concentric pattern, while the blocklets are semi-crystalline domains containing amylose and amylopectin arranged in crystalline and amorphous lamellae alternating every 9–11 nm (Figure 1-2). The organization of amylose and amylopectin in blocklets is the key to the reactivity of starch granules.[24,25] Reactions may occur on the surface, or in the interior of the granules, depending on the ability of reagents to penetrate them. The polar nature of the granule surface, and capillaries between the granules allow starch to absorb solvent and to swell, improving their reactivity.[26] As shown in Figure 1-2, the most commonly accepted model for amylopectin is a tree-like structure, where helical clusters are surrounded by longer chain segments.[23] Amylose chains are scattered around the amylopectin clusters, facing the outside of the granules.[23]

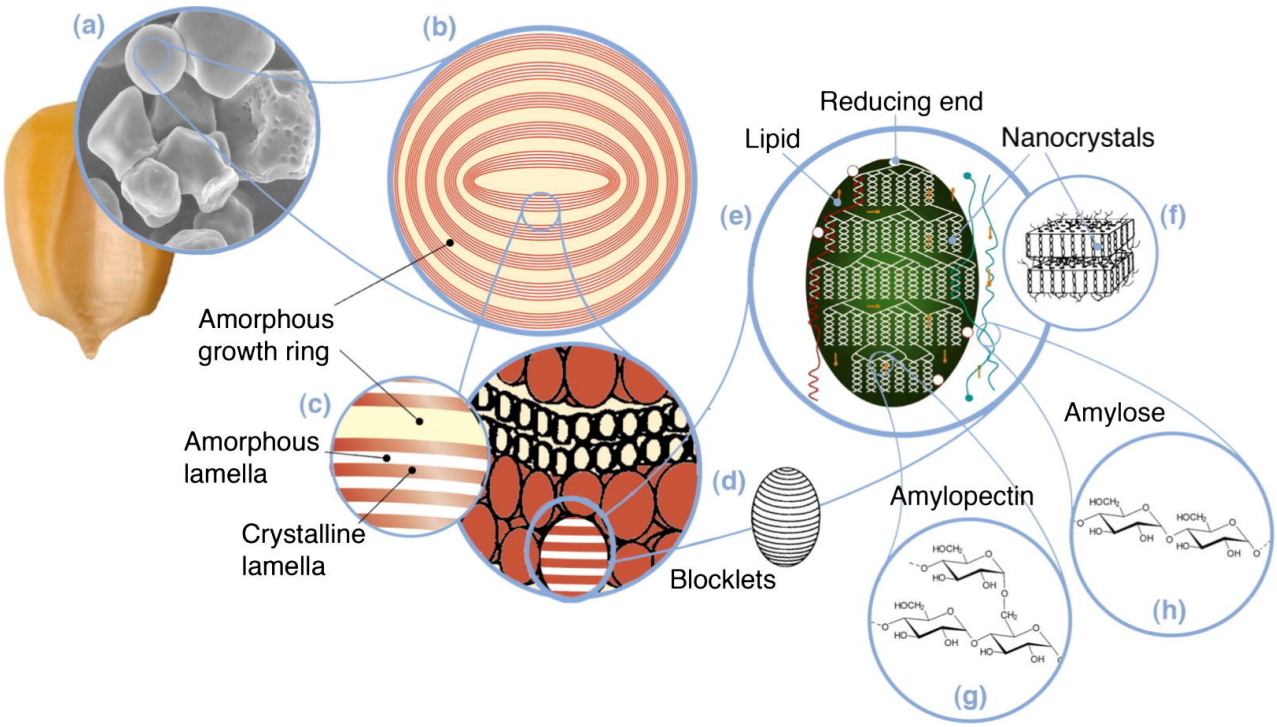

Figure 1-2: Structure of a starch granule. Reprinted with permission from reference 22. Copyright (2010) American Chemical Society.

Starch in its native granular form has several limitations such as a high viscosity and limited dispersibility in water. Gelatinization is a process whereby starch is subjected to heat in the presence of water and shear forces.[23] During heating water diffuses into the amorphous regions, and along with heat and shear, disrupts the crystalline regions.[23] The native starch granules swell as water occupies the tightly bound amylopectin regions, and the amylose chains start to dissolve. The crystalline regions then become amorphous and gradually collapse to form

a paste.[23] When the starch paste is cooled, the amylose and amylopectin chains can realign and start forming crystalline domains again (albeit not to the extent present in the starch granules), whereby the starch molecules aggregate to form a gel in a process known as retrogradation.[27] The gel is formed due to hydrogen bonding between water, amylose, and amylopectin. Amylopectin forms a soft gel, while the gel formed by amylose is more rigid. Starch undergoing gelatinization (and potentially retrogradation) is commonly known as cooked starch. Instruments such as a Brabender Viscoamylograph or a differential scanning calorimeter can be used to examine the properties of starch during and after gelatinization and retrogradation.[28]

Starch can be a more versatile material in the absence of crystalline domains. Since pure starch cannot flow below its decomposition temperature, plasticizers facilitate its uses in a more malleable form.[29] Plasticizers are additives that decrease the viscosity of starch by increasing its free volume. They are essentially solvents with low volatility, reducing intermolecular forces between the polymer chains.[30] Thermoplastic starch is a plasticized form of starch which can flow at moderate temperatures. It is typically prepared with low water contents, using heat and shear forces in the presence of polyol plasticizers such as glycerol and sorbitol.[31] This reduces the glass transition temperature of starch, making it more ductile at lower temperatures, and improves its resistance to impact.[31]

1.4.1 Starch Nanoparticles (SNPs)

Starch nanoparticles are starch fragments with a size on the order of 100 nm, and properties different from cooked starch. The botanical origin, preparation technique, and the amylose/amylopectin ratio of the starch granules all influence the size of the SNPs obtained. For higher amylose concentrations, larger nanoparticles are typically obtained.[32] Reactive extrusion, in which the starch is exposed to water or other plasticizers under high pressure, temperature, and shear, in the presence of cross-linking agents, is the most common industrial method to produce SNPs.[33] For example, Liu *et al.* employed a high-pressure homogenization process to disperse starch granules in water. After subjecting a 5% starch slurry to 20 homogenization cycles through a specifically built microfluidizer at a pressure of 207 MPa, the size of the starch particles was reduced from 3–6 μm to 10–20 nm.[34] The SNPs formed had improved dispersibility in water, while maintaining a crystalline structure and thermal stability comparable to starch granules.[34] Giezen *et al.* were granted the first patent on starch nanoparticle production by starch extrusion in year 2000, whereby a twin-screw extruder was used to generate particles in the 400 nm range,[35] while Song *et al.* was able to bring the size down to 160 nm by introducing a cross-linking agent in the process.[33] Giezen *et al.* demonstrated that a high yield of SNPs was achievable at high solids contents (~ 65%), making the process environmentally friendly due to the use of a substantially lower quantity of water.[35] Eco-Sphere™ are SNPs commercially produced by EcoSynthetix. They are currently used as binder in paper mills, by replacing petroleum-based products such as styrene-butadiene and styrene-acrylate polymer latexes. The

use of EcoSphere leads to price stability, as its price does not depend strongly on oil prices, leading to savings and most importantly, environmental benefits.[36] The biobased nanoparticles are synthesized by extruding the starch granules in a continuous process, whereby the solid granules are converted into a thermoplastic melt phase, and then cross-linked into starch nanoparticles.[36]

Beyond mechanical treatments, milder methods have also been developed to produce starch nanoparticles. For example, Ma *et al*. obtained SNPs by precipitating gelatinized starch in ethanol.[37] The SNPs obtained were smaller when a surfactant was added in the process, with sizes in a range of 50–100 nm.[37] After determining that enzymatic hydrolysis was insufficient on its own, Sun *et al.* used a combination of enzymatic hydrolysis and recrystallization to create SNPs with sizes between 20 and 100 nm.[38] Gelatinized starch was allowed to retrograde for 12 hours before it was digested with pullulanase, after which a high yield of SNPs was attained.[38] Kim *et al.* were successful in further reducing the size of SNPs to 10–20 nm by combining *n*-butanol precipitation with enzymatic hydrolysis.[39]

SNPs are safe for human consumption, but can also serve in industries catering non-food applications. For example, modified SNPs have been employed as novel drug carriers and emulsion stabilizers.[32] Beyond their application as binders and for paper coating in paper mills, by replacing petroleum-based products such as styrene-butadiene and styrene-acrylate polymer latexes,[36] SNPs have also been used in the replacement of poly(vinyl acetate), commonly used as wood glue.[36]

1.4.2 Chemical Modification of Starch

The chemical modification of starch mostly takes advantage of the many hydroxyl groups present in the molecules. The extent of modification in starch is often described by the degree of substitution (DS), defined as the average number of hydroxyl groups modified per GPy unit of starch. The GPy units in amylose contain a primary hydroxyl group at the C6 position and secondary hydroxyl groups at the C2 and C3 positions. Each β-(1,6) branching in amylopectin reduces the number of primary hydroxyl groups at C6 by one. Thus, due to the presence of 3 hydroxyl groups per GPy unit, the maximum theoretical degree of substitution (DS) of starch is 3.

Some of the techniques used to characterize the chemical modification of the hydroxyl groups on starch include ^{1}H nuclear magnetic resonance (NMR) and Fourier-transform infrared (FTIR) spectroscopy. For ^{1}H NMR, the anomeric proton on C1 is usually compared with protons on the modified groups attached to starch. A limitation of this technique is that there should be protons present on the modified groups, and they should not overlap with the anomeric proton signal. For example, in xanthated starch (Scheme 1-1a), there are no detectable protons on the xanthate group attached to starch. ^{13}C NMR may still be used, but compared to ^{1}H NMR, it has a lower sensitivity and requires a longer analysis time. Another example is fatty acid starch esters synthesized by Muljana *et al.*, for which the olefinic protons of fatty acid chains overlapped with the anomeric proton signal.[40] FTIR analysis can also serve to detect modified groups on starch.

For example, the etherification of starch with maleic acid derivatives produced starch-diethyl maleate, starch-dipropyl maleate, and starch-dibutyl maleate.[41] The presence of absorption bands at 1721, 1550 and 1126 cm^{-1} representing the stretching of the maleate C=O, the C-H adjacent to the carbonyl group, and the C-O-C groups, respectively, in the modified starch confirmed the success of the reactions,[41] while these peaks were not observed in the FTIR spectrum of the unmodified starch. Forrest *et al.* analyzed the extent of hydroxypropylation after reacting starch with propylene oxide (Scheme 1-1b, where R represents a methyl group), since the absorbance bands specific to the methyl group were identified as a C-H deformation at 1350–1475 cm^{-1}, and a C-H stretch at 2850–3000 cm^{-1}.[42] Even though this characterization method for hydroxypropylation was relatively easy and quick, it was not suitable for quantification due to the contribution of the C-H stretch from unmodified starch at 2974 cm^{-1}.[42] Some of the chemical modifications of starch such as esterification, etherification, oxidation, and grafting of vinyl monomers to starch are discussed in Sections 1.4.2.1–1.4.2.4.[26,43,44]

1.4.2.1 Esterification and Etherification

The hydroxyl groups of the starch backbone can be esterified with acids or carboxylic acid derivatives. There are two types of starch esters, namely organic and inorganic.[43]

Starch phosphates naturally occur in the amylopectin of potato starch, where phosphate groups are attached to the primary alcohol of one out of every 212–273 GPy units.[26] Starch nitrates are the oldest starch derivatives produced commercially, which can be obtained by

dissolving starch in chilled nitric acid and precipitating the product by adding water.[45] They were considered excellent explosives used for mining and quarrying.[45] Starch sulfates can be formed by esterifying starch with sulfuric acid.[45] Both starch nitrates and sulfates have molecular weights lower than native starch, as the starch backbone is prone to hydrolysis when exposed to acids. Xanthation is another form of esterification, whereby thiocarbonylthio groups are introduced by reacting starch with carbon disulfide in the presence of a base (Scheme 1-1a).[46] The properties of starch xanthates are determined by reaction conditions such as the reagent concentration, temperature, and duration. To obtain 5–20% xanthation per GPy unit (DS = 0.05–0.20), 20–25 mL of carbon disulfide can be reacted with 10 g of starch and 3 moles of NaOH at room temperature for 24 h.[26] The reaction temperature is a critical parameter, as sodium hydroxide reacts with carbon disulfide to form trithiocarbonate above 49 °C.[47] Xanthates can serve as flocculants for coal powder,[48] to collect heavy metal ions,[46] and as solvents to produce sulfide dyes.[26] Xanthates are also used as additives in the paper industry, to improve the strength and foldability of paper.[26]

The hydroxyl groups in starch can be deprotonated with a base, and nucleophilic attack of the alkoxide anions on the carbonyl group of acid anhydrides, cyclic anhydrides (Scheme 1-1c), and acid chloride (Scheme 1-1d) yields organic starch esters. For example, starch can be reacted with acetic anhydride in the presence of pyridine, serving as both catalyst and solvent, to produce starch acetate.[49] The presence of water is one of the most significant limitations in organic starch ester synthesis, as it competes with the hydroxyl groups of starch and forms carboxylic acids by

reacting with acid chlorides and anhydrides. As a result, low DS starch esters are formed in water, which are less hydrophobic.[50] When reactions are carried out in an organic solvent such as pyridine, the starch esters have a high DS, increased thermoplasticity, and hydrophobicity.[43]

The etherification of starch can improve its thermal stability.[43] Typically, starch is etherified with alkenyl oxides (Scheme 1-1b) or alkyl chlorides (Scheme 1-1e) in water or DMSO. Commercially, starch etherification conducted in water results in DS levels up to 0.4, while maintaining the granular structure of starch.[51] Similarly to cyclic anhydrides, nucleophilic attack of the deprotonated hydroxyl groups on the epoxide ring of alkenyl oxides results in ether linkage formation and generates another hydroxyl group, with no by-products in the reaction.[21] In contrast, reactions with alkyl chlorides results in the formation of chloride ions (e.g. NaCl) that need to be removed to purify the etherified starch. Cationic and anionic starches can also be produced by etherification. The cationic modification of starch is typically achieved by introducing ammonium groups,[52] and amylopectin-rich starch yields a higher DS. For example, Almonaityte *et al.* modified starch with 3-chloro-2-hydroxypropyltrimethylammonium chloride and achieved DS values of up to 0.84 in the presence of calcium oxide, but the DS dropped to 0.28 in the absence of calcium oxide.[53] It was found that calcium oxide allowed the reaction to proceed in the deeper layers of the starch granules, resulting in a more uniform distribution of cationic groups.[53] Haack *et al.* similarly reacted starch with 3-chloro-2-hydroxypropyltrimethylammonium chloride in a sodium hydroxide solution and obtained DS values up to 1.05, which did not increase further upon increasing the reagent concentrations, due

to starch swelling leading to a gel-type consistency in the initial stage of the reaction.[54] Cationic starches are effective flocculants for wastewater sludge, whose effectiveness strongly depends on the DS.[54] Recently, these materials were also explored as flocculants for oil sands mature fine tailings.[55] Anionic ether starches such as carboxymethyl starch (CMS) are manufactured on a large scale to serve as thickeners, binders, and emulsifying agents.[43] Stojanovic *et al.* synthesized CMS by reaction with monochloroacetic acid in the presence of sodium hydroxide. For a reaction mixture with monochloroacetic acid and NaOH in a molar ratio of 6.83, the highest DS obtained was 0.6.[56] Hydrolysis of the alkyl halide is a side reaction that can be regulated by reducing the amount of water used in the reaction, although some water is required to swell the starch granules.

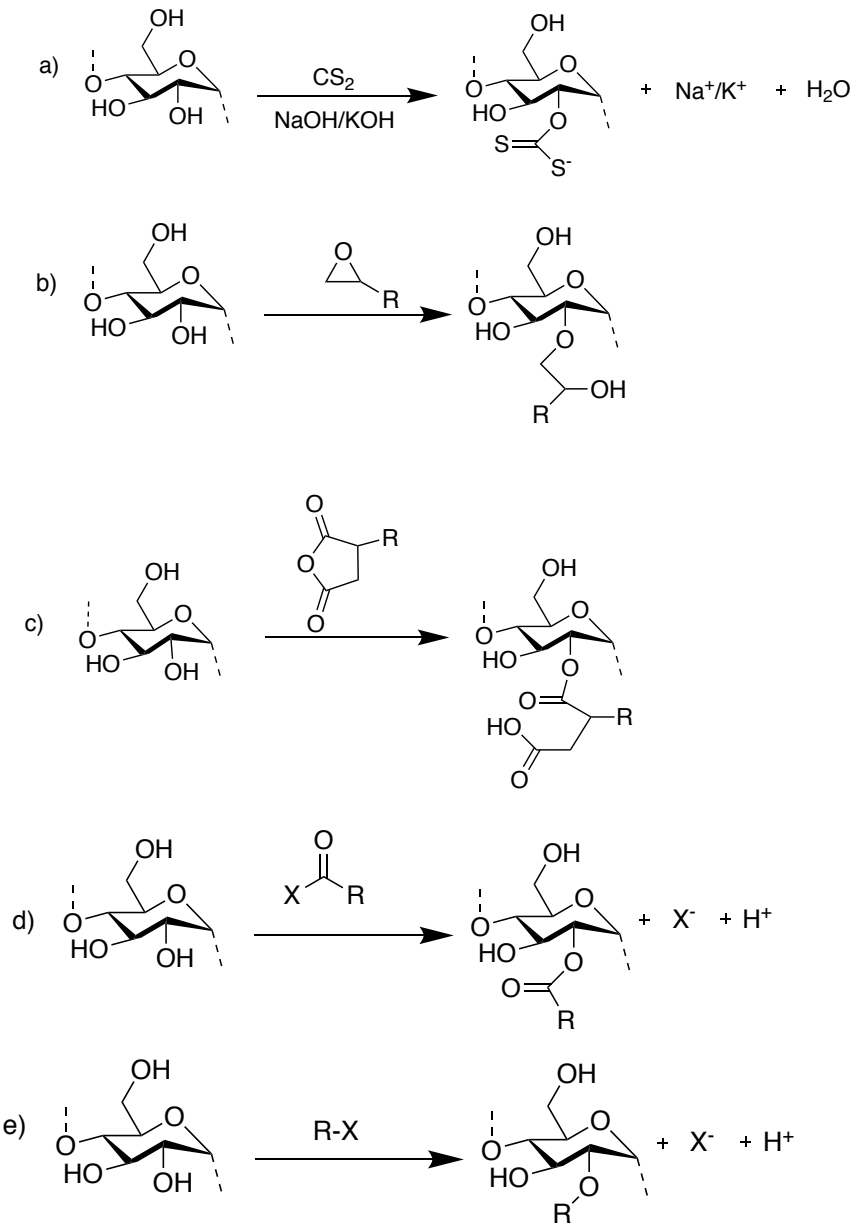

Scheme 1-1: Reaction of starch with a) alkenyl oxide, b) carbon disulfide (xanthation), c) cyclic anhydride, d) acid chloride, and e) alkyl halide, where R is an aliphatic group and X is a halide.

1.4.2.2 Oxidation

Different reagents such as NaOCl, H_2O_2, and ozone can be used to oxidize starch. The paper industry has been using NaOCl to oxidize starch for over 150 years, using it as sizing agent to improve the mechanical properties of paper and paper board.[57] Starch oxidation can take place at the C2, C3, and C6 positions, whereby the hydroxyl groups are first converted to carbonyl groups, and then to carboxylic acids. The extent of oxidation is determined by the proportions of carbonyl and carboxylic functional groups present. The oxidation of starch by NaOCl depends on several factors such as the pH, the reaction time and temperature, the NaOCl concentration, and the origin of the starch.[57] Partial depolymerization can take place as the hydroxyl groups are oxidized to carbonyls and carboxylic acids, with amylose being more prone to degradation than amylopectin.[58] NaOCl oxidation is strongly pH-dependent,[57] and mildly to moderately alkaline conditions are preferred due to the production of carboxyl groups, which stabilize the viscosity of the starch solutions and prevent their retrogradation.[57] For example, Sanchez-Rivera *et al.* obtained a high DS of 0.33 for carboxyl groups in the oxidation of banana starch with NaOCl at pH 11.5 for 4 h, as compared to a DS of 0.08 at pH 7.5.[59] On the other hand, Sangseethong *et al.* reported higher DS values of carbonyl (0.25) and carboxyl groups (0.85) for cassava starch at pH 7–8, regardless of the reaction duration from 25–300 min.[60] Thus, not only the pH and the reaction time, but also the origin of the starch are critical for starch oxidation. Kuakpetoon *et al.* oxidized potato, rice, and maize starch with NaOCl by dispersion in water with 8 wt% NaOH and 2 wt% of NaOCl at pH 9.5. When the reaction was allowed to proceed for 50 min, the highest

DS (0.21) was achieved for potato starch, followed by rice and maize starch.[61] It was shown by small-angle X-ray scattering that oxidation occurred mainly in the amorphous regions, and that the crystalline domains were more difficult to oxidize.[62,58] H_2O_2 has also been used to oxidize starch, albeit not commercially. In contrast to NaOCl, H_2O_2 does not form any harmful byproducts. In the presence of a metal catalyst, H_2O_2 readily decomposes to hydroxyl radicals, a potent oxidizing agent. Tolvanen *et al.* thus oxidized potato starch with 30 wt% H_2O_2 and iron tetrasulfophthalocyanine as catalyst in a semi-batch glass reactor at 55 ^oC.[63] At pH 7 the catalyst was inactive, but the highest DS of 0.53 for carbonyls was achieved at pH 8.4, while the maximum DS of 0.16 for carboxyl groups was obtained at pH 10.[63] While NaOCl and H_2O_2 are the most extensively studied oxidizing agents, they may lead to undesirable by-products. Oxidation with ozone is a cleaner technique, as the final products are carbon dioxide, water, and less toxic by-products. This was achieved by Chan *et al*. for corn, sago and tapioca starch over 10 min in a reaction vessel connected to an ozone generator.[64] The DS of the oxidized starches ranged from 0.061–0.25, with a combination of carbonyl and carboxyl groups.[64] Significant limitations of ozone oxidation include a decrease in molecular weight due to depolymerization, and an increase in polydispersity index (PDI) as compared to the unmodified starch.[64] It can also be expensive to set up and operate an ozone generator, and ozone readily decomposes to hydroxide ions in alkaline media.[65] Some by-products of starch oxidation with ozone are small molecules including glucaric, glucuronic, gluconic, and oxalic acids.[26]

1.4.2.3 Metal Starchates

The stabilization of metallic nanoparticles with starch, acting as ligand for the metal, is relevant to many applications in the pharmaceutical and biomedical areas.[66] Since starch is soluble in water, its incorporation as a steric stabilizer improves the dispersibility of metallic nanoparticles in aqueous environments.[67] Hydrogen bonding in starch can inhibit metallic nanoparticle aggregation and shield them from external environmental stresses.[68] As a result, such complexes are stable in liquids for extended time periods in comparison to bare metallic nanoparticles. The weak starch-metal OH group interactions are reversible at high temperatures, allowing particle separation and surface modification via ligand exchange.[67] The lone electrons of the oxygen atoms in starch can form Werner complexes through coordination, in which case amylose and amylopectin act as ligands for the metal atoms.[14] The secondary alcohols on the C2 and C3 atoms of the GPy units are primarily involved in coordination.[14] For example, metal alkoxides of Cr(III), Mg(II), Mo(V), V(III), and W(V) were reacted with pregelatinized starch (1:1 molar ratio) under solid-state conditions in a microwave-assisted process.[69] This resulted in cross-linking of the starch, as the metals can coordinate with two GPy units on different starch chains. The Cr(III) and V(III) complexes were found to hydrolyze entirely in water, while the other metal complexes only hydrolyzed partially.[69] Werner complexation depends upon the orientation of the ligating groups, and complex stability is related to the dimensions of the ligands.[70] Thus, Cu(II) forms stable starch-Cu(II) complexes in the presence of acetate and chloride counter-ions, but not in the presence of nitrate counter-ions,[70] while Ni(II) coordinates

with the GPy units irrespective of the counter-ion type present.[14] Werner complexes of starch with Mn(II), and Co(II) were found most stable.[14] With the exception of lithium, most alkali metal ions form Werner complexes with starch.[14]

In particular, starch has been documented as a "capping" agent in the precipitation of mixtures of ferric and ferrous salts to produce iron oxide nanoparticles, as starch can bind to the metal oxide under certain conditions,[71] or with heat treatment.[72] For example, Somsook *et al.* heated an aqueous starch suspension at 90 ^{o}C for 1 h before adding an $FeCl_3$ solution and adjusting the pH to 9 with NaOH. After stirring for 2 h the solution was centrifuged, and the starch-stabilized iron oxide particles were washed and collected. The authors could not determine how the Fe^{3+} ions interacted with starch with certainty, but suggested two models.[73] In the site-binding (Werner complex) model, the hydroxyl groups of starch were assumed to coordinate Fe^{3+} individually along the polysaccharide backbone. Conversely, the colloidal model assumed that iron precipitated as FeOOH colloidally stabilized by the hydrophilic starch in solution.[73] Janardhanan *et al.* dissolved starch and $FeSO_4{\cdot}7H_2O$ in water for 30 min before the solution was evaporated and then calcinated at 800 ^{o}C for 2 h, thus using starch as a template for the synthesis of iron oxide nanoparticles.[72] The average size of the iron oxide nanoparticles was 130 nm, much smaller and more uniform than in the absence of starch.[72]

In the textile industry, starch-metal complexes are used for dyeing.[14] These complexes can also absorb heavy metal ions from solutions.[74] Starch in combination with d-group metal ions has been used as curing agent for burns and wounds, and a few skin and hair care products

contain starch-metal complexes.[75] Aluminium starchate has been tested to treat gastrointestinal ulcers.[76] Anti-mold additives include arsenous, cupric, and titanium starchates to manufacture paperboard and plywood.[14]

1.4.2.4 Polymer-grafted Starch

While starch is a high molecular weight polymer of GPy units, graft polymerization further increases its molecular weight.[26] Graft polymerization uses an initiator to create radical sites on the starch substrate, to which vinyl monomers are added through radical polymerization.[77] Irrespective of the exact method employed to generate radical centers, graft polymerization involves initiation, propagation, and termination as essential steps. The radicals are introduced on starch by hydrogen radical transfer to the initiator in the initiation process. The radical sites on the starch then react multiple times with vinyl monomers in the propagation step. The termination of chain growth can involve two reactive radical-carrying chains, chain transfer to the initiator, or other side reactions. The polymer-grafted starch can be purified by removing any homopolymer contaminant, for example by Soxhlet extraction or dialysis.[78]

1.4.2.4.1 Free Radical Polymerization

Cerium(IV), or ceric salts, can form redox initiator systems with alcohols, thiols, glycols, aldehydes, and amines.[79] Cerium(IV) is thought to form intermediate complexes with starch

before undergoing reduction to Ce(III), generating radical centers on the starch backbone (Scheme 1-2).[77] This is the most commonly used initiator system to graft polymers onto starch by a free radical mechanism. One significant advantage of this approach is that the product obtained may contain very little, if any, non-grafted polymer because the radicals are only generated on the starch backbone. Furthermore, the reaction can also be carried out at room temperature.[77] On the other hand, the Cerium(IV)-starch system can only be applied to a limited number of monomers. For example, the reaction with a mixture of styrene and acrylonitrile yielded starch-*g*-poly(acrylonitrile-*co*-styrene), while styrene by itself did not react.[80] Other monomers that could be grafted with different degrees of success by that approach are vinyl acetate, acrylates, alkyl methacrylates, and acrylic acid.[81,78] Li *et al.* grafted methyl methacrylate (MMA) onto corn starch with cerium (IV) ammonium nitrate (CAN) as initiator at 40 °C for 3 h.[82] The reaction had a 92% grafting efficiency for a GPy to MMA molar ratio of 0.67, dropping to 75% when the ratio was decreased to 0.43.[82] As expected, the molecular weight of the grafted product increased with the MMA concentration in the reaction. Lai *et al.* used gelatinized starch and vinyl acetate in combination with a 0.6 M of CAN and 0.5 N nitric acid solution at 50 °C for 4 h.[83] The monomer conversion reached 85%, but the grafting efficiency was only 16%. This is because VAc can also homopolymerize in the presence of CAN, which creates radicals directly on the monomer.[84]

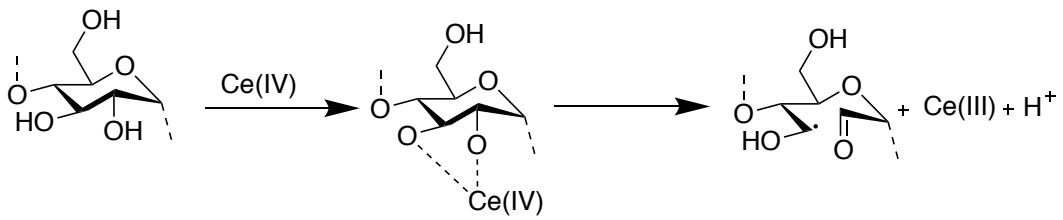

Scheme 1-2: Reaction of starch with Ce(IV) to generate radicals on the starch backbone.

The thermal decomposition of free radical initiators can be used to graft polymers onto starch by abstracting hydrogen radicals from the substrate, albeit in that case a significant amount of homopolymer contaminant is also formed due to direct initiation of the polymerization by the initiator radical fragments. The reaction is conducted at a temperature providing a sufficient rate of thermal initiator decomposition, but while an increase in the number of radicals generated promotes propagation, it also increases the rate of termination. Thus, for each initiator, there is an optimal temperature maximizing the grafting efficiency. Benzoyl peroxide was used successfully to graft poly(acrylic acid), poly(methyl methacrylate), and polymethacrylamide on hydrolyzed starch at temperatures above 70 °C.[78] Other thermal initiators such as potassium or ammonium persulfate were also used to generate active sites on starch above 60 °C, and to graft poly(alkyl methacrylates) onto starch.[78,85] The grafting efficiency was found to decrease as the length of the methacrylate alkyl chain increased, presumably due to steric hindrance, similarly to Ce(IV) activation.[78,85] Acrylamides, acrylic acid, methacrylic acid, and styrene are several other monomers grafted onto starch with potassium persulfate as initiator.[86,87,88] The grafting

efficiency was less than 70% in most cases with thermal initiators. Hebeish *et al.* compared the grafting of acrylamide onto starch with potassium persulfate and benzoyl peroxide. When the reaction was performed for 4 h at 60 °C with potassium persulfate the grafting efficiency reached a maximum of 32%, as compared with 25% when the reaction was carried out at 75 °C for 6 h with benzoyl peroxide.

Cobalt-60 as a source of γ-irradiation has been investigated to generate active radical sites on starch, among others to graft polystyrene.[89] Fanta *et al.* achieved 68% grafting efficiency for poly(VAc) using 0.87–0.67 Mrad/h cobalt radiation for 2 h in the presence of the monomer.[90] The same group achieved a similar grafting efficiency of 70% for the grafting copolymerization of VAc with MMA.[90] UV radiation has likewise been used to graft acrylic acid onto starch.[91] Other radical initiation methods include ozone treatments, enzymatic initiation and hydrogen peroxide, all of which can generate active radical sites on the starch backbone.[78] The molecular weight of the grafted polymer chains can be determined by gel permeation chromatography analysis, provided that the high molecular weight starch component is degraded (by enzymatic or acid hydrolysis) prior to the analysis.[78]

1.4.2.4.2 Reversible Deactivation Radical Polymerization

Reversible deactivation radical polymerization (RDRP) is a chain polymerization technique in which propagation takes place with radicals that are deactivated reversibly, such that the radical species are involved in an equilibrium between active and dormant states

minimizing termination. This results in controlled growth of the polymer chains, and in many cases a low PDI. RDRP is also popularly known as "living" radical polymerization, albeit this term is discouraged by the International Union of Pure and Applied Chemistry (IUPAC) because radical polymerization is never truly living – there is always some degree of termination.[92] Popular RDRP techniques include reversible addition-fragmentation chain transfer (RAFT) polymerization, atom transfer radical polymerization (ATRP), and nitroxide-mediated polymerization (NMP).[93] Each technique will be reviewed below in relation to the formation of starch-based graft polymers.

1.4.2.4.2.1 Reversible Addition-Fragmentation Chain Transfer (RAFT)

The RAFT technique uses thiocarbonylthio compounds to polymerize monomers by a chain transfer mechanism.[94] The number of radical centers present remains constant during the course of the reaction, and a small amount of an initiator is required to start the chain reaction.[94]

RAFT is considered one of the simplest polymerization methods currently available. It does not require the use of extreme temperatures nor metal catalysts, and thus can serve in biological applications.[95] RAFT allows the synthesis of well-defined polymers because the number of side reactions occurring is limited. The monomers generally do not require functional group protection, and the polymers obtained can be subjected to further modification if necessary. To achieve a low PDI it is important to maintain a low initiator concentration relatively to the RAFT agent in the reaction, so as to generate a low number of initiator-derived

polymer chains and maintain control over the polymerization reaction.[96] Compatibility of the monomer with the RAFT agent is critical for controlled polymerization. This is achieved by carefully selecting the 'R' and 'Z' groups in the RAFT agent in Scheme 1-3. The 'R' group, which plays an important role in RAFT reactions, should be a good homolytic leaving group that can re-initiate polymerization.[97] The chain transfer constant of the RAFT agent, which is the ratio of the chain transfer and propagation rate constants in the polymerization reaction, is determined by steric and polarity variables.[98] The 'R' group may also stabilize the radical intermediate, but to a lesser extent than the 'Z' group. When RAFT agents with the general structure S=C(Ph)S-R were used for the polymerization of MMA at 60 ^{o}C, the polymerization efficiency strongly depended on the structure of the 'R' group in the order -C(alkyl)$_2$CN ~ -C(CH$_3$)$_2$Ar > -C(CH$_3$)$_2$C(O)(O(alkyl) > -C(CH$_3$)$_2$C(O)NH(alkyl) > -C(CH$_3$)$_2$CH$_2$C(CH$_3$)$_3$ ≥ -C(CH$_3$)HPh > -C(CH$_3$)$_3$ ~ -CH$_2$Ph.[99] The cumyl (-C(Ar)(CH$_3$)$_2$) and cyanoisopropyl (-C(Ar)$_2$CN) groups were found to be most efficient in the reinitiation step for the polymerization of most monomers.[99] For example, a very low PDI of 1.07 was obtained when MMA was polymerized using 2-cyanoprop-2-yl dithioester at 60 ^{o}C, with 96% monomer conversion attained after 16 h.[100] When the 'R' group was -C(CH$_3$)$_2$CO$_2$R' or -CHCH$_3$CO$_2$R' the polymerization was well-controlled for styrene and acrylate derivatives, but not for methacrylates.[99] This is because the polymethacrylate radical is a better leaving group than the 'R' group, shifting the equilibrium to the left in Step II of Scheme 1-3. Farmer *et al.* polymerized MMA with a thiobenzoyl-2-thiopropionate having a -CHCH$_3$CO$_2$CH$_3$ 'R' group and obtained a

PDI of 1.64 with M_n = 49,000 g/mol, when the reaction was allowed to proceed for 16 h at 60 ^oC.[101] Thus, cumyl and cyanoisopropyl 'R' groups are certainly more effective at controlling MMA polymerization, while the -$CHCH_3CO_2CH_3$ 'R' group yielded a more polydisperse product. Nonetheless, non-polar and bulky 'R' groups are not recommended for RAFT polymerization.[97]

The 'Z' group must be likewise carefully designed, as it influences the stability of the thiocarbonylthio intermediate and its reactivity toward radical addition (Scheme 1-3).[102] The stability of the thiocarbonylthio group must be fine-tuned to favor 'R' group fragmentation, yielding the R• radical which can add to the monomer and form a polymeric radical chain, P_n• or P_m• in Scheme 1-3. Good compatibility of the RAFT agent and the monomer is essential to obtain polymers with low PDI values. Overall, the phenyl group is considered an ideal 'Z' group for most monomers as it efficiently stabilizes and allows the fragmentation of R• from the RAFT agent. Benzyl group-based RAFT agents were shown to be useful to polymerize styrene,[103] N-isopropyl acrylamide (NIPAM),[104] and acrylamide,[105] with monomer conversions over 80%, and PDI values of 1.5, 1.07, and 1.3, respectively. Since benzyl group-based RAFT agents are less stable than phenyl-based RAFT agents, they poorly control the polymerization of more reactive monomers such as styrene, as compared with NIPAM and acrylamide. When the thiocarbonylthio group is directly attached to a nitrogen or oxygen atom in the 'Z' group, the electron pairs on N or O are delocalized on the -S=C double bond.[99] This lowers the reactivity of the thiocarbonylthio group towards the addition of propagating radicals P_n• or P_m• (Scheme

1-3) which may lead to polymers with higher PDI values, or poor control over the molecular weight. Conversely, these RAFT agents may be effective for monomers that are electron-withdrawing such as VAc. Thus xanthate derivatives, where the -S=C group is directly attached to an oxygen atom, were used to polymerize VAc to molecular weights exceeding 5×10^4 g/mol and PDI < 1.2 over 10 h.[106]

Overall, a general classification of 'Z' groups in terms of their compatibility with different monomers is as follows: Dithiobenzoates, dithioesters and trithiocarbonates are effective at controlling the polymerization of so-called more activated monomers (MAM, or monomers more reactive in radical addition) such as methyl methacrylate, styrene, methyl acrylate, acrylamide and acrylonitrile, while inhibiting or delaying the polymerization of less activated monomers (LAM, or monomers less reactive in radical addition) such as VAc and its derivatives.[99,98] RAFT agents such as xanthates and N,N-dialkyl or N-alkyl-N-aryl dithiocarbamates effectively control the polymerization of LAMs but are ineffective at controlling the polymerization of MAMs. [99,98]

The relative stability of the RAFT adduct radical (P_n-S-C•(Z)-S-P_m) and its fragmentation products, namely S=C(Z)S-P_n and the polymeric radical (P_m•), influence the position of the main RAFT equilibrium (Step V in Scheme 1-3). When the formation of the RAFT adduct radical is sufficiently thermodynamically favorable, the concentration of active species P_m• is decreased to the point where the rate of monomer addition is also reduced. Under these conditions the rate of initiation is far higher than the rate of propagation, such that the rate of RAFT polymerization

(the rate of monomer conversion into polymer) is primarily determined by the rate of the propagation reaction. The rate of propagation is proportional to the concentration of active species [P•], while the rate of termination, which is second-order, is proportional to $[P•]^2$. This implies that the rate of termination is suppressed more than the rate of chain growth in RAFT polymerization.[95]

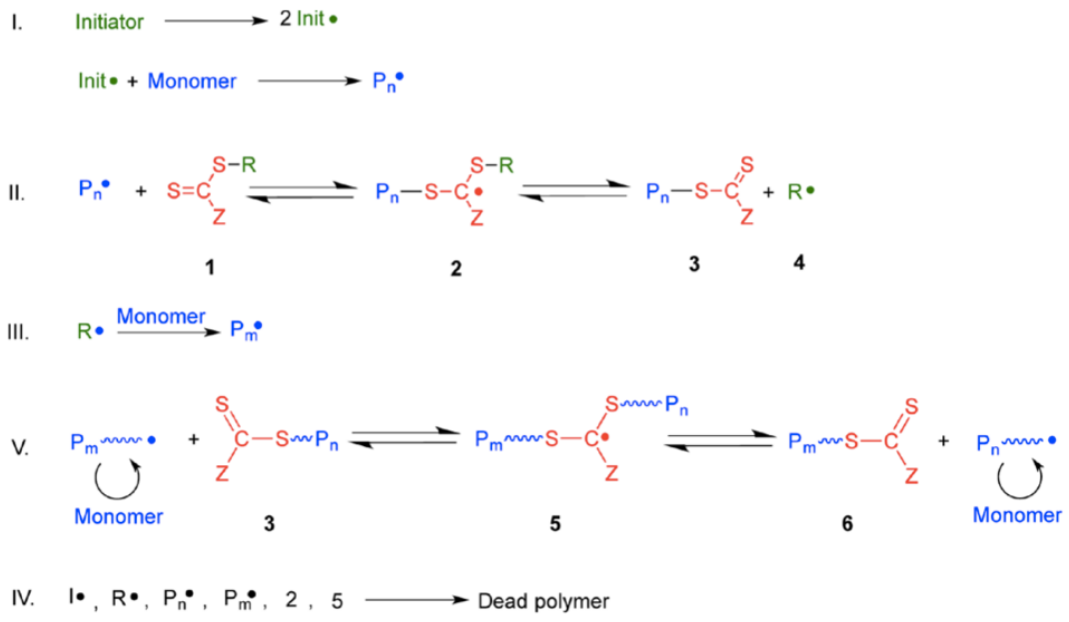

Scheme 1-3: General reaction mechanism for RAFT polymerization. Reprinted with permission from reference 95. Copyright (2015) American Chemical Society.

RAFT polymerization has several benefits. The polymers synthesized are metal-free and

thus easier to purify. The RAFT polymerization is insensitive to many impurities including water, allowing the reaction to be performed under less challenging conditions, while the exclusion of oxygen is critical to radical-based chemistry. Even though RAFT-mediated grafting has several advantages, few reports are available in the literature concerning the use of RAFT to graft polymers onto starch. The complexity in designing suitable starch-based RAFT agents and the limited availability of commercial RAFT agents make it unpopular for grafting polymers onto starch. Lu *et al.* nevertheless developed a starch-based RAFT agent by first reacting starch with bromoacetyl bromide to form a brominated starch derivative, which was reacted with potassium ethyl xanthogenate to form a starch-based RAFT agent. A VAc conversion of 70% was achieved when the reaction was allowed to proceed for 14 h, the poly(VAc) having a M_n of 104,000 g/mol and a PDI of 1.19.[107] The same group refluxed the starch-*g*-poly(VAc) product with a mixture of NaOH/methanol to obtain starch-*g*-poly(vinyl alcohol).[108] While starch-*g*-poly(VAc) self-assembled to micelles in water, starch-*g*-poly(vinyl alcohol) formed hydrogels due to hydrogen bonding.[107,108] VAc was the only monomer in the literature reported to be grafted onto starch by RAFT polymerization. In Chapter 2 of this thesis, a starch-based RAFT agent was synthesized by a relatively simpler procedure, namely the introduction of thiocarbonylthio groups with carbon disulfide, followed by reaction with methyl 2-bromopropionate.

1.4.2.4.2.2 Atom Transfer Radical Polymerization (ATRP)

Similarly to RAFT polymerization, ATRP relies upon an equilibrium between dormant and active states of the polymer chain ends. In the dormant state (halide-capped chains) the radicals are trapped in a covalent C-Br bond, so they are protected from termination and cannot participate in polymerization.[109] The radicals are produced when the dormant species react with a transition metal complex in its lower oxidation state, Mt^n/L in Scheme 1-4, where Mt^n represents the transition metal species in oxidation state n, and L is a ligand, such that the metal becomes oxidized to the n+1 state.[109] While in the active state, the radical propagating centers can continue to grow by inserting monomers for a short time before returning to the dormant state in the reverse reaction. The goal is to release only a small number of radical chains at any time, and to recapture them quickly so as to prevent termination.

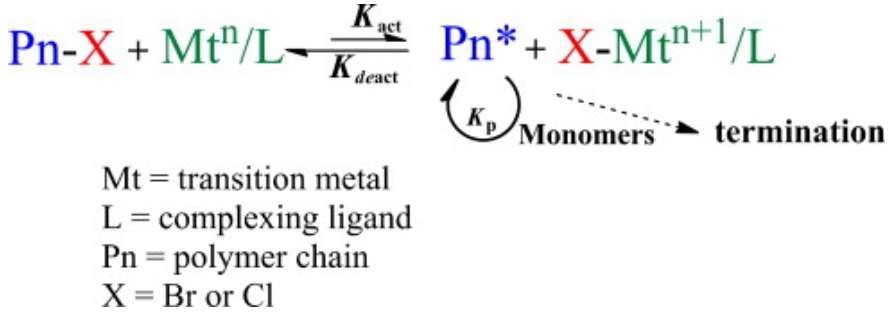

Scheme 1-4: Mechanism of ATRP. Reprinted with permission from reference 109. Copyright (2014) Elsevier.

In the first reported application of the ATRP technique to graft polymers on starch, Liu *et al*. first modified the hydroxyl groups by esterification with bromoacetyl bromide.[110] The macroinitiator was activated with CuBr and 1,10-phenanthroline to graft poly(butyl acrylate) onto the modified starch. After 5 h of reaction, 21% of poly(butyl acrylate) was grafted onto starch by weight,[110] and a linear increase in poly(butyl acrylate) content over time confirmed that the polymerization was controlled or "living". Moghaddam *et al.* also used starch modified with bromoacetyl bromide, and CuBr with N,N,N′,N″,N″-pentamethyldiethylenetriamine (PMDETA) to graft polystyrene and acrylamide by ATRP.[111] Similarly, Avval *et al.* performed ATRP using a chloroacetylated starch macroinitiator to graft poly(acrylic acid) and poly(2-hydroxyethyl acrylate).[112] In both cases the grafting efficiency was not determined, but grafting of the polymers was confirmed by FTIR, differential scanning calorimetry, and thermogravimetric analysis.[111,112] PMMA was also grafted on acylated starch oligomers by ATRP, using a starch-isobutyryl bromide initiator. Activation of the macroinitiator with CuBr and bipyridine resulted in 31% conversion.[113] A starch-isobutyryl bromide macroinitiator was also used to graft glycidyl methacrylate with a PMDETA/$CuBr_2$ catalyst system to obtain 70% monomer conversion and PDI values of 1.3–1.6 for the grafted chains.[114] Fan *et al.* synthesized a starch-based macroinitiator by reacting waxy potato starch with 2-bromopropionyl bromide, which was then used to copolymerize NIPAM and acrylamide by activation with Cu powder/tris[2-(dimethylamino)ethyl]amine.[115] Over 80% conversion was accomplished for both

monomers at 65 ^{o}C over 48 h.[115]

Even though ATRP allowed the controlled grafting of polymers to starch, the monomer conversion attained was low in most cases. The most significant drawback of the ATRP technique is that it is tedious and expensive to remove the metal catalyst, which limits its commercial applications.[116] It can also be difficult to graft acidic monomers, as they require protection before the ATRP reaction.

1.4.2.4.2.3 Nitroxide-mediated Polymerization (NMP)

NMP also follows the general process of reversible deactivation of the propagating polymer radical, in this case by capping with nitroxide radicals. Cleavage of the C-ON bond produces reactive carbon-centered radicals, which may react with the alkene group in monomers to extend the polymer chain, or recombine with a nitroxide radical to regenerate a dormant alkoxyamine end group.[117] NMP was used on a few occasions to modify dextrans, cellulose and chitosan, but was implemented on starch for the first time by Cazotti *et al.* to graft methyl acrylate, MMA, styrene, and acrylic acid on starch nanoparticles (SNPs) in 2019.[118] The SNPs were modified with a vinylbenzene group that was reacted with an alkoxyamine to form an NMP macroinitiator. For reactions carried out for 2 h at 115 °C, 120 °C, and 90 °C, the monomer conversion for methyl acrylate, acrylic acid and an MMA-styrene mixture reached 71%, 39%, and 71%, respectively.[118]

1.5 Chitosan

Chitosan is the deacetylated form of chitin, including both β-(1,4) linked D-glucosamine and N-acetyl-D-glucosamine units (Scheme 1-5). Chitin exists as ordered crystalline microfibrils serving as structural material in crustaceans, some insects, fungi, and yeast cell walls.[119] It is the second most abundant biopolymer, next to cellulose.[4] It is generally a white, hard, inelastic nitrogen-rich polysaccharide sometimes causing pollution in coastal areas such as beaches.[16] The extraction from crustacean shells is the most cost-effective way to produce chitin with molecular weights ranging from 1 to 2 MDa.[120] Impurities such as minerals and proteins are also found in the shells. The minerals are extracted from the ground shells with a dilute acid solution, while residual protein is removed with a dilute base solution.[121] To obtain a colorless material, bleaching with $KMnO_4$ is typically carried out as the final step.[121] The purified chitin is then boiled for several hours under nitrogen in a 40–50% NaOH solution.[122] The degree of deacetylation and molecular weight of the chitosan are determined by the NaOH concentration, the temperature, and the duration of the treatment.

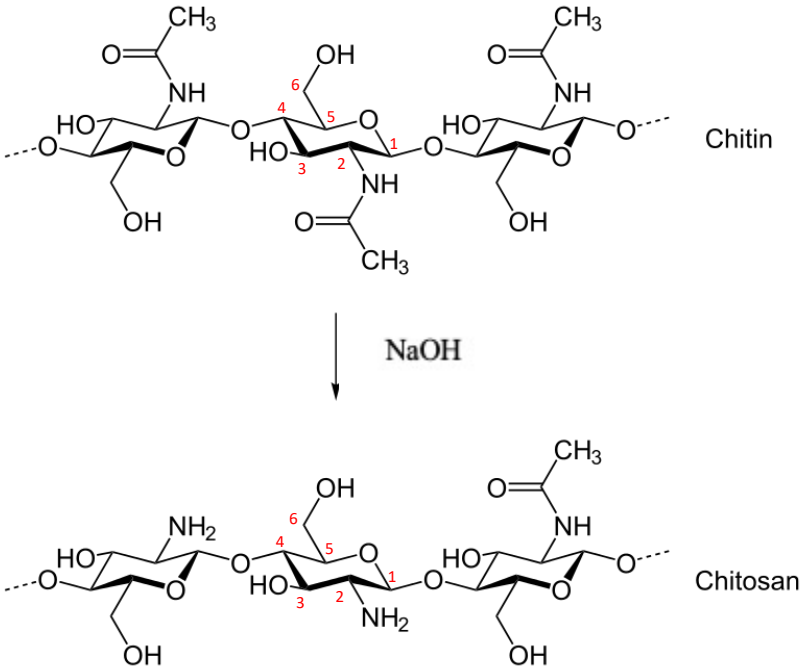

Scheme 1-5: Deacetylation of chitin to form chitosan.

Since NaOH is used to deacetylate chitin, the molecular weight decreases.[123] At about 50% deacetylation, the material can be dispersed in aqueous acidic media and is known as chitosan.[123] The solubility of the polymer increases for increasing deacetylation levels. Protonation of the amino groups of chitosan under acidic conditions makes it a polyelectrolyte soluble in aqueous media.[4] This allows the use of chitosan in various forms including films, gels, and fibers. Other factors affecting the dispersibility of chitosan are the molecular weight and the distribution of acetyl groups along the chains.[4]

1.5.1 Molecular Structure of Chitosan

X-ray crystallography was used by Clark and Smith in 1936 to determine the structure of chitosan fibers derived from lobster tendon chitin, thus named the "tendon" model (Figure 1-3).[124] Each chitosan chain can adopt a two-fold helix or zig-zag structure. The white circles in Figure 1-3 represent carbon atoms, the dark-shaded circles are nitrogen atoms, the dashed lines represent hydrogen bonding interactions, and W represent the oxygen atoms of water molecules. The chitosan chains are shown in Figure 1-3a along the c-axis arranged in an antiparallel fashion, where the chains are stabilized by intramolecular O3-O5 hydrogen bonding. The b-axis represents hydrogen bonding between the up-chain and the down-chain connected by NH_2-O hydrogen bonding. This forms sheets of chitosan stacked on the a-axis. The hydrated chitosan crystals include water molecules between the sheets, which stabilize the crystal structure by hydrogen bonding.[125] The X-ray pattern shown is for a hydrated crystal, due to the presence of water. This crystal pattern is typical for commercially available chitosan, albeit the degree of crystallinity can vary.

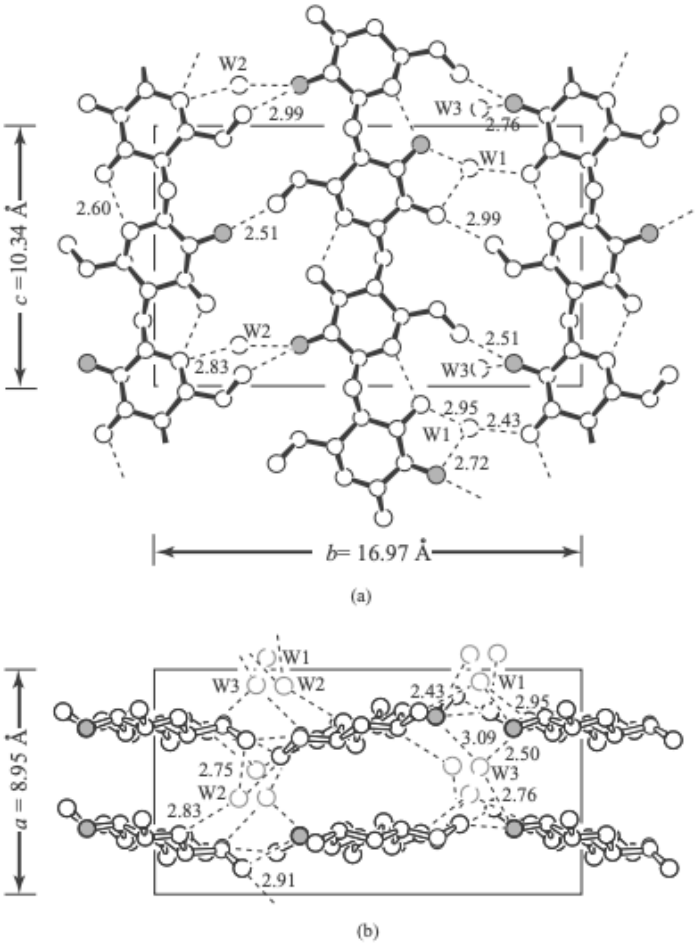

Figure 1-3: Packing arrangement of hydrated tendon chitosan project along the (a) bc plane, and (b) a axis. Dark circle are nitrogen atoms, white circles are carbon and dashed lines are hydrogen bonds. W represents oxygen atoms of water molecules. Reprinted with permission from reference 125. Copyright (2003) Elsevier.

1.5.2 Chitosan Solubility and Film Forming Properties

When using a solvent casting process to make films, the proper dispersion of chitosan is crucial. Chitosan is insoluble in water or basic solutions due to its high molecular weight, partially crystalline structure, and inter- as well as intramolecular hydrogen bonding.[126] Unless it is functionalized by alkylation or acylation, chitosan is insoluble in halogenated, aromatic, or common organic solvents such as DMSO, dimethylformamide (DMF), and tetrahydrofuran (THF).[127] On the other hand, chitosan dissolves easily in dilute aqueous organic and mineral acid solutions, including acetic and hydrochloric acids. This is due to protonation of the amino groups and electrostatic repulsions, which cause chitosan to swell and break apart by disrupting hydrogen bonds.[6] Regardless of the acid used, chitosan requires a minimum of 50% protonation for dispersion.[128] Residual acid counterions affect the film microstructure and material properties. As the water evaporates during the casting process, the acid and chitosan concentrations rise, creating a gel and then a film. Thicker films result from larger acid counterions, which disrupt the packing of chains and recrystallization.[6] Begin *et al.* studied the effects of 0.1% w/v HCl, and of 2 % w/v acetic acid, formic acid, citric acid, and lactic acid on film formation.[6] Films cast from HCl and formic acid solutions were strong but brittle. Citric acid and lactic acids form thicker but weaker films. Citric acid can form multiple interactions during film formation, but it does not improve film strength.[6] Films prepared with acetic acid have much better strength than with lactic acid and citric acid, and comparable to HCl and formic acid. They are excellent barriers against moisture, oxygen and carbon dioxide, and have better

mechanical properties (tensile strength and elastic modulus) than films produced with other acid. Thus, acetic acid is the most popular choice to prepare chitosan films.

1.5.3 Chemical Modification of Chitosan

The reactive groups of chitosan are -NH_2 (C2), -OH (C3), and -OH (C6). The primary amino group can react twice with a methyl halide to yield secondary and tertiary amines,[129] giving chitosan a theoretical maximum degree of substitution of 4.[130] The consensus on relative reactivity is NH_2 > OH (C6) > OH (C3).[129] Modifications on the backbone of chitosan are difficult due to the limited dispersibility of chitosan.[131] Thus, whereas homogeneous reactions occur in dilute acid solutions, heterogeneous reactions occur in non-acidic solvents, as the reactions occur mainly on the surface of chitosan. Some of the more common chitosan derivatives include carboxymethylchitosan, trimethylchitosan, chitosan 6-O-sulfate, chitosan N-sulfate, alkylated chitosan and polymer-grafted chitosan.[4]

For example, Bidgoli *et al.* synthesized amphoteric carboxymethylchitosan by reacting chitosan with NaOH and monochloroacetic acid in water/2-propanol (1:4) for 4 h at 50 ^oC.[132] Chitosan potentially could be carboxymethylated at either the O or the N positions (Scheme 1-6a). The overall DS achieved was 0.96, and FTIR analysis showed that the amide (C-N) stretch at 1321 cm^{-1} did not change as compared to unmodified chitosan, indicating that no significant amount of N-carboxymethylation occurred.[132] It was suggested that in a polar protic solvent like water or 2-propanol, the amino groups are surrounded by more water molecules than the

hydroxyl groups, resulting in the OH groups being more reactive. The C6 OH, being attached to a methylene spacer, is also less sterically hindered than the C3 OH and the NH_2 groups, both attached directly to the GPy ring. The presence of two hydroxyl groups per GPy unit, as compared to one amino group, further contributes to making O-carboxymethylation the dominant product. Interestingly, O-carboxymethylated chitosan is known to be a better antimicrobial agent than N-carboxymethylated chitosan, because substitution of the hydroxyl groups at C6 and C3 positions enhances protonation of -NH_2 group.[132]

Trimethylchitosan was synthesized by reacting chitosan with methyl iodide and sodium iodide in the presence of NaOH (Scheme 1-6b).[133] The reaction was conducted in N-methylpyrrolidone, a polar aprotic solvent, which resulted in the quaternization of chitosan.[133] This is because in an aprotic organic solvent like N-methylpyrrolidone, the amino group is a stronger base than the hydroxyl group, favoring its nucleophilic attack on methyl iodide and resulting in quaternized chitosan as the dominant product. These derivatives are cationic polymers used as flocculating agents, among others to settle clays in tailings.[133] Alkylated chitosan is also used as a papermaking additive, and can form gels when alkylated with long-chain hydrocarbons.[134,4]

Chitosan can be sulfated at either the N or O positions to form chitosan N-sulfate or chitosan 6-O-sulfate, respectively (Scheme 1-6c). When the reaction is carried out in pyridine·SO_3, an aprotic polar solvent which also takes part in the reaction, the N position of

chitosan needs to be protected to obtain chitosan 6-O-sulfate. Both sulfated derivatives are good anticoagulating agents.[135,136]

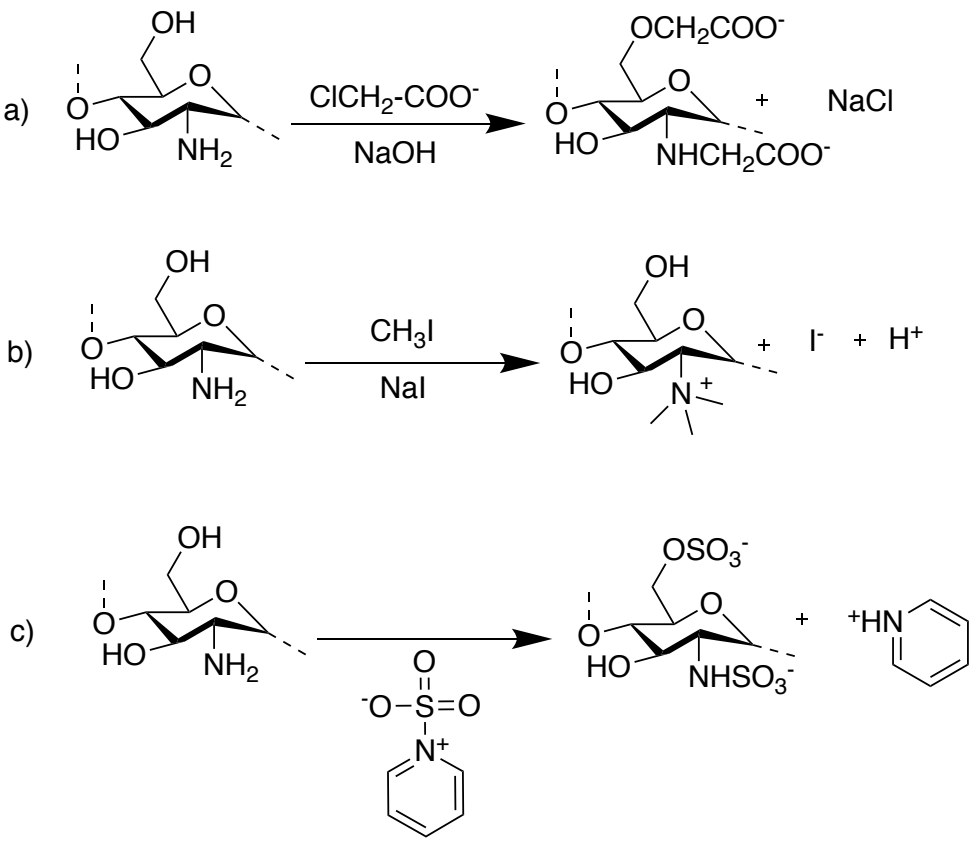

Scheme 1-6: Reaction of chitosan with a) chloroacetic acid, b) methyl iodide and sodium iodide, and c) pyridine-SO_3.

1.5.4 Polymer-grafted Chitosan

Different initiators such as ceric ions, gamma radiation, and Fenton's reagent have been explored to introduce radicals on chitosan for grafting.[137] Pourjavadi *et al.* thus reacted chitosan, acrylonitrile and ceric ammonium nitrate (CAN) in a 1 wt% acetic acid solution for 2 h at 50 °C and achieved a grafting efficiency of 80%, with only 2% homopolymer formed in solution.[138] Chitosan grafted with polyaniline (PANI), which may increase sensitivity in chemical sensor applications,[139] was obtained from chitosan and aniline in 0.5 M HCl solution. Ammonium persulfate served as initiator and a grafting efficiency of 70% was achieved after 1 h at 25 °C. Because PANI-grafted chitosan/indium/tin oxide electrodes can be used to detect changes in current due to DNA hybridization, they are regarded as potentially useful for the early detection of breast cancer (gene BRCA1).[140]

Casimiro *et al*. grafted 2-hydroxyethyl methacrylate onto chitosan using γ-radiation in a heterogeneous reaction.[141] To this end, chitosan was suspended in a methanol solution of 2-hydroxyethyl methacrylate, the dispersion was purged with nitrogen, and irradiated at 7.4 kGy/h with a cobalt-60 source. The grafting efficiency reached 38% when the reaction was carried out for 7 h at room temperature.[141] Lagos *et al.* also grafted MMA onto chitosan using Fenton's reagent (Fe^{2+} and H_2O_2), by dispersing chitosan and MMA in water before adding Fe and H_2O_2 in a 0.01 : 1 ratio.[142] For a reaction performed for 2 h at 70 °C, a maximum grafting efficiency of 57% was obtained, with 20% homopolymer remaining in solution.[142] The Fenton reaction produces hydroxyl radicals in solution which can contribute to chain transfer reactions, while

exposure to γ-radiation may lead to depolymerization and poorly defined structures.[138] Consequently, the highest grafting efficiency and lowest homopolymer contents were obtained with CAN-initiated graft polymerization. Similarly to starch, CAN generates radicals efficiently on the chitosan backbone, while minimizing chain transfer reactions during polymerization.

Grafting of polymers on the surface of chitosan was also achieved via RAFT polymerization. For example, Abbasian *et al.* modified chitosan by esterification with S-1-dodecyl-S′-(α,α′-dimethyl-α′′-acetic acid)trithiocarbonate to obtain a chitosan-based RAFT agent, which was used to polymerize acrylic acid.[143] The reaction had a grafting efficiency of 60%, and an M_n of 12000 g/mol was achieved for the grafted polymer after 6 h.[143] Abbasian *et al.* also modified chitosan with 4-cyano-4-[(phenylcarbothioyl)sulfanyl]pentanoic acid to serve as RAFT agent and graft poly(acrylic acid) . The reaction was allowed to proceed at 4 ^oC for 20 min, but the molecular weight and PDI obtained were not determined in that case. The chitosan-*g*-poly(acrylic acid) samples were used to stabilize silver nanoparticles in solution and tested on *Escherichia coli*, showing good antibacterial activity.

ATRP was used to graft polymers on chitosan via its -OH and $-NH_2$ functional groups. Tahlawy *et al.* synthesized a chitosan-based ATRP macroinitiator by reaction with 2-bromoisobutyryl bromide in heterogeneous reactions on films.[144] The amino group was protected by modifying it into an imine prior to the reaction, so that coupling with the acid bromide occurred only at the -OH groups. The macroinitiator, activated with 2,2'-bipyridine and Cu(I)Br, was used to polymerize ethylene glycol methyl ether methacrylate efficiently, as 90% monomer

conversion was achieved over 1 h at 25 °C.[144] The polymerization was controlled, and a PDI of 1.6 was obtained for grafted chains with M_n = 140 kg/mol.[144] ATRP was also investigated to synthesize chitosan-*g*-polyacrylamide beads by using chitosan modified with 2-bromoisobutyryl bromide as the macroinitiator. Since the amino group was not protected in that case, the modification reaction took place at both hydroxyl and amino groups. The grafting efficiency was not determined, but the chitosan-*g*-polyacrylamide beads were determined to adsorb 323 mg of mercury per g of chitosan-*g*-polyacrylamide.[145] As compared with unmodified chitosan, the graft polymer had a higher mercury adsorption capability, and at pH < 6 it preferentially adsorbed mercury over lead, while the unmodified chitosan displayed no such selectivity.[145] Starting from a chitosan macroinitiator obtained by reacting chitosan with bromoacetyl bromide and triethylamine in THF, with 1,10-phenanthroline and Cu(I)Br as catalysts, ATRP was also used to graft polystyrene on chitosan, although the grafting reaction proved to be ineffective, with only 19% monomer conversion reached after 5 h.[146]

One example of the application of nitroxide-mediated polymer grafting on chitosan was provided by Garcia-Valdez *et al.*, who reacted 1-oxoammonium-4-hydroxy-2,2,6,6-tetramethylpiperidinium bromide with chitosan in the presence of triethylamine to form 4-hydroxy-2,2,6,6-tetramethylpiperidin-1-oxyl (TEMPO)-functionalized chitosan. The macroinitiator was tested in the copolymerization of styrene and maleic anhydride via NMP,[147] at 130 °C in supercritical CO_2 with camphorsulfonic acid. After 5 h, the monomer conversion was a mere 3.8%, but an excess of monomer (monomer : TEMPO initiating site molar ratio of

63) was used to ensure that chains were grafted on the chitosan.[147] The M_n of the chains was still estimated to be only 1640 g/mol, assuming that all the nitroxide moieties were able to initiate the radical addition of monomers. The same group functionalized chitosan with glycidyl methacrylate and then prepared a chitosan-based macroalkoxyamine by addition of [N-(2-methylpropyl)-N-(1-diethylphosphono-2,2-imethylpropyl)-O-(2-carboxylprop-2-yl)hydroxylamine], commonly known as BlocBuilder. This NMP macroinitiator was used to graft polystyrene, poly(butyl acrylate), and poly(acrylic acid).[147] For reactions carried out for 3 h at 100 °C, conversions of 22%, 23%, and 51% were achieved for polystyrene, poly(butyl acrylate), and poly(acrylic acid) grafting, respectively. The reaction was well-controlled, as the PDI of the grafted polymers ranged from 1.13–1.19, while their M_w ranged from 3760–3980 g/mol.[147]

All the techniques mentioned so far are "grafting from" strategies, whereby polymer chains are grown from the chitosan-based macroinitiator. The amino groups of chitosan also enable "click" chemistry reactions, for example between an azide and alkyne to form a covalent bond, and allow the coupling of preformed polymer chains with a chitosan substrate in a "grafting onto" scheme. Chitosan was thus azidated as shown in Scheme 1-7 to achieve degrees of azidation of up to 0.4.[148] PEG monomethyl ether was coupled with propargyl bromide to introduce an alkyne chain end. The N-PEGylation of chitosan was achieved by reacting the azidated chitosan substrate with the O-propargyl PEG (Scheme 1-7).[148] The "click" chemistry reaction was very efficient, as the DS of the product correlated with the degree of azidation of the chitosan substrate, at least when O-propargyl PEG was used in excess.[148] Unfortunately, the

complexity of the reactions involved to obtain the final product would make this approach less practical than the “grafting from” techniques described earlier.

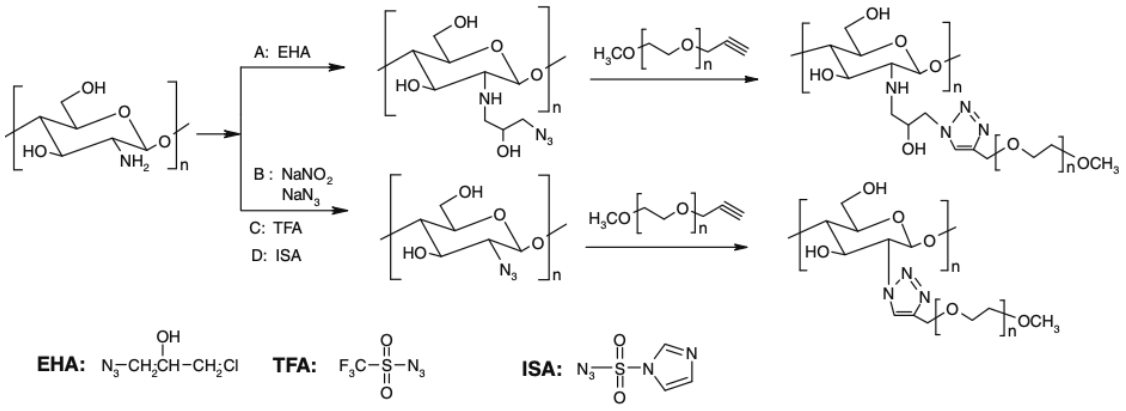

Scheme 1-7: N-PEGylation of chitosan via "click" chemistry reaction. Reprinted with permission from reference 148 . Copyright (2009) Elsevier.

1.6 Thermoresponsive Polymers

Thermoresponsive polymers undergo reversible changes in their physical or chemical properties triggered by subtle changes in temperature.[149] Heat as a trigger can be used to create smart materials for a variety of applications. Some of these materials are ideal for biomedical applications, because they are biocompatible. Shape-memory polymers, liquid crystalline polymers, and responsive polymer solutions are the three main types of thermoresponsive

materials. Due to their direct relevance to the projects described in this thesis, only basic concepts of responsive polymer solutions will be reviewed here.

The lower critical solution temperature (LCST) and the upper critical solution temperature (UCST) are temperatures at which abrupt changes in polymer dispersibility (solubility) are observed. Above a specific temperature, thermoresponsive polymers with an LCST appear to precipitate; this is also known as the cloud point. UCST polymers are insoluble below a specific temperature, and dissolve above that temperature (Figure 1-4).

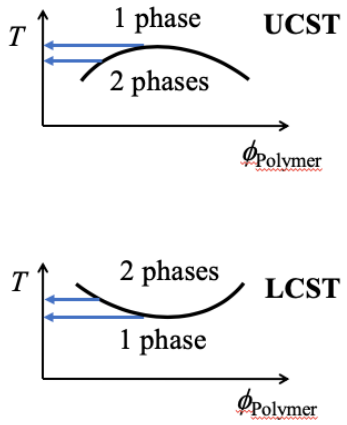

Figure 1-4: The LCST and UCST are concentration-dependent; φ represents the volume fraction of the polymer in the solution.

The LCST typically depends upon H-bonding between the polymer and water molecules. Below the LCST, the ordered arrangement of water molecules around the polymer reduces their

entropy (ΔS_{mix} is negative), and hydrogen bonding between the polymer and the water molecules ensures that ΔH_{mix} is likewise negative.[150] In the Gibbs equation ($\Delta G_{mix} = \Delta H_{mix} - T\Delta S_{mix}$), the ΔH_{mix} term represents the main contribution to ΔG_{mix}. As a result, at low temperatures ΔG_{mix} of the system is negative overall and the polymer remains dispersed as a homogeneous solution. Hydrogen bonding between the polymer and the water molecules is disrupted as the temperature rises above LCST, such that the enthalpy of mixing becomes less negative. This also increases the entropy of the water molecules, to the point where the polymer collapses into a globule and phase-separates from the solvent. Above the LCST, entropic effects outweigh enthalpic effects.[150] The terms lower critical aggregation temperature (LCAT) and lower critical aggregation temperature (LCST) are interchangeable to some extent. The LCAT is the point at which the phase separation process is initiated, while the inflection point (change in the shape of the curve from concave to convex) represents the LCST in UV-visible spectroscopy transmittance measurements as a function of temperature (Figure 1-5). In contrast, the occurrence of a UCST is driven by enthalpic effects.[151] It is dependent on inter- and intramolecular interactions, whereby polymer-polymer and water-water interactions are favored over polymer-water interactions below the UCST.[151]

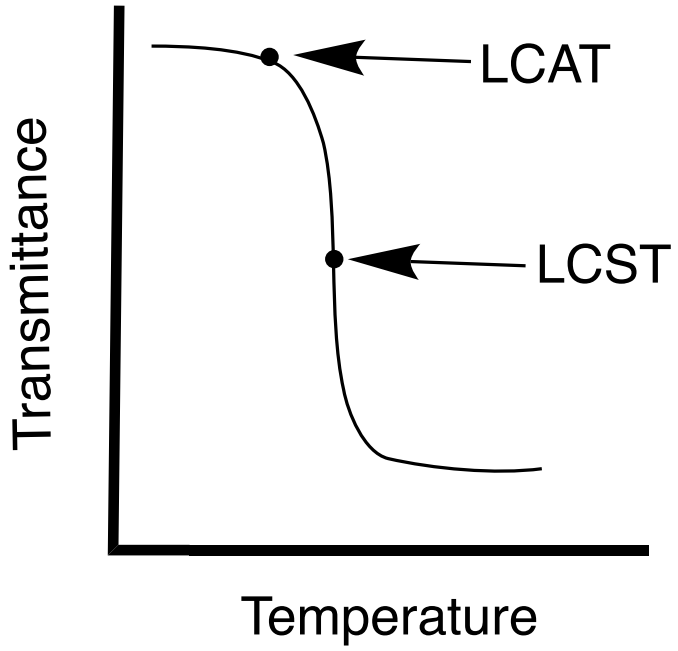

Figure 1-5: Plot of transmittance vs temperature depicting the LCST and LCAT.

1.6.1 Factors Affecting the LCST

The LCST of thermoresponsive polymers depends on several factors such as the types of hydrophobic and hydrophilic groups present in the polymer, the molecular weight, the polymer concentration, and the presence of small molecules such as salts. These parameters can be tuned to obtain polymers with desired LCST/LCAT values. PNIPAM is the most widely studied thermoresponsive polymer; it has an LCST value of 32 ^{o}C.[152] The influence of the parameters listed above on the LCST of PNIPAM is discussed in Sections 1.6.1.1–1.6.1.4.

1.6.1.1 Effect of Hydrophobic and Hydrophilic Groups

The LCST of a polymer is determined by the balance of hydrophobic and hydrophilic components in its structure. The transition temperature of polymers containing more hydrophobic groups is lower than for polymers with more hydrophilic moieties. A few N-alkyl-substituted polyacrylamides (PAMs) display LCST behavior, thus PNIPAM (NR^1R^2 = NH-(CH-$(CH_3)_2$) in Table 1-1) is not unique.[153] Since intermolecular H-bonds exist between neighboring amide groups, they also regulate the LCST of PAMs. Above their LCST, the polymers precipitate due to the disruption of H-bonds between the amide groups and water, with increasing interactions between the hydrophobic alkyl groups.[153]

An increase in size of the hydrophobic groups R^1 and R^2 decreases the LCST, as seen in Table 1-1. The contribution of alkyl groups to hydrophobicity can be observed in the characterization of its association with surfactants.[153] As compared with their linear equivalents, cyclic or ring structures have a lower conformation energy and are more stable in aqueous solutions,[153] thus the polymers exhibit higher LCST values. By copolymerizing thermoresponsive acrylamide monomers with hydrophilic or hydrophobic monomers, the LCST of thermoresponsive PAMs can be likewise adjusted.

Table 1-1: LCST of various N-alkyl substituted PAMs. Reprinted with permission from reference 153. Copyright (1999) The Society of Polymer Science, Japan.

NR^1R^2	$(-CH_2-CH-)_n$ $C=O$ NR^1R^2
	°C
$-NH_2$	—
$-NH-CH_3$	—
$-N(CH_3)_2$	—
$-NH-C_2H_5$	73
$-N(CH_3)(C_2H_5)$	56—57
$-N(CH_2-CH_2)_2$	56
$-NH-CH(CH_2)_2$	47
$-N(C_2H_5)_2$	36
$-NH-CH(CH_3)_2$	32
$-N(CH_3)(CH(CH_3)_2)$	25
$-NH-(CH_2)_2CH_3$	22
$-N(CH_3)((CH_2)_2CH_3)$	15
$-N(CH_2-CH_2)_2CH_2$	5

1.6.1.2 Effect of Molecular Weight and Concentration

As the LCST is in principle inversely related to the molecular weight, the influence of molecular weight on the LCST is mostly noticeable for lower molecular weight polymers. When the molecular weight reaches the hundreds kg/mol range, the impact of molecular weight on the LCST is significantly reduced. Thus as the M_w of poly(N,N-diethylacrylamide) increased from 13 kg/mol to 58 kg/mol, Lessard *et al.* observed a 2 °C decrease in LCST (32.9 to 30.9 °C).[154] When the molecular weight was increased from 593 kg/mol to 1300 kg/mol, no change in LCST was observed.[154] The LCST of PNIPAM was also reported to vary slightly (< 1 °C) with the polymer concentration in the high molecular weight range:[155] For M_w = 350 kg/mol, the LCST decreased by 0.2 °C as the polymer concentration was increased from 10 to 100 mg/mL.[156]

1.6.1.3 Effect of End Groups

The effect of end groups such as 2-chloropropionamide (CP), N-isopropyl-2-chloropropionamide (i-PrCP), methyl 2-chloropropionate (MCP), ethyl 2-chloropropionate (ECP), and N-phenyl-2-chloropropionamide (PhCP) on the cloud point/LCST was evaluated for PNIPAM modified at one of the chain ends, in both the low and high molecular weight ranges (Figure 1-6).[157] The effect of the end groups was again more prominent at low molecular weights. Thus PNIPAM with M_w = 3 kg/mol and a hydrophilic CP end group had an LCST of 46 °C, decreasing to 40.6 °C for PNIPAM with the same molecular weight but with a hydrophobic ECP end group.[157] When the molecular weight of PNIPAM-CP was increased from 3 to 16 kg/mol,

the LCST decreased from 45.3 to 34.4 ºC. The drop in LCST was much less dramatic (from 37.4 to 32.8 ºC) for PNIPAM-PhCP, however, when the molecular weight was increased from 3.2 to 18.3 kg/mol. The LCST only decreased by 1.6 ºC, from 34.4 ºC for PNIPAM-CP to 32.8 ºC for PNIPAM-PhCP with 16–18 kg/mol.[157] Thus for longer PNIPAM chains, the influence of the end groups decreased substantially. Overall, hydrophilic end groups increased the LCST of PNIPAM, while hydrophobic end groups decreased the LCST more significantly in the lower molecular weight range.

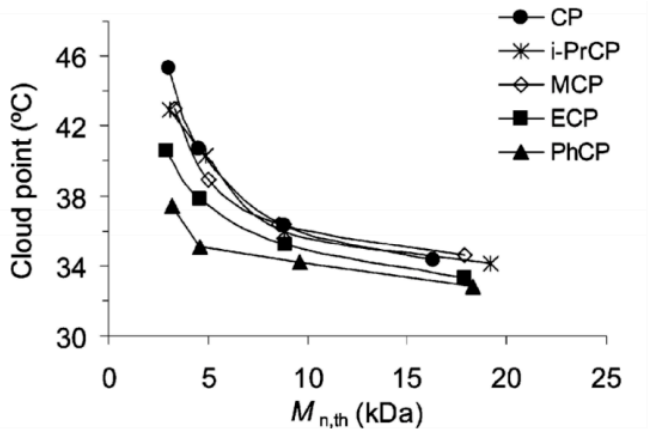

Figure 1-6: Effect on the cloud point of PNIPAM of single end group modification: 2-chloropropionamide (CP), N-isopropyl-2-chloropropionamide (i-PrCP), methyl 2-chloropropionate (MCP), ethyl 2-chloropropionate (ECP), and N-phenyl-2-chloropropionamide (PhCP). Reprinted with permission from reference 157. Copyright (2006) American Chemical Society.

1.6.1.4 Effect of Salts

Salts can significantly impact the LCST of thermoresponsive polymers (Figure 1-7). The LCST of PNIPAM is 32 ºC. In 0–0.8 M NaCl, NaBr, and NaF solutions, the transition temperature of PNIPAM (at a concentration of 1.4 wt%) dropped to 25, 28, and 17 ºC, respectively. This is because only the outer hydration shell of PNIPAM interacts with salts.[158] NaI did not affect the LCST much, but the other salts decreased the LCST more significantly. Cations have a strong affinity for the oxygen atom in the amide group, and the polymer cannot form hydrogen bonds as efficiently with water.[158] Anions can also influence the LCST, but they do not interact with the polymer directly. The anions lower the LCST of the polymer by interacting with water and promoting association among the water molecules, while also competing with the polymer for hydration.[158]

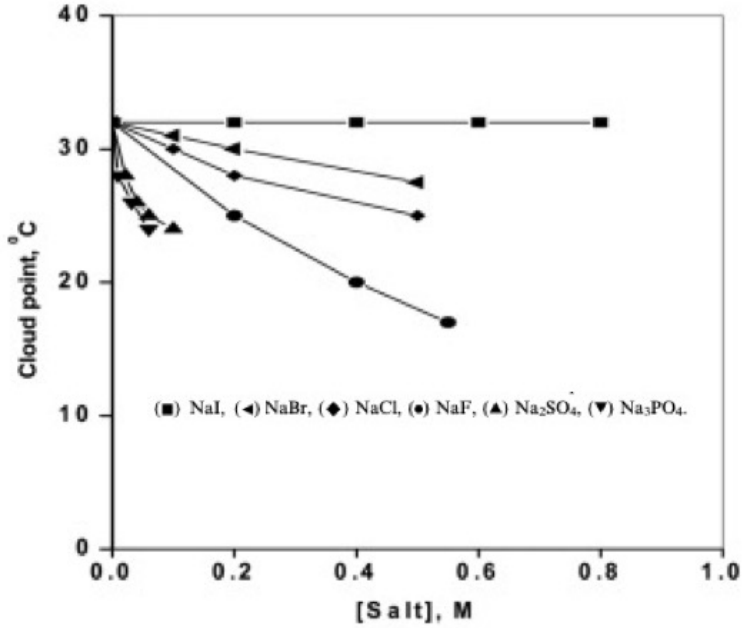

Figure 1-7: Effect of salts on cloud point of PNIPAM. Reprinted with permission from reference 161. Copyright (2011) Taylor & Francis Group.

1.6.2 Applications of Thermoresponsive Polymer Solutions

PNIPAM is a thermoresponsive polymer characterized by the presence of amide (-CONH-) and propyl (-$CH(CH_3)_2$) groups in its structural units (Figure 1-8a). PNIPAM is a very promising thermoresponsive polymer due to its well-defined structure, properties, and its LCST close to the human body temperature, which can be fine-tuned by different methods. Consequently, PNIPAM has found many applications in aqueous media, but it nevertheless has

several drawbacks. For example, PNIPAM hydrogels are not biodegradable and need to be surgically removed after drug delivery[159] and tissue engineering applications.[160] The hydrogels also swell to a high degree, which leads to poor mechanical strength due to a low density of polymer chains.[160] Moreover, the NIPAM monomer is toxic and has a strong odor. An interesting alternative to PNIPAM is $PMEO_2MA$ (Figure 1-8b). The MEO_2MA monomer is non-toxic and costs about 10 times less than NIPAM. For analogous polymethacrylate systems with an oligoethylene glycol monoether side chain, the LCST increases with the length of the oligoethylene glycol segment.[161] In contrast to PNIPAM, it has been found that the molecular weight of $PMEO_2MA$ has a minimal influence on the LCST, but lower M_w chains tend to have broader phase transitions than the longer chain materials.[162] In turbidity measurements, $PMEO_2MA$ displays good reversibility in the heating and cooling cycles, in contrast with the large hysteresis that is observed upon cooling for PNIPAM.[163] These characteristics may make $PMEO_2MA$ a better candidate for certain thermoresponsive applications. Some of the applications of PNIPAM and $PMEO_2MA$ are discussed in this section.

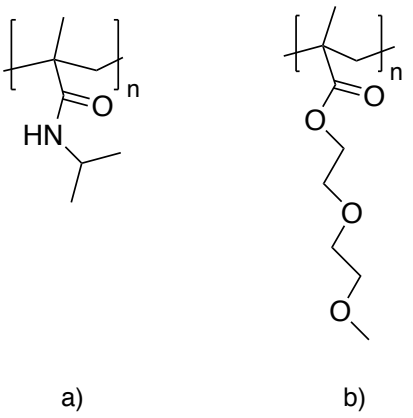

Figure 1-8: Structure of a) PNIPAM b) $PMEO_2MA$.

PNIPAM became popular in part because of its sharp and rapid phase transition in aqueous solutions at 32 °C,[159] and it has been explored for drug delivery applications due to its LCST close to body temperature. The interactions of drugs with PNIPAM are an essential factor in using that material as a drug carrier.[164] Some of the drugs tested for delivery with PNIPAM include benzoate, diltiazem, vitamin B-12, calcitonin, insulin, and many others.[165,166] The drug can be loaded in PNIPAM at temperatures below 32 °C, and the PNIPAM solution is then injected to form a hydrogel in the body, where the temperature is around 36–37 °C. The volume of the PNIPAM hydrogels rapidly decreases after injection, which results in release of the drug (Figure 1-9). Block copolymers of poly(NIPAM-*b*-butyl methacrylate) were also used to form micelles and tested for drug delivery.[167] The hydrophobic poly(butyl methacrylate) block was found to interact with hydrophobic drugs even at temperatures below the LCST, while PNIPAM

remained hydrophilic, forming the shell of the micelles. After injection of the micelles in the body, where the temperature is above the LCST of PNIPAM, the outer hydrophilic PNIPAM shell became hydrophobic, resulting in deformation of the micelles, and rapid but sustained release of the drugs.[167]

PNIPAM has also been employed in tissue engineering, by encapsulating cells in PNIPAM gels to repair damaged tissues. To this end PNIPAM serves as a 3D porous hydrogel structure, which is seeded with live cells and growth factors to promote cell proliferation, and finally transplanted into a patient.[168] PNIPAM has likewise been tested as a medium for cell culture, allowing detachment of the cells from the surface by changing the temperature. PNIPAM was thus covalently grafted onto culture dishes, and cells were allowed to grow and proliferate at 37 ^{o}C, as PNIPAM was hydrophobic and provided an adhesive surface for cell growth. Upon reducing the temperature to 20 ^{o}C, the PNIPAM became hydrophilic and the cells spontaneously detached from the PNIPAM surface as a single sheet.[169]

There are a few limitations to using PNIPAM for biomedical applications. In drug delivery, where interactions between the drug and the polymer are essential, the sharp phase transition of PNIPAM at its LCST may hinder controlled release of the drug. PNIPAM also can have a slow response to stimuli under certain conditions, and can undergo biodegradation before reaching the target site. Furthermore, the high toxicity of the NIPAM monomer makes it difficult to purify PNIPAM sufficiently after its synthesis to make it suitable for biomedical applications. Consequently, none of the PNIPAM-based biomedical applications have been commercialized.

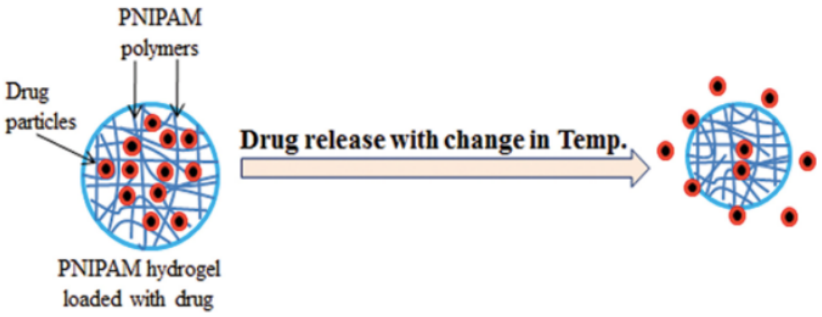

Figure 1-9: Role of PNIPAM hydrogels in drug delivery. Reprinted with permission from reference 170. Copyright (2016) Springer.

High molecular weight $PMEO_2MA$ has an LCST of 26 °C, detected as the temperature at which an aqueous solution of the polymer becomes turbid,[171] and that material also has been explored recently as a drug carrier. For example, Zhu *et al.* prepared a dual responsive block copolymer of poly(MEO_2MA-*b*-2-(*tert*-butylaminoethyl) methacrylate), where $PMEO_2MA$ was the thermoresponsive component, and poly(2-(*tert*-butylaminoethyl) methacrylate) was a pH-responsive segment.[172] The block copolymer was found to have excellent blood compatibility, low toxicity, and antibacterial activity. At 37 °C it formed highly protective vesicles for the controlled release of doxorubicin, making it a suitable drug delivery carrier for the safe delivery of the drug.[172] Huang *et al.* used micelles of an amphiphilic block copolymer PEG-*b*-$PMEO_2MA$ to encapsulate erythromycin.[173] The size of the PEG-*b*-$PMEO_2MA$ micelles was found to increase three-fold after loading with erythromycin. The release rate of erythromycin was stable

over 3 h, demonstrating that erythromycin-loaded micelles had good, sustained release characteristics.

Finally, Yang *et al.* explored the extraction of bitumen from oil sands with PEG-*b*-$PMEO_2MA$.[174] An aqueous dispersion of PEG-*b*-$PMEO_2MA$ was added to the oil sands with a small amount of toluene, and the mixture was gently shaken for 24 h at a temperature above the LCST. This allowed interactions of the bitumen droplets with the hydrophobic $PMEO_2MA$ segments, while the hydrophilic PEG segments allowed the block copolymer micelles to remain dispersed in solution. As the mixture was cooled below the LCST, the bitumen droplets were released by the hydrophilic $PMEO_2MA$ segments, and floated to the surface of the aqueous solution to be skimmed off.[174] This application is further explored in Chapter 3 of this thesis, using starch in replacement for PEG as a hydrophilic component.

1.6.3 Applications of Thermoresponsive Starch

Starch has not been investigated extensively as a substrate for thermoresponsive modifications, despite being an inexpensive and biodegradable polymer. Smart starch microspheres with sulfonic groups were nevertheless modified by grafting with poly(N-isopropyl acrylamide-*co*-N,N-dimethyl acrylamide), with an LCST around 36 ^{o}C. The microspheres were complexed with metoclopramide, and encapsulated in cellulose acetate butyrate microcapsules by an oil-in-water solvent evaporation process.[175] These may be useful as implanted drug delivery systems triggered by local hypothermia: As the body temperature is

locally brought below normal physiological levels, the implants can become swollen by body fluids. The microcapsules burst open and release the drug, while keeping vital organs functional.[175] Zheng *et al.* used butene oxide to modify starch nanoparticles into thermoresponsive hydroxybutylated SNPs. The LCST of these particles could be tuned through their butene oxide content, as well as added solvents and salts. These could potentially be used in drug delivery applications.[176]

ATRP was investigated to graft copolymers of acrylamide and NIPAM onto starch functionalized with 2-bromopropionyl bromide, using Cu powder and tris[2-(dimethylamino)ethyl]amine as catalysts. It was suggested that these modified starches may be useful in the paint industry, due to their high viscosity and salt resistance at temperatures above their LCST.[115] Finally, Dai *et al.* developed a thermoresponsive hydrogel containing sodium alginate and 2-hydroxy-3-isopropoxypropyl starch to remove Cu(II) from aqueous solutions.[177] A maximum adsorption capacity of 26 mg Cu(II)/g was achieved for the hydrogels, which could be reused for five adsorption cycles, even though the adsorption capacity gradually decreased to 12 mg Cu(II)/g by the fifth cycle.[177]

1.6.4 Applications of Thermoresponsive Chitosan

Chitosan has been mainly grafted with PNIPAM for thermoresponsive applications, including hydrogels which can imitate soft tissues.[178] They have a low surface tension, which allows the movement of cells, and the diffusion of oxygen, nutrients and waste products across

the tissue implant boundary. The cartilage and meniscus of knee joints, which cannot repair on their own, can be replaced with chrondocytes and meniscus cells by that approach. When these cells are cultivated as monolayers, they take on a flat, fibroblast-like shape and excrete incorrect extracellular matrices, resulting in damaged tissues.[179] According to Chen *et al.*, this may be remedied by employing 3D chitosan-*g*-PNIPAM hydrogels to stimulate *in vitro* cell development, where the injectable hydrogel may serve as a chondrocyte and meniscus cell carrier.[179] To this end, NIPAM was polymerized by free-radical polymerization in the presence of mercaptoacetic acid as a chain transfer agent to obtain PNIPAM-COOH, which was reacted with the amine groups of chitosan to form amide linkages and graft the PNIPAM chains. The grafting efficiency achieved by that method was as high as 89%.[179] The hydrogel obtained was found to have a comb-like structure. Solutions of chitosan-*g*-PNIPAM with different PNIPAM contents were free-flowing below their LCST, and formed hydrogels at body temperature (37 ^{o}C).[179] These hydrogels displayed good mechanical strength without defects appearing during the sol-gel transition, in contrast to pure PNIPAM hydrogels.

Chitosan has been found to accelerate wound healing.[180] This is because the high tensile strength of chitosan increases collagen production by fibroblasts, and it is bacteriostatic and fungistatic. Unfortunately, pure chitosan has the disadvantage of adhering tightly to injured tissues, thereby worsening the wounds. Chitosan-*g*-PNIPAM might provide better control over chitosan adhesion to the wound. These materials were grafted onto polypropylene fabric, using direct current pulsed oxygen plasma to introduce acrylic acid units on the surface of the fabric,

that were used to produce polypropylene-*g*-chitosan-*g*-PNIPAM.[180] The PNIPAM chains of the graft polymer were hydrophobic and adhered to the wound at body temperature (> LCST), but could be peeled off easily by locally lowering the temperature below the LCST, which caused PNIPAM to become hydrophilic, swell up with water and detach from the tissue.[180] Miguel *et al.* also developed a comparable system for wound healing, in which agarose served as thermoresponsive component instead of PNIPAM, making the system fully biocompatible and biodegradable.[181]

Thermoresponsive chitosan can also act as a flocculating agent to remove pollutants from water.[182] Poly(N-*n*-propylacrylamide)-COOH (PNNPAM-COOH) was grafted on chitosan by coupling in the presence of tetrabutylammonium, N-hydroxysuccinimide, and 1-(3-dimethylaminopropyl)-3-ethylcarbodiimide hydrochloride.[182] The chitosan-*g*-PNNPAM product, containing 20% PNNPAM, was soluble in water below the LCST of PNNPAM (~25 ^{o}C). Above the LCST, chitosan-*g*-PNNPAM coordinated with Cu(II) and hydrogen-bonded with itself, creating flocs that phase-separated from the water and precipitated from the aqueous solution together with the Cu(II). The salt was removed from chitosan-*g*-PNNPAM by treatment with a 0.04 M HCl solution in acetone, and the chitosan-*g*-PNNPAM could be reused for another cycle of Cu(II) extraction.[182] In the first extraction cycle and at a flocculant dosage of 0.4 g/L, 93% of Cu(II) at a concentration of 0.7 g/L could be removed.[182]

Chapter 2

Synthesis of Thermoresponsive Starch Nanoparticles Grafted with Poly(di(ethylene glycol) Methyl Ether Methacrylate)

2.1 Abstract

Polysaccharides, known for their good biocompatibility and biodegradability, can be modified by grafting with thermoresponsive polymers to take advantage of their unusual solution properties. In the current investigation, starch nanoparticles (SNPs) were modified to yield novel starch-based reversible addition-fragmentation chain transfer (RAFT) initiators. Poly(di(ethylene glycol) methyl ether methacrylate) ($PMEO_2MA$) segments were then grown from the SNPs by RAFT polymerization. Since $PMEO_2MA$ exhibits an LCAT (lower critical aggregation temperature), the polymer-grafted SNPs are hydrophilic below the LCAT, but amphiphilic above the LCAT of the thermoresponsive polymer. The degree of substitution (DS) of the starch-based RAFT agent and the amount of monomer added in the reactions were varied to control the characteristics of the grafted SNPs (number and length of the grafted $PMEO_2MA$ segments), and therefore their hydrophilic–lipophilic balance (HLB). The addition of a shell of poly(2-hydroxyethyl acrylate) (PHEA) segments to increase the hydrophilicity of the grafted SNPs was also investigated. ^1H NMR analysis confirmed the efficient grafting of $PMEO_2MA$ and PHEA on the SNPs. The polymer-grafted SNPs were characterized by UV-visible spectroscopy and dynamic light scattering (DLS) to determine their LCAT. The core-shell

structure of SNP-*g*-$PMEO_2MA$ was analyzed by transmission electron microscopy (TEM). The grafted $PMEO_2MA$ chains were also cleaved from the starch substrates for analysis by ^1H NMR and gel permeation chromatography (GPC), so that the structure and composition of the grafted SNPs could be correlated with their LCAT behavior.

2.2 Introduction

Starch, the second most common polysaccharide found in nature after cellulose, is a mixture of amylose, a linear polymer where anhydroglucose units are connected through α-1,4 linkages, and amylopectin, also containing α-1,6 linkages introducing branching in the molecules. The proportions of amylose and amylopectin depend on the source of starch, such that amylose-rich maize contains over 50% amylose, whereas waxy maize only has about 3%.[1] However in most cases amylopectin typically accounts for 70-80% of the starch composition, the balance being amylose.[2] Starch can be modified easily due to the secondary hydroxyl groups present at the C2 and C3 positions of the glucopyranose residues, and the primary hydroxyl group at the C6 position.[3] The reactivity of native starch is limited by its granular nature, as the penetrating ability of a reagent determines whether the reaction takes place on the surface or inside the granules. Starch reactivity can be altered by hydrothermal treatment, whereby the granules are heated with water, ideally in the presence of shear forces (such as in extrusion) to destroy their crystallinity in a process is known as gelatinization. As the starch is cooled, it may undergo partial recrystallization or retrogradation yielding ordered structures, albeit not at the level present in the native granules. The extent of gelatinization and retrogradation depends on the source of the native starch, the duration of heating, the temperature, the magnitude of the shear forces, and the cooling rate.[4]

The research-grade starch nanoparticles (SNPs) used in this project were prepared by extruding starch granules in a continuous process, whereby the solid granules are converted into

a thermoplastic melt phase in the presence of a cross-linker.[5] These nanoparticles mainly consist of amylopectin, as illustrated in Figure 2-1, where the darker regions represent clusters of double helices, and the lighter regions (small circles) are more flexible single helix strands. The use of SNPs as materials is advantageous, as their price is not strongly correlated with oil prices, but also for its environmental benefits. For example, it has been estimated that the production of SNP-based latexes produce 73% less CO_2 emissions than petroleum-based latexes used in paper coating for the same mass of latex.[6]

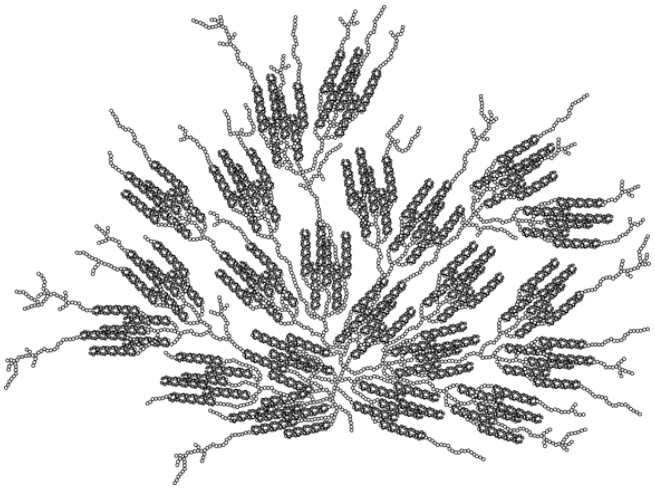

Figure 2-1: Pictorial Representation of a SNP. Reprinted with permission from reference 7. Copyright (2020) L. Li.

The main objective of the current project was to synthesize thermoresponsive SNPs, through grafting with a thermoresponsive polymer, such that they could serve in the extraction

of oil from tar sands. Thermoresponsive polymers exhibit a lower critical aggregation temperature (LCAT), representing the temperature at which they become insoluble in water.[8] Poly(N-isopropylacrylamide) or PNIPAM is by far the most widely investigated thermoresponsive polymer, partly because its LCAT (32 ^{o}C) is close to physiological conditions, making it useful for biomedical applications such as drug delivery and tissue engineering.[9] Interestingly, another family of thermoresponsive polymers, the poly(oligo(ethylene glycol) methacrylate)s (POEGMA), were also investigated more recently and found to be advantageous over PNIPAM for similar applications.[10] For example, the monomer di(ethylene glycol) methyl ether methacrylate (MEO_2MA) costs about 10 times less than NIPAM, while NIPAM is also toxic and has a strong odor.[11] The LCAT of the $PMEO_2MA$ homopolymer is 26 ^{o}C, close to that of 32 ^{o}C for PNIPAM, but the LCAT of these materials can also be tuned through the copolymerization of oligo(ethylene glycol) methacrylates with different oligomer chain lengths to yield POEGMA copolymers, and the resulting materials also have a good biocompatibility. Moreover, while PNIPAM was found to display hysteresis in the coil-globule transition occurring at the LCAT, POEGMA copolymers exhibited more gradual thermal transitions and better reversibility than PNIPAM.[12]

To regulate the characteristics of the $PMEO_2MA$-grafted SNPs synthesized by RAFT, different techniques were used and the hydrophilic-lipophilic balance (HLB) was controlled by varying the DS and the monomer content. A hydrophilic polymer block can be added to improve the colloidal stability of these modified SNPs in water if required.

2.3 Experimental Procedures

2.3.1 Materials

Research-grade starch nanoparticles (SNPs), with M_n = 102,000 g/mol and M_w = 304,000 g/mol, were provided by EcoSynthetix (Burlington, ON, Canada). Methanol (ACS reagent, ≥ 99.8 %), N,N-dimethylformamide (DMF, HPLC, ≥ 99.9 %), LiCl (≥ 99%), deuterium oxide (99.9 % atom), deuterated DMSO (99.9 % atom), CS_2 (ACS reagent, ≥ 99.9 %), potassium persulfate (ACS reagent, ≥ 99.0%), NaOH pellets (ACS reagent, ≥ 98%), methyl 2-bromopropionate (98%), di(ethylene glycol) methyl ether methacrylate (MEO_2MA, 95%), 2-hydroxyethyl acrylate (2-HEA, 96%), hydrogen peroxide (30 % w/w in H_2O), aluminium oxide and inhibitor remover cartridges were purchased from Sigma-Aldrich (Oakville, ON, Canada). Spectra/Por dialysis tubing with 50 kDa molecular weight cut-off (MWCO) was purchased from Spectrum Laboratories Inc. (Shewsbury, MA, USA). The inhibitors in MEO_2MA and 2-HEA were removed with neutral alumina and inhibitor remover columns.

2.3.2 Synthesis of Xanthanted SNPs

Starch nanoparticles (7.2 g, 6.15 g dry weight or 38 mmol of glucopyranose units) were dispersed in water (18 mL) in a 50-mL round-bottom flask (RBF). The mixture was vortexed for

15 min and stirred with a magnetic stir bar for 30 min to disperse the nanoparticles. A 2 M solution of NaOH (4.5 mL, 9.0 mmol) was then added and the dispersion was stirred for 30–60 min. CS_2 (0.24 mL, 3.97 mmol, for a target DS = 0.105) was then added dropwise and the flask was placed in a water bath at 35 °C. The solution, which turned reddish-orange after 2 h, was allowed to cool to room temperature and precipitated in methanol. The precipitate was collected by suction filtration, allowed to dry in a fume hood overnight, and dried in a 60 °C vacuum oven overnight.

2.3.3 Synthesis of Starch-based RAFT Agent

The xanthated SNPs (6.14 g, 37.5 mmol glucopyranose units) were added to deionized (DI) water (19.2 mL) in a 50-mL RBF. The solution was vortexed for 15 min and stirred for 60 min, until the polymer was fully dispersed. Methyl 2-bromopropionate (1.20 mL, 10.8 mmol) was then added dropwise and the flask was placed in a water bath at 80 °C for 40 min. The dispersion turned light yellow by the end of the reaction. The product was collected by precipitation in methanol and suction filtration to obtain a powder that was further dried in a vacuum oven overnight at 60 °C.

2.3.4 Synthesis of SNP-*g*-PMEO$_2$MA

The starch-based RAFT agent (1.0 g, 5.44 mmol, DS 0.022, 0.12 mmol initiating sites) was added to 9.5 mL of DI water in a 25-mL RBF. The solution was vortexed for 15 min and stirred for 30 min until the solid was fully dispersed in water. Potassium persulfate (19 mg, 0.069 mmol) and MEO$_2$MA (176 mg, 0.935 mmol, for a target PMEO$_2$MA content of 15%) were added to the solution, which was then degassed with gentle N_2 bubbling for 30 min and placed in an 80 ^oC water bath for 60 min. The solution turned milky white by the end of the polymerization reaction but became transparent again upon cooling to room temperature. The crude product was purified against water using a Spectra/Por dialysis bag with 50 kD MWCO overnight. The polymer was dried under a N_2 stream, and then in a vacuum oven at 60 ^oC overnight. The yield was 1.11 g (94%), with PMEO$_2$MA content of 14 wt% by ^{1}H NMR analysis. PMEO$_2$MA contents of 7.5 wt% and 30 wt% were also targeted by varying the amount of MEO$_2$MA added in the reaction. The products were characterized by ^{1}H NMR, UV-visible spectroscopy and DLS analysis.

2.3.5 Synthesis of SNP-*g*-PMEO$_2$MA-*b*-PHEA

The starch-based RAFT agent (1.0 g, DS 0.022, 0.12 mmol initiating sites) was added to 9.5 mL of DI water in a 25-mL RBF. The solution was vortexed for 15 min and stirred for 30 min until the solid was fully dispersed in water. Potassium persulfate (19 mg, 0.069 mmol) and 2-HEA (176 mg, 1.52 mmol, for a target PHEA content of 15 wt%) were added to the solution,

which was then degassed with gentle N_2 bubbling for 30 min and placed in an 80 °C water bath for 60 min. The crude product was purified against water in a Spectra/Por dialysis bag with a 50 kD MWCO overnight. The polymer was dried under a N_2 stream, and then in a vacuum oven at 60 °C overnight. SNP-*g*-PHEA (309 mg, 15 wt% PHEA) was then mixed in 4 mL of water with MEO_2MA (54.5 mg, 0.28 mmol, for a target $PMEO_2MA$ content of 15 wt%) in a 10-mL RBF by stirring with a magnetic stir bar for 15 min. Potassium persulfate (6.6 mg, 0.024 mmol) was added, the flask was capped and the solution was degassed by bubbling N_2 gently for 30 min. The flask was then placed in a water bath at 80 °C for 60 min. The solution turned milky white at the end of the reaction but became clear again upon cooling. The mixture was purified against water in a Spectra/Por dialysis bag (50 kD MWCO) overnight. After dialysis the polymer solution was first air-dried, and the solid residue was placed in an oven at 60 °C overnight. The product was characterized by ^1H NMR and UV-visible spectroscopy. A sample denoted as SNP(DS 0.022)-*g*-$PMEO_2MA$(30%)-*b*-PHEA(15%) was prepared and characterized by the same procedures.

2.3.6 Cleavage of $PMEO_2MA$ from SNP-*g*-$PMEO_2MA$

A 400-mg sample of SNP-*g*-$PMEO_2MA$ (15%, DS 0.022) was dispersed in 4 mL of DI water in a 10-mL RBF. A 1-mL aliquot of H_2O_2 (30 wt% H_2O_2, 32 mmol) was added and the reaction was stirred at 70 °C for 48 h. A white precipitate formed, while the supernatant turned from cloudy to clear over the course of the reaction. The precipitate was separated from the

supernatant and both fractions were air-dried in a fume hood, and then in a vacuum oven at 60 °C overnight. The supernatant and precipitate fractions were analyzed by ^{1}H NMR. The precipitate was also dispersed in DMF for GPC characterization.

2.3.7 Characterization Techniques

The modified SNPs were characterized by ^{1}H NMR, UV-visible spectroscopy, DLS and TEM. GPC analysis was used to characterize the grafted polymer chains.

2.3.7.1 ^{1}H NMR

The samples (20 mg) were dispersed in 1 mL of deuterated solvent. Most spectra were recorded at 25 °C on 300 MHz Bruker instrument, but a 500 MHz Bruker spectrometer was also used for temperature-dependent measurements with 128 scans averaged. The polymer-grafted SNPs and the cleaved SNPs were dispersed in D_2O, and the cleaved polymer chains were dissolved in DMSO-d_6 for the analysis. The reported chemical shifts are relative to the solvent protons at 4.74 ppm for H_2O and 2.50 ppm for DMSO-d_6

2.3.7.2 UV-visible Spectroscopy

Polymer-grafted SNP samples were prepared in water at a concentration of 1 mg/mL for SNP-*g*-PMEO_2MA and SNP-*g*-PMEO_2MA-*b*-PHEA and loaded in a 1 cm path length cuvette.

The lower critical aggregation temperature (LCAT) of the samples was determined on a Carry 4000 spectrometer at 500 nm wavelength, using a temperature ramp of 1 ^{o}C /min. The LCAT was taken as the temperature at which aggregation started, depicted by an initial drop in % transmittance.

2.3.7.3 DLS Analysis

Dynamic light scattering measurements were conducted on a Malvern Zetasizer Nano S instrument with Non-invasive Back Scatter technology. An aqueous solution of SNP-*g*-$PMEO_2MA$ (15%, DS 0.022) was prepared at a concentration of 1 mg/mL and loaded in a 1 cm path length cuvette. A concentration of 1 mg/mL was selected (to obtain a count rate over 100 kcounts/s) and the samples were filtered at 25 °C through 0.45 μm polytetrafluoroethylene membrane filters with a syringe prior to the measurements, taken at 5 ^{o}C intervals.

2.3.7.4 Transmission Electron Microscopy (TEM)

The SNP and SNP-*g*-$PMEO_2MA$ (15%, DS 0.022) samples were diluted to 0.1 mg/mL in DI water. An 8-μL aliquot of the solution was deposited onto a 400-mesh grid coated with carbon-formvar and was allowed to dry overnight. On the following day, 5 mg of iodine was placed with the TEM grid in a covered petri dish to stain the SNPs overnight. The sample was then imaged at 60 kV on a CM10 Philips microscope with a charge-coupled device camera.

2.3.7.5 Gel Permeation Chromatography

The number-average molecular weight (M_n) and polydispersity index (PDI = M_w/M_n) of the grafted polymer chains was determined using a Hewlett Packard 1100 high-performance liquid chromatography (HPLC) system with a refractive index (RI) detector and two Jordi Resolve columns (model number R15076 with 5 μm bead size), each with 300 mm length × 7.8 mm internal diameter. The instrument used DMF with 0.1% LiCl as the mobile phase at a flow rate of 0.9 mL/min and 40 °C, and the samples were injected at a concentration of 3 mg/mL after filtration through 0.2 μm polytetrafluoroethylene membrane filters. Polystyrene standards were used to calibrate the instrument.

2.4 Results and Discussion

Two different strategies were developed to control the characteristics of the target SNP-*g*-$PMEO_2MA$ particles, using SNPs modified with functional groups acting as reversible addition-fragmentation chain transfer (RAFT) initiator for the methacrylate monomer. The first approach was to vary the degree of substitution (DS) of the starch-based RAFT agent, while maintaining a constant SNP-*g*-$PMEO_2MA$ composition. A RAFT agent with a high DS should generate many short polymer chains due to its multiple reactive sites, while a low DS would generate longer polymer chains due to the presence of fewer initiating sites for a same monomer and SNP concentration. The other approach was to vary the amount of monomer added to the starch-based RAFT agent for a set DS, since the length of the $PMEO_2MA$ chains should increase with the

amount of monomer added to the reaction. An additional strategy to control the solution properties of the materials was the addition of a block of poly(2-hydroxyethyl acrylate) (PHEA) forming a hydrophilic shell on the particles. It was expected that PHEA, being hydrophilic, may prevent macrophase separation of the thermoresponsive SNPs above their LCST.

2.4.1 Synthesis of the RAFT Agent and SNP-*g*-PMEO$_2$MA

The first step in the synthesis involved the modification of the SNPs to introduce thiocarbonylthio groups, serving as RAFT initiating sites. This was done by first reacting the hydroxyl groups of the glucopyranose units with carbon disulfide in the presence of sodium hydroxide. The resulting xanthated starch was then reacted with methyl 2-bromopropionate to obtain the RAFT agent (Scheme 2-1). Methyl 2-bromopropionate was selected because the methyl 2-propionyl group is known to be an efficient free radical homolytic leaving group in RAFT agents.[13,14] It is polar due to the presence of carbon-oxygen bonds and is less bulky than aromatic substituents. It generates a secondary radical, which provides good control over methacrylate monomer polymerization. It is also comparable in structure to the methacrylate propagating radical centers, and thus should be capable of initiating the polymerization efficiently.[15]

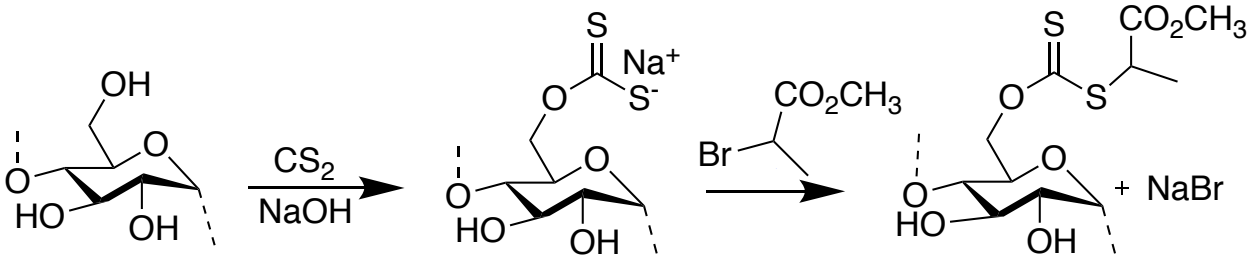

Scheme 2-1: Synthesis of the SNP RAFT agent.

The number of sodium xanthate groups introduced on the SNPs in the first step was controlled by varying the concentration of CS_2 in the reaction. The DS was determined in the second step, after reacting the xanthated SNP with methyl 2-bromopropionate. The degree of substitution (DS) achieved in the second reaction step, corresponding to the number of thiocarbonylthio groups per glucopyranose unit, was calculated by integrating the signal for the anomeric C-1 proton (1H, 5.0-5.5 ppm) of starch and the three methyl protons (3H, 1.4-1.7 ppm) of the methyl 2-propionate fragment, as shown in Figure 2-2a. The peak at 4.5-4.8 ppm is from residual water in the D_2O used as solvent.[16] RAFT agents with different DS were synthesized by varying the amount of CS_2 used in the first step of the reaction, while keeping all other variables constant. Using the spectrum provided in Figure 2-2a as an example, the DS of the RAFT agent was calculated from the Equation 2-1.

$$DS = \frac{Area\ of\ methyl\ peak/3}{Area\ of\ anomeric\ proton\ peak} = \frac{0.066/3}{1.000} = 0.022 \qquad (2-1)$$

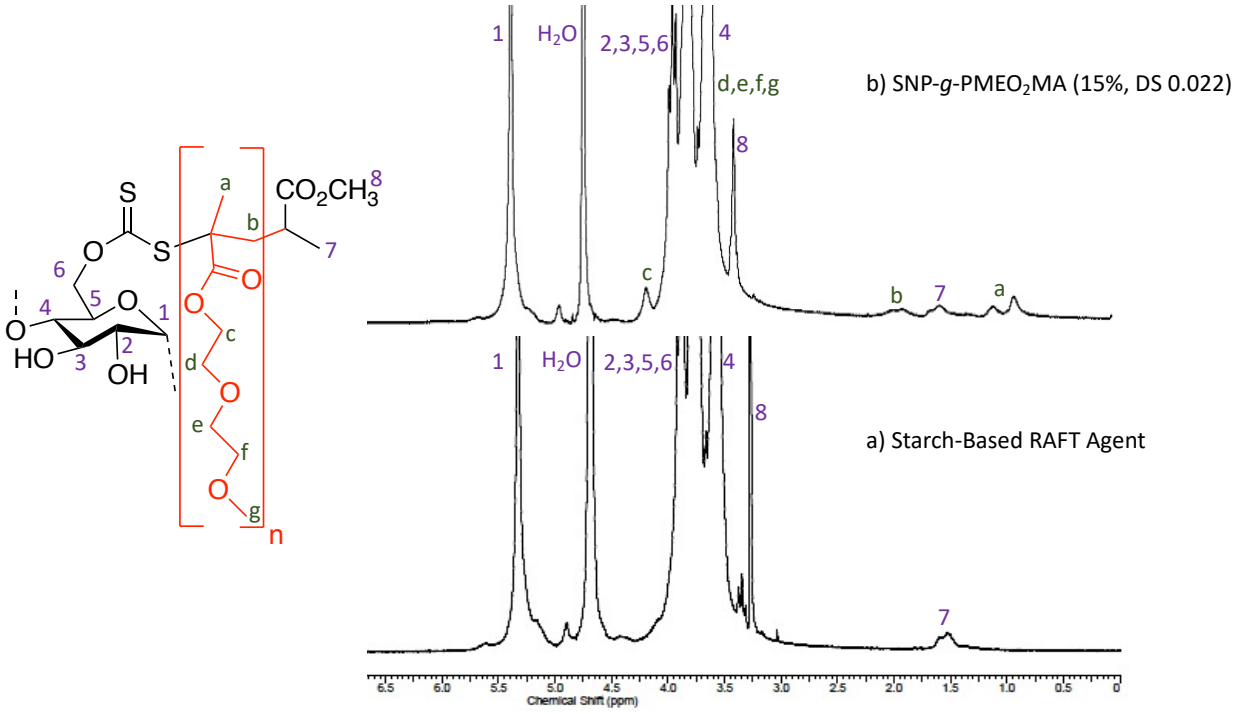

Figure 2-2: ^{1}H NMR spectra in D_2O at 25 °C for a) starch-Based RAFT agent, b) SNP-g-PMEO$_2$MA (15%, DS 0.022).

It was assumed that the amount of CS_2 used determined the outcome of the two-step reaction. Indeed, as the amount of CS_2 in the xanthation step was increased, the DS of the RAFT initiator was observed to increase (Figure 2-3). Unfortunately, the DS attained in the xanthation

step could not be determined, as no distinct ^{1}H signals were observed in the NMR spectrum of the product. ^{13}C NMR was also considered for the DS analysis, but the signal was too noisy due to the low concentration of initiating sites. The overall reaction efficiency for the combined xanthation and bromide displacement steps is provided in Figure 2-3. The reaction was not very efficient, decreasing from 97% to 27% as CS_2 concentration was increased. There was clearly variability in the reaction, causing the error bars from successive data points to overlap with each other. This may be partly because the reaction was heterogeneous, but also because of relatively large integration errors on the small peaks obtained at the very low DS values (0.01– 0.02) used in most cases. The solubility of CS_2 in water is very low (2 g/L at 20 ^{o}C), and that compound can also react with NaOH to form carbonates and thiocarbonates as by-products. For example, Weeldenburg *et al*. showed that 1 mol of CS_2 reacting with 2 mol of NaOH yielded sodium trithiocarbonate and carbonate in a 2:1 ratio. Since this reaction is known to be dominant at temperatures over 49 ^{o}C, the xanthation step was done at 35 ^{o}C.[17] Similar observations were made for cellulose, where the reactions of CS_2 with NaOH competed with xanthation. Cellulose xanthation was shown to follow a complex mechanism with different consecutive and parallel reactions, until equilibrium was attained.[18] Starch degradation is also possible in the presence of NaOH, albeit it was shown that while amylose is sensitive to NaOH, amylopectin is more stable under alkaline conditions.[19] Potential side reactions of starch, following deprotonation of the hydroxyl groups by NaOH, are breakdown of the glucopyranose units into formic, acetic, glycolic, 2-hydroxybutanoic, 2-hydroxy-2-ethylpropanoic and 2-hydroxypentanoic acids.[19] This

is the reason why the xanthated starch intermediate was isolated by precipitation prior to the reaction with ethyl 2-bromopropionate in the synthesis of the RAFT agent.

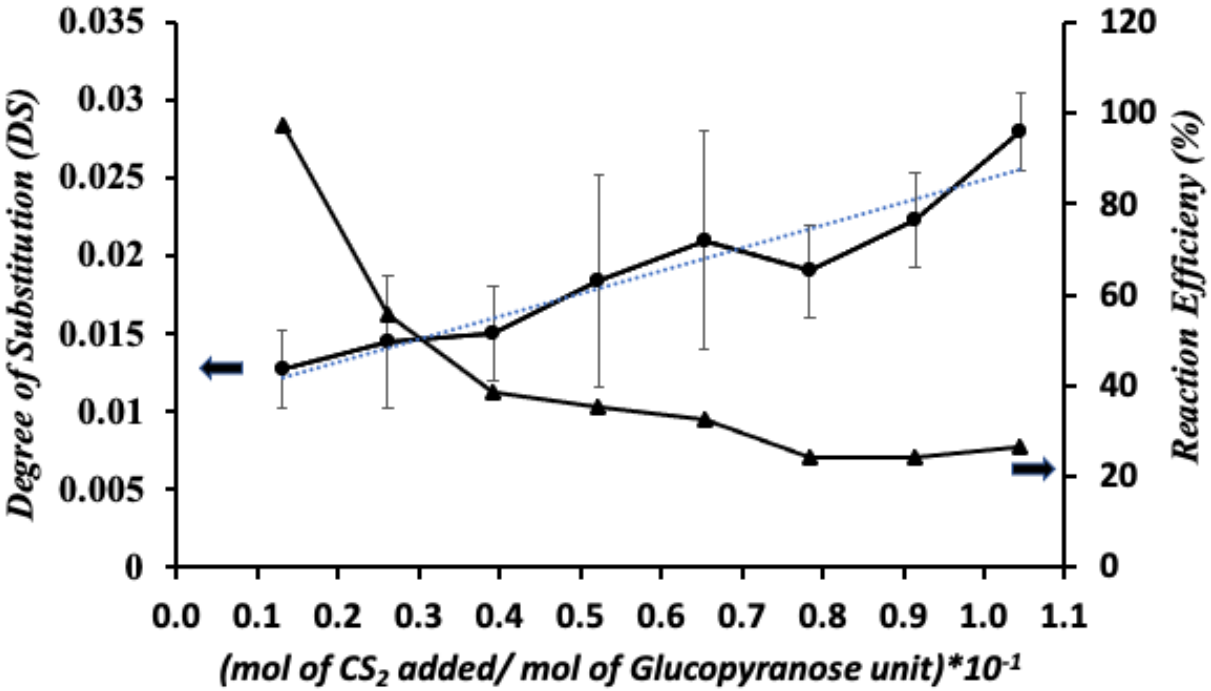

Figure 2-3: Control of degree of substitution (DS) of RAFT agents by varying the amount of CS_2 added in the xanthation step.

RAFT agents were synthesized with DS values ranging from 0.012 to 0.06, to maintain good water dispersibility and to generate relatively few thermoresponsive polymer chains per starch nanoparticle. A RAFT agent with a low DS should generate longer grafted polymer chains, due to the presence of fewer initiating sites in the reaction (Figure 2-4 left). On the other

hand, it was also observed that SNP-*g*-PMEO$_2$MA derived from a RAFT substrate with a higher DS (0.06) had poor water dispersibility, even at room temperature. While shorter polymer chains could be expected to have increased ability to hide within the SNPs at temperatures above the LCST, thus maintaining better water dispersibility, a large number of chains may have more difficulty rearranging within the SNPs due to steric limitations. Increased intramolecular hydrophobic interactions between neighboring grafted SNPs may also have led to poor dispersibility in water.

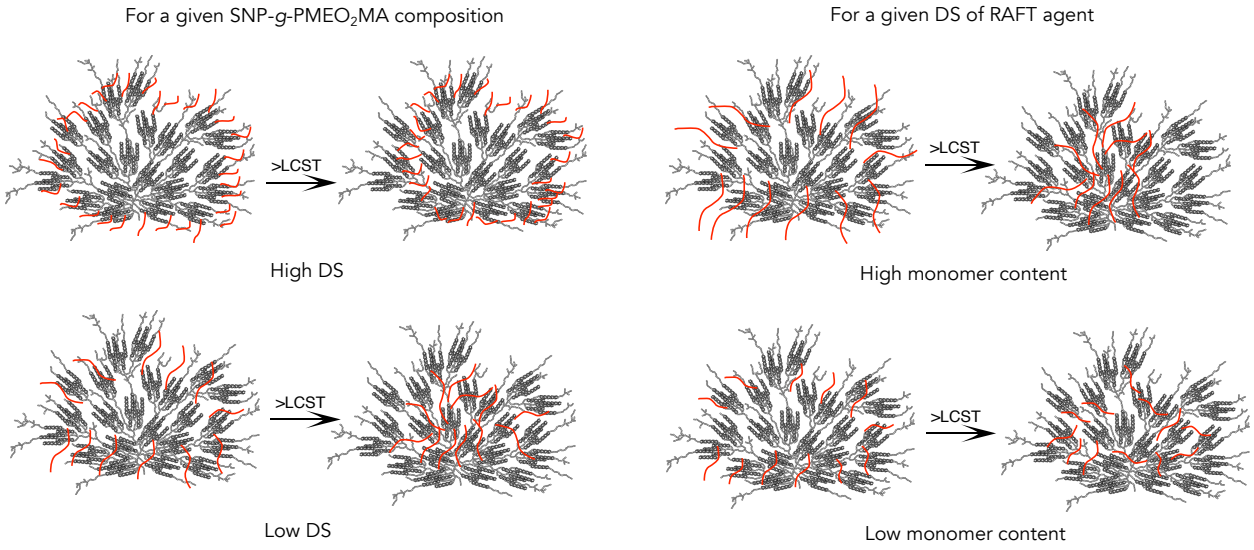

Figure 2-4: Control of SNP-g-PMEO$_2$MA characteristics through variations in the DS of the RAFT agent (left) and the amount of monomer added (right).

^{1}H NMR analysis was performed for the SNP-*g*-PMEO$_2$MA samples prepared by RAFT, and a spectrum is provided in Figure 2-2b as an example. The weight fraction of PMEO$_2$MA in the samples was calculated by integrating the methyl protons (3H, 0.71–1.14 ppm) along the polymethacrylate backbone and the anomeric proton peak for the SNP (1H, 5.00–5.55 ppm). An example of PMEO$_2$MA weight fraction (wt%) calculation is provided below.

$$Wt\%\ \mathrm{PME}O_2\mathrm{MA} = \frac{\frac{Area\ of\ PMEO_2MA\ peak}{3} \times MW_{MEO_2MA}}{MW_{glucopyranose\ unit} + \frac{Area\ of\ PMEO_2MA\ peak}{3} \times MW_{MEO_2MA}} \times 100\% \quad (2-2)$$

$$Wt\%\ \mathrm{PME}O_2\mathrm{MA} = \frac{\frac{0.42}{3} \times 188.2}{162.16 + \left(\frac{0.42}{3}\right) \times 188.2} \times 100\% = 14.0\ \% \quad (2-3)$$

The monomer conversion in the RAFT reaction was calculated as follows:

$$Monomer\ convesion\ \% = \frac{Experimental\ wt\%\ \mathrm{PME}O_2\mathrm{MA}}{Theoretical\ wt\%\ \mathrm{PME}O_2\mathrm{MA}} = \frac{14.0\%}{15\%} = 93.3\% \quad (2-4)$$

This indicates that most of the monomer was successfully grafted to the SNPs. The conversion of the MEO$_2$MA monomer was monitored by removing aliquots 7, 15, 30, 45 and 60 min after the beginning of the reaction. These samples were dialyzed and the ^{1}H NMR spectra

obtained for these samples are provided in Appendix A-1. The polymer peak at 0.71–1.14 ppm increased in intensity with time, confirming the growth of the grafted polymer chains. The monomer conversion was almost complete (> 90 %) after one hour (Figure 2-5).

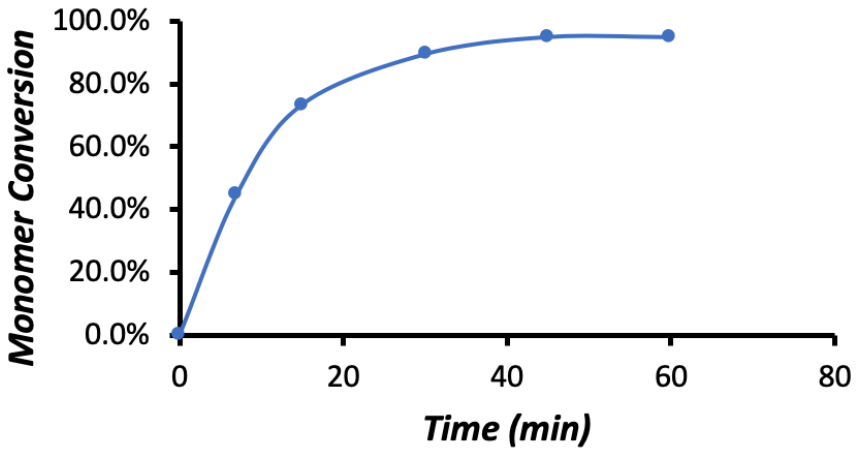

Figure 2-5: Conversion of MEO_2MA with time.

^{1}H NMR measurements were conducted at temperatures ranging from 5 to 25 °C for the characterization of SNP-*g*-$PMEO_2MA$ samples. Since high molecular weight $PMEO_2MA$ has an LCST of 26 °C[20] and is prone to aggregation at higher temperatures, it was decided to carry out the measurements below that temperature to determine the optimal conditions for composition quantification. The composition, expressed as the percentage of grafted $PMEO_2MA$ in the material by weight, was calculated from the NMR spectra of the dialyzed products, by integrating the signal for the methyl group of $PMEO_2MA$ (3H, 0.71–1.14 ppm) and the anomeric

C-1 proton of the glucopyranose units (1H, 5.0–5.5 ppm) shown in Figure 2-2b. The results of the temperature-dependent analysis, attempted for three representative samples at five different temperatures, are summarized in Table 2-1. The NMR spectra confirmed that the grafted polymer content increased with the amount of monomer added in the reactions, and that the apparent composition (wt% $PMEO_2MA$) did not vary significantly between 5 and 25 ^oC. For example, the composition obtained for SNP-*g*-$PMEO_2MA$ (DS 0.038, 15%) varied from 15.1% at 5 ^oC to 14.9% at 25 ^oC, which is comparable to the expected (theoretical) value in both cases. A similar trend was observed for SNP-*g*-$PMEO_2MA$ (DS 0.038, 30%). The larger variations in composition observed for SNP-*g*-$PMEO_2MA$ (DS 0.038, 7.5%) at 5 and 10 ^oC is attributed to decreased mobility of the starch component in water at low temperatures.[21] A temperature of 20–25 ^oC therefore appears optimal for the analysis of the samples, since the NMR composition data agree best with the target compositions.

Table 2-1: Comparison of experimental compositions determined by ^{1}H NMR analysis of SNP-g-$PMEO_2MA$ in D_2O at different temperatures.

Temperature (°C)	$PMEO_2MA$ (7.5%)/SNP Integral Ratio	Wt% $PMEO_2MA$ by NMR	$PMEO_2MA$ (15%)/SNP Integral Ratio	Wt% $PMEO_2MA$ by NMR	$PMEO_2MA$ (30%)/SNP Integral Ratio	Wt% $PMEO_2MA$ by NMR
5	0.10	3.7	0.46	15.1	1.17	31.2
10	0.08	3.0	0.35	12.0	1.24	32.5
15	0.13	4.8	0.45	14.9	1.04	28.8
20	0.13	4.8	0.47	15.5	1.07	29.4
25	0.14	5.1	0.45	14.9	1.12	30.3

2.4.2 Cleavage of $PMEO_2MA$ from SNP-*g*-$PMEO_2MA$

The RAFT polymerization mechanism involves the addition of monomer units at the C-S bond of the RAFT agent connected to the starch substrate. The resulting polymer therefore retains the thiocarbonylthio group, derived from the xanthated SNPs in this case. The thiocarbonylthio group can be cleaved from the attached polymer chain,[22] however, such that characterization of the grafted $PMEO_2MA$ chains by GPC analysis would be possible after cleavage from the starch substrate. Thiocarbonylthio groups can undergo different reactions such as nucleophilic addition, aminolysis, ozonolysis, thermolysis, and cleavage through the addition of excess initiator.[22] It should also be considered that the ether (C-O-C) and ester linkages in the glycol side chains of $PMEO_2MA$ can be cleaved in the presence of a strong acid and/or

nucleophile. Consequently, radical-induced cleavage was selected to isolate the $PMEO_2MA$ chains from the starch substrate, using H_2O_2 as a water-soluble reagent. In the presence of heat and/or UV light, the peroxide breaks down to ·OH radicals that can penetrate the grafted SNPs and degrade the thiocarbonylthio groups, inducing the cleavage reaction. These conditions are also mildly acidic, since H_2O_2 solutions are maintained slightly acidic to improve their stability. The use of H_2O_2 is interesting because water and oxygen are the only by-products generated in the reaction.[23,24] The polymer-grafted SNP samples were thus heated to 70 °C in the presence of H_2O_2 for 48 h to cleave the thiocarbonylthio moieties in SNP-*g*-$PMEO_2MA$ (15%, DS 0.022). Two fractions were visible at the end of the reaction: A white sticky precipitate was formed at the bottom, while the supernatant was a clear liquid that did not exhibit an LCST upon heating. Analysis by ^1H NMR spectroscopy in D_2O of the sample fraction remaining soluble in water at 70 °C (Figure 2-6d), well above the LCST of $PMEO_2MA$, showed that the SNPs underwent oxidative degradation to shorter chains and/or oxidized saccharide derivatives. Since the ·OH radicals are also strong oxidants, they are indeed capable of oxidizing the primary and secondary alcohol moieties in starch to carbonyl groups, more specifically aldehydes for primary alcohols and ketones for secondary alcohols. The proposed mechanism for the formation of oxidized starch is shown in Scheme 2-2b, where a secondary alcohol oxidized to form a ketone.[3] The intensity of the anomeric proton signal (1H, 5.0–5.5 ppm) was strongly decreased, and the H_b proton peak at 8.0–8.3 ppm likely corresponds to an aldehyde group.[25] The sample fraction insoluble in water at 70 °C was only partially soluble at room temperature, so it was analyzed by

^{1}H NMR spectroscopy in DMSO-d_6 (Figure 2-6c) and corresponded to cleaved PMEO$_2$MA chains: The methyl protons (0.71–1.14 pm) and the diethylene glycol groups (3.25–3.50 ppm) from PMEO$_2$MA are clearly visible, while there is no peak at 5.0–5.5 ppm, confirming that the polymer was cleaved from the SNPs.

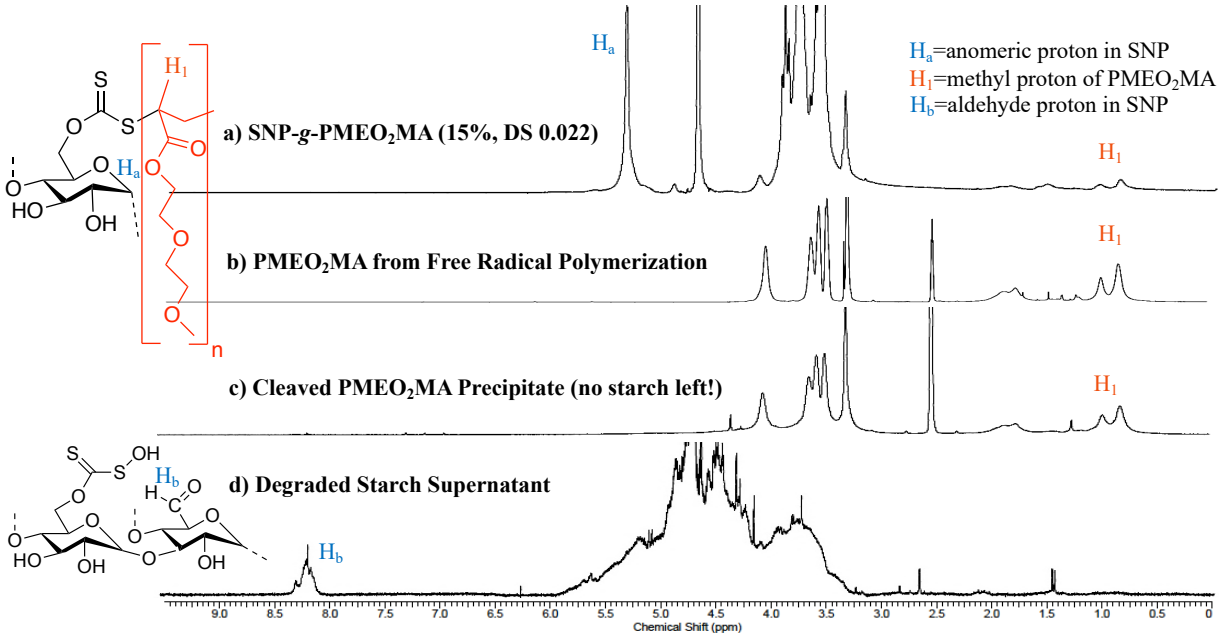

Figure 2-6: ^{1}H NMR spectra for a) SNP-g-PMEO$_2$MA (15%, DS 0.022), b) PMEO$_2$MA, c) cleaved PMEO$_2$MA precipitate, d) oxidized and degraded starch supernatant at 25 ^{o}C.

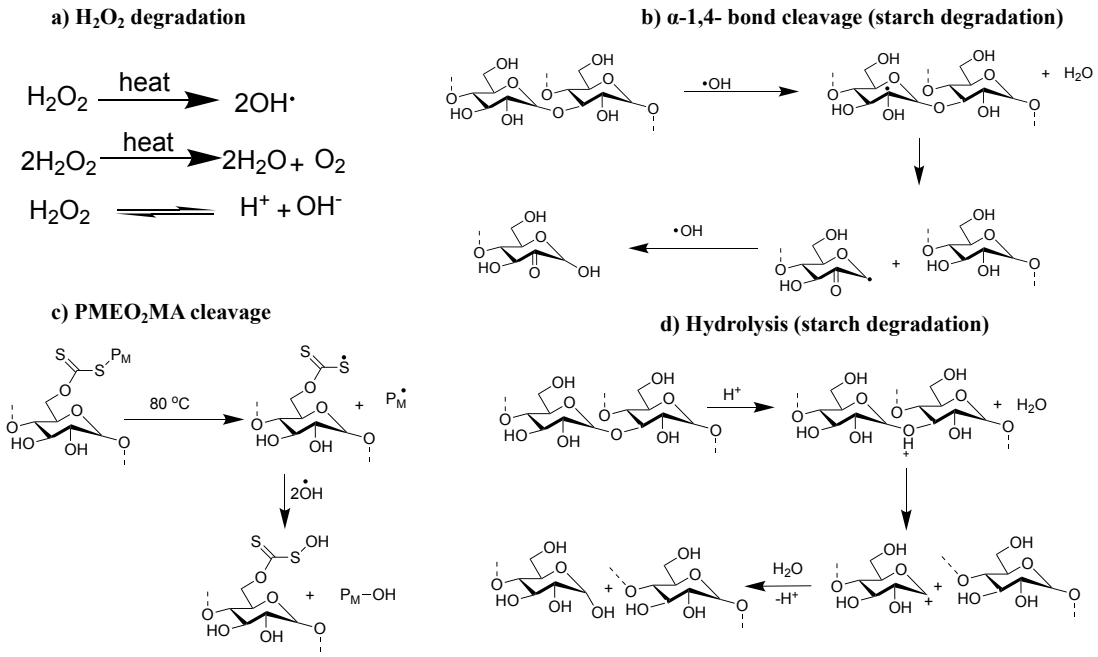

Scheme 2-2: Possible reactions in the radical-induced cleavage of SNP-g-PMEO₂MA with H₂O₂.

SNP-*g*-PMEO$_2$MA with a DS of 0.022, with 7.5, 15 and 30 wt% target PMEO$_2$MA contents, and SNP-*g*-PMEO$_2$MA with 15 wt% target PMEO$_2$MA content at DS 0.012, were analyzed to demonstrate control over the molecular weight of the grafted PMEO$_2$MA chains as a function of the reaction conditions used. The apparent M_n of the cleaved PMEO$_2$MA chains for SNP-*g*-PMEO$_2$MA with a 7.5 to 30 wt% target PMEO$_2$MA and DS of 0.022 increased from 30.8 to 57.5 kg/mol, with polydispersity index (PDI) values of 1.59–1.64 (Table 2-2). The SNPs had a comparatively higher PDI of 3.0. A PDI of 1.3 was obtained by Pfukwa *et al.* when the Z

group was removed by heating a RAFT-synthesized poly(N-vinylpyrrolidine) with H_2O_2.[24] Nevertheless, the grafted $PMEO_2MA$ chains obviously increased in length when more monomer was added at constant DS in our system. The cleaved $PMEO_2MA$ chains of SNP-*g*-$PMEO_2MA$ (15%, DS 0.012) had an M_n = 58.6 kg/mol (PDI = 1.86), as compared with M_n = 43.3 kg/mol (PDI = 1.64) for SNP-*g*-$PMEO_2MA$ (15%, DS 0.022 (Table 2-2). The $PMEO_2MA$ chains were therefore shorter for the DS 0.022 substrate as compared to DS 0.012. This is expected, as a RAFT SNP substrate with a higher DS should generate more shorter polymer chains due to its numerous reaction sites, while a lower DS will produce fewer longer polymer chains due to its decreased number of reaction sites.

The theoretical M_n values estimated from NMR analysis, by considering the DS of the substrate and the amount of monomer added in the reactions, were much lower than the apparent M_n values obtained by GPC analysis with a polystyrene standards calibration curve. The theoretical M_n calculations assumed that all the RAFT initiating sites participated in the polymerization reaction (initiation efficiency = 1). This was clearly not the case, as the experimental M_n (from GPC) was much higher than the theoretical M_n in all cases. The large (up to 50-fold) M_n differences simply cannot be explained using a polystyrene calibration curve in the GPC analysis, but more likely by the fact that very few RAFT sites on starch initiated the polymerization. The ratio of experimental to theoretical M_n values corresponds to initiator efficiencies of 0.020–0.055 (2.0–5.6%), indicating that polymerization only involved a small fraction of the RAFT sites on starch (Table 2-2). This could be due to the inability of the

MEO_2MA monomer to reach the RAFT sites present within the SNPs. Since the reaction was carried out at 80 °C, monomers added to the hydrophobic $PMEO_2MA$ chains on the surface of the SNPs would have favored their growth, while RAFT sites buried within the SPN substrates would have become increasingly inaccessible.

Table 2-2: Comparison of the number-average molecular weights (M_n) obtained from GPC and NMR.

Sample	M_n from GPC (kg/mol)	PDI	Theoretical M_n (kg/mol)	Initiator Efficiency
SNP-*g*-$PMEO_2MA$ (30%, DS 0.022)	57.5	1.60	3.21	0.056
SNP-*g*-$PMEO_2MA$ (15%, DS 0.022)	43.3	1.64	1.33	0.031
SNP-*g*-$PMEO_2MA$ (7.5%, DS 0.022)	30.8	1.59	0.61	0.020
SNP-*g*-$PMEO_2MA$ (15%, DS 0.012)	58.6	1.86	2.41	0.041

2.4.3 Synthesis of SNP-*g*-$PMEO_2MA$-*b*-PHEA

Since RAFT polymerization involves the insertion of monomer units at the C-S bond connected to the starch substrate, SNP-*g*-PHEA had to be synthesized first, so as to insert the $PMEO_2MA$ block between the SNP and the PHEA chain segment. The idea was indeed to produce nanoparticles with a SNP core, $PMEO_2MA$ chains attached to it, and a shell of hydrophilic PHEA segments. Since PHEA increases the hydrophilicity of SNP-*g*-$PMEO_2MA$, it

should prevent macrophase separation above the LCST which might be helpful for some applications.[25]

Sample SNP-*g*-PMEO$_2$MA-PHEA (30 wt% PMEO$_2$MA, 15 wt% PHEA), derived from the RAFT substrate with DS 0.022, was analyzed by ^{1}H NMR. The grafted PHEA content was determined after dialysis, by integration of the CH signal from the PHEA backbone (1H, 2.3 ppm) and the anomeric proton (1H, 5.0–5.5 ppm, Figure 2-7).

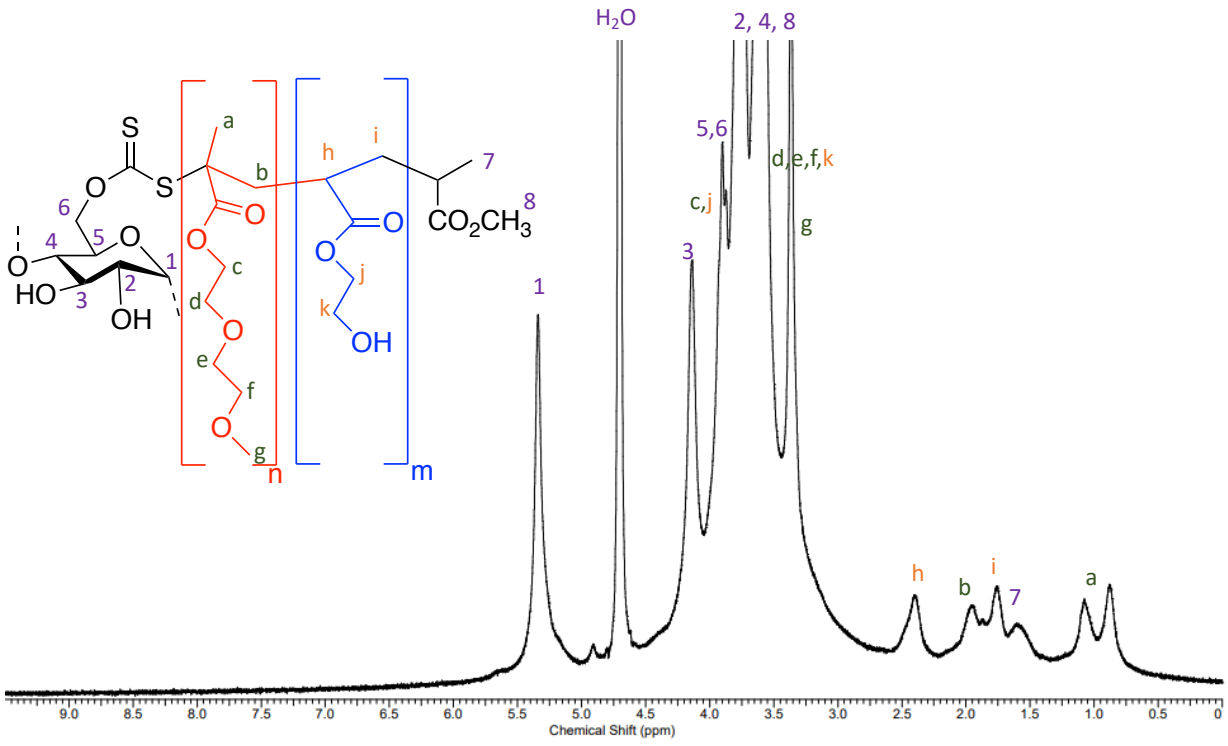

Figure 2-7: ^{1}H NMR spectrum of SNP-g-PMEO$_2$MA-PHEA in D$_2$O at 25 °C.

An example of PHEA weight fraction calculation is provided in Equations 2-5 and 2-6:

$$Wt\%\ \text{PHEA} = \frac{Area\ of\ PHEA\ peak \times MW_{HEA}}{MW_{glucopyranose\ unit} + Area\ of\ (PHEA \times MW_{HEA} + \frac{PMEO_2MA}{3} \times MW_{PMEO_2MA})} \times 100\% \quad (2-5)$$

$$Wt\%\ \text{PHEA} = \frac{0.35 \times 116.12}{162.16 + ((0.35 \times 116.12) + (0.90/3 * 188.2))} \times 100\% = 15.6\ \% \quad (2-6)$$

The monomer conversion in the polymerization reaction was calculated according to Equation 2-7, its value corresponds to full conversion within experimental error limits:

$$Monomer\ convesion\ \% = \frac{Experimental\ wt\%\ \text{PHEA}}{Target\ Theoretical\ wt\%\ \text{PHEA}} = \frac{15.6\%}{15\%} = 104\% \quad (2-7)$$

2.4.4 UV-visible Spectroscopy

The series of polymer-grafted SNPs synthesized were characterized by UV-visible spectroscopy to determine their lower critical aggregation temperature (LCAT), corresponding to the temperature at which aggregation of the thermoresponsive particles begins.

The LCAT (or more accurately the cloud point of the system) is the temperature above which the polymer becomes insoluble and precipitates out of the solution. This involves a steep decrease in %transmittance for a thermoresponsive polymer solution. The LCAT, and more generally the lower critical solution temperature (LCST) of a polymer solution typically depends upon H-bonding between the polymer and water molecules. The water molecules bind to the polymer chains below the LCST, which results in a decrease in the enthalpy of mixing (ΔH_{mix}

negative) favorable to solubility, but ΔS_{mix} which is the entropy of mixing also becomes negative due to enhanced ordering of the water molecules.[26] The Gibbs free energy of mixing, $\Delta G_{mix} = \Delta H_{mix} - T\Delta S_{mix}$, will be favorable (negative) below the LCST because the ΔH_{mix} term is dominant, such that the polymer remains dispersed. As the temperature increases above the LCST, ΔH_{mix} becomes less negative due to the disruption of hydrogen bonding between the polymer and water molecules, such that ΔG_{mix} becomes positive (unfavorable) overall, inducing the collapse of the polymer chains.

In the current case of the polymer-grafted SNPs, the thermoresponsive $PMEO_2MA$ segments covalently bound to hydrophilic starch should confer thermoresponsive character to the starch. A drop in transmittance is indeed observed for the $PMEO_2MA$-grafted SNPs (Figure 2-8), albeit the transition is different from the sharp transitions observed for thermoresponsive homopolymers such as PNIPAM, likely due to the presence of the hydrophilic SNP component.[27] Variations in the LCAT, reflecting changes in the LCST of the materials, was defined as the temperature at which particle aggregation was initiated, leading to an initial drop in %transmittance.

Since the LCAT is concentration-dependent, the measurements were performed at 1 mg/mL, which is the same concentration at which the DLS analysis was conducted.[12] The weight fraction of $PMEO_2MA$ and the DS of the substrates were varied to determine their influence on the LCAT of the samples. The influence of a hydrophilic PHEA block forming a shell on the aggregation of SNP-*g*-$PMEO_2MA$ (15%, DS 0.022) was also investigated. The LCAT values

indeed varied with the structure and the composition of the grafted SNPs (Table 2-3). For example, as the $PMEO_2MA$ content increased from 15 to 30 wt% at DS 0.022 (or as the $PMEO_2MA$ chains became longer), the LCAT decreased from 32 to 20 ^oC. Interestingly, the LCAT or LCST of thermoresponsive polymers is normally only M_n-dependent in the low M_n range. For example, Lessard *et al.* observed a mere 2 ^oC decrease in LCST from 32.9 ^oC to 30.9 ^oC as the M_w of poly(*N*,*N*-diethylacrylamide) increased from 13 kg/mol to 58 kg/mol. The change in LCST was even less significant as the molecular weight was increased further, with no change observed from 593 to 1300 kg/mol.[28] As the $PMEO_2MA$ content was increased from 7.5 to 15 wt%, the LCAT increased from 28 ^oC to 32 ^oC which could be due to the ability of these longer chains to hide within SNPs delaying the hydrophobic interactions between the chains themselves but as the temperature was further increased, SNP-*g*-$PMEO_2MA$ (15 wt%) had a larger drop in transmittance than SNP-*g*-$PMEO_2MA$ (7.5 wt%).

Comparisons can be done among the samples, for example at constant $PMEO_2MA$ content while the DS is varied, to understand the influence of the number of $PMEO_2MA$ segments grafted on the LCAT: The LCAT increased from 32 to 36 ^oC when the DS was increased from 0.022 to 0.038. This is expected, since shorter $PMEO_2MA$ chains formed at DS 0.038 than 0.022 due to the larger number of initiating sites. Shorter chains should take longer to aggregate through intramolecular hydrophobic interactions, but the extent of aggregation above the LCAT was also lower (or the %transmittance higher) for SNP-*g*-$PMEO_2MA$ (15%, DS 0.038; Figure 2-8). Furthermore, no clear LCAT was observed for SNP-*g*-$PMEO_2MA$ (15%, DS 0.06), but

rather a gradual increase in turbidity (Figure 2-8). This is attributed to the presence of a large number of initiating sites on that substrate, forming shorter chains. Aggregation of the shorter $PMEO_2MA$ segments through intramolecular hydrophobic interactions is expected to be more difficult, as these can more easily rearrange to hide within the SNPs above the LCAT. Finally, the addition of a PHEA block to SNP-*g*-$PMEO_2MA$ (30%, DS 0.022) decreased aggregation significantly above the LCST. This is inferred from the corresponding curves in Figure 2-8, as the %transmittance above the LCST increased by over 30% for the sample including the PHEA shell relatively to the SNP-*g*-$PMEO_2MA$ substrate.

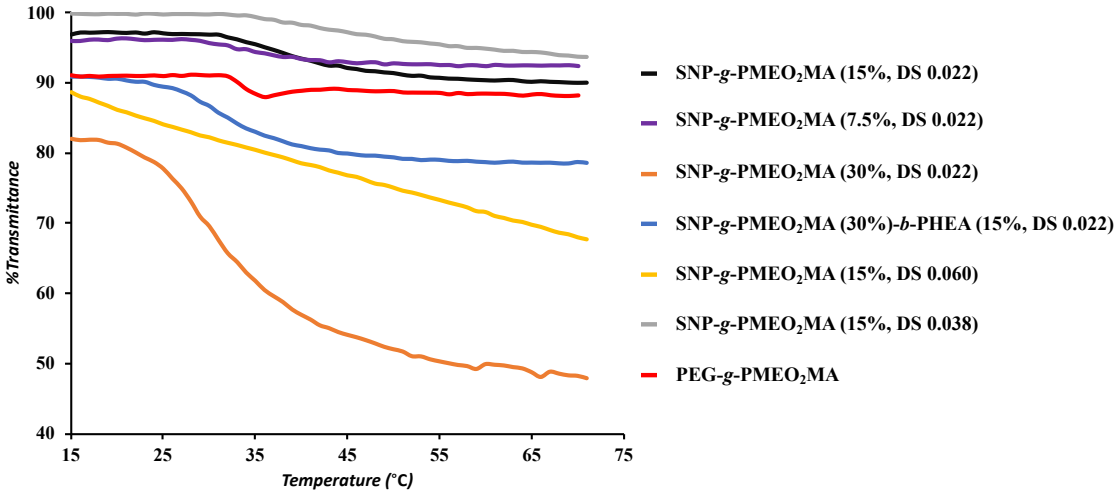

Figure 2-8: Transmittance curves as a function of temperature for the polymer-grafted SNPs.

Table 2-3: LCAT values obtained from the transmittance curves in Figure 2-8.

PMEO$_2$MA-grafted Sample	LCAT (^{o}C)
SNP-*g*-PMEO$_2$MA (15%, DS 0.022)	32
SNP-*g*-PMEO$_2$MA (7.5%, DS 0.022)	28
SNP-*g*-PMEO$_2$MA (30%, DS 0.022)	20
SNP-*g*-PMEO$_2$MA (30%)-*b*-PHEA (15%, DS 0.022)	26
SNP-*g*-PMEO$_2$MA (15%, DS 0.060)	-
SNP-*g*-PMEO$_2$MA (15%, DS 0.038)	36
PEG-*g*-PMEO$_2$MA	32

2.4.5 DLS Analysis

The hydrodynamic diameter of the SNP-*g*-PMEO$_2$MA samples was monitored as a function of temperature, to explore the use of DLS as an alternate method to determine the LCAT. In contrast to the UV-vis measurements, where the temperature was ramped continuously at 1 °C/min, it was necessary to set a temperature and wait for equilibration before the DLS measurements, which made that method much more time-consuming, such that measurements were only carried out at 5 °C intervals in that case. In spite of the rather crude approach used, a sharp increase in the number-average diameter was observed (Figure 2-9) at temperatures comparable to the LCAT determined in the UV-vis measurements. This is understandable, as

the polymers become hydrophobic at their LCAT, which promotes aggregation. For example, the transition temperatures between 35–40 °C for SNP-*g*-$PMEO_2MA$ (15%, DS 0.038) and 30–35 °C for SNP-*g*-$PMEO_2MA$ (15%, DS 0.022) determined by DLS are consistent with the LCAT obtained by UV-visible spectroscopy (36 and 32 °C, respectively). As expected, the sample with a DS of 0.022 and longer $PMEO_2MA$ chains began aggregating at a lower temperature than the sample with a DS of 0.038. In addition, the size distribution of the aggregated thermoresponsive SNPs was narrower than below the LCAT, as shown in Figure 2-9: The PDI values decreased to 0.16 for the sample with a DS of 0.022 and 0.25 for the sample with a DS of 0.038, indicating the formation of micellar aggregates of more uniform size. It therefore appears that DLS measurements are equivalent to the UV-visible method for the determination of the LCAT, albeit the technique would be much more time-consuming if comparably accurate results were desired, which would require carrying out DLS measurements at less than 5 °C intervals.

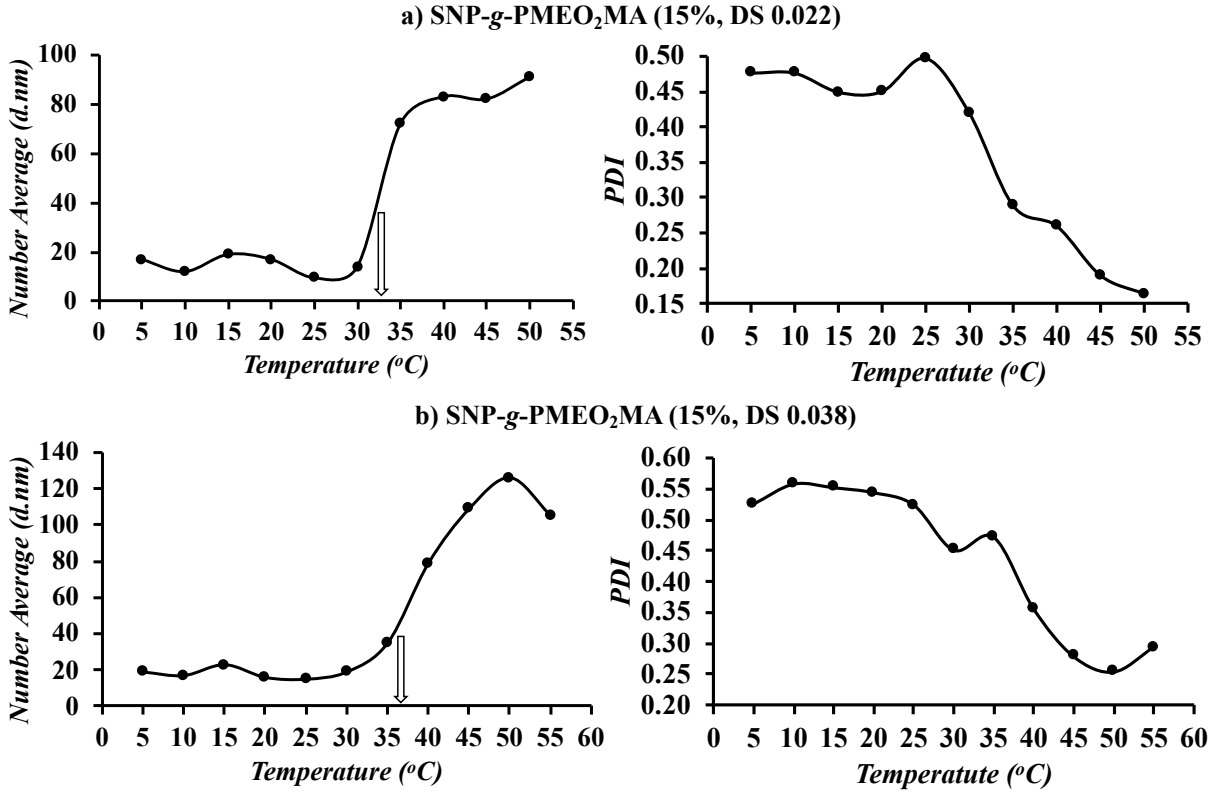

Figure 2-9: Temperature-dependent variations in size and polydispersity of SNP-g-PMEO$_2$MA (15%) with a DS of (a) 0.022 and (b) 0.038.

2.4.6 Transmission Electron Microscopy

The core–shell structure of the unmodified SNP and SNP-*g*-PMEO$_2$MA (15%, DS 0.022) samples was visualized after staining the starch component with iodine (Figure 2-10). It is clear

that the dark core in Figure 2-10a, corresponding to the SNPs, is surrounded by a lighter shell of $PMEO_2MA$ chains in Figure 2-10b.

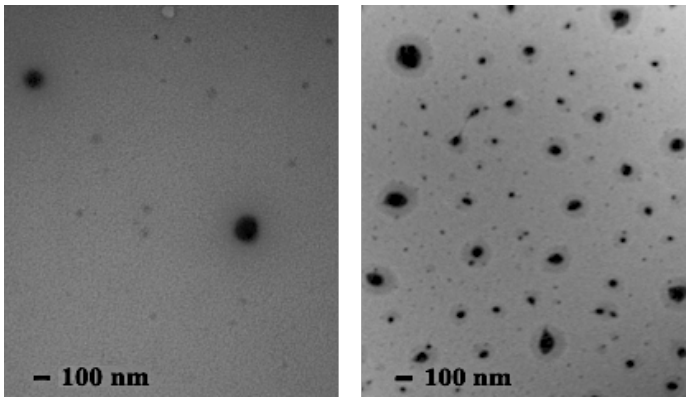

(a) (b)

Figure 2-10: TEM pictures corresponding to the unmodified SNPs (a) and SNP-g-$PMEO_2MA$ (15%, DS 0.022, b) stained with iodine.

2.5 Conclusions

RAFT polymerization was successfully applied to the synthesis of thermoresponsive polymer-grafted SNPs which provided an easy control over the characteristics of modified SNPs in terms of the number and length of the $PMEO_2MA$ segments and the hydrophilic-lipophilic balance (HLB) of the nanoparticles. These materials formed micelles over their LCAT, due to the hydrophobicity of $PMEO_2MA$ and the hydrophilic nature of SNP. Moreover, the LCAT of

the particles could be controlled by adjusting either the DS of the RAFT macroinitiator or the monomer content. Hydrophilic PHEA segments also increased the LCAT of SNP-*g*-$PMEO_2MA$ and stabilized the nanoparticles in solution. Different types of thermo-responsive polymers with various combinations of smart monomers offer a new class of bio-relevant applications by utilizing many benefits such as their ‘on–off' reversible switching and ‘on-demand' controllable and repeatable properties in response to temperature changes. Drug and gene delivery, tissue adhesion prevention, and wound covering are only a few of the uses.[29] Every application has its own set of requirements, and the ability to alter the polymer's properties may make $PMEO_2MA$-grafted SNPs a viable smart material choice.

Chapter 3

Thermoresponsive Starch Nanoparticles for the Extraction of Bitumen from Oil Sands

3.1 Abstract

Starch nanoparticles (SNPs) grafted with thermoresponsive poly(di(ethylene glycol) methyl ether methacrylate) ($PMEO_2MA$), synthesized with systematic variations in grafting density and $PMEO_2MA$ chain length, were investigated for the extraction of bitumen from oil sands. Because $PMEO_2MA$ exhibits temperature-dependent solubility, the polymer-grafted SNPs are amphiphilic above their lower critical aggregation temperature (LCAT) and form micellar aggregates remaining dispersed in water, while interacting with and solubilizing the bitumen component from the sand and silt mixture in the extraction process. Upon cooling below the LCAT, the $PMEO_2MA$ domains become hydrophilic again and the grafted SNPs partition to the water phase, which enables their recovery and reuse in additional extraction cycles, while the extracted bitumen can be skimmed off from the aqueous phase. The performance of the thermoresponsive SNP additives was investigated with an oil sand sample containing 10.5 wt% bitumen and 2 wt% fines, by tumbling oil sand–water–SNP mixtures and a small amount of toluene diluent in vials at 45 °C. The optimal SNP-*g*-$PMEO_2MA$ composition, structure and concentration were determined through multiple cycles of bitumen extraction. The addition of 0.5 M NaCl was also shown to be beneficial to precipitate fines and improve the bitumen

extraction efficiency, which reached over 80% under optimal conditions. The extraction efficiency was maintained over 4 cycles by adding incremental amounts of $PMEO_2MA$-grafted SNPs to compensate for losses in the extraction process.

3.2 Introduction

Oil sands or tar sands are loose, incoherent deposits of sand containing petroleum in the form of bitumen. The bitumen deposits in Canada are considered to be among the largest in the world, with about 175-300 billion barrels of bitumen covering over 141,000 km^2 in the province of Alberta.[1,2] The formation of petroleum is an extremely lengthy process involving the accumulation of dead organisms on the Earth's surface, and sedimentary rock deposits creating extreme heat and pressure. Over millions of years, these organic deposits transformed into bitumen which can be processed into oil today. Most of the Athabasca bitumen is located in the McMurray Formation, deposited about 110 million years ago.[3]

When bitumen is found beneath the earth surface, it is mixed with quartz sand, clay and water. Bitumen is a dense, viscoelastic material with a semi-solid texture. It is the heaviest form of petroleum, needing to be purified, treated and upgraded to obtain gasoline, jet fuel, heating oil and diesel fuel.[2] It has a color that varies from dark brown to black, a high molecular weight and a low hydrogen to carbon ratio, in addition to nitrogen, oxygen, sulfur, trace metals and organometallic compounds.[4] Rich oil sands can reach up to 18% bitumen by weight, but the average for Alberta's Athabasca oil sands is 12%.[3] An oil content of 5-10% is considered intermediate, while 2-5% oil is lean.[3] Bitumen forms a continuous phase in oil-rich sands and the quartz sand forms the bulk phase, while lean oil sands tend to have more water than bitumen in their continuous phase.[5]

There are currently two main methods used to extract bitumen from oil sands. The open-pit mining strategy involves transporting the oil sands from the deposit to the processing plant, where a large amount of hot water is added to allow the bitumen to float on the water, and the quartz sand to settle by gravity. This process, known as the Clark hot water extraction (CHWE) process, was commercialized by Karl Clark in the 1920s (Figure 3-1). It involves crushing lumps of the mined ore into smaller aggregates, followed by mixing with water and sodium hydroxide in rotatory drums at 50-80 ^{o}C.[6] Strong hydration forces acting at the surface of the sand grains result in the release of bitumen from the sand particles. Chemical additives such as polymers, and air are introduced into the slurry to separate the bitumen by floatation. Separation vessels with a conical shape are used to allow the sand to settle at the bottom, while the aerated bitumen floats to the top to be skimmed off.[2,7] The slurry, still containing a lower amount of bitumen (middling), is collected from the vessel to be mixed with coke naphtha and centrifuged to separate the remaining bitumen from minerals and water. The sand, clay and water are disposed in a tailing pond, and the water is partly recycled.[7] This extraction method is only suitable for oil sands close to the ground surface. When they are located deep underground transporting the oil sands to the surface becomes inefficient, thus the steam-assisted gravity-drainage (SAGD) process was implemented.[6] This in situ method can extract bitumen from underground deposits by injecting high-temperature steam into the sand, causing the bitumen to melt. The melted bitumen and the hot water rise to the ground surface, while the heavy quartz sand remains deep underground.[6]

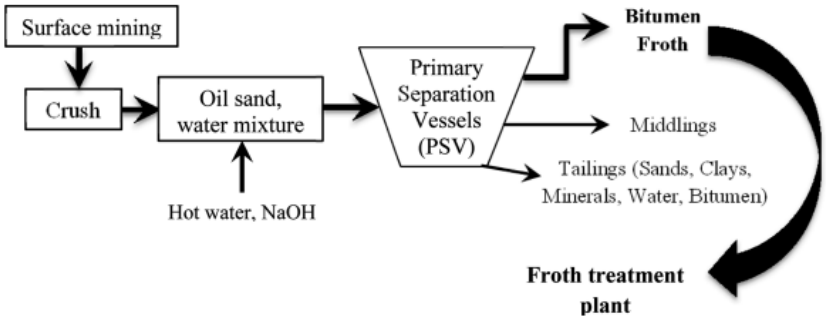

Figure 3-1: The Clark hot water extraction (CHWE) process. Reprinted with permission from reference 6. Copyright (2013) American Chemical Society.

The CHWE is typically operated at 75–80 ^{o}C to reduce the viscosity of the bitumen which favors the separation of the sand from the bitumen.[8] NaOH is commonly used to neutralize organic acids and to improve the wettability of the bitumen. This releases natural surfactants acting at the water-bitumen interface. It can also prevent the attachment of air bubbles to the bitumen particles, however, which is necessary for separation by floatation. Clay minerals, especially fines, also hinder the separation of bitumen from the sand.[3] They bind to the surface of the bitumen droplets and prevent the attachment of air bubbles, thus impeding bitumen floatation. Poor clay flocculation is the primary reason for reduced bitumen recovery. For that reason, the addition of 0.01 to 0.2 wt% NaOH is required to achieve an optimal pH, around 8.5, for efficient bitumen recovery.[9]

While the extraction processes described above have been broadly applied to oil extraction, they cause significant environmental issues. The CHWE and SAGD techniques use large volumes of water heated to over 50 ^{o}C, resulting in the consumption of large amounts of energy to produce the crude oil. As the bitumen is separated from the water and quartz sand components in the processing plant, large volumes of residual water contaminated with extremely fine sand particles and oil residues are produced. The fine particles (fines), in particular, can take 30-40 years to settle. The contaminated water is dumped into large engineered dams (tailing ponds), in the form of an oil-in-water emulsion[10] containing large amounts of sodium hydroxide, in addition to other harmful chemicals including ammonia, mercury and naphthenic acids, which have detrimental effects on wildlife, especially marine organisms.[11] The water consumption can be reduced in oil extraction, but this involves using large amounts of paraffinic and naphthenic solvents to reduce the viscosity of the bitumen and separate it from the sand component, which is even less environmentally friendly and further complicates water treatment.[12]

The above-mentioned issues may be alleviated by using polymeric surfactants exhibiting temperature-dependent solubility behavior in the form of a lower critical solubility temperature (LCST) or lower critical aggregation temperature (LCAT). These polymers become hydrophobic, and either adopt a globular conformation or form aggregated species at temperatures above the LCAT. Yang *et al*. indeed demonstrated that block copolymers of poly(ethylene glycol) and poly(di(ethylene glycol) methyl ether methacrylate) (PEG-*b*-$PMEO_2MA$) could serve to extract bitumen from oil sands. It was suggested that since PEG-*b*-

$PMEO_2MA$ becomes amphiphilic above the LCAT of $PMEO_2MA$, the PEG component favors the formation of micelles in water while $PMEO_2MA$ can interact with bitumen, facilitating its extraction.[13] Unfortunately, this system was only effective for low clay oil sands samples. The PEG-*b*-$PMEO_2MA$ copolymer was also relatively expensive to synthesize. In the current investigation, the hydrophilic PEG component of PEG-*b*-$PMEO_2MA$ was replaced with starch, by grafting starch nanoparticles (SNPs) with $PMEO_2MA$, such that the graft polymer would be soluble in water below the LCAT. Above the LCAT, the hydrophobic $PMEO_2MA$ domains should interact with oil, in analogy to the PEG-*b*-$PMEO_2MA$ system, while maintaining sufficient water dispersability.[4] It will be shown that these characteristics can be exploited for the efficient extraction of bitumen from oil sands at relatively low temperatures.

3.3 Materials and Methods

3.3.1 Materials

Research-grade starch nanoparticles (SNPs) with M_n = 102,000 g/mol and M_w = 304,000 g/mol provided by EcoSynthetix (Burlington, ON, Canada) were modified by grafting with $PMEO_2MA$, and in some cases with poly(2-hydrohyethyl acrylate) (PHEA) as described in Chapter 2. The characteristics of the SNP-*g*-$PMEO_2MA$ and SNP-*g*-$PMEO_2MA$-*b*-PHEA samples investigated for bitumen extraction are provided in Table 3-1. The sample nomenclature

used refers to the composition of the modified SNPs and the degree of substitution (DS) of the starch-based RAFT agent used to synthesize them. For example, the sample identified as SNP-*g*-$PMEO_2MA$ (15 wt%, DS 0.022) has a $PMEO_2MA$ content of about 15% by weight, and was derived from a SNP-based RAFT with a DS = 0.022.

Table 3-1: Characteristics of $PMEO_2MA$- and PHEA-grafted SNPs used in the bitumen extraction experiments.

Sample Number	Description	$PMEO_2MA$ (wt%)	PHEA (wt%)	DS	LCAT (°C)
1	SNP-*g*-$PMEO_2MA$ (15 %, DS 0.022)	15	0	0.022	32
2	SNP-*g*-$PMEO_2MA$ (30 %, DS 0.022)	30	0	0.022	20
3	SNP-*g*-$PMEO_2MA$ (30%)-*b*-PHEA (15%, DS 0.022)	30	15	0.022	26
4	SNP-*g*-$PMEO_2MA$ (15%)-*b*-PHEA (7.5%, DS 0.022)	15	7.5	0.022	28
5	SNP-*g*-$PMEO_2MA$ (15%, DS 0.038)	15	0	0.038	36
6	SNP-*g*-$PMEO_2MA$ (15%, DS 0.060)	15	0	0.06	-

Methanol (ACS reagent, ≥ 99.8 %), tetrahydrofuran (THF, HPLC grade, ≥ 99.9 %), cumene (98%), toluene (ACS reagent, ≥ 99%), and NaCl (ACS reagent, ≥ 99%) were purchased from Sigma-Aldrich (Oakville, ON, Canada). Oil sands samples, labelled as SBos and IOos, were obtained from the Alberta Innovate Technology Futures Sample Bank (Edmonton, AB, Canada) and from Imperial Oil (Edmonton, AB, Canada), respectively. HiSol-10, HiSol-15 and D-40 were obtained from Whitaker Oil (Atlanta, GA, USA).

3.3.2 Measurement of Fines and Bitumen Contents in IOos and SBos

A 1.00 g oil sands sample was loaded in a 20-mL vial and toluene (10 mL) was added. The vial was vortexed for 5 min to dissolve the bitumen and suction filtration was used to separate the dissolved bitumen from the quartz sand and clay components. The solid residue was air-dried for 30 min, water (10 mL) was added and the sample was vortexed for 5 min. The mixture was then allowed to settle on the benchtop for 7 h for a qualitative analysis based on the turbidity of the solution.

Soxhlet extraction was used to determine the bitumen content of the oil sand samples. Filter paper was wrapped around the 1 g oil sands sample and loaded in the Soxhlet extractor. The extraction was performed with refluxing THF in a 50 mL tared round bottom flask for 3 h. After extraction the THF was evaporated under a nitrogen flow, leaving a film of bitumen in the flask. The sample was dried in a vacuum oven at 70 ºC. The mass of bitumen recovered divided by the

mass of the oil sands sample was used to estimate the bitumen content of the sample. The experiments were repeated three times to determine the oil content of each type of oil sand. The remaining solid residue of sand particles, passed through a sieve with a mesh size of 44 μm after bitumen extraction, was used to distinguish fine particles from coarse sand particles.

3.3.3 Bitumen Extraction Procedure

In a typical extraction experiment, 15 mg of SNP-*g*-PMEO$_2$MA or SNP-*g*-PMEO$_2$MA-*b*-PHEA was dispersed in water (15 mL) in a beaker by stirring for 30 min. When used, NaCl (0.44 g, 7.53 mmol) was added to the dispersion and stirring was continued for 5 min. An oil sand sample (1.00 ± 0.01 g) was loaded in a 61 mm × 28 mm screwcap vial, after removing large stones and debris by hand. The SNP-*g*-PMEO$_2$MA solution was then added to the vial, followed by toluene (60 mg). The amounts of polymer and toluene used were varied to investigate the effects of these parameters on the extraction process. Triplicate samples were prepared for each experiment and the vials were mounted on a mechanical rotating arm in an oven at 45 °C. The vials were tumbled in the oven for 24 h at 53 rotations/min. The vials were then removed and left to stand on the bench to allow the sand, bitumen and water to separate for 24 h.

After the mixture settled, drops of toluene were added with a Pasteur pipette to remove the bitumen on the walls of the vial and the cap. The bitumen layer at the top was removed with a Pasteur pipette, a mixture of THF and toluene (1:4 ratio by volume) was used to extract the bitumen remaining in the top and middle (emulsified) layers with a Pasteur pipette, and the two

sample fractions were combined in a clean tared vial for quantification. Residual bitumen in the bottom layer, mixed with the quartz sand, was extracted with THF and transferred to a clean tared vial for quantification. The bitumen solutions in the collection vials were dried on a hot plate at 120 °C overnight and weighed. The bitumen extraction efficiency was calculated as the mass of bitumen from the top and middle layers over the total amount of bitumen collected (Eq. 3-1).

$$Extraction\ Efficiency = \frac{m_{top\ layer} + m_{middle\ layer}}{m_{top\ layer} + m_{bottom\ layer} + m_{middle\ layer}} \qquad (3-1)$$

3.4 Results and Discussion

The purpose of this investigation was to achieve efficient bitumen extraction from oil sands using the SNPs grafted with thermoresponsive $PMEO_2MA$ as described in Chapter 2, whose most relevant characteristics are summarized in Table 3-1. These samples were derived from SNPs functionalized with RAFT initiating sites at different DS, and grafted with $PMEO_2MA$ of different chain lengths. Most samples are best described as having a core–shell morphology (with a SNP core and a shell of $PMEO_2MA$ segments), but two samples also included an additional corona of PHEA chains (Figure 3-2). These thermoresponsive polymer-grafted SNPs are therefore hydrophilic below their LCAT, but become amphiphilic above it. The goal was to optimize the characteristics of the grafted SNPs for efficient oil recovery. Longer $PMEO_2MA$

chains, for example, may have enhanced interactions with bitumen droplets, but also a lower water solubility above their LCAT, whereas shorter chains should lead to higher LCAT values and water solubility. Varying the DS at constant $PMEO_2MA$ content should not only affect the length of the grafted $PMEO_2MA$ chains, but it may also alter the dispersibility of the samples. It is indeed expected that, for high DS samples, it may be more difficult for the hydrophobic $PMEO_2MA$ chain segments to hide within the SNPs above their LCAT, resulting in lower dispersibility. An ideal $PMEO_2MA$-grafted SNP would therefore maintain an optimal hydrophilic-lipophilic balance (HLB) to extract bitumen efficiently over its LCAT, such that it can be reused multiple times due to its temperature-dependent dispersibility and polymer-bitumen interactions.

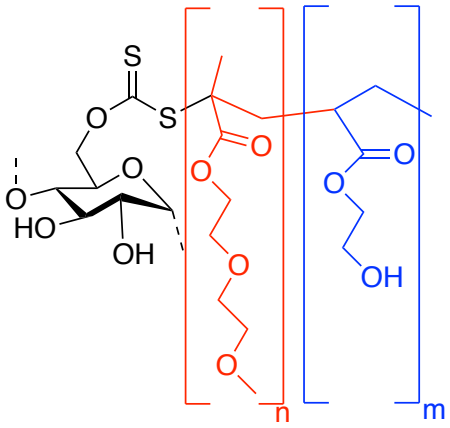

Figure 3-2: Blocks of PHEA (blue) and $PMEO_2MA$ (red) grafted to SNP by RAFT polymerization.

Yang *et al.* previously showed that thermoresponsive PEG-*g*-$PMEO_2MA$ block copolymers can serve to extract bitumen from oil sands.[13] The proposed extraction mechanism for that system relied upon the fact that PEG-*g*-$PMEO_2MA$ becomes amphiphilic above its LCAT, leading to the formation of polymeric micelles with hydrophobic $PMEO_2MA$ segments in their core and a hydrophilic PEG shell. Above the LCAT, the hydrophobic $PMEO_2MA$ domains can associate with bitumen droplets, shuttling them through the water phase to the air-water interface (Figure 3-3). When the mixture is again cooled to room temperature, the micelles dissociate and PEG-*g*-$PMEO_2MA$ becomes completely soluble in the water phase. The sand mixture is found at the bottom of the vial, while the bitumen and toluene collect on the water surface, and the aqueous phase contains most of the hydrophilic PEG-*g*-$PMEO_2MA$ copolymer, but is also turbid due to unsettled sand particles. PEG-*g*-$PMEO_2MA$ was found to work well with the Imperial Oil low-fines oil sand (IOos) sample, but did not work with the high-fines SBos sample.[14] The synthesis of SNP-*g*-$PMEO_2MA$ was thus considered for comparison with PEG-*g*-$PMEO_2MA$ in the extraction of bitumen from oil sands, but also because the cost of synthesizing PEG-*g*-$PMEO_2MA$ makes it economically impractical to implement in the industry.[13]

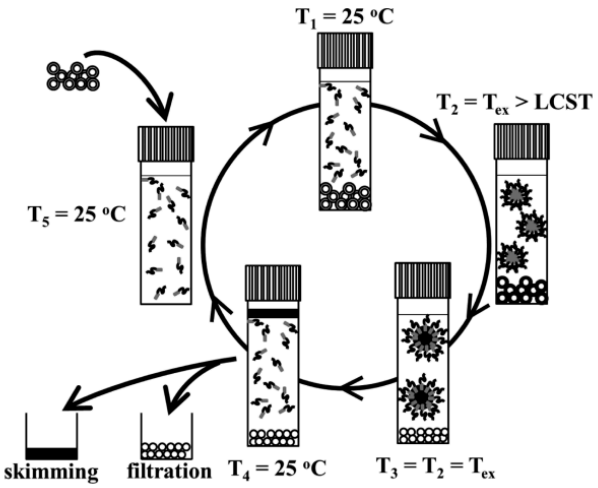

Figure 3-3: Proposed mechanism for the extraction of bitumen from oil sands with PEG-g-PMEO$_2$MA. Reprinted with permission from reference 13. Copyright (2015) American Chemical Society.

The most widely investigated thermoresponsive polymer is poly(N-isopropylacrylamide) (PNIPAM), but applying PNIPAM to bitumen extraction would have several disadvantages. The polymer is toxic, so using large amounts of PNIPAM for bitumen extraction could create potential environmental hazards.[15] Furthermore, when investigated earlier, PNIPAM failed to extract bitumen from tar sands.[13] Consequently, a more environmentally-friendly and lower cost polymer with a low LCST was selected for oil extraction, namely PMEO$_2$MA. The PMEO$_2$MA-grafted SNPs were designed to be amphiphilic similarly to PEG-*g*-PMEO$_2$MA, but would extract bitumen from oil sands in a more environment-friendly manner since the particles are partly

biodegradable, easy to scale-up, and can reduce energy consumption as compared with the previously mentioned conventional extraction methods.

3.4.1 Determination of Bitumen and Fines Contents of IOos and SBos

Fines are clay particles in the water-bitumen interfacial layer that are smaller than 44 μm.[16] They form a layer around the sand particles and are embedded within the bitumen droplets. Due to their strong interactions with bitumen, the fine solids can affect the extraction process adversely, among others by making it difficult for air bubbles to attach to the bitumen droplets. The presence of fines thus hinders bitumen floatation and decreases the consistency of the froth.[16] The two available samples, namely the Imperial Oil oil sand (IOos) and the Athabasca Sand Bank oil sand (SBos), were tested for their fines contents after removal of the bitumen component.

Soxhlet extraction[17] yielded bitumen contents in IOos and SBos of 11.1 (±0.1) and 10.5 (±0.2) wt%, respectively. The two samples were therefore comparable in terms of bitumen contents. Separation of the solid sample on a sieve with a mesh size of 44 μm yielded a fines content of 2% by weight for the SBos sample, while the amount measured for the IOos sample was negligible (< 0.05%). Most of the fines consist of clay particles that can impact the extraction of bitumen from oil sands.[14]

After extraction of the bitumen, the solid component was redispersed by vortex mixing with water and allowed to settle on the benchtop for 7 h. After that time the supernatant of the

IOos sample was comparatively clear, since much of the quartz sand and clay settled at the bottom of the vial, while the SBos supernatant remained much more turbid (Figure 3-4).

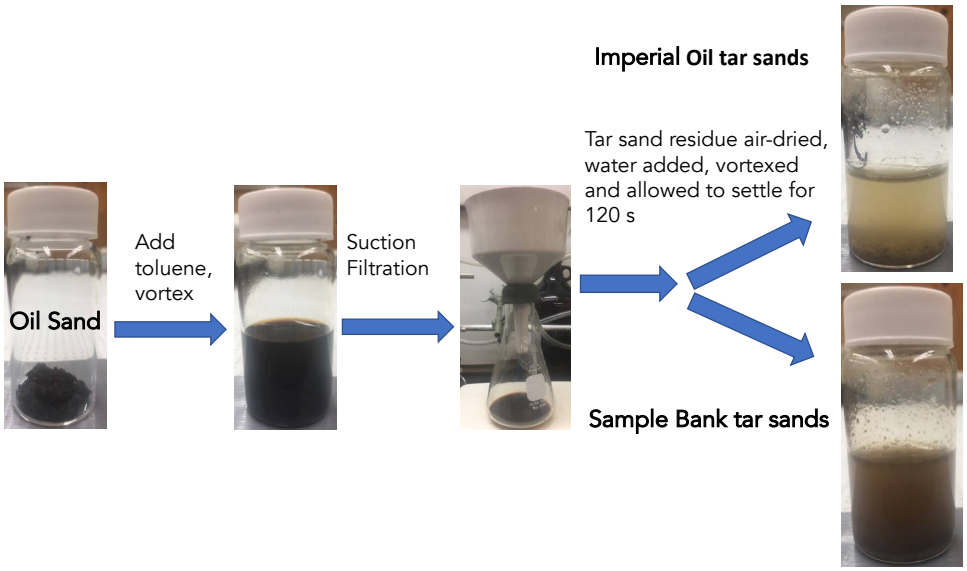

Figure 3-4: Qualitative comparison of fines settling in the SBos and IOos samples after 7 h.

3.4.2 Bitumen Extraction

Established extraction methodologies include using high-temperature water (about 80-90 ºC) to extract the bitumen from oil sands. These are the CHWE and SAGD methods, which consume large quantities of energy and water, and are also responsible for tailing pond formation. At a much lower temperature (45 ºC), the thermoresponsive polymer-grafted SNPs

were able to extract efficiently bitumen from oil sands, so they could represent an alternative to traditional methods.

Yang *et al.* used a shaker to extract bitumen from the IOos sample with PEG-*g*-$PMEO_2MA$.[13] Since IOos did not contain fines, it was relatively easy to extract the bitumen, but PEG-*g*-$PMEO_2MA$ was unable to extract bitumen from SBos.[14] Moreover, the synthesis of PEG-*g*-$PMEO_2MA$ is not commercially viable, and that compound is not biodegradable. We wanted to develop a more environment-friendly and economical system for bitumen extraction from oil sands with high fines contents. For example, SNP-*g*-$PMEO_2MA$ (15%, DS 0.022) used for the extraction contained 85% starch by weight. Furthermore, a tumbler system was used to carry out the bitumen extraction, which is closer to the commercial process being used. A clamp attached to a motor was used to tumble the oil sand mixtures in the vials at 53 rotations per minute in an oven maintained at 45 °C (Figure 3-5). Tumbling ensured better mixing of the polymeric surfactant, the organic solvent and the aqueous phase for a more efficient extraction process. Extraction with the shaker was also investigated and while the influence of the polymer could be noted, the overall extraction efficiency with the shaker was much lower than by tumbling.[14]

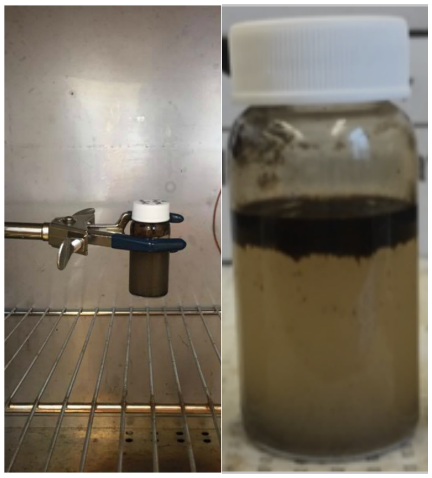

Figure 3-5: Left: Vial containing 1 g of SBos oil (10.5 ± 0.2% bitumen content), 15 mg SNP-g-PMEO$_2$MA (15%, DS 0.022), 0.5 M NaCl, 60 mg toluene and 15 mL water attached to a tumbler arm in an oven at 45 °C Right: Bitumen floating to the surface 24 h after extraction.

The composition of polymer-grafted SNPs, the organic co-solvent, the salt content, and the extraction temperature were crucial parameters needing to be optimized for the effective bitumen extraction from oil sands. SNP-g-PMEO$_2$MA (15%, DS 0.022) was first investigated in control experiments, because its temperature-dependent UV-Vis profile was similar to that of PEG-g-PMEO$_2$MA synthesized by Yang et al. to extract bitumen from the IOos sample.[13] Both samples also had the same LCAT value of 32 °C. The NaCl concentration was set to either 0, 0.05 or 0.5 M to evaluate its effects on fines settling and the bitumen extraction efficiency. To assist in the bitumen extraction process, different non-polar solvents were tested including D40,

HiSol15, HiSol10, and cumene, although toluene was found to yield the highest extraction efficiency and reproducibility. A temperature of 45 °C was selected because it is higher than the LCAT of the different polymer-grafted SNPs tested, and below 50 °C, which is considered the minimum for the industrial extraction of bitumen from oil sands, resulting in lower energy consumption. Moreover, Yang *et al.* also used toluene and performed their extractions at 45 °C.[13]

3.4.2.1 Effect of Toluene Mass on Bitumen Extraction Efficiency

Toluene was added in most cases to decrease the viscosity of the bitumen at the relatively low temperatures used in this investigation (22–45 °C), but it can also affect the interactions between the polymeric surfactant and bitumen. The influence of the amount of toluene added on the extraction efficiency will be discussed in this section. To this end 15 mL of SNP-*g*-$PMEO_2MA$ (15%, DS 0.022) solution at 1 mg/mL concentration, 0.5 M NaCl, and variable amounts of toluene were used in the extraction procedure. From the results reported in Table 3-2, it can be seen that the extraction efficiency strongly depended on the amount of toluene added, improving considerably as the amount increased. Toluene can potentially extract all the bitumen from the oil sands at high levels, but the goal in the current investigation was to use a minimum quantity of toluene. Thus, in subsequent extraction experiments, 60 mg of toluene was conservatively selected.

Table 3-2: Extractions with SBos, 0.5 M NaCl, 15 mg SNP-g-PMEO$_2$MA (15%, DS 0.022), 15 mL water and different amounts of toluene.

Number of Trials	Toluene Added (mg)	Extraction Efficiency (%)
3	50	56±5
6	55	71±3
6	60	78±3
3	65	84±1
3	70	89±2

Analysis of variance (ANOVA) was used to confirm the influence of toluene on bitumen extraction statistically. The ANOVA test was applied to determine whether the correlation between the bitumen extraction efficiency and the amount of toluene added was significant. The data from the 1st extraction cycle was analyzed, for a total of 21 extractions separated into five different groups, depending on the mass of toluene added (Appendix B-1, Table B1-2). The F statistic (50) was found to be greater than the critical F value (6) for a confidence interval $p < 0.01$, which shows that the amount of toluene had a very significant influence on the extraction efficiency. More information about ANOVA can be found in Appendix B-1.[18]

3.4.2.2 Controls for Efficient Bitumen Extraction

In this set of experiments, modifications to the standard procedure were used to examine the influence of the polymer-grafted SNPs, toluene and NaCl on the bitumen extraction efficiency, to determine the optimal extraction conditions.

Preliminary controls were done by comparing 0.05 and 0.5 M NaCl solutions in the separation of the SBos sample. Accelerated settling of the sand and fines was observed in the presence of NaCl (Figure 3-6). The addition of NaCl clearly helped to flocculate the fines, which would favor interactions between the bitumen particles and the polymer. While in the absence of NaCl the fines tended to remain suspended in the water, 0.5 M NaCl led to settling of most of the fines after 20 min, while partial settling was observed with 0.05 M NaCl. Consequently, 0.5 M NaCl was selected as the preferred condition for conducting bitumen extraction from oil sands.

a) 0.05 M NaCl **b) 0.5 M NaCl**

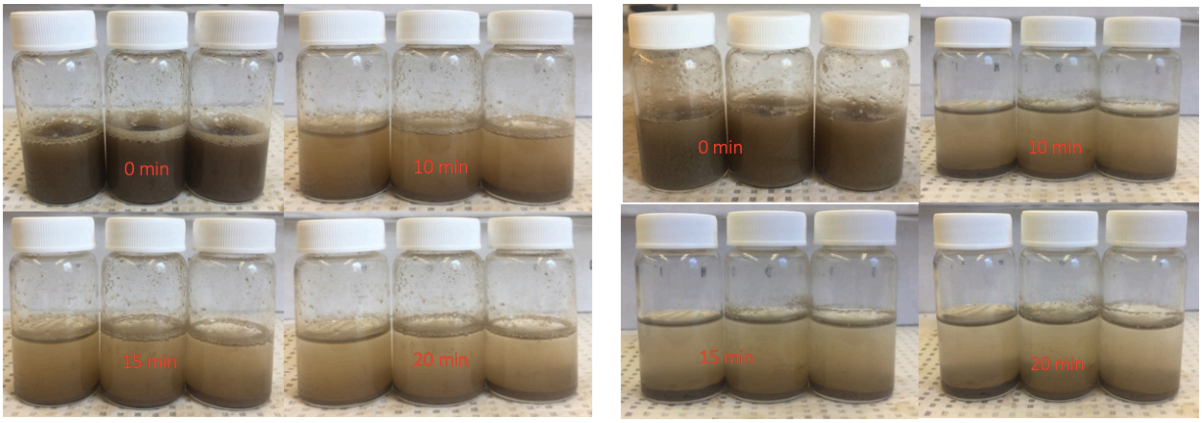

Figure 3-6: Qualitative comparison of fines settling for SBos at a) 0.05 M and b) 0.5 M NaCl.

UV-visible spectroscopy was used to evaluate the LCAT of SNP-*g*-PMEO$_2$MA (15%, DS 0.022) at 1 mg/mL and varying NaCl concentrations. As the concentration of NaCl was increased, the LCAT decreased (Figure 3-7). When NaCl is present in a solution, the LCAT of thermoresponsive polymers generally shifts to a lower temperature.[19] Because the Na^+ cations have a greater affinity for binding to the polymer than the Cl^- anions, direct contact between the Na^+ ions and PMEO$_2$MA plays an essential role in the LCAT change. The ions are known to impact the hydration shell nearest to the polymer, not the bulk water structure around it.[19] Indeed, it was shown in a study of PNIPAM with different salts by Du *et al*.[20] that cations had a significant affinity for the oxygen atom in amide groups, while the anions had no contact with the polymer. Although, the anions of salts are classified as kosmotropic or chaotropic based on their influence on LCAT.[21] Kosmotropic anions substantially reduce the LCAT of a

thermoresponsive polymer by forming strong connections with water while reducing polymer-water interactions and hence polymer stability in solution.[21] Chaotropic anions are less efficient in lowering LCAT than kosmotropic salts, and can occasionally stabilize the thermoresponsive polymer in solution. Some examples of kosmotropic anions are $CH_3CO_2^-$, F^-, OH^-, HPO_4^-, CO_3^{2-} and SO_4^{2-} while examples of chaotropic anions are Cl^-, I^-, Br^-, SCN^- and ClO_4^-.[21] Thus, the decrease in LCAT from 32 °C in pure water to 24 °C in 0.5 M NaCl observed for sample SNP-*g*-$PMEO_2MA$ (15%, DS 0.022) is attributed to decreased hydration of the $PMEO_2MA$ chains in the presence of the Na^+ ions.

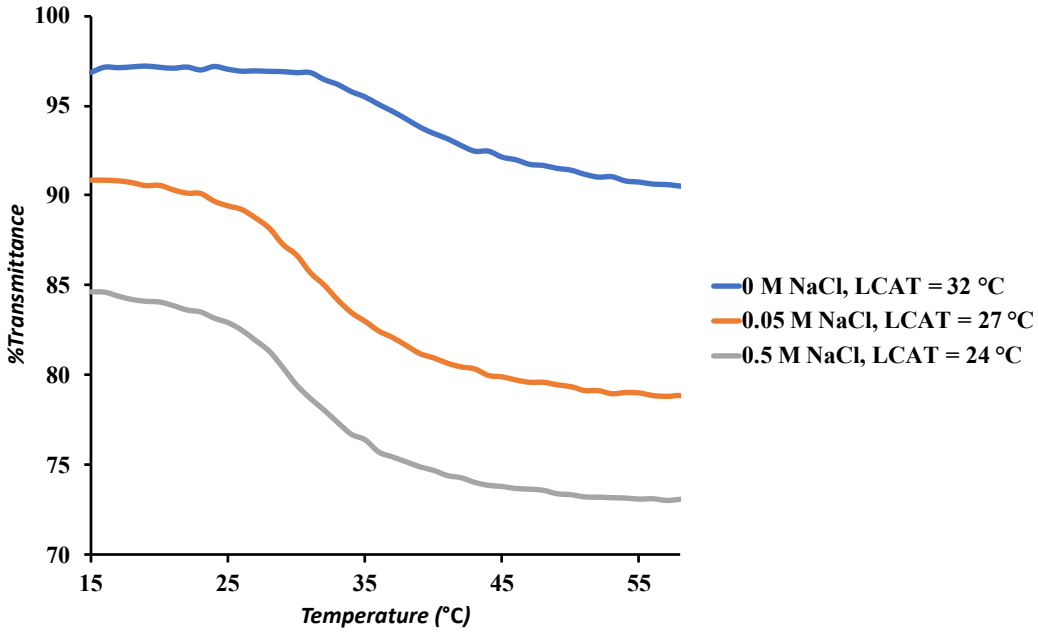

Figure 3-7: Transmittance curves as a function of temperature for 1 mg/mL solutions of SNP-g-$PMEO_2MA$ (15%, DS 0.022) at various NaCl concentrations.

In the absence of both NaCl and modified SNPs, the extraction efficiency was limited to 20% with 60 mg toluene (Trial #1, Table 3-3), increasing to 34% when the amount of toluene was increased to 70 mg (Trial #2). In the absence of modified SNPs, but utilizing 60 mg of toluene and 0.5 M NaCl, the extraction efficiency was 31% (Trial #3). Adding unmodified SNPs did not improve the efficiency of bitumen extraction (Trial #4). After investigating a range of polymer-grafted SNP compositions (discussed later), a high bitumen extraction efficiency of 78% was eventually reached with 60 mg toluene and 15 mg of SNP-*g*-$PMEO_2MA$ (15%, DS 0.022) in 15 mL of 0.5 M NaCl (Trial #5). These were the optimized conditions for bitumen extraction at a modified SNP concentration of 1 mg/mL and on a 1 g scale. These results show that the addition of SNP-*g*-$PMEO_2MA$ (15%, DS 0.022) improved the extraction performance markedly.

To examine the influence of temperature the extraction process was attempted at 22 ^oC, below the LCAT of SNP-*g*-$PMEO_2MA$ (15%, DS 0.022) of 24 ^oC in presence of 0.5 M NaCl (Figure 3-9). The extraction efficiency dropped to 41% at 22 ^oC (Trial #7), a 37% decrease in efficiency from extraction at 45 ^oC. This is presumably the result of reduced interactions between $PMEO_2MA$ and the bitumen phase, as the grafted $PMEO_2MA$ chains should remain hydrophilic below the LCAT; so their ability to interact with, solubilize and shuttle bitumen droplets to the surface of water would be limited.

For bitumen extraction from oil sands in the presence of toluene, surfactants are expected to orient their polar component to be in contact with water, and their non-polar component with toluene and bitumen, so as to minimize the surface tension.[22] This can also result in the creation of stable bitumen in water emulsions. Salts are known to increase the interfacial tension in the case of non-ionic surfactants, but to decrease it for ionic surfactants.[22] While oil sand mixtures can have salt concentrations reaching > 2000 mg/L,[23] this is clearly insufficient to destabilize emulsions, besides the fact that the salts can also participate in flocculating the clay particles. Bitumen also contains asphaltenes, decreasing the surface tension by acting as natural ionic surfactants favoring the formation of emulsions. Because SNP-*g*-$PMEO_2MA$ essentially acts like a non-ionic surfactant above its LCAT, an increased interfacial tension in the presence of salt may be a dominant driving force for the coalescence of bitumen droplets, resulting in improved bitumen separation from the aqueous phase.[22] Furthermore, it was confirmed that PEG-*g*-$PMEO_2MA$, previously used to extract bitumen from IOos, did not perform well with SBos (Trial #9).

Table 3-3: Bitumen extraction under different conditions.

#	Trials	Extraction Conditions	Extraction Efficiency (%)
1	3	No Salt, no polymer, 15 mL water, 60 mg toluene, 45 °C	20±1
2	3	No Salt, no polymer, 15 mL water, 70 mg toluene, 45 °C	34±4
3	3	0.5 M NaCl, no polymer, 15 mL water, 60 mg toluene, 45 °C	31±2
4	3	0.5 M NaCl, 15 mg SNP, 15 mL water, 60 mg toluene, 45 °C	33±4
5	3	0.5 M NaCl, SNP-*g*-$PMEO_2MA$ (15%, DS 0.022), 15 mL water, 60 mg toluene, 45°C	78±3
6	3	No Salt, SNP-*g*-$PMEO_2MA$ (15%, DS 0.022), 15 mL water, 60 mg toluene, 45 °C	48±3
7	12	0.5 M NaCl, SNP-*g*-$PMEO_2MA$ (15%, DS 0.022), 15 mL water, 60 mg toluene, 22 °C	41±5
8	6	15 mL recycled SNP-*g*-$PMEO_2MA$ (15%, DS 0.022) solution, 60 mg toluene, 45 °C	82±3
9	3	0.5 M NaCl,15 mL PEG-*g*-$PMEO_2MA$ solution, 60 mg toluene, 45 °C	36±5

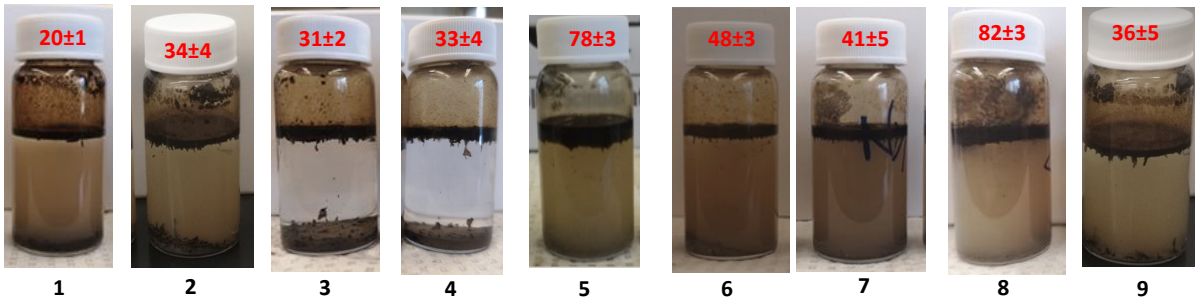

Figure 3-8: Appearance of bitumen extractions corresponding to Table 3-3 after 24 h settling.

3.4.2.3 Optimal SNP-*g*-PMEO$_2$MA Composition and Structure

In this series of experiments, 15 mg of modified SNPs were tested with 0.5 M NaCl, 60 mg of toluene, and 15 mL of water at 45 ºC for SNPs with various characteristics (PMEO$_2$MA contents and SNP substrate DS) as listed in Table 3-1. It was assumed that an optimal hydrophilic-lipophilic balance (HLB) would lead to more efficient bitumen extraction from the oil sands, and that the copolymer would redisperse in the water phase upon cooling. The results obtained for the different samples are compared in Figure 3-9. Overall, SNP-*g*-PMEO$_2$MA (15%, DS 0.022) performed best. It also had a similar UV-visible LCAT profile to that of PEG-g-PMEO$_2$MA synthesized by Yang *et al.* to extract oil from IOos.[13] The poor extraction efficiency of SNP-*g*-PMEO$_2$MA (15%, DS 0.038) illustrates that the PMEO$_2$MA chain length is critical in achieving a high bitumen extraction efficiency. That sample also exhibited the highest LCAT among all the samples investigated, at 36 °C (Table 3-1), but still significantly below the extraction temperature (45 °C). Because of the larger number of chains on the DS 0.038 vs. a

DS of 0.022, the starch nanoparticles should be more rigid, resulting in poorer interactions with the oil droplets at 45°C. While the addition of PHEA to $PMEO_2MA$ (30%, DS 0.022) to obtain SNP-*g*-$PMEO_2MA$ (15%)-*b*-PHEA (7.5%, DS 0.022) considerably reduced the LCAT and stabilized the material in solution, as shown previously in Figure 2-8, it did not enhance extraction efficiency. This further confirms that the $PMEO_2MA$ chain length is a critical parameter controlling the interactions with bitumen, as well as to maintaining suitable water dispersibility during the extraction. While sample SNP-*g*-$PMEO_2MA$ (30%, DS 0.038) was synthesized for comparison with SNP-*g*-$PMEO_2MA$ (15%, DS 0.038), it was not dispersible in water at the required concentration of 1 mg/mL. This may be due to the increased amount and length of $PMEO_2MA$ chains in the SNPs, which made rearrangements of the whole structure difficult. The addition of PHEA segments to SNP-*g*-$PMEO_2MA$ (30%, DS 0.022) to obtain SNP-*g*-$PMEO_2MA$ (30%)-*b*-PHEA (15%, DS 0.022) did not improve the extraction efficiency either.

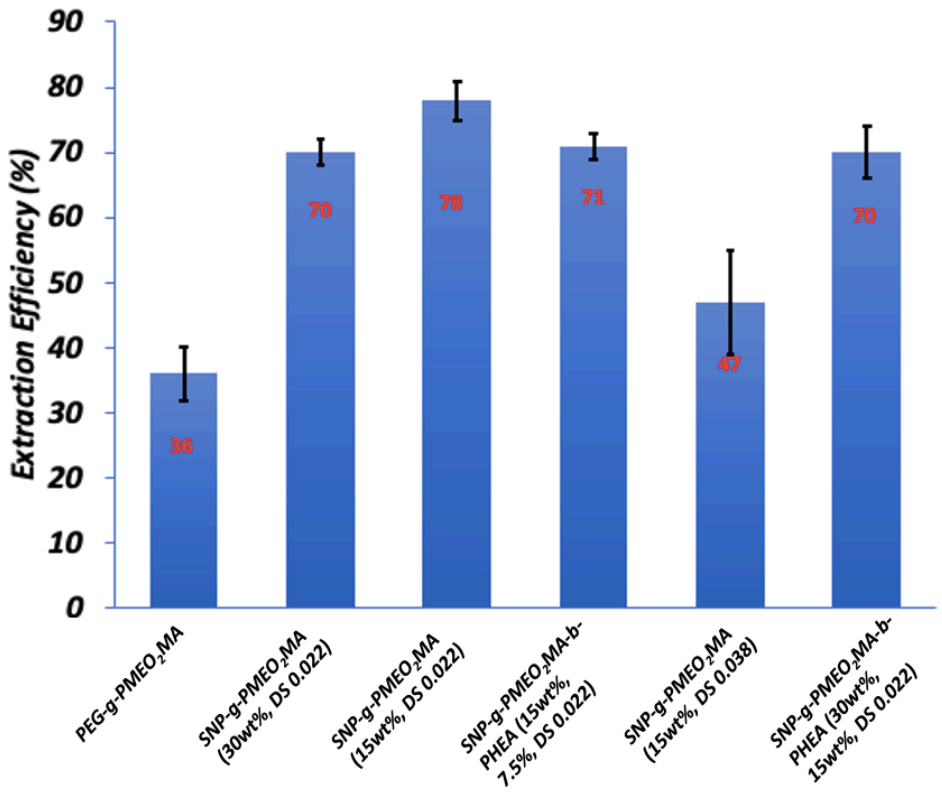

Figure 3-9: Bitumen extraction efficiency with 15 mg of polymer-grafted SNPs, 0.5 M NaCl, 15 mg of water and 60 mg of toluene at 45 °C for various polymer-grafted SNP samples.

3.4.2.4 Effect of Other Organic Solvents on the Bitumen Extraction Efficiency

In the experiments described so far, toluene was used as a solvent to dilute and decrease the viscosity of the bitumen phase, thereby facilitating its separation from the oil sands. Other potentially useful non-polar organic solvents examined in replacement for toluene were cumene, and the commercial solvents HiSol10, HiSol15, and D40. Cumene is structurally very similar to

toluene, while HiSol10, HiSol15 and D40 contain naphtha and other hydrocarbons. The extractions were performed using 15 mg of SNP-*g*-PMEO$_2$MA (15%, DS 0.022), 0.5 M NaCl and 15 mL of water in combination with 60 mg of one of these solvents. The highest (76%) extraction efficiency was obtained using D40 (Figure 3-10), which is dearomatized naphtha, while HiSol10 and HiSol15 contained about 70% naphtha. Naphtha is commonly used to dilute bitumen, to facilitate its transport. The bitumen extraction results obtained with D40 were therefore comparable with toluene.[24]

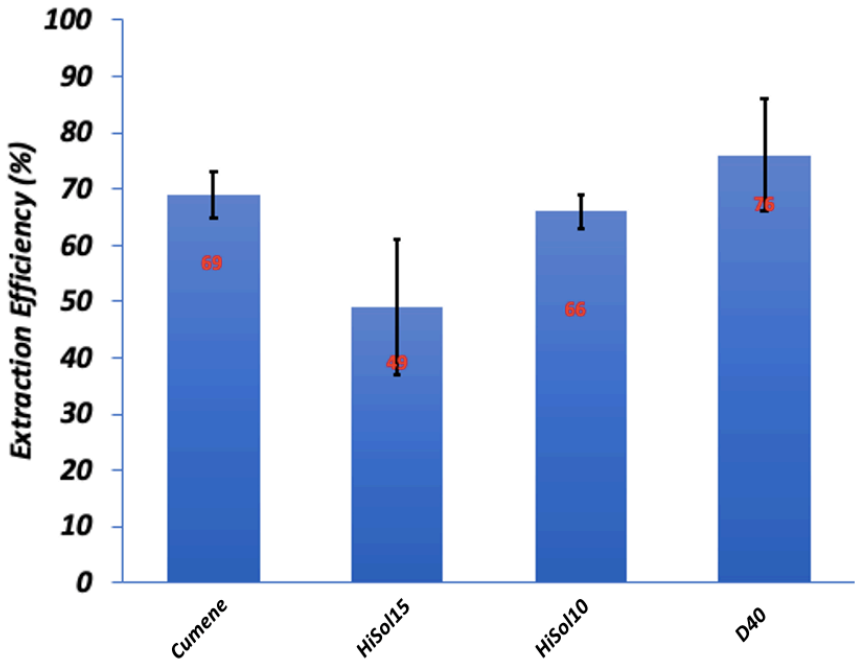

Figure 3-10: Bitumen extraction efficiency with 15 mg SNP-g-PMEO$_2$MA (15%, DS 0.022), 0.5 M NaCl, and 15 mg water at 45 ^{o}C with 60 mg of different organic solvents.

3.4.2.5 Effect of SNP-*g*-PMEO$_2$MA (15%, DS 0.022) Concentration on Bitumen Extraction Efficiency

Bitumen extraction experiments were attempted at different concentrations of SNP-*g*-PMEO$_2$MA (15%, DS 0.022), using solutions at concentrations of 0.75, 1.00, 1.25 and 1.50 mg/mL, while the amounts of water and toluene were maintained at 15 mL and 60 mg, respectively. It should be noted that the polymer concentration used in all the experiments discussed so far was 1 mg/mL (15 mg polymer in 15 mL water). As can be seen in Figure 3-11, the extraction efficiency increased with the SNP-*g*-PMEO$_2$MA (15%, DS 0.022) concentration up to 1.25 mg/mL, but dropped at 1.5 mg/mL. Since the LCAT of thermoresponsive polymers is known to be concentration-dependent, it is postulated that at a concentration of 1.5 mg/mL, the LCAT of SNP-*g*-PMEO$_2$MA (15%, DS 0.022) was lowered to the extent that it became too hydrophobic at the extraction temperature. This result again suggests the existence of an optimal hydrophilic-lipophilic balance (HLB) for efficient bitumen extraction. The optimal concentration for efficient extraction (≈ 80 %) is therefore 1.00–1.25 mg/mL, within experimental error limits.

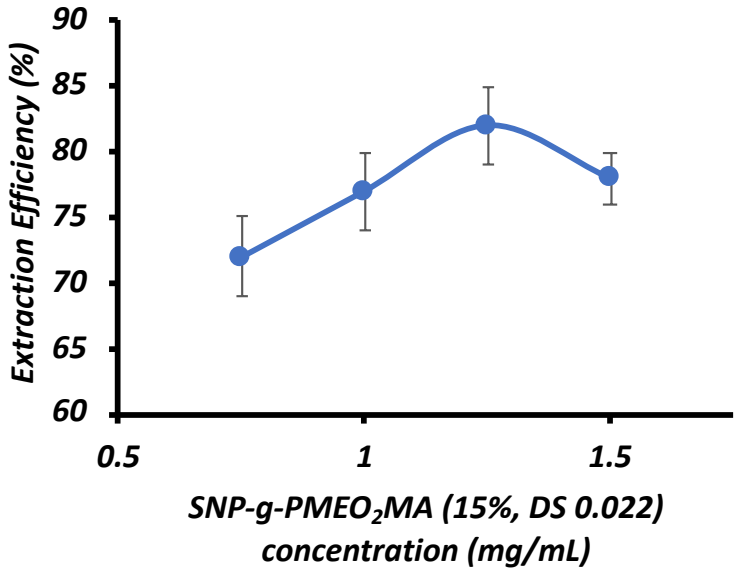

Figure 3-11: Bitumen extraction efficiency of SNP-g-PMEO$_2$MA (15%, DS 0.022) at different concentrations with 0.5 M NaCl, 15 mg water, and 60 mg toluene at 45 °C.

3.4.2.6 Recycling of SNP-*g*-PMEO$_2$MA (15%, DS 0.022) for Bitumen Extraction

SNP-g-PMEO$_2$MA (15%, DS 0.022) was found to perform best among the polymer-grafted SNP samples investigated. While a large volume of toluene can essentially extract all the bitumen from oil sands by itself, 60 mg of toluene was conservatively selected for that purpose. It was also observed that the extraction efficiency increased to ~ 80% at SNP-g-PMEO$_2$MA concentrations up to 1.25 mg/mL. It would be still essential to recycle and reuse the aqueous polymer solution to make the extraction economically viable and environmentally sustainable.

The optimized conditions for bitumen extraction from 1 g of oil sands, using 15 mL of 1.25 mg/mL SNP-g-PMEO$_2$MA (15%, DS 0.022), 0.5 M NaCl and 60 mg toluene, were used in four successive cycles of bitumen extraction, reusing the aqueous phase recovered in the process. The extraction efficiency was found to decrease to 59% for the 3rd cycle, and further to 54% for the 4th cycle under these conditions (Figure 3-12). This is attributed to the loss of of polymer-grafted SNPs as more extraction cycles are conducted. This hypothesis was confirmed, as an increase in extraction efficiency was observed when the equivalent of 0.25 mg/mL of SNP-g-PMEO$_2$MA (15%, DS 0.022) was added to the aqueous polymer solution for the 3rd and 4th cycles, leading to less pronounced decreases.

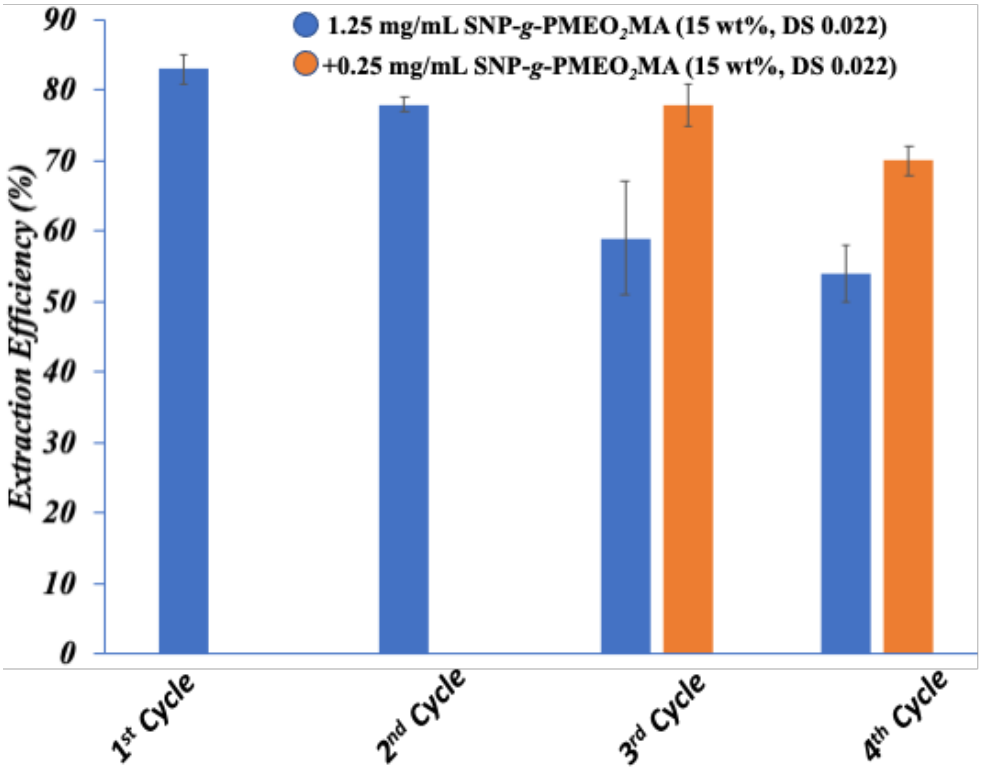

Figure 3-12: Polymer solution recycling in four cycles of bitumen extraction with SNP-g-PMEO$_2$MA (15%, DS 0.022), with and without polymer addition in the 3rd and 4th cycles.

3.4.2.7 Oil Extraction from IOos

As expected, it was much simpler to recover bitumen from the IOos sample, which did not contain detectable amounts of fines. In the presence of 15 mL of SNP-*g*-PMEO$_2$MA (15%, DS 0.022) at 1 mg/mL concentration, and using only 50 mg of toluene for 1 g of IOos, an extraction

efficiency of 86±4 % was achieved (Figure 3-13). It should be noted that not only was the addition NaCl to flocculate fines unnecessary, but it also only required 50 mg of toluene, as compared with 60 mg for the SBos sample. This clearly demonstrates that the presence of fines in oil sands has a significant negative impact on the recovery of bitumen from tar sands.

Figure 3-13: Appearance of bitumen extraction from IOos using 15 mg of SNP-g-PMEO$_2$MA (15%, DS 0.022), 15 mg water, and 50 mg toluene at 45 ^{o}C.

3.5 Conclusions

Extractions were performed mostly with the high clay SBos sample, representing a worst case scenario in bitumen extraction. While the fines present in SBos oil sands reduced the extraction efficiency, it was shown that the addition of 0.5 M NaCl enabled the efficient flocculation of fines and increased the extraction efficiency with PMEO$_2$MA-grafted SNPs at 45^{o}C. Due to the hydrophobicity of PMEO$_2$MA and the hydrophilic nature of the SNPs, these

materials were found to form micellar aggregates above their LCAT. It was shown in Chapter 2 that by changing the DS or the composition of the modified SNPs, the LCAT could be regulated, and the influence of these parameters on bitumen extraction was investigated. The best performing modified SNPs had an LCAT similar to PEG-*g*-$PMEO_2MA$, previously used to extract bitumen from IOos. Using ANOVA, it was shown that a higher amount of toluene resulted in higher extraction efficiency, but good performance (ca. 80 percent) could still be achieved using 60 mg of toluene per g of oil sands with SNP-*g*-$PMEO_2MA$ (15%, DS 0.022) in 15 mL of water and 0.5 M NaCl. The bitumen extraction performance of common napthenic-organic solvents such as D40 was close to that of toluene. Due to the presence of stones, debris and fines, the SBos sample was most difficult to handle. For lower clay samples like IOos, the extraction efficiency was greater (86±4) and much easier. Most significantly, the aqueous phase can be reused over 3 extraction cycles, thereby minimizing the consumption of water and thermoresponsive SNPs in the process.

Chapter 4

Starch-stabilized Iron Nanoparticles for the Photocatalytic Degradation of Methylene Blue

4.1 Abstract

By creating a powerful oxidant in the form of hydroxyl radicals, the photocatalytic Fenton reaction is an effective oxidation method for degrading most organic contaminants in water. The Fenton reaction involves hydrogen peroxide and Fe^{2+} ions under relatively acidic conditions (typically pH 2-3). The low pH required for the reaction, partially to maintain high solubility of the iron catalyst, is troublesome due to the creation of large volumes of decontaminated, yet highly acidic water. Starch-stabilized iron (Fe^{2+}/Fe^{3+}) oxide nanoparticles were synthesized to serve as a colloidally stable catalyst system, as the hydrophilic starch effectively prevents precipitation of the nanoparticles under less acidic conditions. To evaluate the usefulness of this catalyst system for the photo-Fenton degradation of methylene blue as a model dye, the synthetic technique used and the iron loading in the starch were varied. Not only was the starch-stabilized catalyst able to decolorize the dye, but also to mineralize it in part, that is to degrade the dye to carbon dioxide and water. ^{1}H nuclear magnetic resonance (NMR), dynamic light scattering (DLS), transmission electron microscopy (TEM), total organic content (TOC) analysis, UV-Visible and fluorescence spectroscopy were used to characterize the water-dispersible starch-iron complexes. The photocatalytic Fenton reaction, investigated in the pH range, under

conditions much closer to neutrality than typical, enabled the efficient degradation of methylene blue. In addition, the catalysts could be reused in several degradation cycles. This demonstrates that starch is an efficient stabilizer for iron oxide nanoparticles in aqueous media, enabling their use as environmentally friendly and cost-effective photo-Fenton catalysts.

4.2 Introduction

Natural dyes have been in use to dye fabrics for a long time, but the colors obtained are generally dull and limited in range. The first synthetic dyes were discovered by Perkins in 1856, and led to the developed of bright colors and shades, whose use and production culminated during the industrial revolution.[1] More than 10,000 dyes are currently used in the textile business. While dyes represent a minor percentage of water pollution, their color in solution makes them highly noticeable, which prompted governments to impose severe laws requiring textile firms to cleanse their colored effluent water.[2] Depending on the type of dye used, dye loss in effluent water can vary from 2 to 50 %.[3] Out of the roughly 800,000 tonnes of dyes produced worldwide yearly, it is estimated that about 10-15% is lost in various processes used in the textile industry.[4]

Color removal from textile industry effluents is not an easy task, as dyes absorb light strongly at visible wavelengths and can be detected visually at concentrations below 1 mg/L.[5] Decolorizing dyes typically requires several steps, as no single commercially feasible treatment exists. There are three main methods for textile wastewater treatment: physical, chemical, and biological. Physical techniques include filtration, flocculation, and adsorption, which are generally costly and ineffective. Advanced oxidation processes (AOPs, which include the Fenton reaction) and chemical oxidation are two types of chemical methods.[6] The production of iron sludge in the Fenton reaction, owing to flocculation of the catalyst and the dye, as well as the high energy cost of various other chemical oxidation processes, are major disadvantages of the chemical techniques. Enzymatic and microorganism-based approaches can be both cost-

effective and efficient, but the degradation timeframe can be longer than 24 hours.[5] For optimal effectiveness, it has been suggested that AOP could be combined with biological remediation.[7]

The Fenton reaction is an AOP creating hydroxyl radicals from H_2O_2 and iron salts (Fe^{2+}/Fe^{3+}) under acidic conditions. One of the benefits of this reaction is that the iron catalysts used in the process are inexpensive and readily available. Furthermore, the only other component in the reaction is H_2O_2, which is potentially capable of degrading dyes into CO_2 and H_2O to achieve complete mineralization. The reaction times are typically short, and the process can be carried out at ambient temperature and pressure. The Fenton reaction involves multiple reactions that can de classified into three categories, namely initiation, propagation, and termination (Table 4-1). The initiation stage generates radicals such as ·OH, $HO_2\cdot$ and $O_2^{-}\cdot$ that initiate the oxidation process, while the propagation stage involves radical reactions with organic compounds to produce, and further transform alkyl (R·) and alkyl peroxide ($RO_2\cdot$) radicals. In the termination process, the reactive intermediates react to be deactivated (Table 4-1). The key challenge with Fenton reactions is to take advantage of the initiation and propagation steps, and to delay the undesirable termination step as much as possible.

Table 4-1: Possible reaction steps in the Fenton process.

Step	Reaction	Rate constant (M^{-1} s^{-1})	References
Initiation	$Fe^{2+} + H_2O_2 \rightarrow Fe^{3+} + HO\cdot + OH^-$	$40 - 80$	[8, 9, 10]
	$Fe^{3+} + H_2O_2 \rightarrow Fe^{2+} + HOO\cdot + H^+$	$0.001 - 0.01$	[8, 9, 10]
	$HO_2\cdot \leftrightarrow H^+ + O_2^-\cdot$	$pKa = 4.8$	[8, 10]
Propagation	$H_2O_2 + HO\cdot \rightarrow HO_2\cdot + H_2O$	$(1.7 - 4.5) \times 10^7$	[9, 10]
	$H_2O_2 + HO_2\cdot \rightarrow O_2 + H_2O + HO\cdot$	$0.5, 3$	[9]
	$H_2O_2 + O_2\cdot^- \rightarrow O_2 + OH^- + HO\cdot$	$16, 0.13$	[9]
	$RH + HO\cdot \rightarrow R\cdot + H_2O$	$10^8 - 10^9$	[8, 9]
	$R\cdot + O_2 \rightarrow RO_2\cdot$	$-$	[9]
	$R\cdot + Fe^{2+} \rightarrow RH + Fe^{3+}$	$-$	[9, 10]
`	$R\cdot + Fe^{3+} \rightarrow R^+ + Fe^{2+}$	$-$	[9, 10]
Termination	$Fe^{3+} + HO_2\cdot \rightarrow Fe^{2+} + O_2 + H^+$	$10^3 - 10^7$	[8, 9, 10, 11]
	$Fe^{2+} + HO\cdot \rightarrow Fe^{3+} + OH^-$	3.2×10^8	[9, 10]
	$HO\cdot + HO\cdot \rightarrow H_2O_2$	5.5×10^9	[9, 10]
	$HO\cdot + HO\cdot \rightarrow H_2O + O_2$	7.15×10^9	[9, 10]
	$R\cdot + R\cdot \rightarrow R - R$	$-$	[9, 10]
	$HO_2\cdot + HO_2\cdot \rightarrow H_2O_2 + O_2$	2.3×10^6	[9, 10]
	$HO_2\cdot + HO\cdot \rightarrow H_2O + O_2$	7.1×10^9	[9]

The photo-Fenton reaction involves the use of ultraviolet (UV) light in combination with iron ($Fe^{2+/3+}$) salts and H_2O_2. It has been shown that the irradiation of Fe^{3+}/H_2O_2 with UV favors the formation of strong oxidant radicals, capable of degrading organic matter.[6] An important characteristic of the photo-Fenton reaction is the acceleration of the reduction of Fe^{3+} to Fe^{2+} with the energy provided by light, as shown in Figure 4-1. The UV irradiation also results in the direct photolysis of H_2O_2, accelerating the production of hydroxyl radicals.[12]

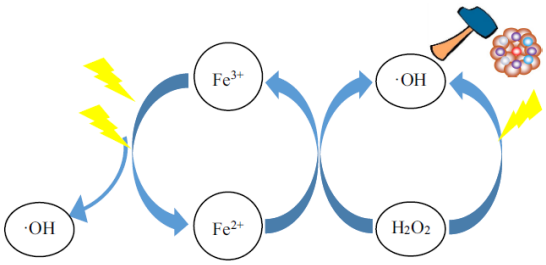

Figure 4-1: Oxidation of pollutants by the photo-Fenton process. Reprinted with permission from reference 12. Copyright (2019) Elsevier.

Homogeneous photo-Fenton reactions only use $Fe^{(2+/3+)}$, H_2O_2, and UV light under acidic conditions. Since Fe^{2+} is easily oxidized, most of the iron species exist as Fe^{3+}. A pH of 2-3 is considered optimal for homogenous Fenton reactions, to avoid the formation of insoluble $Fe(OH)^{2+}$.[12] Possible sources of UV light include UVA (λ = 315–400 nm), UVB (λ = 285-315 nm), and UVC (λ < 285 nm); in all cases, the yield of hydroxyl radicals varies with the intensity

of the light source.[13] This process has been employed to treat several contaminants such as pesticides and pharmaceuticals,[14,15] albeit with possible drawbacks. The stability of iron and H_2O_2 decreases as the pH increases, which makes the Fenton process strongly pH-dependent. Other disadvantages include the formation of oxohydroxides above pH 3, which precipitate as iron sludge.[16]

A solid support is used in the heterogeneous photo-Fenton process to increase the effective surface area of the iron species, by using a matrix promoting the dispersion of the iron nanoparticles. There are some benefits to heterogeneous photo-Fenton reactions over the homogeneous forms. The substrate is selected to improve the catalytic activity of iron and to prevent its leaching in the aqueous environment, and thus minimizes the formation of sludge.[17] Since most heterogeneous catalysts use porous substrates, the pollutants can be adsorbed on their surface, resulting in increased rate of pollutant degradation. It also makes it possible to conduct the reaction over a wider pH range, in contrast to the homogeneous Fenton reaction.[12]

Starch has been used as a support for iron catalysts.[18] Starch is a natural, renewable, biodegradable, and non-toxic material consisting of two key polymers: amylose and amylopectin.[19] Starch is hydrophilic and can stabilize colloidal iron particles in solution. Starch is already used for wastewater treatment, in the adsorption of heavy metals and dyes.[18] The ability of starch to adsorb dyes may facilitate their degradation by concentrating them close to the iron catalyst.

In the current investigation, methylene blue (MB) was used as a model pollutant to study dye degradation by starch-supported iron oxide catalysts. It is a dark green crystalline solid which dissolves in water to form a bright blue solution, even at concentrations below 1 ppm. It absorbs strongly at 650-670 nm, which makes degradation easy to quantify with UV-visible spectroscopy measurements.[20] Starch was used in different amounts to stabilize iron oxide nanoparticles in solution. The starch-stabilized iron oxide nanoparticles were found to exhibit exceptional catalytic activity for the degradation of MB with H_2O_2. The main objective of the work was to use a minimal amount of starch substrate to stabilize the nanoparticles, while achieving an optimal MB degradation efficiency. These starch-stabilized iron oxide nanoparticles have several advantages over conventional homogeneous Fenton catalysts, in that they are non-toxic, biodegradable, and reusable.

4.3 Experimental Procedures

4.3.1 Chemicals and Materials

Research-grade cooked starch with $M_n = 2.2\times10^6$ g/mol and $M_w = 4.4\times10^6$ g/mol was provided by EcoSynthetix (Burlington, Canada). Methylene blue (certified biological stain) was from Fisher Scientific (Mississauga, Canada). Trisodium citrate dihydrate (ACS reagent, ≥ 99.9 %), iron(II) chloride tetrahydrate (≥ 99.9 %), glacial acetic acid (≥ 99.9 %), ammonium

hydroxide (30-33% NH_3 in H_2O), hydrogen peroxide (30 % w/w in H_2O), 1,10-phenanthroline (≥ 99.9 %), terephthalic acid (98%), iron(III) chloride (reagent grade, 97%), ferrous ammonium sulfate hexahydrate (ACS reagent, ≥ 99.9 %), NaOH (ACS reagent, ≥ 98%, pellets), phenol (ACS reagent, ≥ 98%, pellets), sulfuric acid (99.999%), and sodium acetate (anhydrous, ≥ 99.9 %) were all purchased from Sigma-Aldrich (Oakville, Canada). Spectra/Por dialysis tubing with 50 kDa molecular weight cut-off (MWCO) was supplied by Spectrum Laboratories Inc. (Shewsbury, MA).

4.3.2 Instrumentation

^{1}H NMR spectra were obtained at 25 °C on a 300 MHz Bruker instrument, using 20 mg samples dispersed in 1 mL of D_2O with 128 scans averaged. The reported chemical shifts are relative to the solvent protons at 4.74 ppm for D_2O and 2.50 ppm for DMSO-d_6

A Malvern Zetasizer Nano S instrument with Non-invasive Back Scatter technology was used to perform dynamic light scattering (DLS) measurements. Before the DLS characterization, the colloidal dispersions were diluted to 3 mg/mL and transferred to a 1 cm path length cuvette.

For transmission electron microscopy imaging, the starch-stabilized iron NP samples were diluted to 0.1 mg/mL in deionized water. An 8-µL aliquot of the solution was deposited onto a 400-mesh grid coated with carbon-formvar, which was allowed to dry overnight. The sample was then imaged with a charge-coupled device camera on a CM10 Philips microscope operating at 60 kV acceleration voltage.

A Hewlett Packard 8542A diode array spectrophotometer was used to acquire UV-Visible absorbance spectra for the samples. Fluorescence measurements were carried out on a PTI QuantaMaster 400 steady-state fluorescence system.

Total organic carbon (TOC) analysis was achieved on a Shimadzu TOC-L analyzer with a 20 μL injection volume. The combustion is done at 680 ^{o}C and the products are detected by a nondispersive infrared sensor.

4.3.3 Synthesis of Starch-stabilized Iron (Fe^{2+}/Fe^{3+}) Nanoparticles

Two different synthetic protocols were used to obtain the starch-stabilized iron oxide nanoparticles. In each case, the starch content was varied to determine the optimal composition for MB degradation.

4.3.3.1 Synthesis of Starch-Iron (St-Fe) Nanoparticles

A low iron content catalyst system was obtained by the method of Tang *et al.* with modifications.[21] Cooked starch (300–1000 mg, 1.85–6.14 mmol glucopyranose units) was dissolved in water (30 mL) by stirring for 2 h in a 50-mL round bottom flask (RBF). Trisodium citrate dihydrate (90 mg, 0.3 mmol) was added, and the solution was stirred further for 15 min before 2 M ferric chloride (1 mL, 2 mmol) was added, immediately followed by a concentrated sodium hydroxide solution until a pH of 10 was obtained. This solution was placed in a water

bath at 30 °C, stirred for 24 h, and then centrifuged at 10,000 rpm and 20 °C for 20 min. Finally, the supernatant was dialyzed against water for 48 h in a Spectra/Por dialysis bag with 50 kD MWCO.

4.3.3.2 Synthesis of Iron-Starch (Fe-St) Nanoparticles

A high iron content catalyst system was obtained starting from iron oxide nanoparticles prepared by a modification of the co-precipitation method outlined by Krenkova *et al*.[22] Iron (II) chloride tetrahydrate (0.3 g, 1.5 mmol), iron (III) chloride (0.82 g, 5.1 mmol), acetic acid (20 μL, 0.35 mmol) and trisodium citrate dihydrate (1.14 g, 4.4 mmol) were dissolved in 38 mL of water in a 100-mL RBF. A 25% ammonium hydroxide (2.5 mL) solution was then rapidly added under vigorous stirring at room temperature, followed by cooked starch (100–300 mg, 0.62–1.85 mmol), and stirring was continued for ~16 h. Finally, the solution was dialyzed against water for 48 h in a Spectra/Por dialysis bag with 50 kD MWCO.

4.3.3.3 Synthesis of Iron Nanoparticles (Fe_3O_4)

Iron oxide (Fe_3O_4) nanoparticles without starch stabilizer were prepared by the co-precipitation method outlined by Krenkova *et al*.[22] Iron (II) chloride tetrahydrate (0.3 g, 1.5 mmol), iron (III) chloride (0.82 g, 5.1 mmol), acetic acid (20 μL, 0.35 mmol) and trisodium citrate dihydrate (1.14 g, 4.4 mmol) were dissolved in 38 mL of water in a 100-mL RBF. A 25%

ammonium hydroxide (2.5 mL) solution was then rapidly added under vigorous stirring at room temperature. The iron oxide colloid was precipitated with acetone (200 mL) and centrifuged at 12800×g for 10 min. The supernatant was discarded while the pellets were resuspended in water (40 mL) by sonication. The process was repeated 5 times to eliminate excess citrate ions.

4.3.4 Quantification of the Iron Content

The iron content in the starch-stabilized iron nanoparticles was quantified according to the method described by Pitarresi *et al.*[23] To evaluate the iron sequestered in the starch-iron nanoparticles, 0.3511 g (0.8954 mol) of ferrous ammonium sulfate ($Fe(NH_4)_2(SO_4)_2 \cdot 6H_2O$) and 5.0 mL of 6 M sulfuric acid were dissolved in water in a 500 mL volumetric flask. A 5.0 mL aliquot of this solution was transferred to a 100 mL volumetric flask, 10 mL of acetate buffer (5.0 M $HC_2H_3O_2$, 0.5 M $NaC_2H_3O_2$) was added, along with 10 mL of 10% w/v hydroxylamine hydrochloride ($NH_2OH \cdot HCl$). After allowing the reduction of Fe^{3+} to Fe^{2+} for 10 min, 10 mL of 0.1% 1,10-phenanthroline solution were added. The solution was diluted to the 100 mL mark and allowed to sit for 10 min, until a stable reddish-orange color developed. The above steps were repeated using 1.0, 2.0, 3.0 and 4.0 mL of the $Fe(NH_4)_2(SO_4)_2$ standard solution. The same preparation procedure was applied to a 0.3511 g sample of starch-iron nanoparticles for iron quantification. The samples were analyzed in a UV-Vis spectrometer to determine their absorbance at 510 nm. The standard samples were used to obtain a calibration curve, and the

unknown sample was compared with the calibration curve to determine the amount of iron in the unknown.

4.3.5 Photo-Fenton Experiments

The catalytic activity of the starch-iron and iron-starch catalysts produced was investigated with methylene blue as a model pollutant. At pH values ranging from 2–4, a 10 mL aliquot of methylene blue solution at varying concentrations (4–32 mg/L) was treated with different amounts of Fe from the catalyst (9.9–580 μmol/L) and H_2O_2 (45–720 μmol/L). It should be noted that due to the potential presence of different forms of iron oxides and hydroxides in the catalysts, the catalyst content in the reactions is always expressed in μmol Fe/L. Four 350 nm Rayonet tube lamps were used to irradiate the samples inside a UV box (150 cm × 60 cm × 90 cm) at a distance of ~ 18 cm. The experiments were done in triplicate, the samples being measured every 15 min in a UV-Vis spectrometer to determine the residual MB concentration. The reactions were stopped when at least 80% MB degradation was achieved.

The starch-stabilized iron nanoparticles synthesized were tested for their reusability, in which MB at a concentration of 4 mg/L was degraded in multiple cycles. In that case, aliquots of a concentrated (1 g/L) MB solution were added to bring the MB concentration back to 4 mg/L. The additions were made every 60 min, to ensure complete degradation before the next addition.

4.3.6 Spectrophotometric Detection of Hydroxyl Radicals

Terephthalic acid was used as a fluorescence probe for the quantification of hydroxyl radicals. To that end 60 mL of 0.06 M terephthalic acid ($C_8H_6O_4$), 6 mL of acetate buffer (pH 4.0, 0.1 M), 400 µL (9 mM) of H_2O_2, and varying concentrations of 1000 mg St-Fe catalyst were mixed to be analyzed in a fluorescence spectrometer. An excitation wavelength of 315 nm was used, and the emission was monitored from 330 to 600 nm.

4.3.7 Colorimetric Test for Fe^{3+} Leaching

Different concentrations of starch-stabilized iron nanoparticles (0.005–0.01 M Fe) were allowed to equilibrate with phenol (0.06 M) and analyzed in a UV-Vis spectrometer.

4.4 Results and Discussion

4.4.1 Synthesis and Characterization

Two different protocols were used to prepare starch-stabilized iron nanoparticles with different iron : citrate : starch ratios. Spectrophotometry was used to quantify the iron content by weight in the starch-stabilized iron nanoparticles (Table 4-2). To this end, Fe^{3+} was reduced to Fe^{2+} with hydroxylamine hydrochloride, since Fe^{2+} forms a reddish-orange tris complex with 1,10-phenanthroline. The resulting compound absorbs light in the visible range, with maximum

absorption at about 510 nanometers. Starch, iron citrate, the oxygen component of iron oxide, and potentially other impurities constituted the non-iron components of the catalyst, which were calculated by subtracting the weight of iron from the total sample weight (Table 4-2). The St-Fe NPs were formed in the presence of starch (in situ), but for the Fe-St NPs, starch was introduced after the synthesis of the iron NPs (ex situ). The Fe-St nanoparticles were shown to contain more iron than the St-Fe nanoparticles, as indicated in Table 4-2. This is most likely due to the presence of a larger amount of sodium citrate in the Fe-St nanoparticles, serving as ligand for Fe^{3+}ions. Sodium citrate may also act as a bridging agent between the iron ions and the cooked starch in the reaction. Upon dialysis, however, the sodium citrate component may disassociate and allow enhanced interactions between the iron and starch.[23]

Table 4-2: Iron content of catalyst systems investigated.

Catalyst	Iron (mg/mL)	Catalyst Stabilizer (mg/mL)	Initial mol ratio of Iron : Citrate : Starch	Iron (% w/w)
1000 mg Starch St-Fe NPs	3.2	19.8	1 : 0.17 : 0.93	14.0
300 mg Starch St-Fe NPs	1.1	3.7	1 : 0.17 : 0.28	22.9
300 mg Starch Fe-St NPs	3.7	4.6	1 : 0.66 : 0.0025	44.5
100 mg Starch Fe-St NPs	1.8	5.7	1 : 0.66 : 0.0008	24.0

The presence of starch in the St-Fe and Fe-St NPs was also confirmed by ^{1}H NMR analysis using the anomeric proton signal at 5.0-5.5 ppm, but due to the presence of paramagnetic iron oxide, shimming of the samples proved problematic. As a result, the starch peaks in the Starch St-Fe 1000 mg sample was particularly broad and overlapped (Figure 4-2b). The resulting complexation in 300 mg Starch Fe-St sample may be diamagnetic because of the creation of a low-spin situation (Figure 4-2a). This may be possible due to the presence of an even number of $Fe^{2+/3+}$ that may end up paired in certain situations.

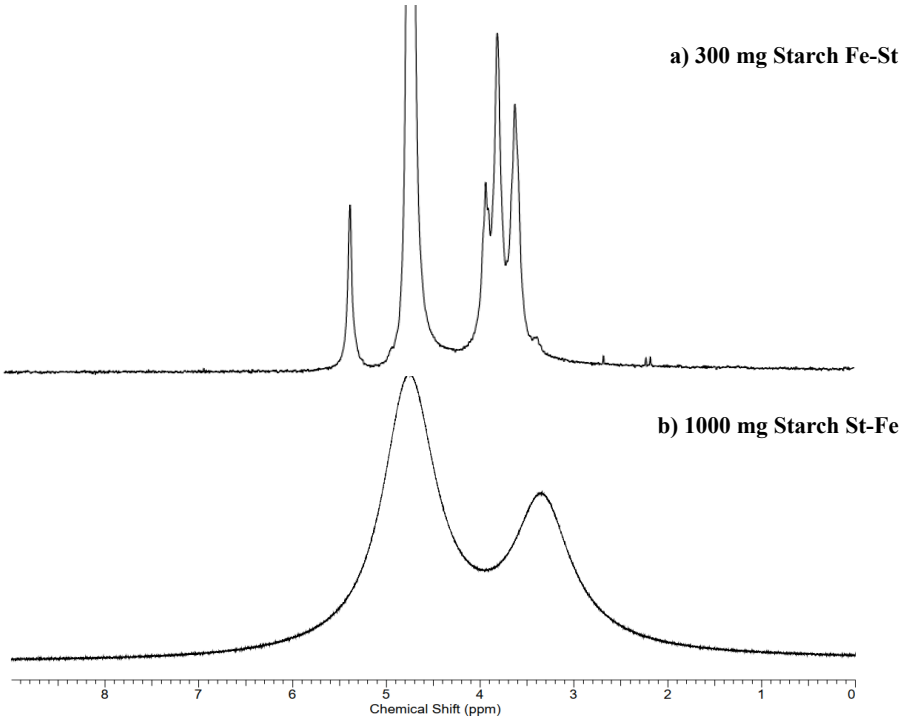

Figure 4-2: ^{1}H NMR spectrum for starch-based iron nanoparticles in D_2O: a) 1000 mg St-Fe NPs, b) 300 mg Fe-St NPs.

To determine the average overall size of the starch-iron complexes, dynamic light scattering (DLS) analysis was performed. For cooked starch and the 100 mg Starch Fe-St catalyst, the Z-average diameter was 89 and 76 nm, respectively. The St-Fe complexes prepared from 1000 and 300 mg starch St-Fe had Z-average diameters of 165 nm and 185 nm, respectively, while the Fe-St catalyst with 300 mg starch had a diameter of 152 nm. The intensity-weighed size distribution curves shown in Figure 4-3 clearly show that the St-Fe sample prepared with 1000 mg of starch was aggregated, while the distribution became narrower as the starch content was decreased for both sample types. The catalyst system with the lowest starch content (100 mg Starch Fe-St NPs) had the least aggregation, with a size closest to the starch substrate. While the presence of starch during the synthesis prevents the immediate agglomeration of iron nanoparticles[24], increasing the starch concentration apparently favors agglomeration of the starch-iron composite. This is clearly observed for 1000 mg St-Fe, which contains the lowest amount of iron by weight and the highest amount of starch in the synthesis.

TEM imaging (Figure 4-4) clearly confirmed the presence of iron ($Fe^{2+/}Fe^{3+}$) oxide NPs embedded within the starch matrix. In the images the dark spots/shaded areas are due to the iron NPs, while the lighter shaded areas are for the starch. During imaging, it was occasionally observed that the catalyst (most likely the starch component) would degrade due to exposure to the high-intensity electron beam. The TEM images demonstrate the presence of a large number of small particles with diameters much smaller than 50 nm, but agglomerated into particles with

diameters sometimes over 50 nm (Figure 4-4). There may be a few reasons for the differences in average particle sizes obtained by TEM and DLS analyses. Because the intensity of the DLS signal relies on the size of a scattering center as $I \sim r^6$, the overall intensity contribution from large particles is very large even though they may be present in large numbers. Because DLS analysis is more sensitive to large particles, the DLS size distribution is always skewed toward large sizes.[25]

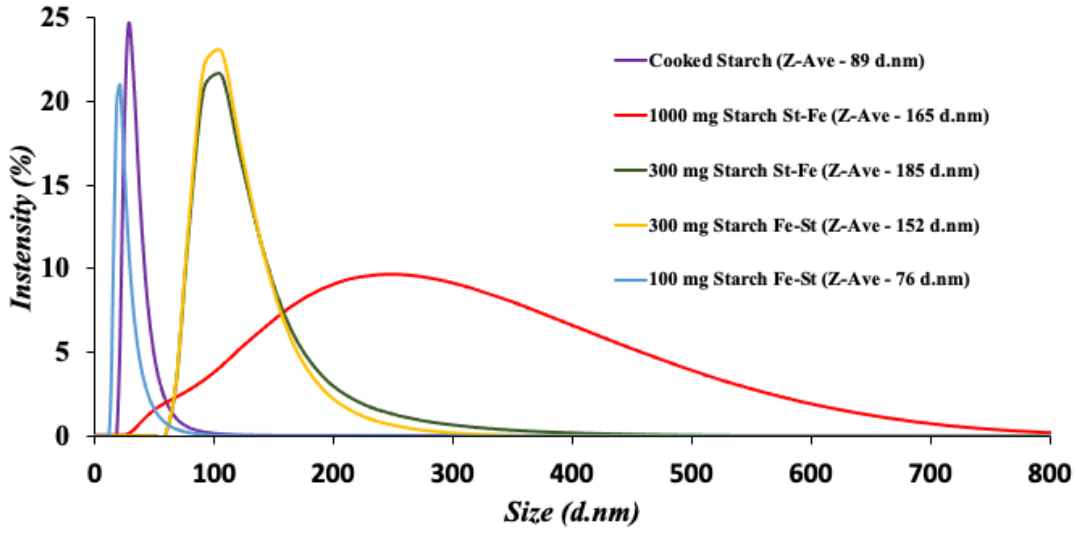

Figure 4-3: Dynamic light scattering measurements of starch-stabilized iron nanoparticles.

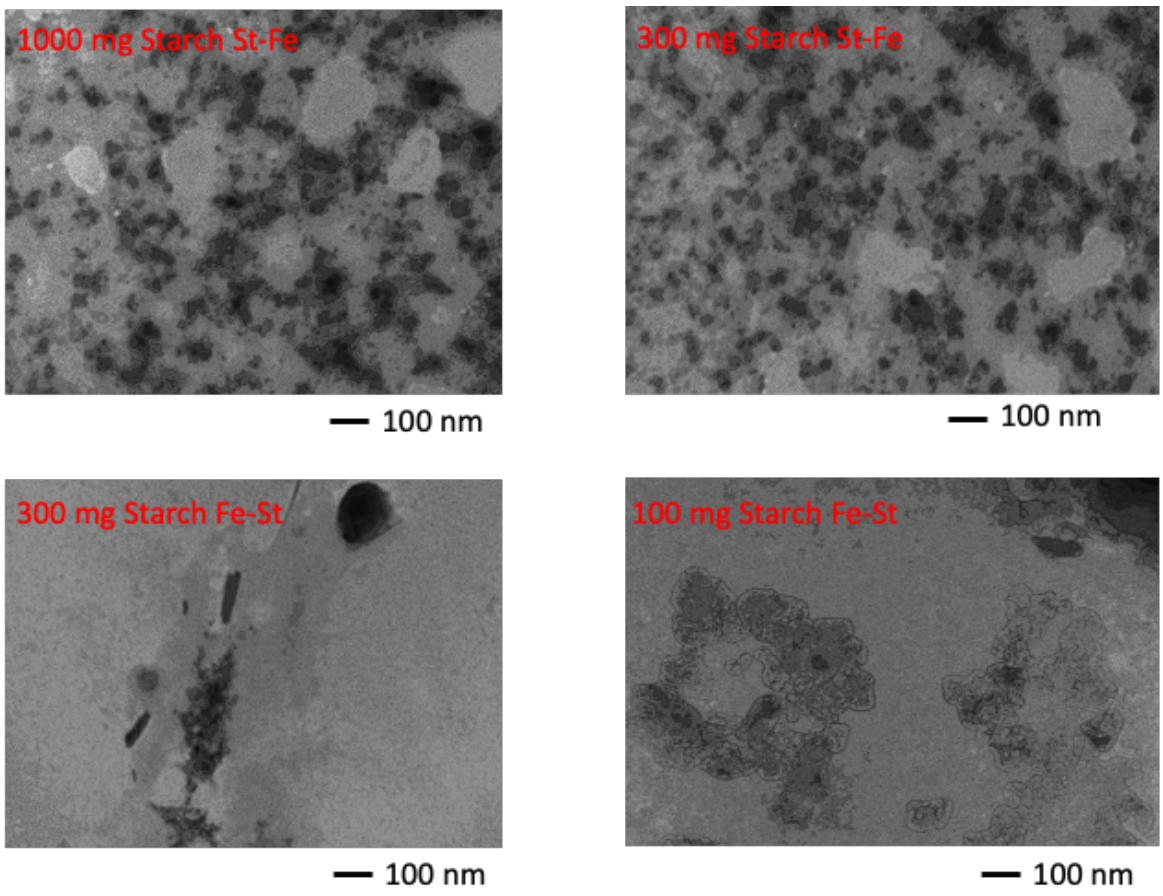

Figure 4-4: TEM imaging of St-Fe and Fe-St NPs as identified above.

4.4.2 Heterogenous Photo-Fenton Degradation of Methylene Blue

The activity of the catalyst is known to decrease at pH values above 3 in homogenous Fenton reactions, due to a decrease in concentration of photoactive iron hydroxide and dissolved iron species. Dissolved iron indeed precipitates as iron hydroxide above pH 4. The stability of iron oxide NPs in solution should be enhanced in the presence of starch in the heterogeneous

Fenton reaction. The synthesis of Starch St-Fe nanoparticles involved significantly more starch than Starch Fe-St nanoparticles (Table 4-2). As H_2O_2 and iron oxide nanoparticles are the two primary components of the Fenton reaction, the main goal of these experiments was to find out how much of the starch-stabilized iron nanoparticles was needed to decolorize and mineralize methylene blue. A H_2O_2 : Fe^{2+} ratio of 2:1 was established by Roudi *et al.* to be the optimal for landfill leachate treatment,[27] while another investigation on landfill leachate reported a H_2O_2 : Fe^{2+} ratio of 5:2 as most favorable for the Fenton reaction.[28] Various factors such as the nature of the pollutants, the solution pH, the type of catalyst and the H_2O_2 concentration likely affect the optimal H_2O_2 : Fe^{2+} ratio. In this study, the H_2O_2 : Fe^{2+} ratio was varied from 0.62 to 3.64, to identify the minimal quantity of starch-stabilized iron nanoparticles necessary for the effective degradation of methylene blue.

4.4.2.1 Degradation with 1000 mg Starch St-Fe Nanoparticles

The catalytic activity of starch-stabilized iron (Fe^{2+}/Fe^{3+}) NPs was studied with MB as a model pollutant. Since pH 3 is considered optimal for Fenton reactions, control reactions were completed at this pH. It should be noted that since the absorbance of a solution was proportional to the MB concentration, the ratio of the absorbance at time t to the initial absorbance (A_t/A_o) was proportional to the relative concentration (C_t/C_o), or the relative amount of dye left in the sample. Control reactions were carried out by excluding one of the components required for the reaction (catalyst, H_2O_2 or UV light), while the concentrations of catalyst and H_2O_2 were set at

290 μmol/L Fe and 360 μmol/L, respectively, which are typical concentrations used in the remainder of the investigation. As can be seen in Figure 4-5a, degradation of the dye was very limited in the absence of catalyst, H_2O_2 or UV light. Fe_3O_4 NPs prepared without starch stabilizer were also ineffective in degrading MB, as they were colloidally unstable in aqueous solutions at pH 3. Thus, the quick and efficient degradation of MB was only possible when the combination of the developed catalysts, H_2O_2, and UV irradiation was used.

The entire Fenton reaction involves more than 20 reactions, as discussed earlier, but the core reaction is shown below.[12] The hydroxyl radicals generated from the reaction are responsible for MB degradation. These hydroxyl radicals are highly oxidizing in nature, as portrayed by their strong oxidation-reduction potential of 2.8 V.[29]

$$Fe^{2+} + H_2O_2 + H^+ \rightarrow Fe^{3+} + \cdot OH + H_2O \qquad (4-1)$$

The hydroxyl radicals generated could be detected by fluorescence spectroscopy, using terephthalic acid as a fluorescence probe. As expected, there was an increase in fluorescence intensity over 60 minutes of radiation due to the increased production of hydroxyl radicals (Figure 4-5b).

Hereafter all the Fenton reactions were done at pH 4, as efficient MB degradation was not observed above that. One reason for this could be that H_2O_2 is unstable above pH 4 and breaks down into water and molecular oxygen.[30] Moreover, starch hydrolysis and the production of hydroxide ions in the Fenton reaction (Equation 4-2) may lead to an increase in pH, which would accelerate the H_2O_2 decomposition.

$$Fe^{2+} + HO\cdot \rightarrow Fe^{3+} + OH^{-} \quad k = 3.2 \times 10^{8} \qquad (4-2)$$

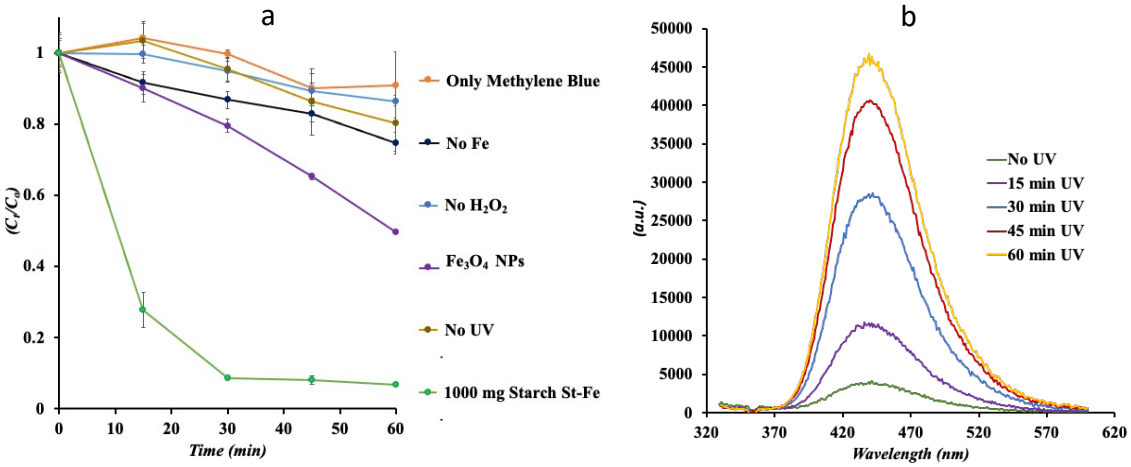

Figure 4-5: a) MB degradation control experiments (10 mL, 4 mg/L) at pH 3 with 290 µmol/L Fe 1000 mg Starch St-Fe, 360 µmol/L of H_2O_2 and UV light unless mentioned otherwise in the legend; b) Hydroxyl radicals detected using 44 µmol/L of 1000 mg Starch St-Fe NPs, 55 µmol/L H_2O_2 and 0.06 mol/L terephthalic acid at pH 4 after UV irradiation for the specified time intervals.

The degradation of MB was examined under various conditions with the different catalysts listed in Table 4-2. The influence of the irradiation source was also investigated by comparing direct sunlight illumination with the Rayonet UV lamp sources (Figure 4-6a). A modest increase in degradation efficiency was detected with direct sunlight (Waterloo, Ontario, October 10th,

2019, 2:00 PM, 17 ºC, 56% humidity), which might be related to a higher UV intensity from sunlight, or else to the broader wavelength spectrum of solar radiation as compared with 350 nm UV sources.[12] Furthermore, in consideration of energy consumption and potential hazards, sunlight is preferable over UV light. It may also significantly lower iron sludge formation and improve H_2O_2 breakdown.[31]

The influence of the H_2O_2 concentration was investigated using the 1000 mg Starch St-Fe catalyst under UV irradiation at pH 4 and 290 μmol/L Fe, as illustrated in Figure 4-6b. The peroxide concentration appears to have little effect on the process, which actually seems to proceed slightly faster at the lower H_2O_2 concentration (180 μmol/L). It has been suggested that this negative impact is due to scavenging of the ·OH radicals by H_2O_2 as described by Equation 4-3, which affects the pollutant degradation efficiency.[9,10] Therefore, in addition to being wasteful, an excessive peroxide concentration has a detrimental influence on the degradation process. Because only a 10% drop in MB degradation occurred when the H_2O_2 concentration was tripled (Figure 4-6b), the H_2O_2 : Fe ratio was allowed to vary among the experiments. In addition to being wasteful, excess H_2O_2 can occasionally have a negative impact on the degradation process.

$$H_2O_2 + HO\cdot \rightarrow HO_2\cdot + H_2O \qquad (4-3)$$

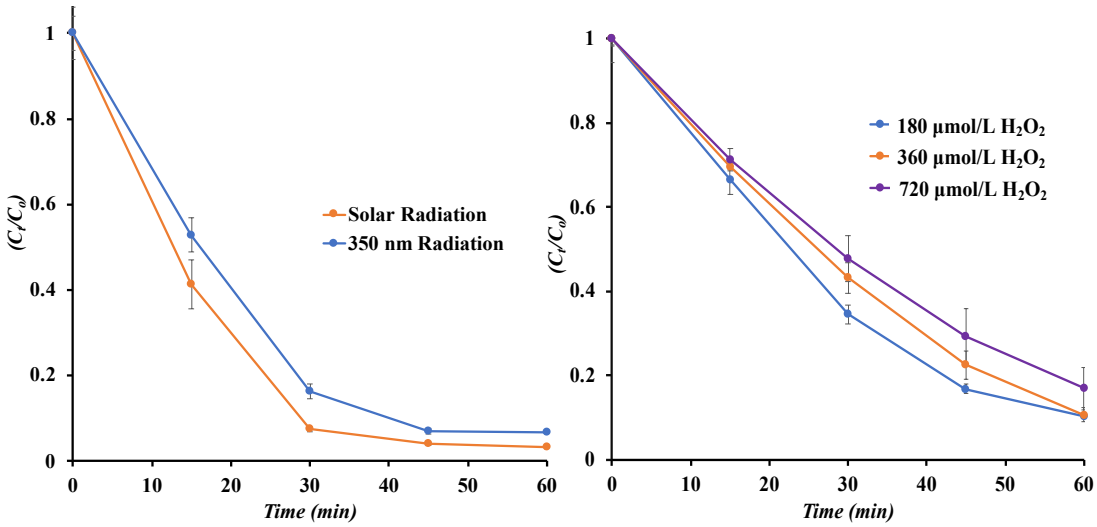

Figure 4-6: a) Influence of sunlight on the degradation of 4 mg/L MB at 290 µmol Fe/L of 1000 mg Starch St-Fe, 360 µmol/L H_2O_2 and pH 4; b) Influence of H_2O_2 concentration on the degradation of 4 mg/L MB at 290 µmol Fe/L of 1000 mg Starch St-Fe and pH 4.

In the following series of experiments, 4 mg/L MB solutions were degraded with different 1000 mg Starch St-Fe catalyst concentrations corresponding to 145, 290, and 580 µmol/L of Fe at initial pH values of 2, 3 or 4, using a constant H_2O_2 concentration (360 µmol/L) and UV irradiation, as shown in Figure 4-7. Despite varying the H_2O_2 : Fe ratio from 0.62 to 2.48, effective (> 80%) degradation was observed in all cases after 60 min. While the degradation reaction was slower at pH 4, the majority of the dye was still discolored after 60 min, particularly when using a higher Fe concentration. Thus, the viable pH range of the Fenton process was

successfully extended by one pH unit, representing a 10-fold decrease in acid concentration, when using the starch-stabilized iron NP catalysts.

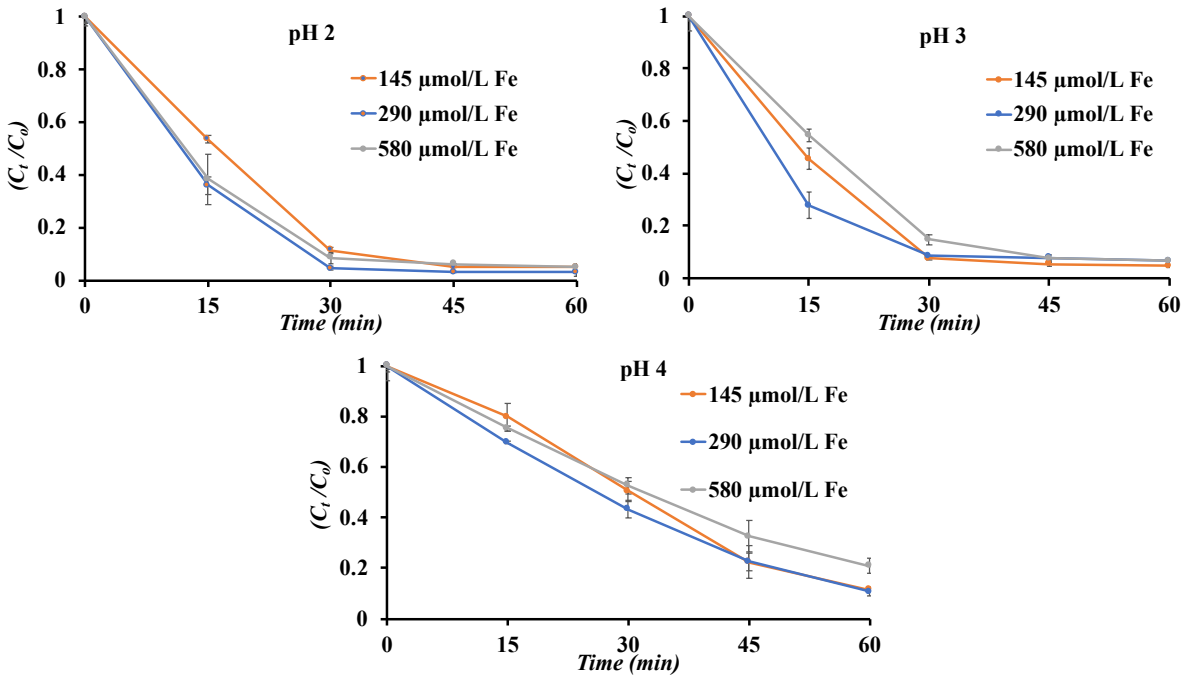

Figure 4-7: Influence of 1000 mg Starch St-Fe catalyst concentration and pH on the degradation of 4 mg/L MB solutions.

The effect of the dye concentration was studied by conducting degradation reactions at MB concentrations of 1–32 mg/L, under UV irradiation and at pH 4. The H_2O_2 : Fe ratio used in the investigation ranged between 1.24–1.55. As shown in Figure 4-8, increasing the reagent

concentrations to 290 µmol/L Fe and 360 µmol/L H_2O_2 allowed the degradation of MB at concentrations of up to 32 mg/L. When the Fe concentration was reduced 10-fold (bottom right pane), only up to 8 mg/L of MB could be degraded, i.e. 4-fold lower. Reaction 4-2 depicts the formation of Fe^{3+} in the Fenton reaction, which may increase the absorption of UV light required for the Fenton process.[32] Excess H_2O_2 may also lead to ·OH radical scavenging.

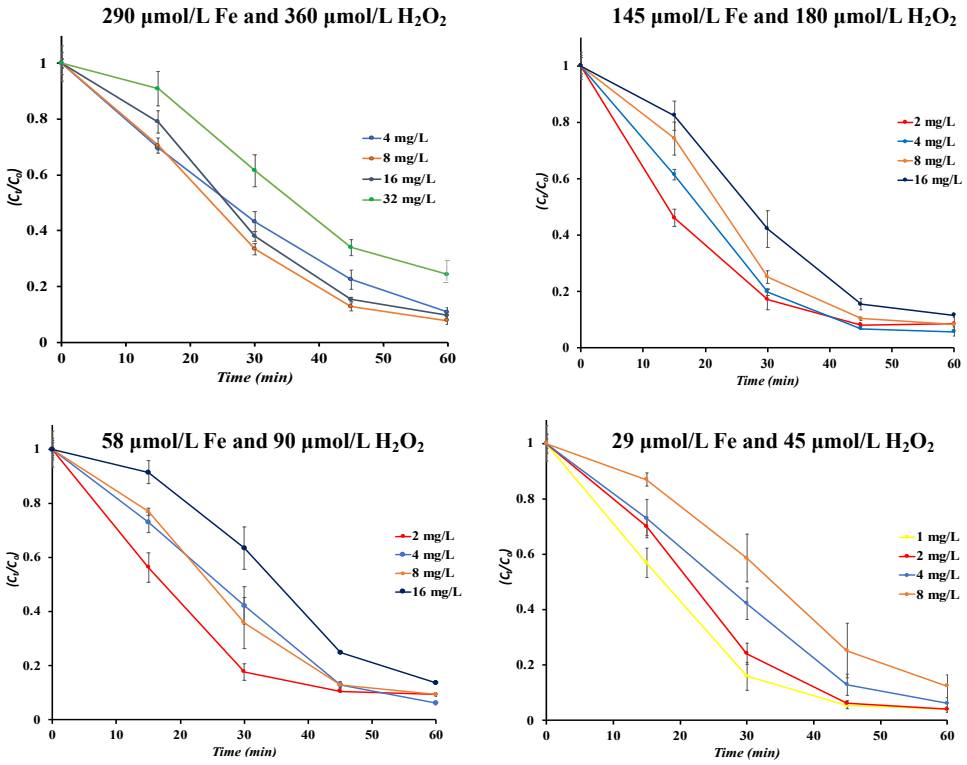

Figure 4-8: Degradation of MB at different concentrations, using 1000 mg Starch St-Fe and H_2O_2 : Fe ratios of 1.24 : 1 (top) or 1.55 : 1 (bottom), and different overall reagent and catalyst concentrations.

An attempt was made to degrade 32 mg/L MB at pH 4 under UV irradiation, by increasing the H_2O_2 concentration to 720 µmol/L but maintaining the Fe concentration at 290 µmol/L, as shown in Figure 4-9. There was a 10% increase in MB degradation upon doubling the H_2O_2 concentration. Such an increase was found to have an inhibitory effect at a MB concentration of 4 mg/L (Figure 4-6). The very modest increase in degradation efficiency observed in Figure 4-9 at the higher concentration of MB (32 mg/L) is therefore attributed to the excess hydroxyl radicals formed from 720 µmol/L H_2O_2 solution which were now being utilized to degrade MB.[8,9]

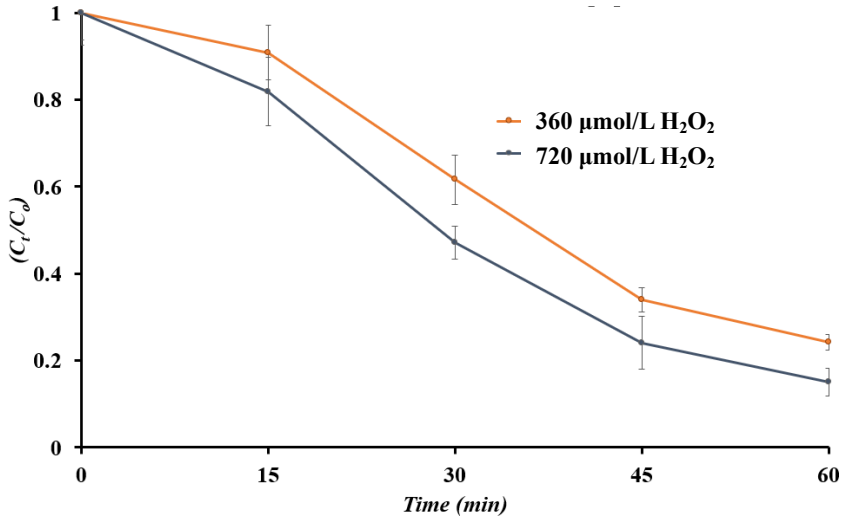

Figure 4-9: Degradation of 32 mg/L MB at two different concentrations of H_2O_2, using 290 µmol Fe/L of 1000 mg Starch St-Fe nanoparticles under UV irradiation at pH 4.

The effect of "excess" iron oxide nanoparticles on MB degradation was also studied, using 16 mg/L MB solutions at pH 4 (Figure 4-10). A 10-fold increase in iron concentration for 1000 mg Starch St-Fe, from 290 to 2900 µmol/L, led to a 30% decrease in degradation efficiency. This is attributed to the excess catalyst capturing hydroxyl radicals (Equation 4-5, rate constant: 3.2×10^8 $M^{-1}s^{-1}$), which is much faster than the formation of hydroxyl radicals by Fe^{2+} (Equation 4-6, rate constant: 40–80 $M^{-1}s^{-1}$), in addition to making the reaction medium less acidic. Beyond reducing the concentration of potent hydroxyl radicals present in the solution, this can also decrease the stability of H_2O_2.[8 9, 10] The presence of excess iron nanoparticles may also have absorbed light participating in the Fenton reaction.

$$Fe^{2+} + HO\cdot \rightarrow Fe^{3+} + OH^- \qquad (4-5)$$

$$Fe^{2+} + H_2O_2 \rightarrow Fe^{3+} + HO\cdot + OH^- \qquad (4-6)$$

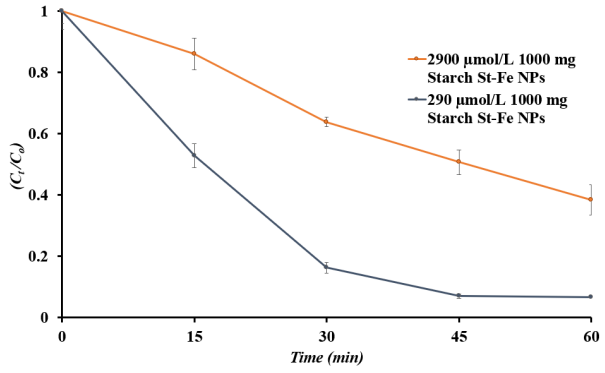

Figure 4-10: Influence of over-saturation of Fe from 1000 mg Starch St-Fe NPs in the degradation of a 16 mg/L aliquot of MB with 360 µmol/L H_2O_2 under UV radiation at pH 4.

4.4.2.2 Degradation with 300 mg Starch St-Fe Nanoparticles

Because starch can also contribute to the consumption of HO· radicals in the photo-Fenton reaction, the St-Fe catalyst was synthesized by decreasing the amount of added starch from 1000 to 300 mg in the procedure described in Section 4.3.3.1. Furthermore, Haddad *et al.* reported that a H_2O_2 : Fe ratio of 1:10 was optimal for the breakdown of Reactive Yellow 84 azo dye, in contrast with the discovery by Tengrui *et al.* that a ratio of 2.5 was optimal for the degradation of landfill leachate.[32,28] It therefore appears that the H_2O_2 : Fe ratio may vary widely amongst different catalyst systems and degradation substrates. A change in starch content may thus alter the optimal H_2O_2 : Fe ratios for MB degradation, and thus the optimal ratio may vary for each of the four catalyst systems mentioned in Table 4-2. The influence of the H_2O_2 concentration was investigated with the 300 mg Starch St-Fe catalyst under UV irradiation at pH 4 and 99 μmol/L Fe, as illustrated in Figure 4-11. It was found that a H_2O_2 : Fe ratio of 0.91 provided the lowest degradation efficiency, but over 80% degradation was nevertheless achieved. For an H_2O_2 : Fe ratio of 3.64, the degradation efficiency was highest for the 300 mg Starch St-Fe NPs (Figure 4-11). The new catalyst system was further tested to degrade 4, 8, 16, and 32 mg/L solutions of MB at pH 4 with 350 nm radiation, using different concentrations of iron catalyst while maintaining a H_2O_2 : Fe ratio of 3.64 : 1 (Figure 4-12). An Fe concentration of only 9.9 μmol/L, in combination with 45 μmol/L H_2O_2, sufficed to degrade 95% of the MB in 60 min at a concentration of 16 mg/L. This represents an Fe concentration almost 3-fold lower than used for

the 1000 mg Starch St-Fe system, at a H_2O_2 concentration of 45 µmol/L and a MB concentration of 8 mg/L. Similar observations were made for the degradation of 32 mg/L MB. Since the iron : starch stabilizer ratio is higher in 300 mg Starch St-Fe than in 1000 mg Starch St-Fe (Table 4-2), increased accessibility of the iron catalytic sites can explain the higher activity of this sample. The decreased amount of starch present also decrease the probability of reaction of starch with the potent hydroxyl radicals in solution.[33] Furthermore, it was shown in Figure 4-3 that a lower amount of starch allowed better dispersion of the iron nanoparticles, due to reduced aggregation. The increased surface area achieved under these conditions should lead to enhanced catalytic performance, resulting in more efficient pollutant degradation.

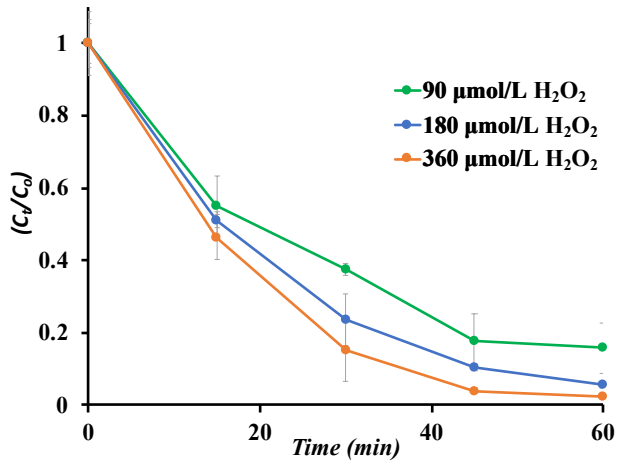

Figure 4-11: Influence of H_2O_2 concentration on the degradation of 4 mg/L MB at 99 µmol Fe/L of 300 mg Starch St-Fe and pH 4.

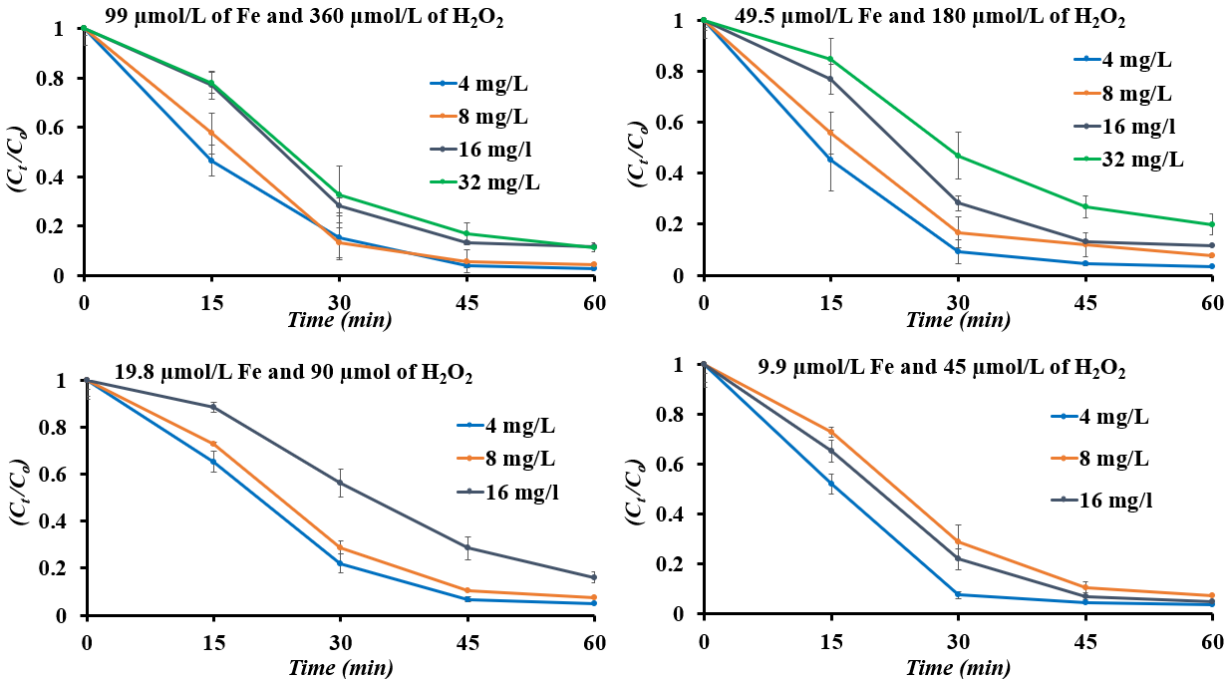

Figure 4-12: Degradation of MB at different concentrations, using 300 mg Starch St-Fe and similar H_2O_2 : Fe ratios (3.64 : 1), and different overall reagent and catalyst concentrations.

4.4.2.3 Degradation with 300 mg Starch Fe-St Nanoparticles

While the St-Fe nanoparticles were synthesized in the presence of starch (in situ method), a different procedure was also developed whereby the starch was added after the formation of the iron nanoparticles (ex situ method). The influence of the H_2O_2 concentration was investigated using the 300 mg Starch Fe-St catalyst under UV irradiation at pH 4 and 165 µmol/L Fe, as illustrated in Figure 4-13. An H_2O_2 : Fe ratio of 2.18 yielded the lowest degradation efficiency,

but nevertheless achieved more than 90% degradation (Figure 4-13). When the amount of H_2O_2 used was increased 4-fold to 720 μmol/L, the degradation efficiency dropped by ~5%. The degradation rate (initial slope) was also faster at lower H_2O_2 : Fe ratios. According to Table 4-2, the amount of starch used to make the Starch Fe-St NPs was less than 1% of the amount used for the Starch St-Fe NPs. This can explain why the rate of MB degradation in the Fenton reaction differed for the Fe-St and St-Fe catalysts. The Starch Fe-St NPs differed from the Starch St-Fe NPs not just in terms of starch content, but also in how they were synthesized. The goal in synthesizing the Fe-St NPs was to break down MB in the presence of the lowest possible amount of starch, while maintaining concentrations of H_2O_2 similar to those used in the Starch St-Fe NP degradation tests. To investigate the influence of the dye concentration, these NPs were used to degrade 4, 8, 16, and 32 mg/L solutions of MB at pH 4 with 350 nm radiation, at different concentrations of 300 mg Starch Fe-St NPs, while maintaining H_2O_2 : Fe ratios of either 1.09 : 1 or 1.36 : 1 (Figure 4-14). Over 90% degradation of the 16 mg/L MB solution was achieved in 60 min with 66 μmol/L of Fe and 90 μmol/L H_2O_2, using the 300 mg Starch Fe-St catalyst. For the 1000 mg Starch St-Fe sample at a comparable iron concentration (58 μmol/L Fe and 90 μmol/L H_2O_2), up to 80% degradation of a 16 mg/L MB solution was achieved. Decreasing the iron and H_2O_2 concentrations to 33 and 45 μmol/L, respectively, therefore decreased the efficiency to 80%. However, as compared with the St-Fe NPs, the degradation occurred much faster at higher iron and H_2O_2 concentrations, with over 90% degradation achieved in 15–30 minutes. This may be due to the lower quantity of starch in Fe-St NPs, requiring fewer HO·

radicals to break down the starch component around Fe NPs. This is a significant result, as the degradation time of MB was essentially cut in half when using the Fe-St NPs synthesized with a lower amount of starch. Differences in the synthetic procedure, namely the addition of starch after the formation of the iron nanoparticles and the use of a larger amount of sodium citrate (complexing agent), apparently improved the accessibility of the iron nanoparticles to H_2O_2 and UV light. The 300 mg Starch Fe-St sample had almost the same iron content as the 1000 mg Starch St-Fe sample, but the difference in the synthetic route affected the activity of the catalyst. The presence of excess starch in 1000 mg Starch St-Fe, combined with enhanced aggregation, would also have yielded a thicker starch coating around the iron NPs, and thus a less accessible catalyst surface.

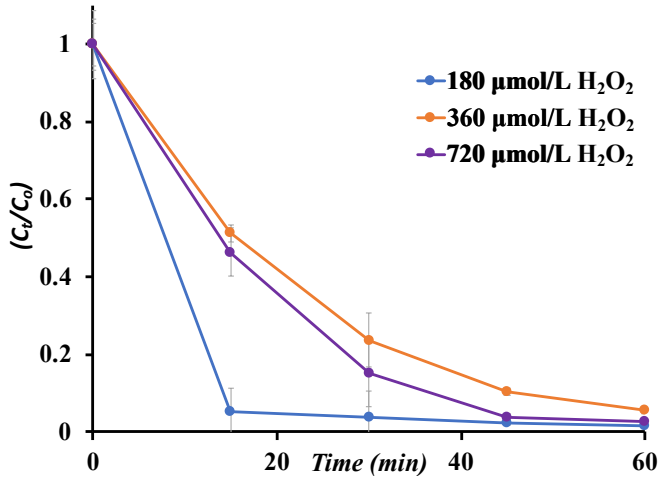

Figure 4-13: Influence of H_2O_2 concentration on the degradation of 4 mg/L MB at 165 µmol Fe/L of 300 mg Starch Fe-St and pH 4.

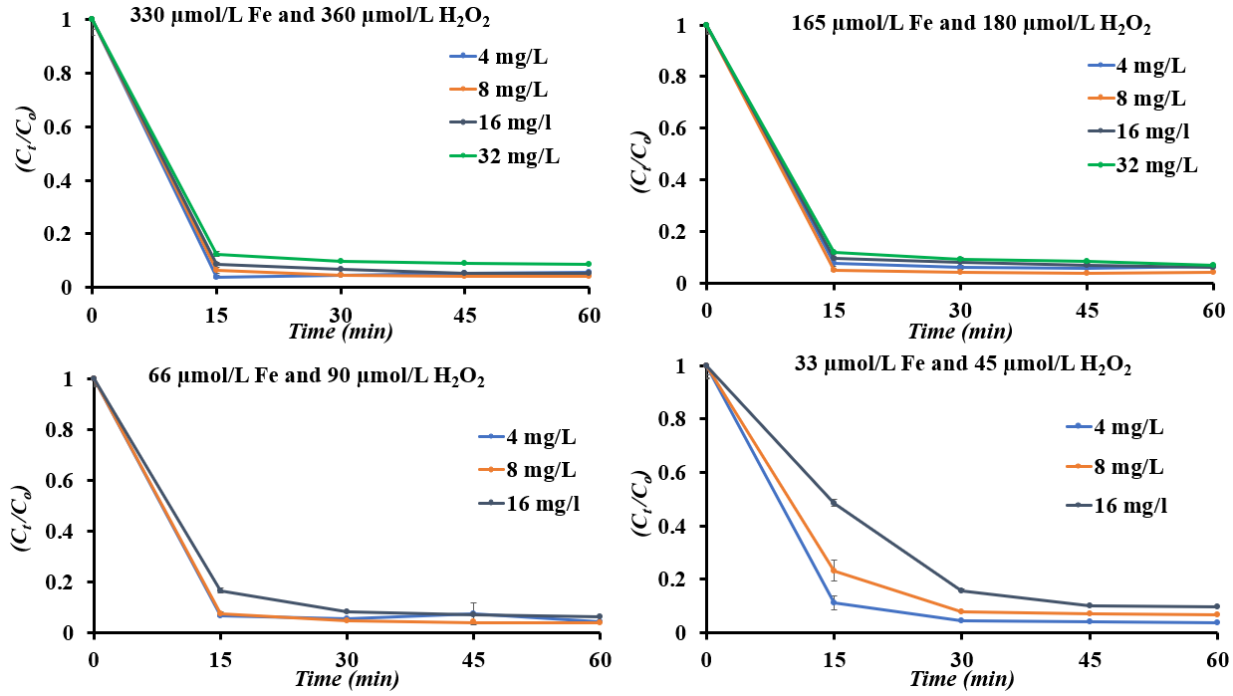

Figure 4-14: Degradation of MB at different concentrations, using 300 mg Starch Fe-St and H_2O_2 : Fe ratios of either 1.09 : 1 (top) or 1.36 : 1 (bottom), and different overall reagent and catalyst concentrations.

4.4.2.4 Degradation with 100 mg Starch Fe-St Nanoparticles

The amount of starch used for the synthesis of the Fe-St NPs was further reduced from 300 mg to 100 mg, to test the limits of iron NP stabilization with starch. The influence of the H_2O_2 concentration was investigated with the 100 mg Starch Fe-St catalyst under UV irradiation at pH

4 and 165 μmol/L Fe, as illustrated in Figure 4-15. The H_2O_2 : Fe ratio of 2.18 yielded the lowest degradation efficiency, which nevertheless still reached over 95% degradation in 60 min (Figure 4-15). To investigate the influence of the initial dye concentration, these NPs were used to degrade 4, 8, 16, and 32 mg/L MB solutions at pH 4 under 350 nm radiation, at four different concentrations of 100 mg Starch Fe-St NPs and H_2O_2, as shown in Figure 4-16. The H_2O_2 : Fe ratio was increased up to 3.64 to degrade higher concentrations of MB (up to 32 mg/L) with a minimum amount of starch-stabilized iron catalyst. Because the Starch 100 mg Fe-St particles were prepared with the least amount of starch relatively to the other samples, most of the HO· radicals produced should be available to break down MB rather than the starch. The catalyst was indeed found to be highly effective, as over 80% degradation was achieved for 32 mg/L MB within 30 min when using 32.4 μmol/L Fe and 90 μmol/L H_2O_2. Only 16.2 μmol/L of Fe and 45 μmol/L of H_2O_2 still sufficed to achieve 90% degradation of 16 mg/L MB in 60 min. This is an iron concentration similar to that used for the 300 mg starch St-Fe catalyst, likewise yielding 90% degradation for 16 mg/L of MB. However, since only 100 mg of starch was added in the synthetic procedure, the starch encapsulation would be even thinner than for the 300 mg starch St-Fe catalyst, leading to faster degradation rates. The catalytic efficiency of these particles is time-dependent, i.e. the time taken to degrade >80% MB was indeed much higher than for the other catalysts mentioned so far. Moreover, the 100 mg Starch Fe-St NPs were narrowly dispersed, as seen in the DLS measurements (Figure 4-3). This means that minimal aggregation was observed for these particles.

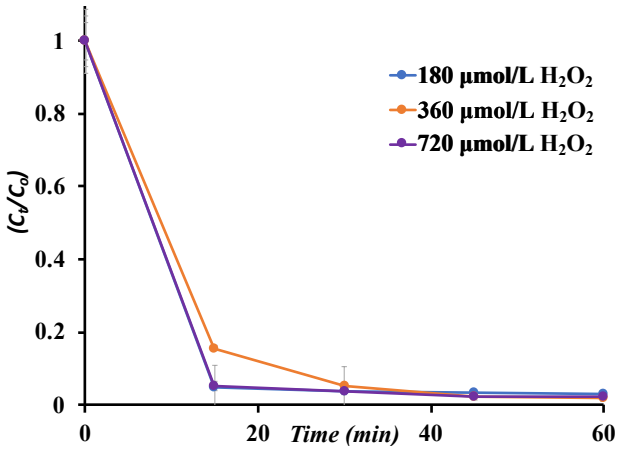

Figure 4-15: Influence of H_2O_2 concentration on the degradation of 4 mg/L MB at 165 µmol Fe/L of 100 mg Starch Fe-St and pH 4.

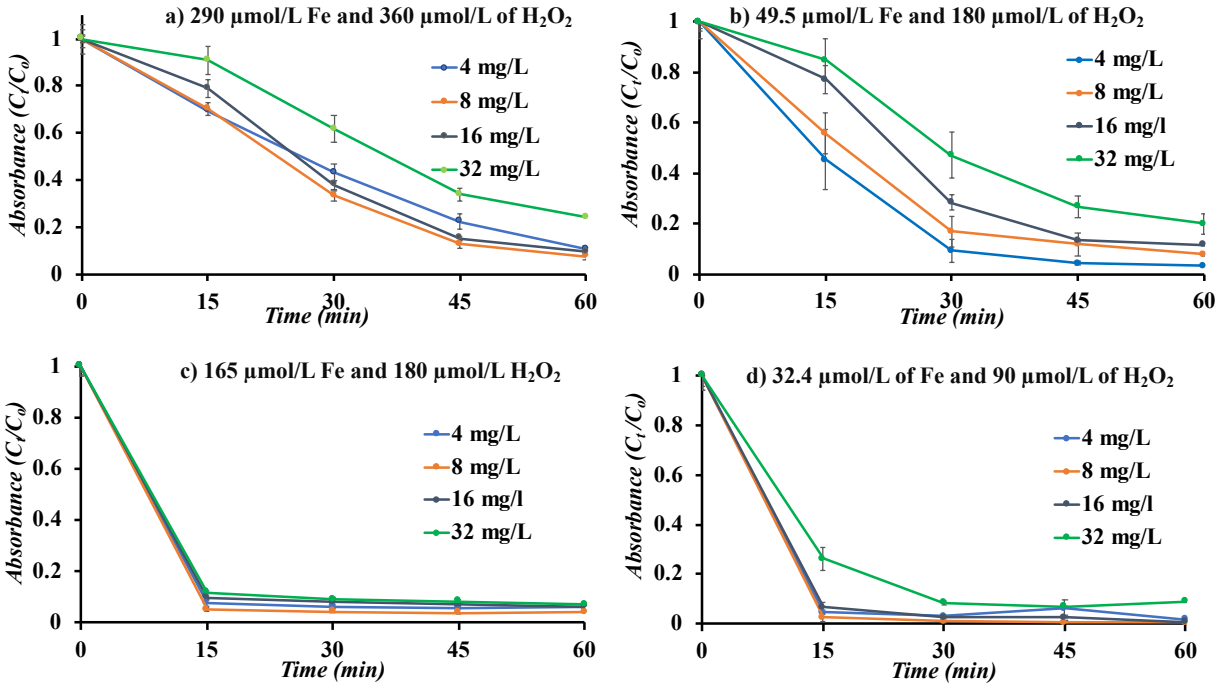

Figure 4-16: Degradation of MB at different concentrations, using 100 mg Starch Fe-St and Fe : H_2O_2 ratios of 1.09–3.64 to 300 mg Starch Fe-St but different overall reagent and catalyst concentrations.

There is clearly a relation between the synthetic route used, the starch content and the colloidal stability of the nanoparticles, since the Fe-St NPs flocculated over time when stored in the dark at 4 °C. Upon stirring the NPs immediately redispersed, however. The St-Fe samples, on the other hand, did not show this behavior and were more stable. This suggests that there may be a delicate balance between access to the iron catalyst and the colloidal stability of the NPs in

solution: The Fe-St NPs were more active for MB degradation, but at the expense of decreased solution stability, while the St-Fe NPs were less active but were stable in solution, even after months of storage. This indicates that in the St-Fe procedure, the iron NPs formed in the presence of starch lead to stronger complexation between starch and Fe, or else to the physical incorporation of starch segments around the NPs.

4.4.2.5 Repeated Additions of Methylene Blue

The different starch-stabilized iron nanoparticles were tested for their reusability, by conducting successive degradation cycles of 4 mg/L MB solutions as shown in Figure 4-14. To this end a few μL of a 1 g/L (concentrated) MB solution were added every hour, so that the reaction mixture contained 4 mg/L of MB at the beginning of each degradation cycle. The hourly timing of the additions was to guarantee full dye degradation before re-addition. The number of consecutive completed cycles (> 80% degradation) for each sample is provided in Table 4-3.

Even though the 1000 mg Starch St-Fe and 100 mg Starch Fe-St samples could degrade MB at concentrations of up to 32 mg/L, they were only able to perform less than three degradation cycles with 4 mg/L MB. This could be owing to a shortage of HO· radicals or a lack of Fe NP accessibility, especially for the 1000 mg St-Fe NPs. Recombination of the HO· radicals to create water and oxygen is also a possibility:[9,10]

$$HO\cdot + HO\cdot \rightarrow H_2O + O_2 \qquad (4-7)$$

Another reason might be the strong pH dependence of the self-decomposition of H_2O_2. In practice, H_2O_2 is supplied as slightly acidic solutions (pH below 5) to avoid fast self-decomposition at higher pHs:[810]

$$2H_2O_2 \rightarrow 2H_2O + O_2 \qquad (4-8)$$

While the initial pH of the reaction was set to 4, it gradually increased to 4.20 after the first degradation cycle and remained within 4.50 for subsequent cycles, presumably due to the differences in rate constants for the following Fenton termination reactions favoring the production of basic OH^- anions:

$$Fe^{2+} + HO\cdot \rightarrow Fe^{3+} + OH^- \quad k = 3.2 \times 10^8 \qquad (4-9)$$

$$Fe^{3+} + HO_2\cdot \rightarrow Fe^{2+} + O_2 + H^+ \quad k = 10^3 - 10^7 \qquad (4-10)$$

This causes a large drift in the formation and consumption of H^+ ions as the reaction proceeds.

The most successful catalyst in this test was the 300 mg Starch St-Fe NPs, which completed seven MB degradation cycles at a concentration of 4 mg/L (Table 4-3, Figure 4-17). Moreover, an increase in the rate of degradation was observed after the first degradation cycle, while all the other catalysts had decreased degradation rates in successive cycles. This could be due to degradation of the starch encapsulating the iron, allowing easier access to the catalyst. The degradation of starch was obvious from the decrease in total organic carbon (TOC) in the analysis of the blank after degradation, as shown in Table 4-4 for the 300 mg Starch St-Fe catalyst, discussed in detail below.

Table 4-3: Complete cycles of MB degradation at 4 mg/L.

Catalyst	Number of Cycles
1000 mg Starch St-Fe NPs	2
300 mg Starch St-Fe NPs	7
300 mg Starch Fe-St NPs	3
100 mg Starch Fe-St NPs	2

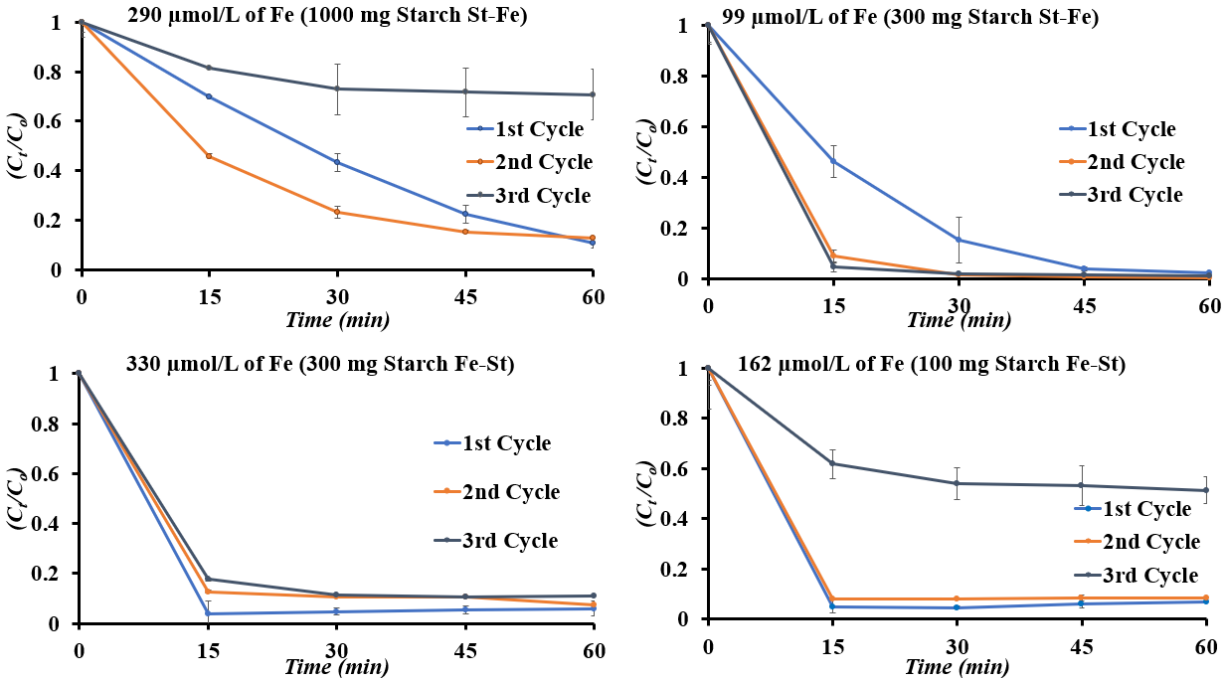

Figure 4-17: Degradation of MB in successive addition cycles for each catalyst (360 µmol/L H_2O_2, 350 nm UV irradiation, pH 4) at 4 mg/L for each cycle.

4.4.3 Total Organic Carbon (TOC) Analysis

The degraded samples were analyzed in a TOC analyzer after 60 min of UV irradiation. Unfortunately it was not possible to inject the MB solutions into the TOC instrument for analysis prior to degradation, since the dye could stain the tubing in the instrument. A blank for each example, namely a solution of the starch-stabilized iron catalyst and H_2O_2, was analyzed first. The TOC of the blank solution was measured again after a 60 min of UV exposure as described in Section 4.3.5, without MB. The initial organic carbon content of MB solutions at concentrations of 4, 8, and 16 mg/L was calculated by adding the contribution from MB to the blank reading. Finally, the TOC content was determined by injecting the degraded MB solutions into the TOC analyzer. Even though starch and citrate degradation was only partial, the extent of MB mineralization could be calculated by taking into account the residual TOC of the blank according to the procedure described below. The theoretical (initial) TOC of the MB solutions was calculated as follows:

$$Molecular\ weight\ of\ MB\ (C_{16}H18N3SCl) = 319.85\ g/moL$$

$$Molecular\ weight\ of\ organic\ carbon\ in\ MB\ (C_{16}H18N3SCl) = 192.16\ g/moL$$

$$\%\ of\ organic\ carbon\ in\ MB\ (C_{16}H18N3SCl) = \left(\frac{192.16\frac{g}{mol}}{319.85\frac{g}{mol}}\right) = 60.1\%$$

$$Organic\ carbon\ in\ 4\ mg\ L^{-1}\ MB\ = 4\ mg\ L^{-1} \times 0.601 = 2.404\ mg\ L^{-1}\ \ (4-11)$$

$$Initial\ TOC\ of\ MB\ = Initial\ TOC\ of\ blank\ + 0.601 \times conc.of\ MB\ (4-12)$$

The Final TOC value obtained after degradation was used to calculate the % mineralization of MB as follows:

$$\%\ Mineralized$$

$$= \left(1 - \frac{Final\ TOC\ of\ MB\ sample - Final\ TOC\ of\ blank}{TOC\ contribution\ from\ MB}\right) \times 100\ \ (4-13)$$

The starch-stabilized iron nanoparticles were tested at 4, 8, and 16 mg/L of MB and at different concentrations of Fe and H_2O_2 (Tables 4-4 through 4-8). The iron and H_2O_2 concentrations were selected based on the performance of the various starch-based iron NPs in the UV-visible tests discussed above (Figures 4-11 through 4-16). It was not possible to test the 1000 mg Starch St-Fe catalyst, as the MB concentration was much lower than the starch concentration in the samples (<10%), leading to large errors in the calculations.

4.4.3.1 Degradation with 300 mg Starch St-Fe Nanoparticles

MB mineralization level of 40 – 57 % was observed (Table 4-4). A mineralization level of 56.7% was obtained when degrading 4 mg/L of MB, which dropped to 40.4% for 16 mg/L MB. Although, as seen previously in the UV-visible experiments (Figure 4-17), the reaction rate and efficiency increased in the second degradation cycle, which could lead to more promising results. Albeit, due to instrumentation limitations, it was not possible to measure % mineralization for successive cycles of MB degradation. The instrument is non-specific for the organic compounds present in the solution, and unmineralized organic carbon from earlier cycles will add to the TOC of subsequent cycles, limiting the accuracy of the findings. According to Table 4-2, the 300 mg Starch St-Fe NPs contained the most starch of the three catalyst systems studied in these tests, suggesting that HO· radicals may have aided starch oxidation/mineralization in addition to MB mineralization. Although the starch is only partially degraded, as seen by the TOC values of the blank before and after UV irradiation, this suggests that the affinity of HO· radicals for MB for this catalytic system is higher than starch.

Table 4-4: TOC results in the degradation of MB at various concentrations with 300 mg Starch St-Fe 49.5 µmol/L of Fe and 180 µmol/L of H_2O_2.

Sample	Initial TOC, prior degradation (mg/L)	Final TOC after degradation (mg/L)	% MB Mineralized
Blank	4.127	3.353	–
4 mg/L MB	6.567	4.409	56.7
8 mg/L MB	8.935	5.878	47.5
16 mg/L MB	13.743	9.085	40.4

4.4.3.2 Degradation with 300 mg Starch Fe-St Nanoparticles

As seen in Tables 4-5 and 4-6, the amount of mineralization reduced dramatically as MB concentrations increased. As seen by the TOC values of the blank before and after UV irradiation, the catalyst support containing starch and citrate had undergone a higher percentage of mineralization as compared to 300 mg Starch St-Fe NPs. At lower Fe concentrations, the % mineralization was observed to be lower with these NPs compared with the 300 mg Starch St-Fe NPs. This might be an instance where MB is degrading into smaller fragments but not getting mineralized, as UV-visible tests revealed >80% degradation in an hour, as shown in Figure 4-14. A much higher concentration of reagents (Fe and H_2O_2) might be required to degrade MB at higher concentrations. Although, the relationship may not be linear as % mineralization

decreased drastically for 8 and 16 mg/L MB as the iron and H_2O_2 concentrations were doubled in Table 4-6.

Table 4-5: TOC results from degrading various concentrations of MB with 33 µmol Fe/L 300 mg Starch Fe-St 45 µmol/L of H_2O_2.

Sample	**Initial TOC, prior degradation (mg/L)**	**Final TOC after degradation (mg/L)**	**% MB Mineralized**
Blank	1.409	0.4612	–
4 mg/L MB	3.813	1.658	50.2
8 mg/L MB	6.217	3.398	38.9
16 mg/L MB	11.025	7.750	24.2

Table 4-6: TOC results from degrading various concentrations of MB with 66 µmol Fe/L 300 mg Starch Fe-St and 90 µmol/L H_2O_2.

Sample	Initial TOC, prior degradation (mg/L)	Final TOC after degradation (mg/L)	% Mineralized includes MB, starch and citrate
Blank	2.148	0.621	–
4 mg/L MB	4.552	1.741	53.4
8 mg/L MB	6.956	5.036	8.2
16 mg/L MB	11.764	9.148	11.3

4.4.3.3 Degradation with 100 mg Starch Fe-St Nanoparticles

The 100 mg Starch Fe-St NPs showed a relatively higher percent mineralization than the two catalyst systems previously tested. The percent mineralization improved significantly for 8 and 16 mg/L MB when the iron and H_2O_2 concentrations were doubled for 100 mg Starch Fe-St NPs. (Table 4-7 and Table 4-8). The best TOC result (69.6% mineralization) was found with the 100 mg starch Fe-St when degrading 4 mg/L at 32.4 µmol/L of Fe and 90 µmol/L H_2O_2. This is a H_2O_2 : Fe molar ratio of 2.78. For comparison, a similar degradation of methylene blue at pH 4 in a heterogeneous Fenton process reported by Zhou *et al.* degraded 50 mg/L of MB with 65% mineralization using 17.9 mmol/L of Fe and 29.4 mmol/L H_2O_2 with a paper sludge-derived heterogeneous catalyst in 80 minutes.[34] This is a H_2O_2 : Fe molar ratio of 1.47. The amount of

iron and H_2O_2 used for starch-stabilized iron NPs is 552 times lesser in the order of µmol/L. Thus, the results are comparable, but a much lesser amount of reagent was used for the starch-stabilized iron nanoparticles.

Table 4-7: TOC results from degrading various concentrations of MB with 16.2 µmol/L 100 mg Starch Fe-St and 45 µmol/L H_2O_2.

Sample	**Initial TOC, prior degradation (mg/L)**	**Final TOC after degradation (mg/L)**	**% Mineralized includes MB, starch and citrate**
Blank	1.339	0.722	–
4 mg/L MB	3.743	1.452	69.6
8 mg/L MB	6.147	2.856	55.6
16 mg/L MB	10.955	7.562	28.9

Table 4-8: TOC results from degrading various concentrations of MB with 32.4 µmol/L 100 mg Starch Fe-St and 90 µmol/L H_2O_2.

Sample	Initial TOC, prior degradation (mg/L)	Final TOC after degradation (mg/L)	% Mineralized includes MB, starch and citrate
Blank	2.115	0.700	–
4 mg/L MB	4.519	1.534	65.3
8 mg/L MB	6.923	2.485	62.9
16 mg/L MB	11.731	6.202	42.8

4.4.4 Iron Leaching from Starch-stabilized Iron NPs

The four catalyst systems being investigated were treated with phenol at different pH values (2−5), and the UV-visible spectra obtained were compared with ferric chloride-phenol standards to verify the occurrence of Fe^{3+} leaching (Figure 4-18). To this end, aliquots corresponding to a 0.01 M Fe concentration for each catalyst were treated with 0.06 M phenol, using H_2SO_4 to adjust the pH of the solutions. Only $FeCl_3$ is known to form a dark blue complex with phenol.[35] No leaching of Fe^{3+} was observed in any of the catalysts over the pH 2–5 range, which shows that they are stable under these conditions.

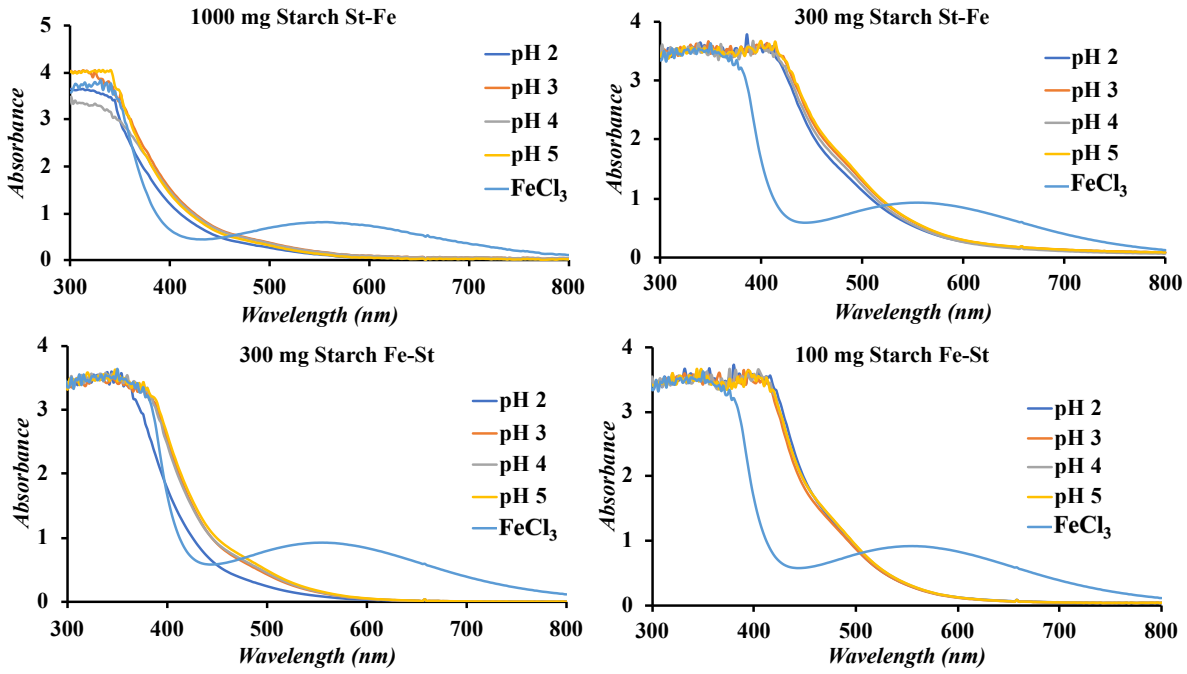

Figure 4-18: UV-Vis absorbance spectra for 0.01 M Fe aliquots of the different catalysts treated with 0.06 M phenol at pH 2, 3, 4 and 5; 0.02 M ferric chloride was used as a control.

4.5 Conclusions

Two different synthetic routes were developed to prepare starch-stabilized iron oxide ($Fe^{2+/3+}$) nanoparticles for the photocatalytic Fenton degradation of methylene blue. The four catalysts were obtained with varying iron : citrate : starch ratios. The overall particle size of the starch-stabilized catalysts determined by DLS analysis increased with the amount of starch used

in their synthesis, presumably due to aggregation. The iron NPs dispersed in starch were observed by TEM, and the presence of starch was confirmed by ^{1}H NMR analysis.

The pH, H_2O_2 and dye concentration were varied in the degradation experiments. All four catalyst systems could degrade methylene blue at concentrations up to 32 mg/L. These catalysts are superior as compared with similar starch-based catalytic systems reported in the literature,[34] as a mineralization level of up to 69.6% was achieved for 4 mg/L MB under UV irradiation at pH 4 when using 32.4 μmol Fe/L and 90 μmol/L H_2O_2 with the 100 mg Starch Fe-St catalyst. Catalyst reusability was also demonstrated for the 300 mg Starch St-Fe system, which remained active in the degradation of up to seven aliquots of 4 mg/L MB in successive additions when 99 μmol Fe/L and 360 μmol/L H_2O_2 was used. Furthermore, the hydrophilic starch increased catalyst dispersibility across a broader pH range, and the small quantities of iron used in the Fenton reactions result in no sludge formation. The catalysts were shown to be stable under acidic conditions over a pH range of 2-5, as Fe^{3+} did not leach out. Due to their successful application to methylene blue degradation, it would be interesting to investigate these catalyst systems in the degradation of other dyes.

Chapter 5

Chitosan Grafted with Thermoresponsive Poly(di(ethylene glycol) Methyl Ether Methacrylate) for Cell Culture

5.1 Abstract

Chitosan is a polysaccharide extracted from animal sources such as crab and shrimp shells. In this work, chitosan films were modified by grafting with a thermoresponsive polymer, poly(di(ethylene glycol) methyl ether methacrylate) ($PMEO_2MA$). The films were modified to introduce functional groups useful as reversible addition-fragmentation chain transfer (RAFT) agents. $PMEO_2MA$ chains were then grown from the films by RAFT polymerization, thus making the chitosan films thermoresponsive. The degree of substitution (DS) of the chitosan-based RAFT agent and the amount of monomer added in the grafting reaction were varied to control the length of the grafted $PMEO_2MA$ chains. The chains were cleaved from the film substrates for characterization by ^1H NMR and gel permeation chromatography (GPC) analysis. Temperature-dependent contact angle measurements were used to demonstrate that the hydrophilic/hydrophobic nature of the film surface varied with temperature. Due to enhanced hydrophobic character as the $PMEO_2MA$ becomes hydrophobic its lower critical solution temperature (LCST), the $PMEO_2MA$-grafted chitosan films can serve as supports for cell growth at 37 ^oC (incubation temperature). As the temperature is lowered, for example to 2–8 ^oC (refrigeration temperature, below the LCST), the grafted chitosan films become less

hydrophobic, and cell adhesion is decreased, facilitating their removal from the surface. Cell proliferation on the modified chitosan films was assessed by microscopy using a live/dead assay.

5.2 Introduction

The applications of biopolymers in different areas are increasing steadily. Chitin, a polymer of acetylglucosamine units linked via 1,4-glycosidic bonds, is a structural polysaccharide found mainly in crustaceans, fungi, and yeast. Chitosan is derived from chitin via N-deacetylation to form glucosamine units, although the complete deacetylation of chitin is difficult.[1,2] The main functional groups present in chitin are therefore a primary alcohol, a secondary alcohol and an amine group, with some acetamide groups remaining due to incomplete deacetylation (Figure 5-1).[2] Chitin can be deacetylated by hot alkali treatment with NaOH, enzymatic deacetylation, or steam explosion; among these, treatment with NaOH is the most common approach. About 70% deacetylation can be achieved by treating chitin with 40% sodium hydroxide at 120 ^{o}C for 1-3 hours.[2] The alkali treatment also ensures the removal of proteins, as chitin is mostly derived from the shell of crustaceans.[3] While chitosan, as a structural polysaccharide, is insoluble in water and most organic solvents,[3] chitosan is obtained when the deacetylation level is sufficient to make the material soluble in a dilute (1–5%) aqueous solution of acetic acid. This is because at acidic pH, the NH_2 functional groups in the D-glucosamine repeat units become protonated, transforming chitosan into a polyelectrolyte.[2]

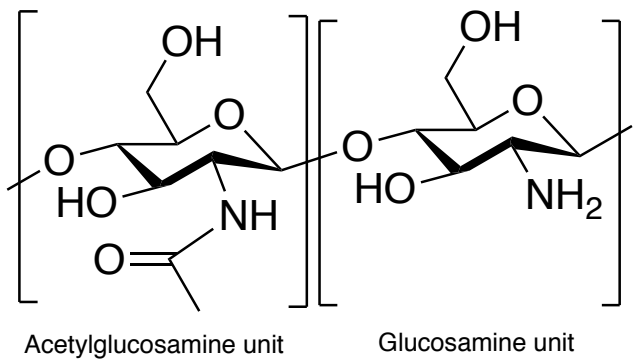

Figure 5-1: Structure of chitosan.

While the properties of chitosan differ depending on its molecular weight and degree of deacetylation, its exceptional film-forming ability makes it ideal for a wide range of applications, including wound healing and drug delivery.[1,2] Chitosan and chitin have been studied and used for implants and wound care for a long time, as ancient Japanese fishermen used powdered crab shells and the United States Army used it to treat battlefield injuries.[4] Chitosan was found to associate with a large number of mitotic cells in the wound bed, to stimulate faster epithelium growth at wound sites, and to promote collagen deposition.[4] Through increased cell attachment, chitosan has also been found to contribute to cytokine and growth factor stimulation.[5,6] Because of its polycationic nature, chitosan also has antibacterial and antifungal properties.[7] All these factors make chitosan films excellent cell growth supports.

The main goal of this project was to create thermoresponsive chitosan films, by grafting with a thermoresponsive polymer, so that they could be used as substrates for cell growth at 37

°C (incubation temperature). A potentially biocompatible polymer, poly(di(ethylene glycol) methyl ether methacrylate) ($PMEO_2MA$),[8] was selected as thermoresponsive component grafted on chitosan, due to its LCST around 26 °C. The chitosan films were modified to form a chitosan-based RAFT agent, followed by RAFT grafting of the di(ethylene glycol) methyl ether methacrylate (MEO_2MA) monomer. The characteristics of the grafted $PMEO_2MA$ chains could be controlled by varying either the degree of substitution of the RAFT agent or the amount of MEO_2MA added in the reaction. The aim was to allow the cells to interact with the $PMEO_2MA$-grafted chitosan films through hydrophobic interactions at 37 °C. Since $PMEO_2MA$ becomes less hydrophobic as the temperature drops below its LCST, the attached cells should become less adherent upon cooling, potentially enabling the $PMEO_2MA$-grafted chitosan films to be reusable supports for efficient cell growth and detachment.

5.3 Experimental Procedures

5.3.1 Materials

High molecular weight deacetylated chitosan (poly(D-glucosamine), molecular weight 310-375 kg/mol, >75% deacetylated), methanol (ACS reagent, ≥ 99.8 %), N,N-dimethylformamide (DMF, HPLC, ≥ 99.9 %), LiCl (≥ 99%), deuterated DMSO (99.9 % atom), CS_2 (ACS reagent, ≥ 99.9 %), potassium persulfate (ACS reagent, ≥ 99.0%), sodium ascorbate

(ACS reagent, ≥ 98%, crystals), NaOH (ACS reagent, ≥ 98%, pellets), methyl 2-bromopropionate (98%), di(ethylene glycol) methyl ether methacrylate (MEO_2MA, 95%), hydrogen chloride (30 % w/w in H_2O), ethanol (HPLC, 95%), Dulbecco's Modified Eagle's Medium (DMEM), aluminium oxide and inhibitor remover columns were all purchased from Sigma-Aldrich (Oakville, ON, Canada). Tryple Express (1X) was obtained from ThermoFisher Scientific (Waltham, MA, USA), and live/dead assay kits were purchased from Life Technologies Inc (Carisbad, CA, USA). XTT cell proliferation kits were purchased from R&D Systems (Mineapolis, MN, USA). Spectra/Por dialysis tubing with 100–500 Da molecular weight cut-off (MWCO) was purchased from Spectrum Laboratories Inc. (Shewsbury, MA, USA). The inhibitors in MEO_2MA and 2-HEA were removed with neutral alumina and inhibitor remover columns.

5.3.2 Synthesis of Chitosan Films

Deacetylated chitosan (2 g, 10.5 mmol glucosamine and acetylglucosamine units) was added to deionized water (100 mL) in a 250-mL beaker, followed by acetic acid (0.6 mL, 0.01 mol). A propeller-type mechanical stirrer at 400 rpm was used to disperse chitosan homogenously for 2 h until a gel-like consistency was achieved. To remove air bubbles from the gel, it was centrifuged at 10,000 rpm for 10 min. The gel was then evenly distributed in 40 mm × 5 mm polytetrafluoroethylene molds, each holding 15 mL of liquid. The water was allowed to evaporate for 2 d and the films were washed with a mixture of methanol and 0.1 M NaOH (1:1

by volume). The films were then dried in a vacuum oven at 60 ºC. For cell growth studies, the films were washed with only 0.1 M NaOH.

5.3.3 Synthesis of Xanthated Chitosan Films

Two deacetylated chitosan films (250 mg, 0.350.40 mm thickness, 1.32 mmol glucosamine and acetylglucosamine units) were dipped in water (5 mL) in a 10-mL round-bottom (RB) flask to be vortexed and stirred with a magnetic stir bar, to allow the films to swell. NaOH (80 mg, 2 mmol) was then added and stirring was continued for 30–60 min before CS_2 (0.20 mL, 3.31 mmol) was added dropwise. The flask was transferred to a water bath at 35 ºC for 2 h, during which time the solution turned reddish-orange. The mixture was allowed to cool to room temperature, the xanthated chitosan (Chito-CS_2) films were removed from the solution, washed with a mixture of methanol and 0.1 M NaOH (1:1) several times, allowed to dry in a fume hood for 4 h, and finally in a vacuum oven at 60 ºC overnight. The films were transparent but had a light red tint. A high DS sample was also made by doubling the amount of CS_2 used, but all other reaction parameters were held constant. For the cell growth studies, the films were washed with only 0.1 M NaOH.

5.3.4 Synthesis of RAFT Agent

Two Chito-CS_2 films (250 mg) were added to DI water (5 mL) in a 10-mL RB flask and the mixture was stirred with a magnetic stir bar for 30 min, to allow the films to swell. Methyl 2-bromopropionate (0.20 mL, 1.8 mmol) was then added dropwise and the flask was placed in a water bath at 80ºC for 40 min. The solution, which turned light yellow by the end of the reaction, was then allowed to cool to room temperature. The resulting chitosan-based RAFT agent (Chito-RAFT) films were removed from the solution, washed several times with a mixture of methanol and water (1:1 by volume), allowed to dry in a fume hood for 4 h, and then dried in a vacuum oven overnight at 60 ºC. The Chito-RAFT films had a light-yellow color. For cell growth studies, the films were washed with only 0.1 M NaOH.

5.3.5 Synthesis of Chito-*g*-$PMEO_2MA$

A Chito-RAFT film (110 mg, 0.35–0.40 mm thickness) was added to DI water (5 mL) in a 10-mL RB flask. The mixture was stirred with a magnetic stir bar for 30 min to allow the Chito-RAFT film to swell. Potassium persulfate (11 mg, 0.04 mmol) and MEO_2MA (47.3 mg, 0.26 mmol, for a target $PMEO_2MA$ content of 15 wt%) were added to the solution, before degassing with a steady flow of N_2 gas for 30 min. Sodium ascorbate (9 mg, 0.045 mmol) was then added to the reaction mixture which was placed in a water bath at 30 ºC for 120 min. After the reaction the solution was allowed to cool to room temperature, the $PMEO_2MA$-grafted chitosan films (Chito-*g*-$PMEO_2MA$) were removed from the solution, washed several times with a mixture of

methanol and water (1:1 by volume), allowed to dry in a fume hood for 4 h, and then in a vacuum oven overnight at 60 °C. Different $PMEO_2MA$ contents were targeted (15 wt%, 30 wt% and 60% of the total weight) by varying the amount of MEO_2MA added in the reaction. The yield was 120 mg, with a $PMEO_2MA$ content of 8.7±1 wt% based on the mass increase. For cell growth studies, the films were washed with only 0.1 M NaOH and then stored in DI water at 22 °C, as drying in a vacuum oven was avoided.

5.3.6 Cleavage of $PMEO_2MA$ Chains from Chito-*g*-$PMEO_2MA$

A 150-mg sample of Chito-*g*-$PMEO_2MA$ film was stirred with 15 mL of 1 M HCl in a 25-mL RB flask. A condenser was attached and the reaction was stirred at 95 °C for 12 h. A white precipitate formed by the end of reaction, which redissolved upon cooling in an ice-water bath. The solution of degraded chitosan (free D-glucosamine) and cleaved $PMEO_2MA$ chains was dialyzed for 72 h in a 100–500 Da dialysis bag. The purified solution was air-dried in a fume hood, and then in a vacuum oven at 60 °C overnight. The dry residue was dissolved in DMSO-d_6 for ^1H NMR analysis, and in DMF for GPC characterization.

5.3.7 Characterization Techniques

The chitosan films were characterized at different steps of the reaction by ATR-FTIR spectroscopy, swelling tests, and contact angle measurements. ^{1}H NMR and GPC analysis were used to characterize the grafted polymer chains.

5.3.7.1 ATR-FTIR

The chemical composition of the films and potential interactions between their components were investigated using attenuated total reflectance-Fourier-transform infrared (ATR-FTIR) spectroscopy. A PerkinElmer Spectrum Two FTIR Spectrometer was used, equipped with a Universal ATR Two accessory of Diamond/ZnSe operating with single bounce reflection. The software used was the PerkinElmer Spectrum IR version 10.6.2. The spectra were generated by averaging 4 scans recorded with a $LiTaO_3$ detector at a resolution of 4 cm^{-1} in the range of 4000 to 370 cm^{-1}.

5.3.7.2 ^{1}H NMR

A sample of cleaved $PMEO_2MA$ chains (20 mg) was dissolved in 1 mL of DMSO-d_6 for the analysis. The spectra were recorded at 25 ^{o}C on a 300 MHz Bruker instrument, by averaging 128 scans. The reported chemical shifts are relative to the solvent protons at 2.50 ppm for DMSO-d_6.

5.3.7.3 Gel Permeation Chromatography (GPC)

The apparent (polystyrene-equivalent) number-average molecular weight (M_n) and polydispersity index (PDI = M_w/M_n) of the grafted polymer chains was determined on a Hewlett Packard 1100 HPLC system equipped with a refractive index (RI) detector and two Jordi Resolve poly(divinylbenzene) columns (7.8 mm internal diameter × 300 mm length). The instrument used DMF with 0.1% LiCl as mobile phase at a flow rate of 0.9 mL/min and a temperature of 40 °C, and the samples were injected at a concentration of 3 mg/mL after filtration through 0.2 μm polytetrafluoroethylene membrane filters. Polystyrene standards were used to calibrate the instrument.

5.3.7.4 Contact Angle Measurements

For the measurements, each film was rehydrated in 15 mL of water for 15 min. Excess water was blotted away using filter paper, and the film was flattened by placing a heavy metal block on it for 30 min. The wetting behavior of the chitosan samples was evaluated at different points of the reaction through contact angle (θ_c) measurements on a customized apparatus with a built-in camera (Basler scA 1000−30 fm). Images were recorded every second after the deposition of a 8 μL droplet with a syringe. The photos were recorded with a custom-made LabVIEW version 14.0 program and processed with ImageJ version 1.52 Java 1.8.0_112 (64-

bit).[9] The wetting contact angles were determined using the 'contact angle' tool as the angle formed by the liquid at the three-phase (liquid, gas, solid) boundary as shown in Figure 5-2. This plug-in function, written by Brugnara at the UFI Innovation Center,[10] calculates the contact angle of a drop on a flat surface using a sphere approximation and an ellipse approximation. The data reported are the average of three independent measurements, and the error on the measurements was taken as the standard deviation.

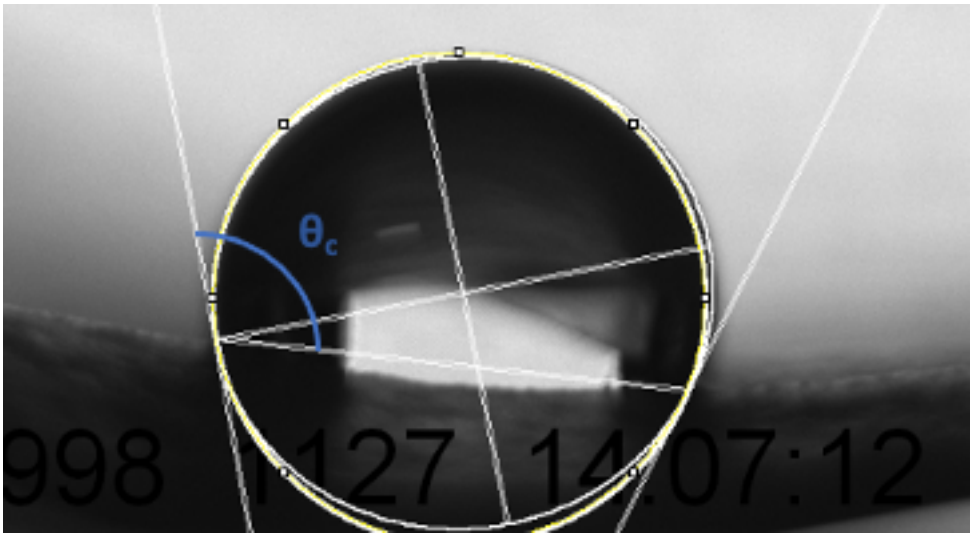

Figure 5-2: Sessile-drop contact angle (θ_c) determination using ImageJ.

5.3.7.5 Swelling Tests

Dry chitosan films (25-40 mg) with different $PMEO_2MA$ contents were submerged in 10 mL of deionized water at room temperature at either 22 or 37 °C, until equilibrium swelling was achieved (~ 2 h). After removing excess water by blotting with filter paper, the mass of the wet sample was calculated. The Swelling index (SI) was calculated using the equation

$$SI = \left[\frac{W_w - W_d}{W_d}\right] * 100\% \qquad (5-1)$$

where W_d and W_w are the masses of dry film and wet film, respectively.

5.3.8 Cells Adhesion, Viability and Proliferation on Chitosan Films

The experiments mentioned in this section were performed by co-op student Duo Sun (Fall 2020) under the supervision of Prof. Maud Gorbet in the Biomedical Engineering lab at the University of Waterloo (Carl A. Pollock Hall, CPH 1335C). Three different cell lines were tested for cell growth and proliferation on modified and unmodified chitosan films. They were also grown on TCPS after temperature-dependent cell detachment.

5.3.8.1 Film Sterilization

Modified and unmodified chitosan films for the cell study were prepared by placing them in a 50 mL tube and washing them for 5 min with sterile water. After decanting the water, the samples were sterilized by washing under agitation (300 rpm) for 15 min in 70% ethanol, and then again with 70% ethanol for 10 min, followed by decantation of the ethanol. The samples

were then washed in phosphate-buffered saline (PBS) for 15 min, decanted, and stored in PBS at room temperature in the dark.

On the day prior to the cell experiments, to provide a consistent surface area for cell growth, discs of 8 mm diameter were cut with a sterile hole hunch under aseptic conditions. The discs were placed in a 48-well tissue culture treated polystyrene (TCPS) plate. To improve cell adhesion, the discs of modified and unmodified chitosan films were incubated overnight at 37°C (5% CO_2) in 500 µL DMEM supplemented with 50% fetal bovine serum (FBS) and 1% penicillin/streptomycin (P/S). The unmodified chitosan films were used as controls.

5.3.8.2 Cell Culture and Seeding on Films

To assess cytotoxicity for a broad spectrum of cells, three types of immortalized cells were tested: the NIH 3T3 murine fibroblast cell line (ATCC), the RAW264.7 mouse monocyte/macrophage cell line, and the HPV-modified human corneal epithelial cell line (HCEC, Gorbet lab). The cells were grown in a flask at 37°C (5% CO_2) until they were 90% confluent, and the medium was changed every 2–3 d. DMEM supplemented with 10% FBS and 1% P/S (DMEM/FBS) was used for the NIH3T3 fibroblasts and RAW264.7 macrophages, while the HCEC were grown in serum-free keratinocyte medium (KM) supplemented with growth factors and P/S. On the day of the experiment, the medium was removed and 3 mL of Tryple Express was added to the flask, which was then incubated at 37 ºC for 12 min. The flask was washed with 10 mL of DMEM/FBS or KM before the cell suspension was transferred to a 15

mL centrifuge tube and centrifuged at 1300 rpm for 5 min. The supernatant was aspirated and the cell pellet was resuspended in 2 mL of DMEM/FBS or KM. The cells were then counted under the microscope. After removing the DMEM/50% FBS from all the wells, 30,000 cells were added per well in a final total medium volume of 400 μL. As controls, cells were also seeded in TCPS wells not containing any disc. The cells were then incubated at 37°C (5% CO_2) for up to 7 d, with the medium changed every 2–3 d.

5.3.8.3 Proliferation as Measured Using XTT Assay

Cell proliferation after 1, 3 and 7 d of culture was characterized with an XTT metabolism test using sodium 3,3′-[1-(phenylaminocarbonyl)-3,4-tetrazolium]-bis(4-methoxy-6-nitro)benzenesulfonic acid hydrate. On the day of the assay, to ensure that only cell proliferation on the discs was measured, the discs were transferred to a new well in a 48-well plate. To this end 600 μL of XTT solution was added to each well and the samples were incubated for 2.5 h at 37°C (5% CO_2). XTT solution was added also to 2 empty wells as background controls. After 2.5 h, the supernatant was transferred to a 96-well plate and the absorbance was measured at 490 nm with a reference wavelength of 630 nm on a SpectraMax Plus 384 Microplate Reader. The results are expressed as corrected absorbance values (by subtracting the absorbance of the background control solution from the sample absorbance).

5.3.8.4 Live and Dead Assay

Following the XTT test, live/dead staining was performed. The modified and unmodified chitosan films, as well as TCPS controls were incubated with 500 µL DMEM/FBS containing 0.25 µL of 1 mmol/L of calcein AM (stains live cells green) and l µL of ethD-1 (stains dead cells red) for 25 min at 37 °C. The samples were then imaged with a Nikon Eclipse TS100 fluorescence microscope (Tokyo, Japan).

5.3.8.5 Temperature-induced Cell Detachments and Viability

After imaging of the NIH3T3 fibroblasts on day 3, and the RAW264.7 macrophages on days 3 and 7 on the films, they were gently washed with PBS and transferred to a new 48-well plate. Each well was filled with DMEM/FBS and the samples were incubated in a refrigerator (2-8 ^{o}C) for 15 min. The medium was then thoroughly mixed with a pipette to collect suspended (adherent/detached) cells. The cell suspension was centrifuged for 5 min at 1300 rpm in 15 mL centrifuge tubes. The supernatant was aspirated, the cell pellet was resuspended in 500 µL of DMEM/FBS, and the cells were seeded into 24- or 48-well plates to be cultured for 3 d at 37 ^{o}C, after which time the live/dead assay was repeated.

5.4 Results and Discussion

5.4.1 Synthesis of Chitosan-based RAFT Agent and Chito-g-PMEO$_2$MA

Chitosan was modified to add thiocarbonylthio groups, serving as RAFT-active sites, as the starting point in the synthesis. This was accomplished by first reacting the hydroxyl groups on the glucosamine units with carbon disulfide in a heterogenous reaction under alkaline conditions, namely in the presence of NaOH. The RAFT agent was obtained by reacting the xanthated chitosan intermediate with methyl 2-bromopropionate (Scheme 5-1).

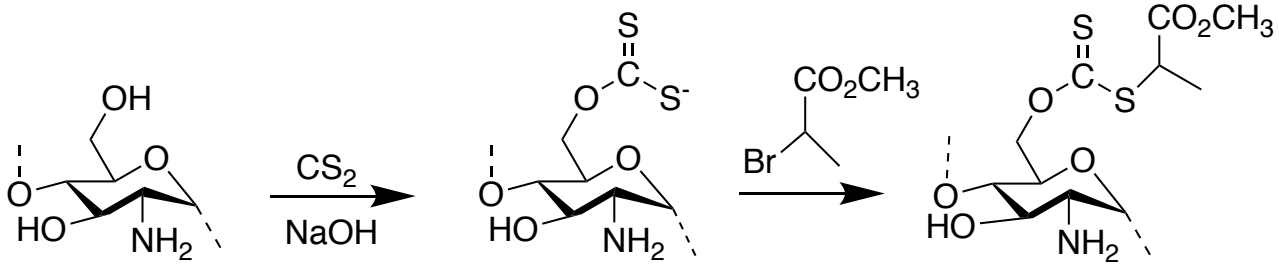

Scheme 5-1: Synthesis of the chitosan-based RAFT agent.

The chitosan-based RAFT (Chito-RAFT) agent obtained was then used to graft PMEO$_2$MA on the film. The RAFT polymerization mechanism involves a chain transfer agent in form of a thiocarbonylthio functional group (RAFT agent) to control the molecular weight of the grafted polymer in a free radical reaction.[11] The free radicals necessary to initiate the reaction

were generated with a redox system consisting of potassium persulfate and sodium ascorbate. Liu *et al.* used this redox initiator to graft poly(2-methoxyethyl acrylate) onto a macromolecular RAFT agent derived from poly(poly(ethylene glycol) methyl ether methacrylate). That initiator system was found to be highly efficient at 30 and 40 ^{o}C, without induction period in either case, and 90% conversion was accomplished within 1 h with a PDI = 1.10.[12]

Attenuated total reflectance–Fourier-transform infrared spectroscopy (ATR–FTIR) was used to characterize the chitosan substrate and the modified chitosan films. The carbonyl amide (C=ONHR stretch) and amine (HN-H bend) bands at 1670 and 1590 cm^{-1}, respectively, are characteristic for chitosan. Since the chitosan used was >75% deacetylated, the C=ONHR stretch was used to normalize the different spectra shown in Figure 5-3. As expected, all four modified chitosan films have a characteristic ester (OC=O carbonyl stretch) band at 1728 cm^{-1}, but chitosan does not. Even though the results are only semiquantitative, the OC=O band first appeared when chitosan was modified to form the Chito-RAFT agent, and the absorbance increased for a higher targeted DS, due to the nucleophilic substitution reaction between xanthated chitosan and methyl 2-bromopropionate with bromine as leaving group. As seen in Figure 5-3, due to the presence of ester groups in MEO_2MA, the intensity of the ester stretch band increased further as the targeted grafted $PMEO_2MA$ content was increased from 15 to 60 wt% for Chitosan-*g*-$PMEO_2MA$ (Chito-*g*-$PMEO_2MA$).

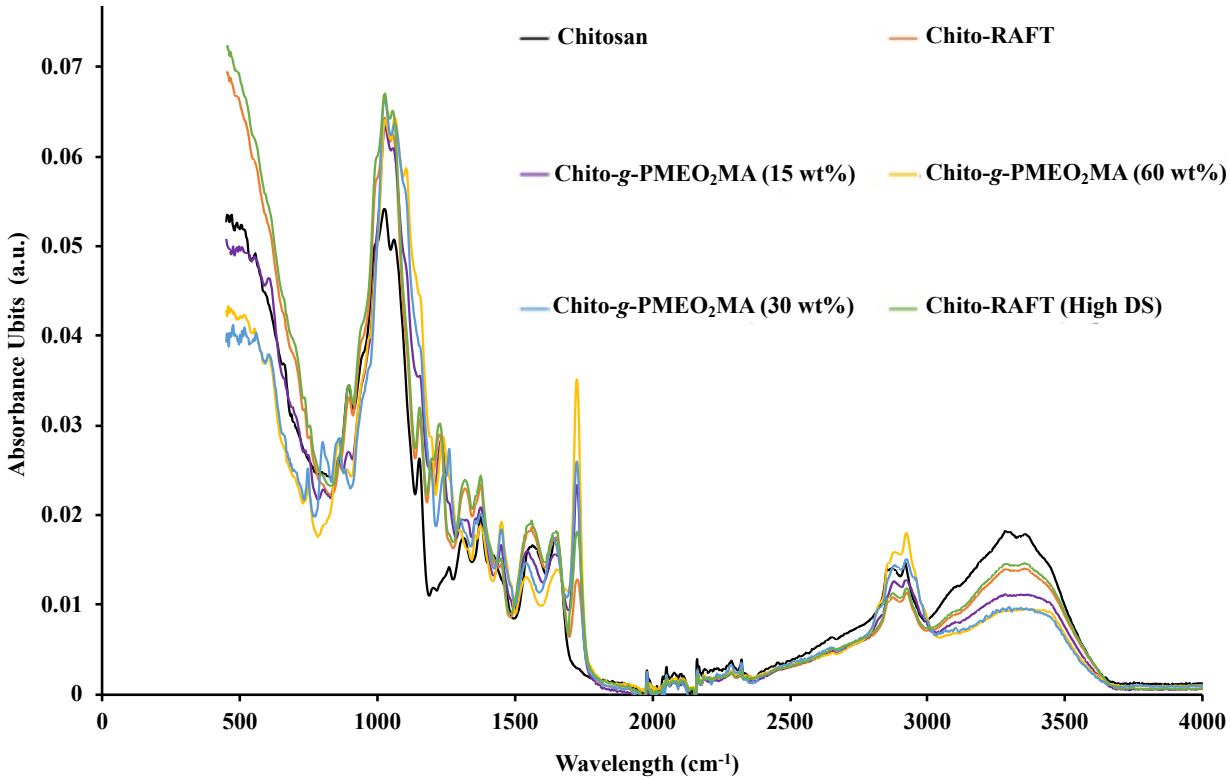

Figure 5-3: FTIR spectra for unmodified and modified chitosan samples.

The $PMEO_2MA$ content in the $PMEO_2MA$-grafted starch samples could be calculated by ^1H NMR analysis in Chapter 2, where $PMEO_2MA$ was similarly grafted to starch by RAFT polymerization. Since chitosan is not dispersible in most organic and aqueous solvents, the composition of the Chito-*g*-$PMEO_2MA$ samples was rather determined by comparing the weight of the films before grafting (Chito-RAFT agent) and after $PMEO_2MA$ grafting, to calculate the percentage of grafted $PMEO_2MA$ in the product. A larger number of chains can be assumed to be grafted on or near the surface of the film, because the aqueous reactions were heterogeneous

in nature. However, since the films were swollen in the reaction medium before the reactions, the occurrence of grafting inside of the films cannot be excluded.

The grafting efficiency was estimated using Equation 5-2

$$Grafting\ efficiency = \left[\frac{W_r - W_i}{W_m}\right] * 100\% \qquad (5-2)$$

and the $PMEO_2MA$ content in the product, expressed as a weight % increase relatively to the initial Chito-RAFT film, was calculated from Equation 5-3

$$PMEO_2MA\ content = \left[\frac{W_r - W_i}{W_i}\right] * 100\% \qquad (5-3)$$

where W_r is the weight of the recovered $PMEO_2MA$-grafted chitosan film, W_i is the weight of the chitosan-based RAFT agent film, and W_m is the weight of monomer added in the grafting reaction. The average grafting efficiency and the average $PMEO_2MA$ content were calculated by taking the average of 3 trials for each sample type. As shown in Table 5-1, the grafting reaction was not very efficient. The highest monomer grafting efficiency (49±2%) was observed for Chito-*g*-$PMEO_2MA$ (15 wt%), which decreased to 29±3 % as the target $PMEO_2MA$ content was increased to 60 wt%. The reaction was conducted for 2 h, during which time Chito-*g*-$PMEO_2MA$ (15 wt%) and Chito-*g*-$PMEO_2MA$ (30 wt%) achieved 50% grafting efficiency within experimental errors, while the remaining chains were not grafted onto chitosan and remained in solution. The non-grafted chains in solution for sample Chito-*g*-$PMEO_2MA$ (60 wt%) were analyzed by GPC. The apparent M_n of the soluble material was determined to be 135 kg/mol, with a PDI of 1.62. As discussed in more detail in Section 5.4.2, these values are

comparable with the apparent M_n and PDI measured for the cleaved $PMEO_2MA$ chains of Chito-*g*-$PMEO_2MA$ (60 wt%). The average $PMEO_2MA$ content determined from the weight measurements was 8.7±1 %, 20±1 %, and 43±3 % for the 15 wt%, 30 wt% and 60 wt% targeted $PMEO_2MA$ contents, respectively. As the monomer content in the grafting reaction was increased, the amount of $PMEO_2MA$ grafted onto chitosan nevertheless still increased, as indicated by the experimental Chito-*g*-$PMEO_2MA$ compositions reported in Table 5-1. The reactions were reproducible, as standard deviations of 1–3 % were obtained for all three samples for the average grafting efficiency and $PMEO_2MA$ content of the Chito-*g*-$PMEO_2MA$ samples. For comparison, Tang *et al*. used RAFT polymerization to graft thermoresponsive PNIPAM onto chitosan, using a RAFT agent obtained by modifying chitosan with phthalic anhydride and S-1-dodecyl-S'-(α,α'-dimethyl-α"-acetic acid) trithiocarbonate.[13] It was reported that RAFT polymerization yielded both grafted chains and soluble, untethered chains. A grafting efficiency of 50% was likewise reported after 10 h, suggesting that some chains remained in solution at the end of the reaction.[13]

A calculation was made to determine whether $PMEO_2MA$ grafting occurred only on the surface, or throughout the Chito-RAFT film. As an example, the initial weight of the Chito-RAFT agent film was 110 mg for Trial 1 for the synthesis of Chito-*g*-$PMEO_2MA$ (60 wt%) in Table 5-1, and the film had an initial thickness of 0.37 mm. If the density of chitosan and $PMEO_2MA$ are assumed to be identical, an increase in $PMEO_2MA$ mass will increase the thickness of the film to the same extent. Equation 5-4 may be used to compute this:

$$Grafted\ film\ thickness = \left[\frac{W_r}{W_i} * initial\ film\ thickness\right]$$

$$= \frac{161}{110} * 0.37\ mm = 0.54\ mm \qquad (5-4)$$

The thickness of the $PMEO_2MA$ layer added on one side of the film would be given by Equation 5-5

$$Added\ thickness = [thickness\ of\ grafted\ film - initial\ film\ thickness]/2$$

$$= (0.54 - 0.37)/2 = 0.09\ \text{mm} \qquad (5-5)$$

Using the data reported in Table 5-2 for the cleaved chains, the apparent degree of polymerization (X_n) of the $PMEO_2MA$ chains cleaved from Chito-*g*-$PMEO_2MA$ (60 wt%) was

$$X_n = \left[\frac{M_n}{M_o}\right] = \frac{128000\ g/mol}{188.2\ g/mol} = 680 \qquad (5-6)$$

where M_n is the apparent number-average molecular weight of the $PMEO_2MA$ chains, and M_o is the molar mass of the MEO_2MA monomer.

A maximum theoretical film thickness can be calculated[14] with Equation 5-7 for $PMEO_2MA$ chains grafted strictly on the surface of the Chito-RAFT agent film if the polymer chains are assumed to adopt a fully extended chain conformation

$$R = \frac{(0.8166 * l * 2X_n)}{2} = \frac{0.8166 * 1.535 * 10^{-7} mm * 2 * 680}{2} = 0.00017\ mm \qquad (5-7)$$

where l is the length of the carbon-carbon (C-C) bond and 0.8166 = sin (109.5°/2) is the projection of each C-C bond on the main axis of the chain.[14]

In spite of the approximations used (using the apparent M_n of the $PMEO_2MA$ chains, and equal density of chitosan and $PMEO_2MA$ in the calculations), it is clear that the maximum film thickness increase expected for $PMEO_2MA$ chains grafted strictly on the film surface (0.00017 mm) is much smaller than the 0.09 mm increase expected based on the weight increase of the film. Furthermore, polymers are not expected to remain in a completely stretched conformation unless they are grafted densely on a surface, which would make the discrepancy between the two values even larger. Consequently, grafting of the $PMEO_2MA$ chains must have occurred throughout the films rather than only on their surface. It nevertheless seems likely that due to the greater accessibility of RAFT sites, the density of $PMEO_2MA$ chains grafted would be larger on or near the surface of the films.

Table 5-1: Grafting efficiency of $PMEO_2MA$ to chitosan using Chito-RAFT agent.

Sample	Trial	Chito-RAFT agent (W_i, mg)	MEO_2MA (W_m, mg)	Recovered (W_r, mg)	Average grafting efficiency (%)	Average $PMEO_2MA$ content (wt%)
Chito-*g*-$PMEO_2MA$ (15 wt%)	1	110	19.5	120	49±2	8.7±1
	2	113	19.9	123		
	3	112	19.7	121		
Chito-*g*-$PMEO_2MA$ (30 wt%)	1	110	47.3	132	47±3	20.3±1
	2	110	47.3	134		
	3	113	48.4	134		
Chito-*g*-$PMEO_2MA$ (60 wt%)	1	110	166	152	29±3	43±3
	2	110	166	161		
	3	112	168	162		

5.4.2 Cleavage of $PMEO_2MA$ Chains from Chito-*g*-$PMEO_2MA$

Using chitosan modified with functional groups acting as RAFT agent (Chito-RAFT) for the methacrylate monomer, two different strategies were developed to control the chain length and the composition of the target Chito-*g*-$PMEO_2MA$ films. The first strategy was to vary the degree of substitution (DS) of the chitosan-based RAFT agent, while keeping the amount of monomer used in the grafting reaction unchanged. To see whether that approach had an impact on chain length, the target DS for the Chito-RAFT substrate used in the synthesis of Chito-*g*-

$PMEO_2MA$ (60 wt%) was doubled. Due to the greater number of reactive sites present in the film, a RAFT agent with a higher DS should generate a larger number of shorter polymer chains. Conversely, a RAFT agent with a lower DS should generate longer polymer chains due to the presence of fewer initiating sites. The other strategy investigated was to vary the amount of monomer added to the Chito-RAFT agent for a given DS, since the length of the $PMEO_2MA$ chains should increase as more monomer is added in the grafting reaction. To verify this hypothesis, the target monomer (MEO_2MA) content was varied from 15 to 60 % of the Chito-RAFT film substrate weight.

The molecular weight of the thermoresponsive $PMEO_2MA$ chains grafted to chitosan was determined by GPC analysis after degrading the chitosan substrate into N-acetylated and deacetylated glucosamine units, using 1 M HCl. The degradation rate of chitosan increases with the acid concentration and the temperature,[15] and refluxing in 1 M HCl for 12 h led to complete degradation of the chitosan component while leaving the $PMEO_2MA$ chains unaffected. After the reaction, $PMEO_2MA$ was separated from the degraded chitosan components by dialysis for 72 h. The integrity of the cleaved $PMEO_2MA$ chains was verified by NMR analysis (Figure 5-4b). The integral of the peak for the methyl protons (3H, labeled 1) was in a 1.45:1 ratio to the methylene protons in the glycol unit next to the ester group (2H, labeled 3) or identical, within error limits, with the expected ratio of 1.5:1. This implies that the diethylene glycol units in $PMEO_2MA$ were not cleaved during the reaction, and that only the glycoside linkages were degraded. In the $PMEO_2MA$ sample recovered after degradation of the chitosan component

(Figure 5-4b) an anomeric proton signal is also absent at 5.20 ppm, confirming the absence of chitosan in the product. These results are consistent with a report by Aljbour *et al*., who determined an average yield of 87% for the depolymerization of chitosan into monomers and dimers of glucosamine when the reaction was conducted under reflux in 2 M HCl for 24 h.[16] It was also shown that chitosan was deacetylated during depolymerization, such that the monomers and dimers contained mostly deacetylated glucosamine units.[17] The deacetylation and depolymerization mechanism suggested by the authors is shown in Scheme 5-2.

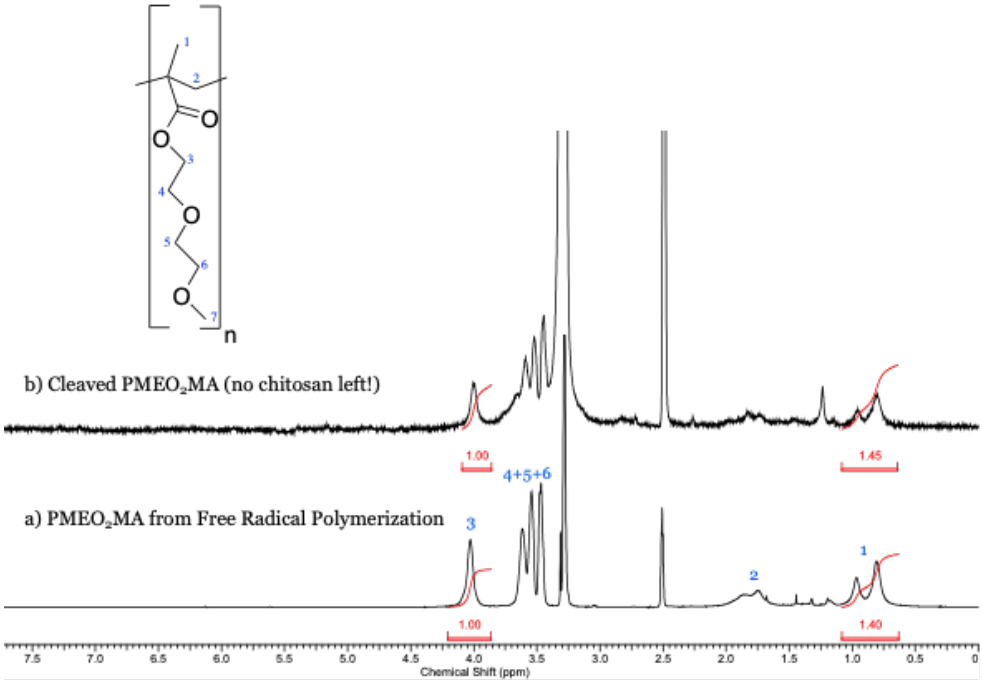

Figure 5-4: ^{1}H NMR spectra for a) PMEO$_2$MA, and b) PMEO$_2$MA chains cleaved from Chito-g-PMEO$_2$MA (15 wt%) in DMSO-d6 at 25 ^{o}C.

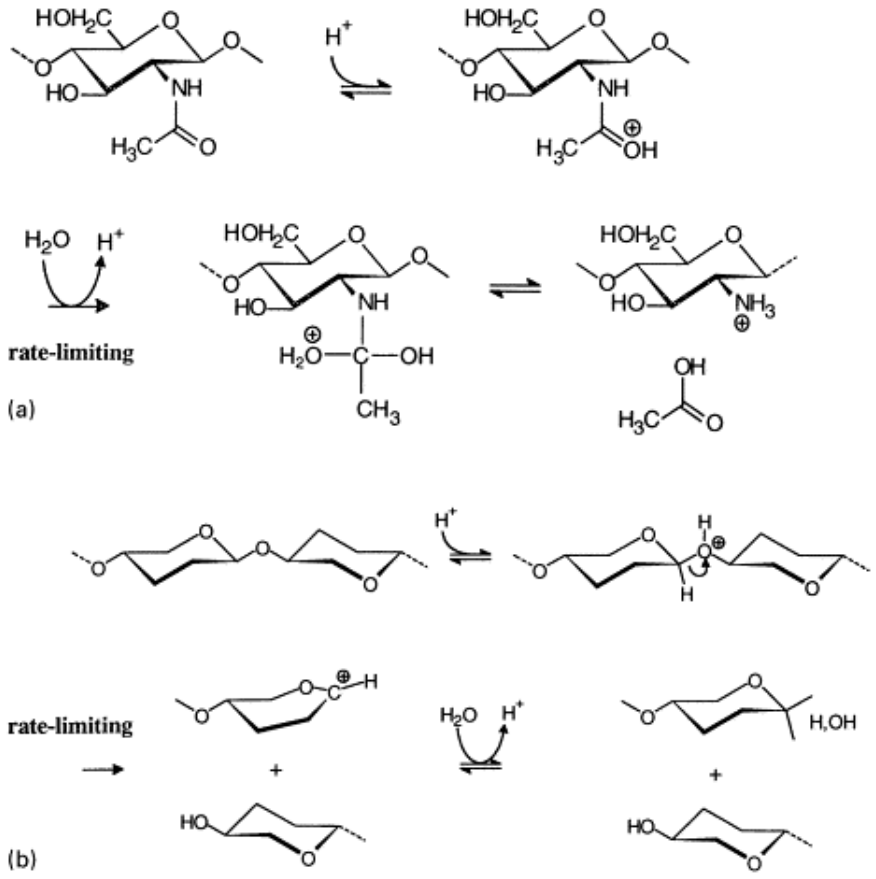

Scheme 5-2: Proposed reaction mechanism for the acid-catalyzed hydrolysis of N-acetyl and glycosidic linkages in chitosan. (a) Hydrolysis of the N-acetyl linkage (S_N2 reaction). (b) Most widely accepted mechanism for hydrolysis of the glycosidic linkage (S_N1 reaction) Reprinted with permission from reference 17. Copyright (2001) Elsevier.

Chito-*g*-PMEO$_2$MA with 15, 30, and 60 wt% target PMEO$_2$MA contents, as well as Chito-*g*-PMEO$_2$MA with 60 wt% target PMEO$_2$MA content obtained with a higher DS Chito-RAFT substrate, were studied by GPC to demonstrate control over the molecular weight of the grafted PMEO$_2$MA chains as a function of the reaction conditions used (Table 5-2). The apparent (polystyrene-equivalent) M_n of the cleaved PMEO$_2$MA chains for Chito-*g*-PMEO$_2$MA with target PMEO$_2$MA contents of 15, 30 and 60 wt% were indeed 43, 85 and 128 kg/mol, respectively, with PDI values in the 1.71–1.88 range (Table 5-2). Therefore when increasing amounts of monomer were added to a constant DS Chito-RAFT substrate, the grafted PMEO$_2$MA chains grew longer as expected. Furthermore, the PMEO$_2$MA chains cleaved from Chito-*g*-PMEO$_2$MA (60 wt%, high target DS) had an apparent M_n of 105 kg/mol and a PDI = 1.88 (Table 5-2), somewhat shorter than for the low DS Chito-*g*-PMEO$_2$MA (60 wt%) sample (M_n = 128 kg/mol). Due to the increased DS, shorter PMEO$_2$MA chains were grown from the chitosan substrate as expected, albeit the variation in M_n was not as pronounced as in the situation where the amount of monomer added was varied. Jiang *et al.* synthesized chitosan-based RAFT agent to graft poly(N-isopropylacrylamide) (PNIPAM), and obtained a PDI of 1.28 for M_n = 16.2 kg/mol.[18] The molecular weights attained for the PMEO$_2$MA chains are much higher in the current investigation, but the PDI values are also higher.

Table 5-2: Comparison of the apparent number-average molecular weights (M_n) obtained by GPC analysis of the cleaved $PMEO_2MA$ chains.

Cleaved Samples	M_n from GPC (kg/mol)	PDI
Chito-*g*-$PMEO_2MA$ (15 wt%)	43	1.82
Chito-*g*-$PMEO_2MA$ (30 wt%)	85	1.71
Chito-*g*-$PMEO_2MA$ (60 wt%)	128	1.80
Chito-*g*-$PMEO_2MA$ (60 wt%, High DS)	105	1.88

5.4.3 Contact Angle Measurements

The sessile water drop contact angle test was used to characterize the hydrophilic or hydrophobic nature of the modified chitosan films above and below the LCST of the grafted $PMEO_2MA$ chains. Hydrophilic surfaces are generally considered to have water contact angles below 90º, while hydrophobic surfaces have contact angles above 90º.[19] Contact angle measurement results are compared for selected Chito-*g*-$PMEO_2MA$ samples with different target thermoresponsive polymer contents in Figure 5-5, and the quantitative results are summarized in Table 5-3. A film of $PMEO_2MA$ synthesized by radical polymerization (M_n = 60.4 kg/mol, PDI = 2.5) cast on a glass slide was also used as a control for comparison with the Chito-*g*-$PMEO_2MA$ samples. The experiment could not be carried out on unmodified chitosan films, because they were too hydrophilic and readily absorbed the water droplets. Not surprisingly, $PMEO_2MA$ was found to be hydrophobic at 40 ºC, above its reported LCST of 26 ºC.[20] An

increase in hydrophobicity is also clearly seen for the different Chito-*g*-$PMEO_2MA$ samples as their $PMEO_2MA$ content increases. The presence of a grafted $PMEO_2MA$ on the surface should reduce the charge density of chitosan, resulting in lower hydrophilicity.[21] Interestingly, the contact angle of all the Chito-*g*-$PMEO_2MA$ samples is significantly higher than for the $PMEO_2MA$ homopolymer reference, suggesting enhanced surface hydrophobicity for these films. This may be explained in part by the much greater M_n of the cleaved $PMEO_2MA$ chains in the 30 wt% and 60 wt% samples than for the reference sample, which had a high contact angle even under LCST. An increase in M_n of the grafted $PMEO_2MA$ chains led to a decrease in the LCAT/LCST of SNP-*g*-$PMEO_2MA$ in solution in Chapter 2 (Table 2-2, and Figure 2-8). For the 30 wt% and 60 wt% Chito-*g*-$PMEO_2MA$ samples, the contact angle measurements may have been lower at temperatures < 22 ^oC, but the Chito-*g*-$PMEO_2MA$ samples tended to form gels when stored in the refrigerator (4 ^oC) overnight. Furthermore, it was impossible to undertake contact angle measurements below 22 ^oC (room temperature), due to the lack of a cooling system on the instrument.

In the low temperature range (22 ^oC, below the LCST of the $PMEO_2MA$ chains), the contact angles also varied in the order Chito-*g*-$PMEO_2MA$ (15 wt%) < Chito-*g*-$PMEO_2MA$ (30 wt%) < Chito-*g*-$PMEO_2MA$ (60 wt%), especially at longer measurement times. This trend can be rationalized in terms of the decreasing influence of the chitosan component of the samples as their $PMEO_2MA$ content increases. Noticeably, the longer $PMEO_2MA$ chains grafted in the 30 and 60 wt% samples results in less drastic changes in contact angle, which may be related to the

long $PMEO_2MA$ chains shielding the chitosan component more effectively from water than in the 15 wt% sample. Furthermore, as seen in Table 5-3, contact angle changes at 40 °C are insignificant within error limits over the 4-second time scale of the measurements, while a small decrease is observed for the Chito-*g*-$PMEO_2MA$ samples at 22 °C. This is presumably due to rearrangement of the hydrophilic chitosan component to contact the water phase, which is facilitated by the increased mobility of the hydrated $PMEO_2MA$ chains at low temperature.

Finally, there is an obvious increase in contact angle for all the Chito-*g*-$PMEO_2MA$ samples as the temperature is increased from 22 °C (below the LCST of $PMEO_2MA$) to 40 °C (above the LCST), as expected for these thermoresponsive materials. Plunkett *et al.* similarly observed that the water contact angle increased from $68.4^o \pm 0.4^o$ to $79^o \pm 1^o$ for PNIPAM monolayers self-assembled on gold surfaces as the temperature was increased from below to above the LCST of PNIPAM.[22] The magnitude of the contact angle changes observed for the Chito-*g*-$PMEO_2MA$ 15 and 30 wt% samples are larger than for PNIPAM monolayers, presumably due to decreased shielding of the chitosan component by the grafted $PMEO_2MA$ chains.

Table 5-3: Contact angle (in degrees) from t = 0 to 4 s for selected samples at 22 and 40 °C.

Time (s)	$PMEO_2MA$ on glass slide		SNP-*g*-$PMEO_2MA$ (15 wt%)		SNP-*g*-$PMEO_2MA$ (30 wt%)		SNP-*g*-$PMEO_2MA$ (60 wt%)	
	@22 °C	@40 °C	@22 °C	@40 °C	@22 °C	@40 °C	@22 °C	@40 °C
0	73±2	88±1	75±3	103.7±2	95±2	109±1.5	91±1.3	102±1.2
1	70.4±1.7	88.7±1.2	66±4.8	102.9±3.4	92.4±2	107±2	92.5±1	100.5±2
2	72±2	89.2±1.5	62.7±5	103.5±4.7	86.7±4	106.8±2	91±1.2	102±2.7
3	73.6±1.5	85.1±2	62.2±4.3	102.3±4.9	81.7±4.7	106.9±2.1	93.2±2	101±3
4	74.8±2.7	85.6±2.6	60.2±6	104.8±3.7	83.3±3.6	106.6±1.7	92.1±3	102±4.2

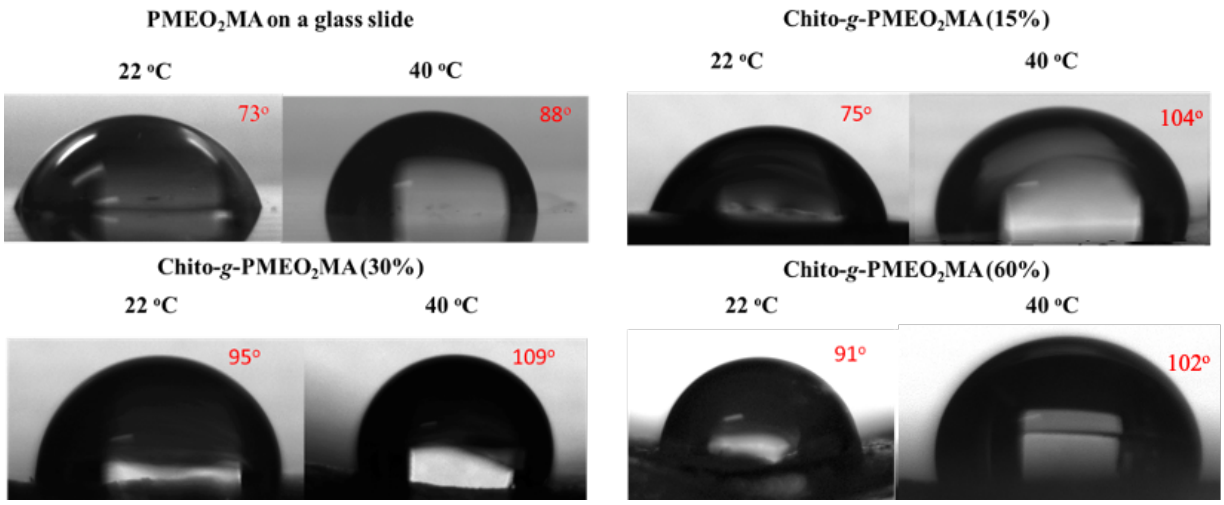

Figure 5-5:Contact angle measurements at t=0 s for different samples at 22 and 40 °C.

5.4.4 Swelling Tests

The swelling properties of modified and unmodified chitosan films are compared in Figure 5-6. The swelling index (SI) of chitosan, expressed as % swelling relatively to the weight of the non-swollen samples, decreased substantially with the amount of $PMEO_2MA$ grafted to chitosan, particularly for target $PMEO_2MA$ contents of 30 and 60 wt%. It is necessary to be cautious in making comparisons due to variability in the measurements leading to large error bars, however. The combination of hydrophilic hydroxyl and amino groups in chitosan allows hydrogen bonding with water, leading to the highest SI for chitosan and Chito-RAFT at both 22 and 37 ^oC. Grafting $PMEO_2MA$ on the chitosan films decreased their average hydrophilicity to some extent, such that bulk swelling of the films was decreased significantly at the higher $PMEO_2MA$ contents, due to the decreasing contribution of the hydrophilic chitosan component. The thermoresponsiveness of the samples manifests itself as a substantial decrease in SI at 37 ^oC, above the LCST of $PMEO_2MA$, even though the error bars overlap for Chito-*g*-$PMEO_2MA$ (60%). This is clearly due to the grafted thermoresponsive $PMEO_2MA$ chains accounting for a significant portion of the sample weight, becoming hydrophobic at the higher temperature and making the bulk material less hydrophilic on average. As mentioned earlier, the LCST of the chains at the surface of the Chito-*g*-$PMEO_2MA$ (30%) and for Chito-*g*-$PMEO_2MA$ (60%) films could potentially be below 22 ^oC, which would explain why no drastic changes in SI were observed as the temperature was increased from 22 ^oC to 40 ^oC.

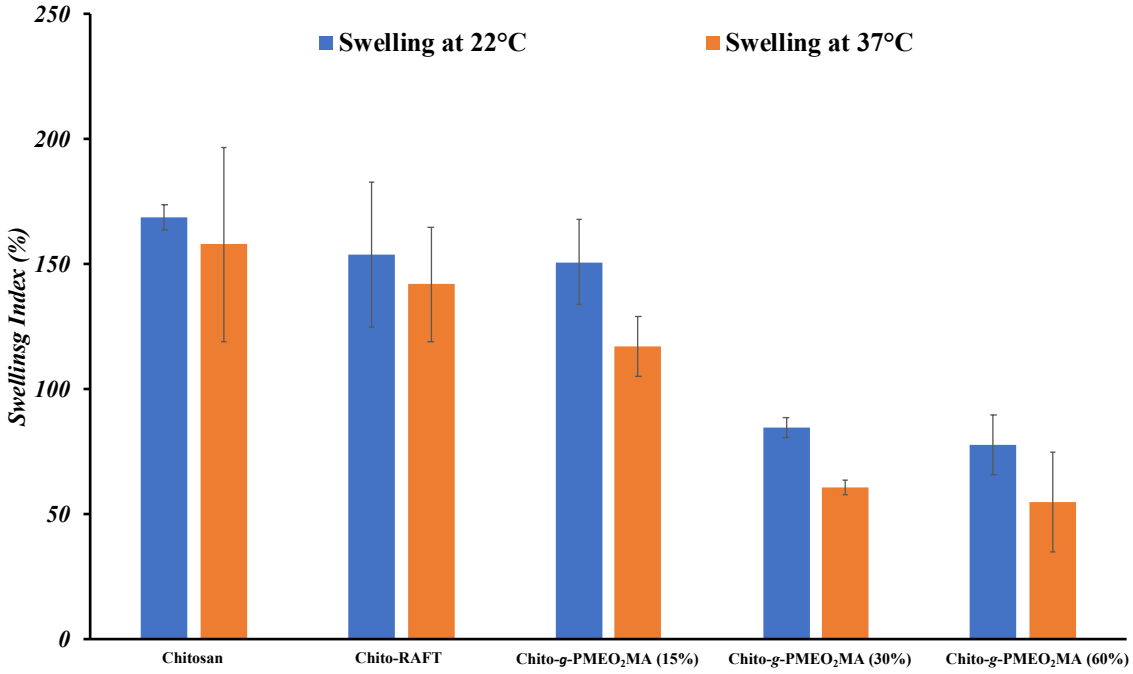

Figure 5-6: Swelling behavior of selected chitosan films.

5.4.5 Cells Adhesion, Viability and Proliferation on Chitosan Films

The cell culture experiments were performed on RAW264.7 macrophages, NIH3T3 fibroblasts and immortalized human corneal epithelial cells. The cells were allowed to proliferate on polystyrene plates treated for tissue culture (TCPS) and unmodified chitosan films as controls, as well as on chitosan films grafted with 30 and 60 wt% $PMEO_2MA$, for up to 7 days.

The live/dead assay provides a qualitative evaluation of the cytotoxicity of a biomaterial, with calcein AM staining live cells green and EthD-1 staining dead cells red, which can be

observed on a fluorescent microscope. Overall, the aim was to evaluate the cytotoxicity of the films towards these cells. It is important to understand that a material might not be cytotoxic, but also not necessarily biocompatible. Biocompatibility can be defined as the ability of a material (e.g. the chitosan films) to perform its desired function (cell adherence and detachment) without inducing any local or systemic adverse response by the cells.[23] Thus it is not just the presence of viable cells and the absence of dead cells which make a material biocompatible, but also the way in which the cells adhere and proliferate in contact with the material. The thermoresponsive properties of the modified chitosan films were evaluated with RAW264.7 macrophages and NIH3T3 fibroblasts. This was accomplished by lowering the temperature as described in Section 5.3.8.4, to detach the growing cells on the films. The cells were then cultured for 3 d on a tissue culture plate and visualized by fluorescence microscopy with calcein-AM and EthD-1 staining to determine live and dead cells, respectively.

5.4.5.1 Macrophages

The RAW 264.7 macrophage, originating from the Abelson leukemia virus derived from BALB/c mice, are capable of performing pinocytosis and phagocytosis by producing nitric oxide.[24] Macrophages, in comparison to other types of cells, are difficult to remove from any film surface; consequently, they were selected as a relevant cell type for the cell adhesion experiments.[25] As seen in Figure 5-7, the RAW 264.7 macrophages proliferated well on both modified and unmodified chitosan, as demonstrated by the increase in absorbance values in the

XTT assays between day 1 and day 7. Cell proliferation was further confirmed with the live/dead assay (Figure 5-8); a significant increase in cell density can be observed between day 1 and day 7. It is important to note that despite the fact that an almost confluent layer of macrophages could be seen on both TCPS and Chito-*g*-$PMEO_2MA$ (30 wt%), the XTT absorbance values for Chito-*g*-$PMEO_2MA$ (30 wt%) were about 30% of that for TCPS (Figure 5-9). This is because the metabolized dye adsorbed on the films, and thus was not present in the supernatant. Indeed, it can be seen in Figure 5-10 that as the XTT solution was metabolized, it was sorbed (adsorbed and/or absorbed) on the chitosan films, and thus the values reported at day 7 are underestimating the actual cell proliferation level. This was further supported by fluorescence microscopy (Figure 5-8), as cell proliferation at day 7 on Chito-*g*-$PMEO_2MA$ (30 wt%) appeared to be very similar to the control TCPS. The results from the live/dead assay (Figure 5-8, day 1) and XTT assay (Figure 5-7) also suggest that macrophages adhere well on the modified chitosan films. At day 1, more dead cells were observed on Chito-*g*-$PMEO_2MA$ (60 wt%) (red-stained cells) as compared with Chito-*g*-$PMEO_2MA$ (30 wt%), indicating some initial cytotoxicity with Chito-*g*-$PMEO_2MA$ (60 wt%) (Figure 5-8). The number of dead cells was negligible by the end of day 7, however. The live/dead results indicate that the RAW264.7 macrophage cells proliferated well on the modified chitosan films, reaching a level of confluence similar to the TCPS control, especially for Chito-*g*-$PMEO_2MA$ (30 wt%).

Overall, the results indicate that $PMEO_2MA$-grafted chitosan films are excellent surfaces for the growth of macrophages, displaying limited and no cytotoxicity for Chito-*g*-$PMEO_2MA$

(60 wt%) and Chito-*g*-PMEO$_2$MA (30 wt%), respectively. As seen in Figure 5-8, the cells appear to grow as large clumps on both chitosan and Chito-*g*-PMEO$_2$MA (60 wt%), with bare areas (day 3 for Chito-*g*-PMEO$_2$MA (60 wt%), day 7 for chitosan), suggesting that these films are not as biocompatible as Chito-*g*-PMEO$_2$MA (30 wt%). Physicochemical properties such as the surface roughness are important to optimize cell adhesion. Zan *et al.* studied the effects of the surface roughness of chitosan microspheres on cell adhesion and found that Mouse MC3T3-E1 osteoblasts preferred rough surfaces over smooth ones.[26] An increase in PMEO$_2$MA content from 30 to 60 wt% may have led to increased film roughness, reducing the cytocompatibility of the Chito-*g*-PMEO$_2$MA (60 wt%) films.

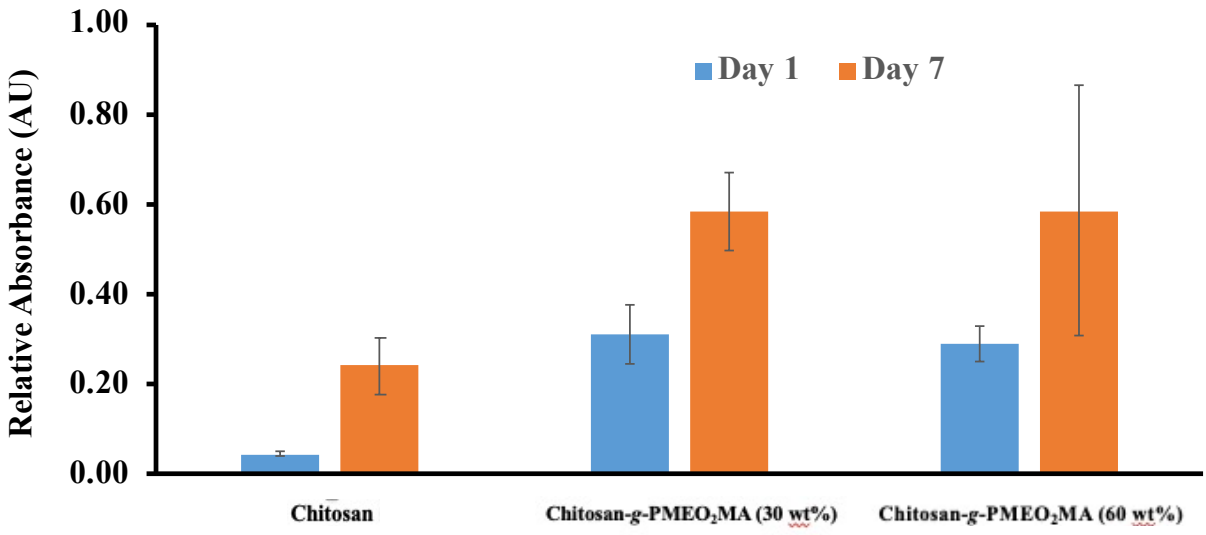

Figure 5-7: XTT assay for proliferation of RAW 264.7 cells on modified and unmodified chitosan films.

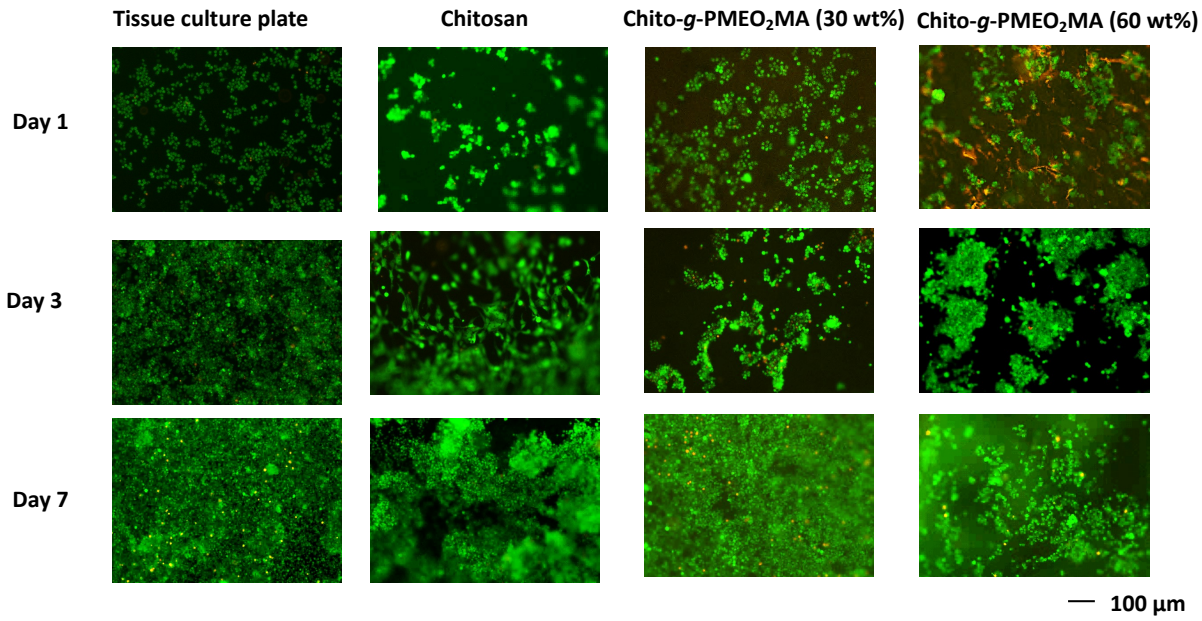

Figure 5-8: RAW264.7 macrophage viability on chitosan, Chito-g-PMEO$_2$MA (30 wt%), Chito-g-PMEO$_2$MA (60 wt%) and TCPS (control). Representative live/dead staining of cells on chitosan films and TCPS at day 1, 3 and 7 days after seeding. Calcein AM stains live cells green, and EthD-1 stains dead cells red.

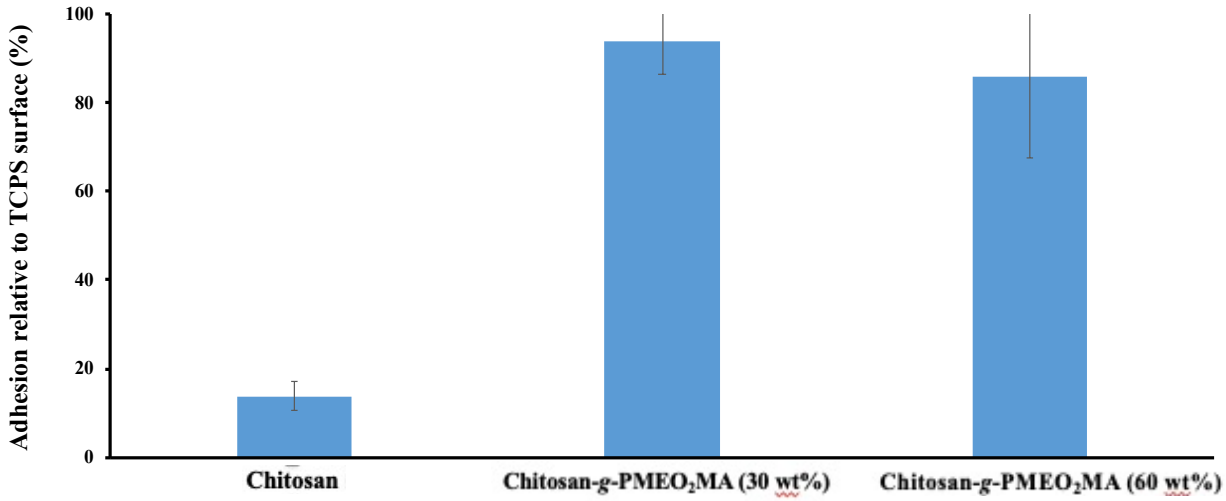

Figure 5-9: XTT assays for the proliferation of macrophage RAW 264.7 on chitosan films relatively to control surface (TCPS).

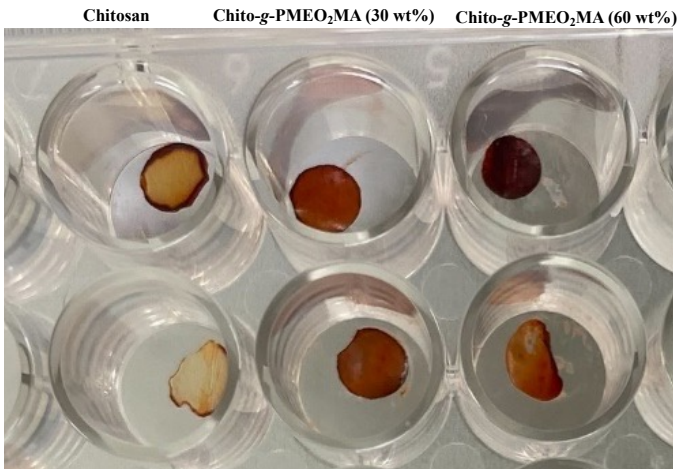

Figure 5-10: Sorption of the dye on the films.

5.4.5.2 Fibroblasts

Fibroblasts are among the most common cell types used in cytotoxicity studies.[27] Chitosan and *O*-carboxymethylchitosan films were found to enhance the adhesion and proliferation of fibroblasts.[28] Cells can attach to the surface via specific adhesion proteins present in fetal bovine serum (FBS), or through direct interactions with chitosan.[28] The poor adhesion of fibroblasts on the chitosan films was reflected in the XTT results (Figure 5-11), where cell proliferation decreased drastically from day 1 to 7. A low number of adherent NIH3T3 fibroblasts were also observed on the chitosan films as compared with TCPS on day 1 after seeding (Figure 5-12, day 1). Despite the low cell densities, the cells appeared to proliferate to some extent on the films and to stay alive over the 7-day culture period. On the modified chitosan films, the adherent NIH3T3 fibroblasts did not display the spindle cell morphology typical for fibroblasts, which was observed on both the unmodified chitosan and TCPS substrates. Therefore while the modified chitosan films were not cytotoxic (no red spots), they were definitely not as biocompatible as for the RAW 264.7 macrophages. Cell adhesion and morphology have been shown to depend on the presence of proteins and the properties of the surface, namely the topography, roughness and stiffness of the material. [26,27] It is currently unclear which of these factors played a role in the poor cell morphology observed on the modified chitosan films.

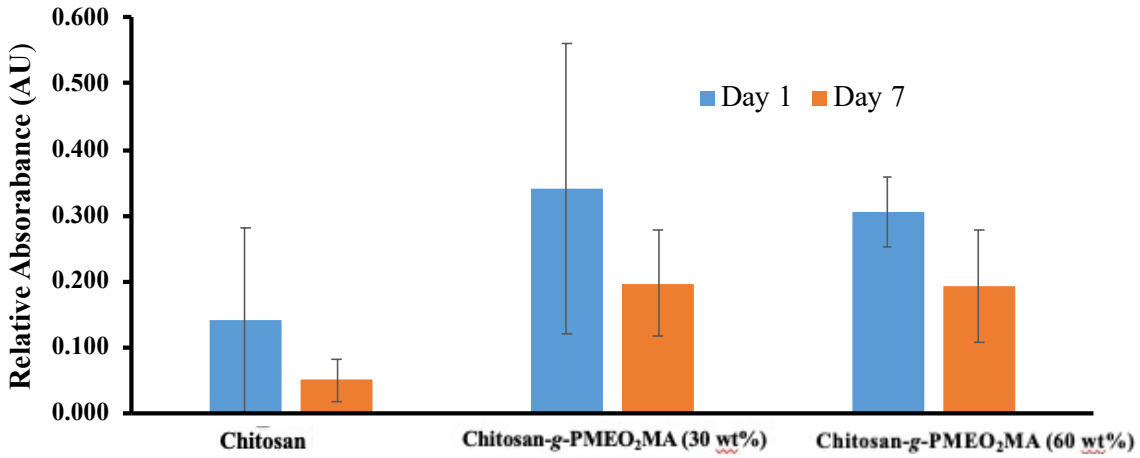

Figure 5-11: XTT assay for proliferation of NIH3T3 cells on modified and unmodified chitosan films.

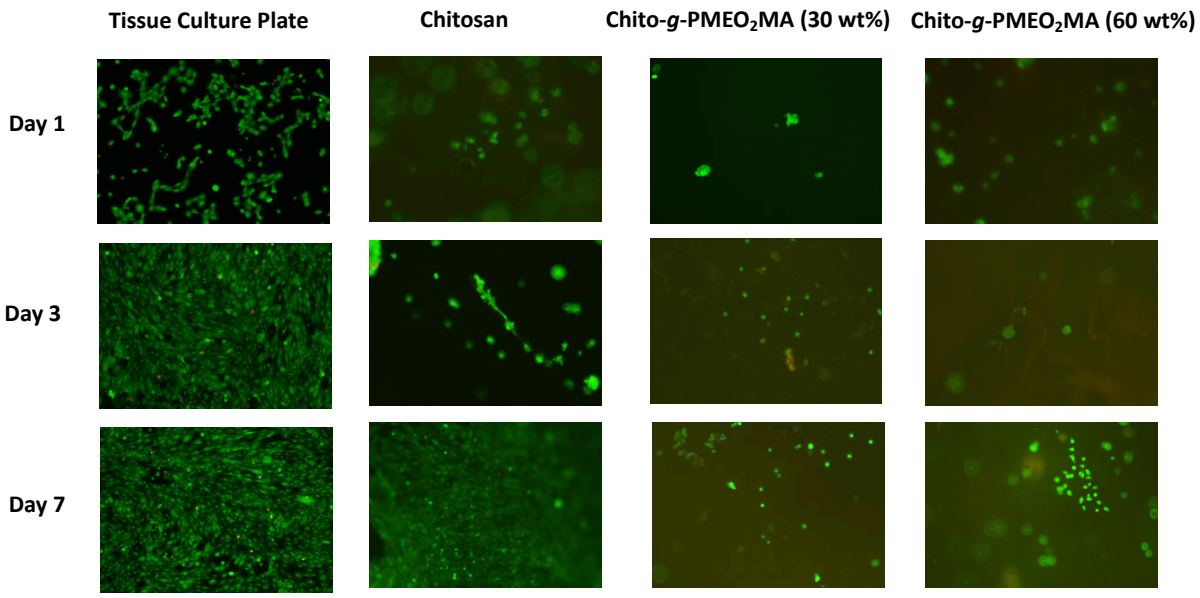

Figure 5-12: Fibroblasts 3T3 viability on chitosan, Chito-g-PMEO$_2$MA (30 wt%), Chito-g-PMEO$_2$MA (60 wt%) and TCPS (control). Representative live/dead staining of cells on chitosan films and TCPS at day 1, 3 and 7 days after seeding. Calcein AM stains live cells green, and EthD-1 stains dead cells red.

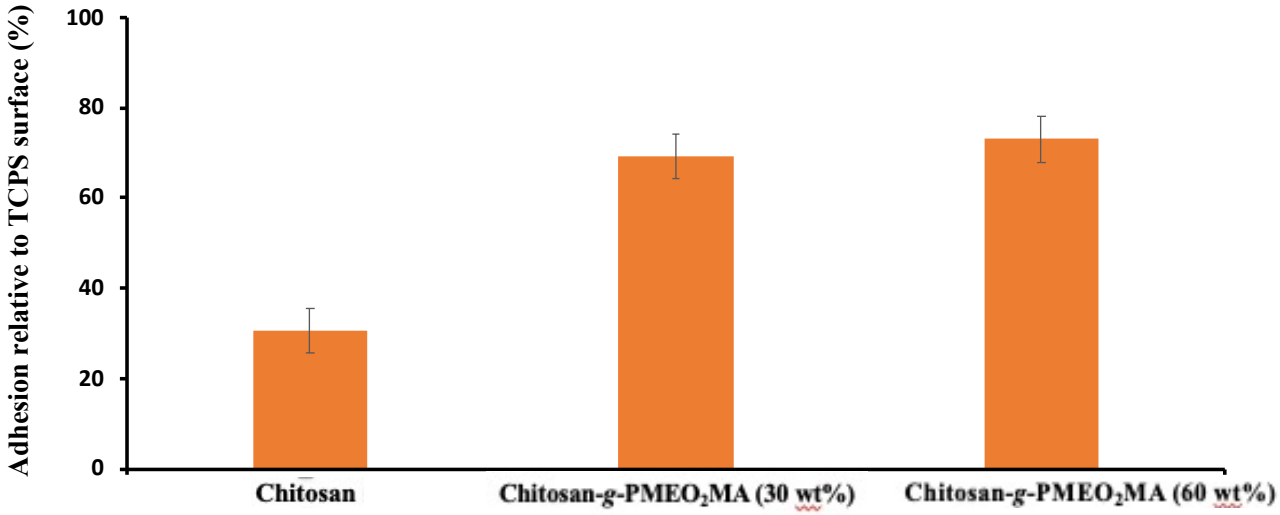

Figure 5-13: XTT assay of fibroblast NHI3T3 adhesion on chitosan films relatively to control surface (TCPS).

5.4.5.3 Human Corneal Epithelial Cells (HCEC)

The HPV-modified human corneal epithelial cell line (HCEC) was selected for cytotoxicity determination because it is highly sensitive to external stresses, such as the presence of undesirable compounds or byproducts on the film surface.[29] This was the reason why FBS was not used to promote cell adhesion and proliferation in the experiments with HCEC. At day 1 after seeding, the modified films had a smaller number of adhering HCEC than the unmodified chitosan films (Figure 5-14, day 3). After 3 days, it appears that the HCEC cells did not proliferate much on the 30 and 60 wt% Chito-*g*-PMEO$_2$MA substrates; in fact, there was a

significant drop in the number of cells for Chito-*g*-PMEO$_2$MA (30 wt%), with a few dead cells (red spots). The unmodified chitosan films, on the other hand, displayed enhanced in cell proliferation over days 1–3. Benhabbour *et al.* studied the effects of hydrophilic hydroxyl-terminated dendrons and PEG on HCEC adhesion to modified gold surface.[30] The authors reported that the presence of oxyethylene moieties in PEG resulted in cell-resistant surfaces, due to the absence of proteins promoting cell adhesion, but when the PEG chains were end-modified with the hydrophilic dendrons, the high density of peripheral hydroxyl groups increased their affinity for HCEC adhesion and proliferation.[30] This may have been the case for the modified chitosan films, where the density of grafted PMEO$_2$MA chains (containing oxyethylene units) on the surface may have reduced the exposure of hydroxyl groups from chitosan, thus reducing the ability for HCEC to adhere and proliferate.

It should be noted that this observation is specific to HCEC, and the biocompatibility of the material differed for other cell lines such as macrophages RAW 264.7 and fibroblasts NHI3T3, as discussed in the previous sections.

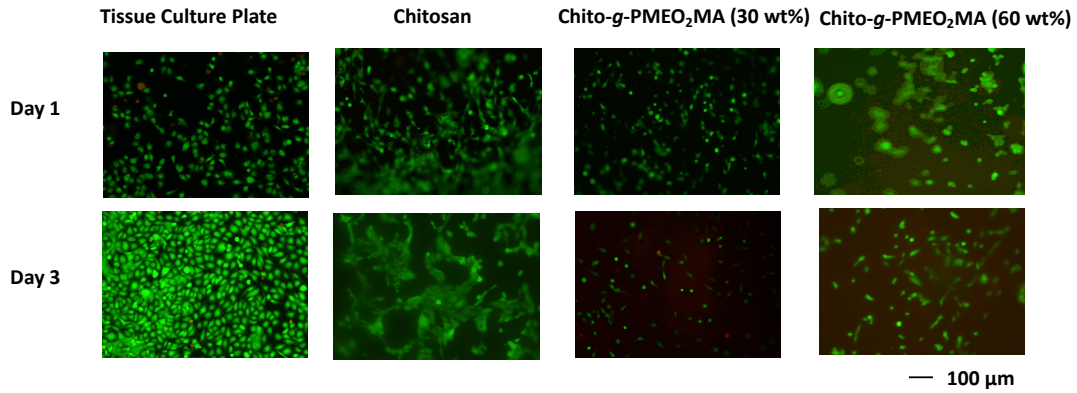

Figure 5-14: HCEC viability on chitosan, Chito-g-PMEO$_2$MA (30 wt%), Chito-g-PMEO$_2$MA (60 wt%) and TCPS (control). Representative live/dead staining of cells on chitosan films and TCPS at day 1 and 3 days after seeding. Calcein AM stains live cells green, and EthD-1 stains dead cells red.

5.4.5.4 Temperature-induced Cell Detachment and Viability

Chen *et al.* synthesized chitosan films grafted with poly(acrylic acid) and PNIPAM to make them thermoresponsive, and examined cell adhesion and detachability with fibroblast cells. The films were found to be non-cytotoxic and allowed cell detachment as the temperature was lowered.[31] Similarly, the modified chitosan films were incubated for 15 min at 2–8 ^{o}C to test their thermoresponsive properties, with the unmodified chitosan film used as control, to determine whether cells would detach from the surfaces upon cooling, be viable and continue to proliferate. These experiments were performed with RAW264.7 (cells detached on day 3 and

day 7) and NIH3T3 (cells detached on day 3). Unfortunately, the chitosan films started disintegrating when they were put in the refrigerator after day 7 of incubation with macrophages RAW 246.7, and thus could not be imaged by fluorescence microscopy. The cells that detached from the films were then cultured on TCPS for 3 days, after which live/dead staining was performed. As seen in Figure 5-15, all the films produced viable cells, with no observable dead cells. Unfortunately it was not possible to obtain quantitative results by the XTT assay, as the chitosan films seemed to adsorb the dye, preventing it from being released in the supernatant. Even though the analysis is only qualitative, it seems that Chito-*g*-PMEO$_2$MA (60 wt%) yielded a larger number of viable cells after day 3 of proliferation than Chito-*g*-PMEO$_2$MA (30 wt%) for both macrophages, and more so for the 3T3 fibroblast cells (Figure 5-15). As discussed earlier, several factors may play a role in the interactions of chitosan with the cells, among which the amino group in chitosan may be important. According to Freier *et al.*, the adhesion of dorsal root ganglion cells on chitosan was reduced as the acetylation level increased.[32] Chitosan with only 0.5% acetyl groups had the highest cell viability, approximately 8 times higher than for chitosan with 11% residual acetyl groups.[32] In the current case, the presence of the PMEO$_2$MA chains likely also have affected cell adhesion and detachment. Since Chito-*g*-PMEO$_2$MA (60 wt%) contained longer polymer chains than Chito-*g*-PMEO$_2$MA (30 wt%), its interactions with the cells via hydrophobic interactions at 37 ^{o}C (above its LCST) should have improved cell adhesion relatively to the shorter PMEO$_2$MA chains in Chito-*g*-PMEO$_2$MA (30 wt%). This would explain why higher cell densities were observed after culturing the cells detached from

Chito-*g*-PMEO$_2$MA (60 wt%). Nevertheless, it should be noted that hydrophobic interactions are just one of the factors responsible for cell adhesion, while other parameters such as fibronectin in FBS[33] and film roughness[26] may also make significant contributions to cell adhesion.

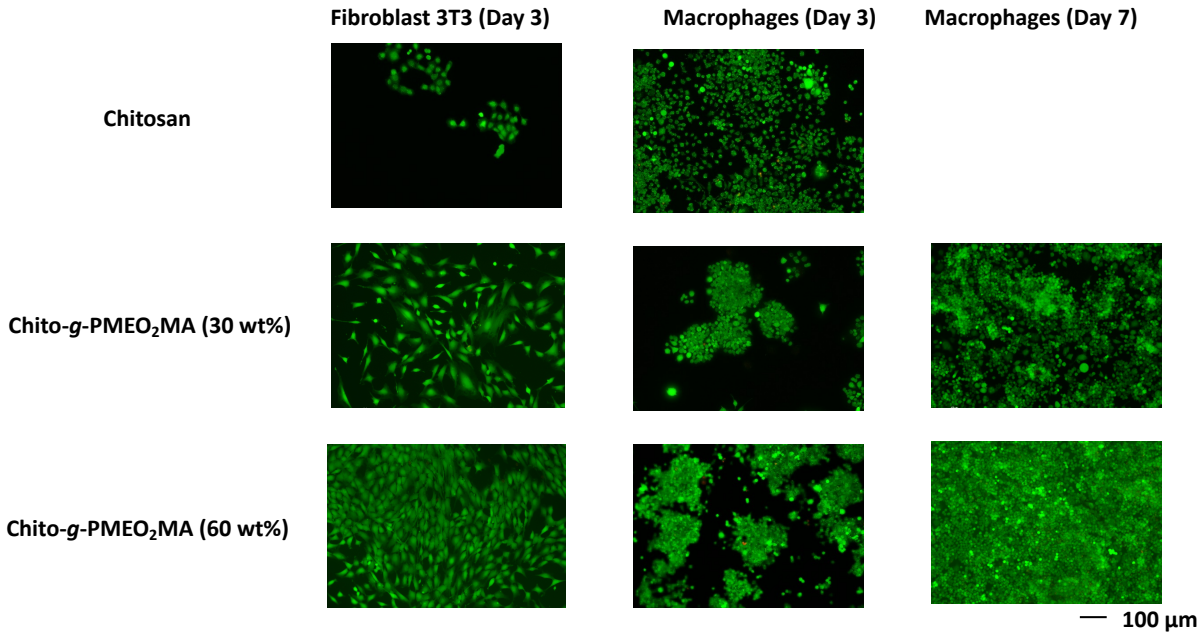

Figure 5-15: Fibroblasts and macrophages detached from chitosan (day 3), Chito-g-PMEO$_2$MA (30 wt%) (day 3 and 7), Chito-g-PMEO$_2$MA (60 wt%) (day 3 and 7) and seeded in on TCPS. Representative live/dead staining of cells on TCPS after 3 days of incubation. Calcein AM stains live cells green, and EthD-1 stains dead cells red.

5.5 Conclusions

RAFT polymerization was successfully applied to the synthesis of PMEO$_2$MA-grafted chitosan films, where the length of the PMEO$_2$MA segments could be tuned by varying the DS of the Chito-RAFT substrate and the monomer content in the reaction. The presence of

$PMEO_2MA$ chains on the surface of the modified chitosan films was confirmed by ATR-FTIR spectroscopy, and contact angle measurements confirmed the thermoresponsive character of the modified films. It was clearly shown, from mass balance calculations, that grafting of the thermoresponsive polymer took place throughout the whole films rather than exclusively on their surface, although the presence of a concentration gradient, with the formation of a $PMEO_2MA$-rich layer at or near the surface would be expected on the basis of reactive RAFT site accessibility in the grafting reaction. Despite the successful grafting of $PMEO_2MA$ on chitosan and the promising preliminary results obtained for cell adhesion, culture and detachment obtained, the characteristics of these films still need to be optimized to improve their performance in the cell culture experiments. Beyond tailoring the characteristics of the films (DS of the substrate, length of the $PMEO_2MA$ chains), heat treatment of the films may also need to be optimized by adjusting the temperature and duration of drying, to control swelling and promote $PMEO_2MA$ grafting predominantly on the surface.

The films were found to be non-toxic to RAW 264.7 macrophages, NIH3T3 fibroblasts and HCEC. While the results are preliminary, Chito-*g*-$PMEO_2MA$ (30 wt%) was found to be most biocompatible for the RAW 264.7 cell line, while cell detachment was apparently easiest for Chito-*g*-$PMEO_2MA$ (60 wt%). The films were designed to allow the detachment of cells as a function of temperature, but the results could not be quantified because chitosan seemed to adsorb the XTT dye. Thus, a more robust method needs to be developed to allow the quantification of cell growth and detachment from the modified chitosan films, so as to better

understand the role of the $PMEO_2MA$ chains grafted on the films in the interactions with the different cell lines.

Chapter 6

Concluding Remarks and Suggestions for Future Work

6.1 Original Contributions to Knowledge

The research presented in this thesis focused on the chemical modification of polysaccharides, specifically starch nanoparticles and chitosan, under aqueous conditions. The modified starch nanoparticles were investigated as amphiphilic polymers in the extraction of bitumen from oil sands, and the modified chitosan as cell culture substrates. Starch was also modified with iron oxide nanoparticles to serve as catalyst in the photo-Fenton degradation of organic pollutants.

6.1.1 Starch Modification with Thermoresponsive Polymer

The first reaction involved modifying the hydroxyl groups of starch nanoparticles (SNPs) with carbon disulfide to obtain xanthated starch, which was subsequently reacted with methyl 2-bromopropionate to form starch-based reversible addition-fragmentation chain transfer (RAFT) agents. While starch has been modified to serve as RAFT agent before,[1] this involved the coupling of a RAFT-active molecule with starch to graft poly(vinyl acetate).[1,2] The strategy developed herein is much simpler and cheaper to implement, in that RAFT-active sites were produced in situ on the starch substrate with simple reagents (CS_2 and methyl 2-

bromopropionate). To synthesize thermoresponsive SNPs, RAFT polymerization was used to attach a thermoresponsive polymer onto the SNP substrates. While PNIPAM is the most widely investigated thermoresponsive polymer due to its lower critical aggregation temperature (LCAT) of 32 ^{o}C,[3] near body temperature, poly(di(ethylene glycol) methyl ether methacrylate) ($PMEO_2MA$) was selected as thermoresponsive polymer in the current investigation. The LCAT of the $PMEO_2MA$ homopolymer is 26 ^{o}C,[4] comparable to PNIPAM. The LCAT behavior of these materials was also tuned for the first time by adding a block of hydrophilic poly(2-hydroxyethyl acrylate), and the resulting materials were found to maintain improved water dispersibility at high temperatures. Moreover, while PNIPAM was found to display hysteresis in the coil-globule transition occurring at the LCAT, $PMEO_2MA$ exhibited more gradual thermal transitions and better reversibility than PNIPAM.[5]

To investigate the efficiency of the functionalization reaction, RAFT agents with degrees of substitution (DS) ranging from 0.012 to 0.06 were synthesized. One strategy examined to graft $PMEO_2MA$ in a controlled manner was to react RAFT agents with different DS with a set amount of monomer, whereas the second approach involved varying the quantity of monomer added to a starch-based RAFT agent with a set DS. The RAFT agents were found to be highly effective, in that they enabled grafting of $PMEO_2MA$ on the SNPs with ~ 100% efficiency in 1 hour. This approach was found to be very effective to control the characteristics of the SNP-*g*-$PMEO_2MA$ obtained. The $PMEO_2MA$ chains were cleaved from the SNPs using H_2O_2 to generate ·OH radicals as powerful oxidant. GPC analysis of the cleaved chains revealed that as the DS of the

RAFT substrate used for the synthesis of SNP-*g*-$PMEO_2MA$ (15%) was reduced from 0.022 to 0.012, the apparent M_n for the cleaved chains increased from 43.3 to 58.6 kg/mol. When the monomer content was increased from 15 to 30% by weight at a constant DS of 0.022, the apparent M_n of the chains increased from 30.8 to 57.5 kg/mol. This clearly confirmed that due to the presence of fewer RAFT initiating sites, a drop in DS or an increase in monomer content in the reaction both increased grafted polymer chain length. This was also confirmed by dynamic light scattering (DLS) and UV-visible measurements, where the SNP-*g*-$PMEO_2MA$ systems with longer $PMEO_2MA$ chains displayed lower LCAT values. All the samples, except for SNP-*g*-$PMEO_2MA$ with DS 0.06, had good water dispersibility at temperatures both below and above their LCAT, as no macrophase separation was observed.

To demonstrate further control over the solution properties of the SNP-*g*-$PMEO_2MA$ systems, a hydrophilic PHEA block forming a corona outside the molecules was added to decrease aggregation of the modified SNPs above their LCAT. The UV-vis transmission measurements indeed confirmed that PHEA improved the dispersibility of the SNP-*g*-$PMEO_2MA$ above their LCAT, as the turbidity was lowered at high temperatures.

Overall, the results obtained clearly demonstrated that the characteristics of these novel thermoresponsive SNPs could be tuned by varying their DS and monomer content, and the addition of hydrophilic PHEA segments, which provided a simple handle to control of the hydrophilic-lipophilic balance in these thermoresponsive SNPs.

6.1.2 Thermoresponsive SNPs for Bitumen Extraction from Oil Sands

In a former investigation, Yang *et al.* demonstrated the extraction of bitumen from Imperial Oil oil sands (IOos) using thermoresponsive PEG-*g*-$PMEO_2MA$ block copolymers in the presence of a small amount of toluene as diluent.[4] The IOos sample used had a bitumen content of 11.1±0.1 wt% and no detectable amount of fines. Above its LCAT, amphiphilic PEG-*g*-$PMEO_2MA$ formed polymeric micelles, with the hydrophobic $PMEO_2MA$ segments in their core and a hydrophilic PEG shell. It was postulated that the hydrophobic $PMEO_2MA$ segments above the LCAT interacted with bitumen droplets, shuttling them through the water phase to reach the air-water interface. The PEG-*g*-$PMEO_2MA$ became mostly soluble in the water phase when the mixture was cooled again, potentially allowing its reuse in the extraction process. The sand mixture settled at the bottom of the vial, while the bitumen and toluene floating on top of the water could be separated from the mixture. This procedure with PEG-*g*-$PMEO_2MA$ worked well with the low-fines IOos sample, but not with high-fines Athabasca Sand Bank Oil Sands (SBos).

The SNP-*g*-$PMEO_2MA$ samples used in this project had similarities to PEG-*g*-$PMEO_2MA$, in that the hydrophilic PEG core of the micelles was substituted with a hydrophilic SNP substrate. The thermoresponsive SNPs are cost-effective materials since the SNP substrates are inexpensive, whereas the synthesis of PEG-*g*-$PMEO_2MA$ is relatively costly and impractical to implement industrially. As discussed above, the characteristics and the LCAT of the SNP-*g*-$PMEO_2MA$ samples could be tailored by varying the DS or the composition of the modified SNPs, and the impact of these parameters on bitumen extraction was examined. The SNP-*g*-

$PMEO_2MA$ samples were tested on SBos with a bitumen content of 10.5±0.2 wt% and a fines content of 2 wt%. Fines have been shown to impede extraction by adhering to the bitumen droplets and preventing them from floating to the surface.[6] It has been shown that this problem could be solved by adding 0.5 M NaCl to the aqueous phase, which precipitates the fines and allows polymeric surfactants to interact with the bitumen component.[7] This approach was used for the bitumen extractions with SNP-*g*-$PMEO_2MA$ as thermoresponsive surfactant, by carrying out the extractions on a 1-g oil sand sample scale in an oven at 45 °C, by tumbling the oil sand mixtures in 20 mL vials. This temperature is much lower than in conventional extraction methods, where the water temperature can reach up to 80 °C.[8] Toluene was used as diluent to enhance the interactions of bitumen with SNP-*g*-$PMEO_2MA$ in solution. It was demonstrated with ANOVA analysis that toluene played a significant role in bitumen extraction, and that a large increase in toluene can extract essentially all the bitumen from oil sands. However, since excessive usage of organic solvents can be hazardous to the environment, but necessary to facilitate transport of the bitumen, 60 mg of toluene were conservatively used in the extraction process. The SNP-*g*-$PMEO_2MA$ (15%, DS 0.022) sample was shown to perform the best among the SNP-*g*-$PMEO_2MA$ compositions examined. Within experimental error limits, for 1 g of oil sand mixtures, 15 mL of a solution containing 1.25 mg/mL SNP-*g*-$PMEO_2MA$ (15%, DS 0.022) and 0.5 M NaCl, in combination with 60 mg of toluene, could extract ~ 80% of the bitumen from tar sands in the presence of fines. The aqueous solution recovered after cooling, when utilized for four extraction cycles, displayed a decrease in extraction to 54% by the 4^{th} cycle. The

extraction efficiency increased significantly when 0.25 mg/mL of SNP-*g*-PMEO$_2$MA (15%, DS 0.022) was added to the 3rd and 4th cycles, however, suggesting that the loss of polymer-grafted SNPs was the cause of the decline in extraction efficiency.

Furthermore, it was shown that the SNP-*g*-PMEO$_2$MA polymeric surfactants were highly effective at extracting bitumen from IOos, that had no detectable fines. For 1 g of IOos, 50 mg of toluene, and 15 mL of 1 mg/mL SNP-*g*-PMEO$_2$MA (15%, DS 0.022) solution, an extraction efficiency of 86±4% was attained. As compared with the SBos samples, the extraction of bitumen from IOos did not require any NaCl addition due to the absence of fines, and a higher extraction efficiency was achieved with lower amounts of toluene (50 mg).

The bitumen extraction procedure developed using the novel SNP-*g*-PMEO$_2$MA thermoresponsive surfactants therefore represents an interesting alternate method for the treatment of oil sands, due to the low cost of the surfactants, the high efficiency of the extraction process, and the ability to recycle the water used.

6.1.3 Starch-stabilized Iron ($Fe^{2+/3+}$) Oxide Nanoparticles for the Photocatalytic Degradation of Methylene Blue

The homogeneous photo-Fenton reaction only uses $Fe^{(2+/3+)}$, H_2O_2, and UV light under acidic conditions to generate hydroxyl radicals capable of degrading water contaminants such as dyes, pesticides and pharmaceuticals.[9,11] The main drawback of that reaction is that the solubility

of iron ions and H_2O_2 decreases when the pH increases above 3, which makes the Fenton process strongly pH-dependent. It also leads to the generation of iron sludge above pH 3 due to the formation of oxohydroxide species.[12] While different catalyst supports such as zeolites,[13] clays,[14] chitosan beads[15] and polymers including polyethylene, polypropylene, poly(methyl methacrylate) and polystyrene[16] have been shown to improve the stability of iron nanoparticles (NPs) in aqueous media above pH 3, starch was selected for this thesis work as an inexpensive alternate stabilizer for iron oxide NPs. Starch being hydrophilic, it improved the stability of iron ($Fe^{2+/3+}$) oxide NPs, increasing the surface area of the iron species and improving their dispersion in water.

Two different protocols were examined to combine the starch stabilizer with iron oxide nanoparticles. An in situ method involved the preparation of iron NPs in the presence of starch (Starch St-Fe NPs), while starch was introduced after the synthesis of the iron NPs in the ex situ method (Starch Fe-St NPs). These particles were used as photo-Fenton catalysts in the degradation of methylene blue (MB) at pH 4. Both sets of particles were characterized by ^1H nuclear magnetic resonance (NMR), DLS, and transmission electron microscopy (TEM) which confirmed the presence of starch and iron NPs. Since starch also contributed to the consumption of ·OH radicals during the reaction, catalysts were synthesized with lower amounts of starch to enhance the effectiveness of the Fenton reaction, while at the same time maintaining good dispersibility of the iron NPs in aqueous media.

The H_2O_2 : Fe ratio, which is a key parameter in the Fenton reaction, was optimized for ratios ranging from 0.91 to 3.64. The Fenton reaction comprises several reaction steps that are crucial in determining the optimal H_2O_2 : Fe ratio. All four catalysts were capable of degrading MB at concentrations up to 32 mg/L, with 100 mg Starch Fe-St NPs requiring only 32.4 µmol/L of Fe and 90 µmol/L H_2O_2. When 99 µmol Fe/L and 360 µmol/L H_2O_2 were used, the 300 mg Starch St-Fe system remained active in the degradation for up to seven aliquots of 4 mg/L MB in successive additions, demonstrating catalyst reusability. This showed that the in situ approach may successfully contribute to iron NP stability, allowing the catalyst to be reused for numerous cycles of MB degradation. Total organic content (TOC) measurements were conducted to quantify the extent of mineralization achieved with these catalysts. For example, Zhou *et al.* were able to degrade 50 mg/L of MB with 65% mineralization by using 17.9 mmol/L of Fe and 29.4 mmol/L H_2O_2 at pH 4 with a paper sludge-derived heterogeneous catalyst in 80 minutes.[17] For comparison, the 100 mg Starch St-Fe catalyst, found to be the best performing catalyst, could mineralize up to 70% of 4 mg/L MB under UV irradiation at pH 4 when using only 32.4 µmol Fe/L and 90 µmol/L H_2O_2. Therefore using a 12.5-fold lower concentration in MB, a 552-fold lower concentration of Fe yielded similar mineralization levels with our system. The TOC results were in agreement with the UV-visible measurements. For the 300 mg Starch Fe-St catalyst, the percent mineralization decreased drastically from 39% to 8.2% as the Fe and H_2O_2 concentration was doubled. This illustrates the fact that not only the H_2O_2 : Fe ratio, but also variations in starch and MB concentrations may affect the kinetics of the Fenton reaction. The catalysts were

shown to be stable under acidic conditions over a pH range of 2-5, implying that Fe^{3+} ions were well-coordinated with starch and did not leach out, as confirmed by UV-visible analysis.

The results obtained in this portion of the thesis demonstrated the preparation of starch-stabilized iron oxide nanoparticles, and their use as photo-Fenton catalysts offering interesting features in comparison with previously reported systems, namely a high activity even at pH 4, which represents a 10- to 100-fold decrease in acid content in comparison with typical conditions for these reactions.

6.1.4 Thermoresponsive Chitosan for Cell Culture

To date, chitosan-based RAFT agents have only been prepared by introducing fairly exotic (and expensive) RAFT-active groups such as S-1-dodecyl-S''-(α,α'-dimethyl-α''-acetic acid) trithiocarbonate and S,S′-bis(R,R′-dimethyl-R″-acetic acid) trithiocarbonate in chitosan to graft poly(acrylic acid) and poly(N-(2-hydroxyethyl)prop-2-enamide), respectively.[18,19] A much simpler and cheaper method was developed in this work, namely the modification of chitosan films into RAFT agents using carbon disulfide and methyl 2-bromopropionate. $PMEO_2MA$ chains were then grafted on the films by RAFT polymerization, thus making the chitosan surface thermoresponsive. FTIR analysis confirmed the formation of RAFT sites on the films, and the grafting of $PMEO_2MA$, by the presence of a OC=O carbonyl ester stretch band at 1728 cm^{-1}. In comparison with the SNPs in Chapter 2, $PMEO_2MA$ grafting on chitosan was less efficient, with 29–40% grafting for a reaction time of 2 hours, and some ungrafted chains remaining in solution.

Control over the chain length and the film composition were demonstrated by GPC analysis after cleaving the chains by refluxing with 1 M HCl. The $PMEO_2MA$ chains cleaved from Chito-*g*-$PMEO_2MA$ (60 wt%) had an apparent M_n = 128 kg/mol (PDI = 1.80), while the ungrafted chains in solution had an apparent M_n = 135 kg/mol (PDI = 1.62). Good control over the $PMEO_2MA$ chain length was demonstrated, as shorter chains were obtained when the target DS of the RAFT-functionalized film was increased (to introduce a larger number of reaction sites), or when the monomer content in the reactions was decreased. The swelling index (SI), which quantifies film swelling, was found to decrease as the grafted $PMEO_2MA$ content increased. From a comparison of the film thickness increase for the modified films with the fully extended chain length R calculated[20] for the cleaved chains, it was clear that grafting of $PMEO_2MA$ occurred throughout the films as opposed to exclusively on their surface. It nevertheless seems reasonable that since the reactions were carried out under heterogeneous conditions, increased accessibility to the monomers of RAFT sites at or near the surface would promote the grafting reaction at the expense of the interior of the films.

The hydrophobicity of $PMEO_2MA$-grafted chitosan films above the lower critical solution temperature (LCST) of $PMEO_2MA$ was investigated with contact angle measurements. An increase in contact angle was observed for Chito-*g*-$PMEO_2MA$ at 15, 30, and 60 wt% $PMEO_2MA$ when the temperature was raised from 22 ^oC to 40 ^oC. A similar observation was made for $PMEO_2MA$ homopolymer films cast on a glass slide.

The novel grafting technique reported herein therefore appears promising for the development of temperature-responsive cell culture substrates, as the characteristics of the films ($PMEO_2MA$ grafted chain density and length) can be controlled conveniently and using inexpensive reagents.

Modified chitosan films have been investigated as cell culture substrates on a few occasions. For example, Kato *et al.* used hydroxybutyl-modified chitosan films spin-coated on tissue culture plate (TCPS) and tested them for normal human dermal fibroblasts cell growth, proliferation and detachment, while Nie *et al.* tested chitosan grafted with PNIPAM for the adhesion and detachment of mouse fibroblast cells (L929) as a function of temperature.[21,22] Similarly, the thermoresponsive Chito-*g*-$PMEO_2MA$ films were tested as cell culture substrates for the RAW 264.7, NIH3T3 fibroblasts and HCEC cell lines in this thesis work. While the results obtained are very preliminary, Chito-*g*-$PMEO_2MA$ (30 wt%) was found to be biocompatible for macrophages RAW 264.7, but not as much for 3T3 fibroblasts or HCEC cells, even though neither the modified nor the unmodified films were cytotoxic to any of the cell lines. The thermoresponsive behavior was evaluated for the Chito-*g*-$PMEO_2MA$ (30 wt%) and Chito-*g*-$PMEO_2MA$ (60 wt%) films, and more cells were found to proliferate on standard TCPS after detachment from Chito-*g*-$PMEO_2MA$ (60 wt%). However, it should be emphasized that hydrophobic interactions are only one of the factors contributing to cell adhesion, and that other important parameters include the presence of fibronectin in FBS[23] and film roughness,[24] beyond the density and length of the thermoresponsive $PMEO_2MA$ chains on the surface of the films.

Despite this, the fact that the films were found to be non-cytotoxic to cells, and that cells could be successfully detached from the films when the temperature was lowered, are encouraging results deserving further investigation.

6.2 Suggestions for Future Work

The synthetic techniques described in this thesis are environmentally friendly because they are carried out in aqueous media, and the final products do not require complex purification processes. The modified polysaccharides may be reusable in each of the three applications described above. Nevertheless, the following suggestions might provide a better understanding of these systems, and possibly improve their effectiveness in the desired applications, or may pave the way to other applications for these materials.

6.2.1 Measurement of the Absolute M_n of the cleaved $PMEO_2MA$ chains

The $PMEO_2MA$ chains cleaved from the SNPs and chitosan were analyzed by GPC in Chapters 2 and 5, respectively. The absolute M_n of the cleaved chains was not determined, since the GPC system using DMF as eluent lacked a laser light scattering detector. A GPC instrument operating with DMSO, equipped with a laser light scattering detector, was also used to analyze the cleaved chains, but unfortunately the signal was too noisy as there was minimal light scattering under these conditions. Consequently, the absolute M_n could not be measured. The

grafting density of $PMEO_2MA$ chains on SNP and on chitosan can be determined if the absolute M_n of the chains is available, to provide a better understanding of the $PMEO_2MA$-grafted SNP and chitosan systems. This could be achieved by using DMF as mobile phase on the GPC instrument with the light scattering detector.

6.2.2 Scaling up Bitumen Extraction from Oil Sands

The current investigations were carried on a 1-g scale for the oil sands. This was attempted to understand the influence of the characteristics of the $PMEO_2MA$-grafted SNPs in the extraction of bitumen from oil sands. The conditions were optimized using 1 g of oil sands in 61 mm × 28 mm screwcap vials, with a maximum volume of 20 mL. The next step in the investigation would be to conduct oil extractions on a larger scale. The optimal conditions such as the composition and concentration of SNP-*g*-$PMEO_2MA$, salt, and toluene amount were determined in Chapter 3 for 1-g oil sand samples and may serve as a starting point to conduct extractions on a larger scale. The main challenge would be to design a bitumen extraction rotary drum similar to that used in the industry, which should hold a temperature of 45 ^oC and rotate at a constant speed over 24 hours. The dimensions and the rotating speed of the drum may be key parameters for efficient mixing of the oil sands with the SNP-*g*-$PMEO_2MA$ solution and toluene, so that the grafted $PMEO_2MA$ chains can interact with the bitumen component above the LCAT for efficient extraction. As Yue *et al.* pointed out, optimizing the rotary drum operating

conditions for bitumen extraction, such as the drum speed and inclination, as well as the internal and end-plate design of the drum, may be important to achieve high extraction efficiencies.[25]

6.2.3 SNP-*g*-PMEO$_2$MA as a Polymeric Flocculant for Mature Fine Tailings

Zheng *et al.* used thermoresponsive hydroxybutylated corn starch with LCST values ranging from 36 to 45 ^{o}C as flocculant for oil sands mature fine tailings.[26] Above their LCST, these starch-based thermoresponsive surfactants were found to be efficient flocculants. It was suggested that as it became hydrophobic over its LCST, the modified corn starch absorbed clay particles on its surface, causing it to flocculate due to hydrophobic interactions.[26] Likewise, Li *et al.* tested tailings settling with PNIPAM and obtained fast initial settling rates, reduced solution turbidity, and more condensed sediments.[27] PMEO$_2$MA has thermoresponsive properties comparable to PNIPAM, but it is also more environmentally friendly. The SNP-*g*-PMEO$_2$MA particles, in the form of a polymeric surfactant with a large weight fraction of grafted PMEO$_2$MA by weight, might be an interesting alternative for the settlement of mature fine tailings.

6.2.4 Developing a Method to Determine the TOC of Partially Degraded MB

The total organic content (TOC) of the degraded MB solutions and of a blank (without MB) were determined to calculate the percent mineralization of MB. It was not possible to inject

partially degraded samples into the TOC analyzer, as MB would have stained the tubing inside the instrument. Tubing with a hydrophilic coating on its interior would ensure that MB does not adsorb on its surface and stain it. It was shown by UV-visible spectroscopy that 300 mg Starch Fe-St NPs could discolor up to seven aliquots of 4 mg/L MB. It would be insightful to determine the percent mineralization of MB at each step of the experiment, and then compare it with the performance of the other three catalysts which could degrade up to 3 aliquots of 4 mg/L MB. Commonly used silicon tubing may be made hydrophilic by flowing an aqueous solution of sodium or ammonium hydroxide through it for a while, followed by rinsing copiously with water.[28] This procedure hydrolyzes some of the Si-O-Si or Si-C bonds and replaces them with Si-OH groups, making the material less hydrophobic.[28] The concentration of NaOH, and the duration of the treatment are critical, as long exposures to high NaOH concentrations may damage the tubing.

6.2.5 Optimizing the Synthesis of Chitosan Films for Surface Modification

The chitosan films obtained in the current work had a relatively high swelling index (SI), in that they swelled by more than 150 percent of their dry weight in some cases. Because the reactions took place in water, such high SI values suggest that the reaction may also be taking place inside the chitosan films as well as on their surface. Murray *et al.*, who produced chitosan films from 5% acetic acid solutions, discovered that heating (annealing) the films between 150 and 200 ^{o}C reduced swelling, while increasing their degree of acetylation.[29] It was suggested that

during drying at high temperatures, the chitosan films underwent molecular alterations and partial reacetylation, turning chitosan into a more chitin-like substance.[29] In the current investigation, excessive heating for an extended time period caused the films to become rough and brittle, reduced swelling, and made it harder to conduct the reactions in water. Cell growth on previously dried-out films also proved challenging. Consequently, it seems that the chitosan films should be handled carefully, by partial drying under optimized conditions, so as to minimize swelling and allow the grafting reaction to take place mostly on the surface, while still being flexible enough to be rehydrated and used for cell culture. This could be achieved by experimenting with various heat treatment temperatures and durations, until ideal film characteristics are found.

6.2.6 Developing a Better Method to Quantify Cell Growth on the Films and Temperature-induced Cell Detachment

The number of live cells on the surface of the films was determined by the XTT technique. In the presence of metabolic activity, XTT is transformed into a colorful formazan dye which is easily quantified in the cellular supernatant, as it is water-soluble.[30] This is crucial in biofilm research, since it enables the study of whole biofilms, as well as the testing of biofilm drug susceptibility without disrupting the biofilm structure. Unfortunately, the formazan dye was sorbed by the chitosan films, making its removal exceedingly difficult. The films were also washed with DMSO in an attempt to disperse the formazan in solution, but this approach failed.

MTT, which is similar to XTT, was also used, but the findings were similar since the formazan dye was likewise sorbed by the films.[31] The ATP concentration and DNA synthesis assays are two alternate techniques to determine cell proliferation.[32,33] There is no ATP in dead cells, and there is a linear relationship between the concentration of ATP in cell lysates and the number of cells in a sample. In the presence of ATP, bioluminescent luciferase and its substrate luciferin produce luminescence with an intensity proportional to the ATP concentration.[32] In the laboratory, DNA synthesis assays are most accurate and reliable to quantify cell growth. Radiolabeled 3H-thymine is usually incubated with the cells for many hours or overnight.[33] The radiolabels are incorporated into the DNA of newly proliferating cells, which may then be quantified with a scintillation counter after elution.[33] Thymidine (3H-TdR) has the benefits of providing accurate and repeatable results, in addition to being extremely sensitive.[34] Scintillation counters, on the other hand, are both costly and time-consuming. Another obvious disadvantage is that handling radioactive materials is difficult and dangerous.

The cells were detached from the films, cultured on a TCPS, and then analyzed by fluorescence microscopy after 3–7 days. Quantifying the cells remaining on the films after detachment would also be informative if, as previously mentioned, a quantitative method to determine cell growth on the films can be devised.

References

Chapter 1

(1) Ellis, R. P.; Cochrane, M. P.; Dale, M. F. B.; Duffus, C. M.; Lynn, A.; Morrison, I. M.; Prentice, R. D. M.; Swanston, J. S.; Tiller, S. A. Starch Production and Industrial Use. *Journal of the Science of Food and Agriculture* **1998**, *77* (3), 289–311.

(2) Mostafa, K. M.; El-Sanabary, A. A. Carboxyl-Containing Starch and Hydrolyzed Starch Derivatives as Size Base Materials for Cotton Textiles. *Polymer Degradation and Stability* **1997**, *55* (2), 181–184.

(3) Karsa, D. R. *Industrial Applications of Surfactants IV*. **1999**, (No. 230).

(4) Rinaudo, M. Chitin and Chitosan: Properties and Applications. *Progress in Polymer Science* **2006**, *31* (7), 603–632.

(5) Morin-Crini, N.; Lichtfouse, E.; Torri, G.; Crini, G. Applications of Chitosan in Food, Pharmaceuticals, Medicine, Cosmetics, Agriculture, Textiles, Pulp and Paper, Biotechnology, and Environmental Chemistry. *Environmental Chemistry Letters* **2019**, *17* (4), 1667–1692.

(6) Bégin, A.; Van Calsteren, M. R. Antimicrobial Films Produced from Chitosan. *International Journal of Biological Macromolecules* **1999**, *26* (1), 63–67.

(7) Souza, V. G. L.; Pires, J. R. A.; Rodrigues, C.; Coelhoso, I. M.; Fernando, A. L. Chitosan Composites in Packaging Industry-Current Trends and Future Challenges.

Polymers **2020**, *12* (2), 417.

(8) Doberenz, F.; Zeng, K.; Willems, C.; Zhang, K.; Groth, T. Thermoresponsive Polymers and Their Biomedical Application in Tissue Engineering-A Review. *Journal of Materials Chemistry B* **2020**, *8* (4), 607–628.

(9) Abu-Lail, N. I.; Camesano, T. A. Polysaccharide Properties Probed with Atomic Force Microscopy. *Journal of Microscopy* **2003**, *2012* (3), 217–238.

(10) Lin, N.; Huang, J.; Dufresne, A. Preparation, Properties and Applications of Polysaccharide Nanocrystals in Advanced Functional Nanomaterials: A Review. *Nanoscale* **2012**, *4* (11), 3274–3294.

(11) Whelan, W. J. Recent Advances in the Biochemistry of Glycogen and Starch. *Nature* **1961**, *190* (4780), 954–957.

(12) Flieger, M.; Kantorová, M.; Prell, A.; Řezanka, T.; Votruba, J. Biodegradable Plastics from Renewable Sources. *Folia Microbiologica* **2003**, *48* (1), 27–44.

(13) Baird, J. K.; Sandford, P. A.; Cottrell, I. W. Industrial Applications of Some New Microbial Polysaccharides. *Bio/Technology* **1983**, *1* (9), 778–783.

(14) Staroszczyk, H.; Ciesielski, W.; Tomasik, P. Starch–Metal Complexes and Metal Compounds. *Journal of the Science of Food and Agriculture* **2018**, *98* (8), 2845–2856.

(15) Szejtli, J. Introduction and General Overview of Cyclodextrin Chemistry. *Chemical Reviews* **1998**, *98* (5), 1743–1753.

(16) Ravi Kumar, M. N. V. A Review of Chitin and Chitosan Applications. *Reactive and*

Functional Polymers **2000**, *46* (1), 1–27.

(17) Sharma, N.; Chang, L. P.; Chu, Y. L.; Ismail, H.; Ishiaku, U. S.; Mohd Ishak, Z. A. Study on the Effect of Pro-Oxidant on the Thermo-Oxidative Degradation Behaviour of Sago Starch Filled Polyethylene. *Polymer Degradation and Stability* **2001**, *71* (3), 381–393.

(18) Di Donato P., Poli A., Taurisano V., N. B. Polysaccharides: Applications in Biology and Biotechnology/Polysaccharides from Bioagro-Waste New Biomolecules-Life. *Polysaccharides* **2014**, 1–29.

(19) Kyzas, G. Z.; Deliyanni, E. A. Mercury(II) Removal with Modified Magnetic Chitosan Adsorbents. *Molecules* **2013**, *18* (6), 6193–6214.

(20) Renault, F.; Sancey, B.; Badot, P. M.; Crini, G. Chitosan for Coagulation/Flocculation Processes - An Eco-Friendly Approach. *European Polymer Journal* **2009**, *45* (5), 1337–1348.

(21) Moad, G. Chemical Modification of Starch by Reactive Extrusion. *Progress in Polymer Science* **2011**, *36* (2), 218–237.

(22) Le Corre, D.; Bras, J.; Dufresne, A. Starch Nanoparticles: A Review. *Biomacromolecules* **2010**, *11* (5), 1139–1153.

(23) Wang, S.; Copeland, L. Molecular Disassembly of Starch Granules during Gelatinization and Its Effect on Starch Digestibility: A Review. *Food & Function* **2013**, *4* (11), 1564–1580.

(24) Gallant, D. J.; Bouchet, B.; Baldwin, P. M. Microscopy of Starch: Evidence of a New Level of Granule Organization. *Carbohydrate Polymers* **1997**, *32* (3–4), 177–191.

(25) Pérez, S.; Bertoft, E. The Molecular Structures of Starch Components and Their Contribution to the Architecture of Starch Granules: A Comprehensive Review. *Starch-Stärke* **2010**, *62* (8), 389-420.

(26) Tomasik, P.; Schilling, C. H. Chemical Modification of Starch. *Advances in Carbohydrate Chemistry and Biochemistry* **2004**, *59*, 175–403.

(27) Le Corre, D.; Angellier-Coussy, H. Preparation and Application of Starch Nanoparticles for Nanocomposites: A Review. *Reactive & Functional Polymers* **2014**, *85*, 97–120.

(28) Péret, E. E.; Breene, W. M.; Bahnassey, Y. A. Gelatinization Profiles of Peruvian Carrot, Cocoyam and Potato Starches as Measured with the Brabender Viscoamylograph, Rapid Visco-Analyzer, and Differential Scanning Calorimeter. *Starch-Stärke* **1998**, *50* (1), 14–16.

(29) Cioica, N.; Fechete, R.; Cota, C.; Nagy, E. M.; David, L.; Cozar, O. NMR Relaxation Investigation of the Native Corn Starch Structure with Plasticizers. *Journal of Molecular Structure* **2013**, *1044*, 128–133.

(30) Zhang, Y.; Rempel, C.; Liu, Q. Thermoplastic Starch Processing and Characteristics-A Review. *Critical Reviews in Food Science & Nutrition* **2014**, *54* (10), 1353–1370.

(31) Kirby, A. R.; Clark, S. A.; Parker, R.; Smith, A. C. The Deformation and Failure Behaviour of Wheat Starch Plasticized with Water and Polyols. *Journal of Material*

Science **1993**, *28* (21), 5937–5942.

(32) Sandhu, K. S.; Nain, V. Starch Nanoparticles: Their Preparation and Applications. *Plant Biotechnology: Recent Advancements and Developments* **2017**, 213–232.

(33) Song, D.; Thio, Y. S.; Deng, Y. Starch Nanoparticle Formation via Reactive Extrusion and Related Mechanism Study. *Carbohydrate Polymers* **2011**, *85* (1), 208–214.

(34) Liu, D.; Wu, Q.; Chen, H.; Chang, P. R. Transitional Properties of Starch Colloid with Particle Size Reduction from Micro- to Nanometer. *Journal of Colloid and Interface Science* **2009**, *339* (1), 117–124.

(35) Giezen, F.E.; Jongboom, R.O.J.; Feil, H.; Gotlieb, K.F.; Boersma, A. Biopolymer nanoparticles. South Korea Patent KR100451527B1, **2000**.

(36) Tseitlin, A.; Alstyne, D.A.; Bloembergen, S. Curable biopolymer nanoparticle latex binder for mineral, natural organic, or synthetic fiber products and non-woven mats. United States Patent US20120309246A1, **2000**.

(37) Ma, X.; Jian, R.; Chang, P. R.; Yu, J. Fabrication and Characterization of Citric Acid-Modified Starch Nanoparticles/Plasticized-Starch Composites. *Biomacromolecules* **2008**, *9* (11), 3314–3320.

(38) Sun, Q.; Gong, M.; Li, Y.; Xiong, L. Effect of Retrogradation Time on Preparation and Characterization of Proso Millet Starch Nanoparticles. *Carbohydrate Polymers* **2014**, *111*, 133–138.

(39) Kim, J. Y.; Lim, S. T. Preparation of Nano-Sized Starch Particles by Complex

Formation with n-Butanol. *Carbohydrate Polymers* **2009**, *76* (1), 110–116.

(40) Muljana, H.; Van Der Knoop, S.; Keijzer, D.; Picchioni, F.; Janssen, L. P. B. M.; Heeres, H. J. Synthesis of Fatty Acid Starch Esters in Supercritical Carbon Dioxide. *Carbohydrate Polymers* **2010**, *82* (2), 346–354.

(41) Clasen, S. H.; Müller, C. M. O.; Parize, A. L.; Pires, A. T. N. Synthesis and Characterization of Cassava Starch with Maleic Acid Derivatives by Etherification Reaction. *Carbohydrate Polymers* **2018**, *180*, 348–353.

(42) Forrest, B. Identification and Quantitation of Hydroxypropylation of Starch by FTIR. *Starch - Stärke* **1992**, *44* (5), 179–183.

(43) Chen, Q.; Yu, H.; Wang, L.; Ul Abdin, Z.; Chen, Y.; Wang, J.; Zhou, W.; Yang, X.; Khan, R. U.; Zhang, H.; *et al.* Recent Progress in Chemical Modification of Starch and Its Applications. *RSC Advances* **2015**, *5* (83), 67459–67474.

(44) Fan, Y.; Picchioni, F. Modification of Starch: A Review on the Application of "Green" Solvents and Controlled Functionalization. *Carbohydrate Polymers* **2020**, *241*, 116350.

(45) Whistler, R. L. Preparation and Properties of Starch Esters. *Advances in Carbohydrate Chemistry* **1945**, *1*, 279–307.

(46) Wing, R. E.; Doane, W. M.; Russell, C. R. Insoluble Starch Xanthate: Use in Heavy Metal Removal. *Journal of Applied Polymer Science* **1975**, *19* (3), 847–854.

(47) Weeldenburg, J. G. The Action of Sodium Hydroxide on Carbon Disulphide. *Recueil des Travaux Chimiques des Pays-Bas* **1928**, *47* (6), 496–512.

(48) Maher, G.G. Flocculation of coals with water-soluble xanthates United States Patent US4253970, **1979**.

(49) Singh, A. V.; Nath, L.; Guha, M. Synthesis and Characterization of Highly Substituted Acetylated Moth Bean Starch. *Journal of Polymer Materials* **2011**, *28* (2), 275–283.

(50) Aburto, J.; Alric, I.; Borredon, E. Preparation of Long-Chain Esters of Starch Using Fatty Acid Chlorides in the Absence of an Organic Solvent. *Starch - Stärke* **1999**, *51* (4), 132–135.

(51) Gilet, A.; Quettier, C.; Wiatz, V.; Bricout, H.; Ferreira, M.; Rousseau, C.; Monflier, E.; Tilloy, S. Unconventional Media and Technologies for Starch Etherification and Esterification. *Green Chemistry*. **2018**, *20* (6), 1152–1168.

(52) Wang, Y.; Xie, W. Synthesis of Cationic Starch with a High Degree of Substitution in an Ionic Liquid. *Carbohydrate Polymers* **2010**, *80* (4), 1172–1177.

(53) Almonaityte, K.; Bendoraitiene, J.; Babelyte, M.; Rosliuk, D.; Rutkaite, R. Structure and Properties of Cationic Starches Synthesized by Using 3-Chloro-2-Hydroxypropyltrimethylammonium Chloride. *International Journal of Biological Macromolecules* **2020**, *164*, 2010–2017.

(54) Heinze, T.; Haack, V.; Rensing, S. Starch Derivatives of High Degree of Functionalization. 7. Preparation of Cationic 2-Hydroxypropyltrimethylammonium Chloride Starches. *Starch - Stärke* **2004**, *56* (7), 288–296.

(55) Zheng, B.; Taylor, S. D. Nonthermoresponsive and Thermoresponsive Cationic Starch

for the Flocculation of Oil Sands Mature Fine Tailings. *Energy and Fuels* **2021**, *35* (6), 5163–5171.

(56) Stojanović, Ž.; Jeremić, K.; Jovanović, S. Synthesis of Carboxymethyl Starch. *Starch - Stärke* **2000**, *52* (1–12), 413–419.

(57) Vanier, N. L.; El Halal, S. L. M.; Dias, A. R. G.; da Rosa Zavareze, E. Molecular Structure, Functionality and Applications of Oxidized Starches: A Review. *Food Chemistry* **2017**, 221 1546–1559.

(58) Kuakpetoon, D.; Wang, Y. J. Structural Characteristics and Physicochemical Properties of Oxidized Corn Starches Varying in Amylose Content. *Carbohydrate Research* **2006**, *341* (11), 1896–1915.

(59) Sánchez-Rivera, M. M.; Méndez-Montealvo, G.; Núñez-Santiago, C.; De La Rosa-Millan, J.; Wang, Y. J.; Bello-Péreza, L. A. Physicochemical Properties of Banana Starch Oxidized under Different Conditions. *Starch - Stärke* **2009**, *61* (3–4), 206–213.

(60) Sangseethong, K.; Lertphanich, S.; Sriroth, K. Physicochemical Properties of Oxidized Cassava Starch Prepared under Various Alkalinity Levels. *Starch - Stärke* **2009**, *61* (2), 92–100.

(61) Kuakpetoon, D.; Wang, Y. J. Characterization of Different Starches Oxidized by Hypochlorite. *Starch - Stärke* **2001**, *53* (5), 211–218.

(62) Jenkins, P. J.; Donald, A. M. The Influence of Amylose on Starch Granule Structure. *International Journal of Biological Macromolecules* **1995**, *17* (6), 315–321.

(63) Tolvanen, P.; Mäki-Arvela, P.; Sorokin, A. B.; Salmi, T.; Murzin, D. Y. Kinetics of Starch Oxidation Using Hydrogen Peroxide as an Environmentally Friendly Oxidant and an Iron Complex as a Catalyst. *Chemical Engineering Journal* **2009**, *154* (1–3), 52–59.

(64) Chan, H. T.; Leh, C. P.; Bhat, R.; Senan, C.; Williams, P. A.; Karim, A. A. Molecular Structure, Rheological and Thermal Characteristics of Ozone-Oxidized Starch. *Food Chemistry* **2011**, *126* (3), 1019–1024.

(65) Galdeano, M. C.; Wilhelm, A. E.; Goulart, I. B.; Tonon, R. V.; Freitas-Silva, O.; Germani, R.; Chávez, D. W. H. Effect of Water Temperature and PH on the Concentration and Time of Ozone Saturation. *Brazilian Journal of Food Technology* **2018,** *21*, 2017156.

(66) Raveendran, P.; Fu, J.; Wallen, S. L. Completely "Green" Synthesis and Stabilization of Metal Nanoparticles. *J. Am. Chem. Soc.* **2003**, *125* (46), 13940–13941.

(67) Khlestkin, V. K.; Peltek, S. E.; Kolchanov, N. A. Review of Direct Chemical and Biochemical Transformations of Starch *Carbohydrate Polymers* **2018**, *181*, 460–476.

(68) Sharma, V. K.; Yngard, R. A.; Lin, Y. Silver Nanoparticles: Green Synthesis and Their Antimicrobial Activities. *Advances in Colloid and Interface Science* **2009**, *1* (2), 83–96.

(69) Tomasik, P.; Anderegg, J. W.; Bączkowicz, M.; Jane, J. L. Potato Starch Derivatives with Some Chemically Bound Bioelements. *Acta Poloniae Pharmaceutica - Drug Research* **2001**, *58* (6), 447–452.

(70) Hay, B. P.; Hancock, R. D. The Role of Donor Group Orientation as a Factor in Metal

Ion Recognition by Ligands. *Coordination Chemistry Reviews* **2001**, *212* (1), 61–78.

(71) Baran, W.; Sikora, M.; Tomasik, P.; Anderegg, J. W. Thallium(I) Starchate. *Carbohydrate Polymers* **1997**, *32* (3–4), 209–212.

(72) Kalarical Janardhanan, S.; Ramasamy, I.; Nair, B. U. Synthesis of Iron Oxide Nanoparticles Using Chitosan and Starch Templates. *Transition Metal Chemistry* **2008**, *33* (1), 127–131.

(73) Somsook, E.; Hinsin, D.; Buakhrong, P.; Teanchai, R.; Mophan, N.; Pohmakotr, M.; Shiowatana, J. Interactions between Iron(III) and Sucrose, Dextran, or Starch in Complexes. *Carbohydrate Polymers* **2005**, *61* (3), 281–287.

(74) L. O. Ekebafe. Removal of Heavy Metals from Aqueous Media Using Native Cassava Starch Hydrogel. *African Journal of Environmental Science and Technology* **2012**, *6* (7), 275–282.

(75) Plickart, L.; Wash, B. Starch-Metal Complexes Forskin and Hair, Japan Patent H09510978A, **1997**.

(76) Marusza, K.; Tomasik, P. Aluminum and Arsenic(III) Starchates. *Starch - Stärke* **1994**, *46* (1), 13–17.

(77) Athawale, V. D.; Rathi, S. C. Graft Polymerization: Starch as a Model Substrate. *Journal of Macromolecular Science – Reviews in Macromolecular Chemistry and Physics* **1999**, *39* (3), 445–480.

(78) Meimoun, J.; Wiatz, V.; Saint-Loup, R.; Parcq, J.; Favrelle, A.; Bonnet, F.; Zinck, P.

Modification of Starch by Graft Copolymerization. *Starch - Stärke* **2017,** *69* (1–2), 1600351–1600374.

(79) Leza, M. L.; Casinos, I.; Guzmán, G. M. Graft Copolymerization of 4-vinylpyridine onto Cotton. The Ceric Ion Concentration Effect. *Die Angewandte Makromolekulare Chemie* **1991**, *184* (1), 19–26.

(80) Gugliemelli, L. A.; Swanson, C. L.; Doane, W. M.; Russell, C. R. Preparation of Starch Poly(Styrene-Co-Acrylonitrile) Graft Polymers By Cerium(Iv) Initiation. *Journal of Polymer Science: Polymer Letters* **1977**, *15* (12), 739–743.

(81) Fakhru'L-Razi, A.; Qudsieh, I. Y. M.; Ahmad, W. M. Z. W. Y. M. B.; Rahman, M. Z. A. Graft Copolymerization of Methyl Methacrylate onto Sago Starch Using Ceric Ammonium Nitrate and Potassium Persulfate as Redox Initiator Systems. *Journal of Applied Polymer Science* **2001**, *82* (6), 1375–1381.

(82) Li, M. C.; Lee, J. K.; Cho, U. R. Synthesis, Characterization, and Enzymatic Degradation of Starch-Grafted Poly(Methyl Methacrylate) Copolymer Films. *Journal of Applied Polymer Science* **2012**, *125* (1), 405–414.

(83) Lai, S. M.; Sun, W. W.; Don, T. M. Preparation and Characterization of Biodegradable Polymer Blends from Poly(3-Hydroxybutyrate)/Poly(Vinyl Acetate)-Modified Corn Starch. *Polymer Engineering and Science* **2015**, *55* (6), 1321–1329.

(84) Matsumoto, M.; Ukida, J.; Takayama, G. Polymerization of Vinyl Acetate in the presence of a ceric salt, United States Patent, 3095405, **1994**.

(85) Athawale, V. D.; Rathi, S. C. Effect of Chain Length of the Alkyl Group of Alkyl Methacrylates on Graft Polymerization onto Starch Using Ceric Ammonium Nitrate as Initiator. *European Polymer Journal* **1997**, *33* (7), 1067–1071.

(86) Kaewtatip, K.; Tanrattanakul, V.; Szécsényi, K. M.; Pavličević, J.; Budinski-Simendić, J. Thermal Properties and Morphology of Cassava Starch Grafted with Different Content of Polystyrene. *Journal of Thermal Analysis and Calorimetry* **2010**, *102* (3), 1035–1041.

(87) Pourjavadi, A.; Eftekhar Jahromi, P.; Seidi, F.; Salimi, H. Synthesis and Swelling Behavior of Acrylatedstarch-g-Poly (Acrylic Acid) and Acrylatedstarch-g-Poly (Acrylamide) Hydrogels. *Carbohydrate Polymers* **2010**, *79* (4), 933–940.

(88) Willett, J. L.; Finkenstadt, V. L. Reactive Extrusion of Starch-Polyacrylamide Graft Copolymers Using Various Starches. *Journal of Polymers and the Environment* **2006**, *14* (2), 125–129.

(89) Henderson, A. M.; Rudin, A. Effects of water, methanol, and ethanol on the production of starch-*g*-polystyrene copolymers by cobalt-60 irradiation. *Journal of Polymer Science* **1981**, *19* (7), 1707–1719.

(90) Fanta, G. F.; Burr, R. C.; Doane, W. M.; Russell, C. R. Graft Polymerization of Vinyl Acetate onto Starch. Saponification to Starch-*g*-Poly(Vinyl Alcohol). *Journal of Applied Polymer Science* **1979**, *23* (1), 229–240.

(91) Lee, J. S.; Kumar, R. N.; Rozman, H. D.; Azemi, B. M. N. Pasting, Swelling and

Solubility Properties of UV Initiated Starch-Graft-Poly(AA). *Food Chemistry* **2005,** *91* (2), 203-211.

(92) Corrigan, N.; Jung, K.; Boyer, C. Merging New Organoborane Chemistry with Living Radical Polymerization. *Chem Previews* **2020**, *6* (6), 1212–1214.

(93) Matyjaszewski, K.; Spanswick, J. Controlled/Living Radical Polymerization. *Materials Today* **2005**, *8* (3), 26–33.

(94) Moad, G.; Rizzardo, E.; Thang, S. H. Living Radical Polymerization by the RAFT Process A Second Update. *Australian Journal of Chemistry* **2009**, *62* (11), 1402–1472.

(95) Hill, M. R.; Carmean, R. N.; Sumerlin, B. S. Expanding the Scope of RAFT Polymerization: Recent Advances and New Horizons. *Macromolecules* **2015**, *48* (16), 5459–5469.

(96) Moad, G.; Rizzardo, E.; Thang, S. H. Living Radical Polymerization by the RAFT Process - A First Update. *Australian Journal of Chemistry* **2006**, *59* (10), 669–692.

(97) Mayadunne, R. T. A.; Rizzardo, E.; Chiefari, J.; Krstina, J.; Moad, G.; Postma, A.; Thang, S. H. Living Polymers by the Use of Trithiocarbonates as Reversible Addition-Fragmentation Chain Transfer (RAFT) Agents: ABA Triblock Copolymers by Radical Polymerization in Two Steps. *Macromolecules* **2000**, *33* (2), 243–245.

(98) Moad, G.; Rizzardo, E.; Thang, S. H. RAFT Polymerization and Some of Its Applications. *Chemistry - An Asian Journal* **2013**; *8* (8), 1634–1644.

(99) Perrier, S.; Takolpuckdee, P. Macromolecular Design via Reversible Addition-

Fragmentation Chain Transfer (RAFT)/Xanthates (MADIX) Polymerization. *Journal of Polymer Science Part A: Polymer Chemistry* **2005**, *43* (22), 5347–5393.

(100) Benaglia, M.; Rizzardo, E.; Alberti, A.; Guerra, M. Searching for More Effective Agents and Conditions for the RAFT Polymerization of MMA: Influence of Dithioester Substituents, Solvent, and Temperature. *Macromolecules* **2005**, *38* (8), 3129–3140.

(101) Farmer, S. C.; Patten, T. E. (Thiocarbonyl-A-Thio)Carboxylic Acid Derivatives As Transfer Agents in Reversible Addition-Fragmentation Chain-Transfer Polymerizations. *Journal of Polymer Science Part A: Polymer Chemistry* **2002**, *40* (4), 555–563.

(102) Chiefari, J.; Chong, Y. K.; Ercole, F.; Krstina, J.; Jeffery, J.; Le, T. P. T.; Mayadunne, R. T. A.; Meijs, G. F.; Moad, C. L.; Moad, G.; *et al.* Living Free-Radical Polymerization by Reversible Addition - Fragmentation Chain Transfer: The RAFT Process. *Macromolecules* **1998**, *31* (16), 5559–5562.

(103) Quinn, J. F.; Barner, L.; Barner-Kowollik, C.; Rizzardo, E.; Davis, T. P. Reversible Addition - Fragmentation Chain Transfer Polymerization Initiated with Ultraviolet Radiation. *Macromolecules* **2002**, *35* (20), 7620–7627.

(104) Ray, B.; Isobe, Y.; Matsumoto, K.; Habaue, S.; Okamoto, Y.; Kamigaito, M.; Sawamoto, M. RAFT Polymerization of N-Isopropylacrylamide in the Absence and Presence of Y(OTf) 3 : Simultaneous Control of Molecular Weight and Tacticity. *Macromolecules* **2004**, *37* (5), 1702–1710.

(105) Thomas, D. B.; Convertine, A. J.; Myrick, L. J.; Scales, C. W.; Smith, A. E.; Lowe, A.

B.; Vasilieva, Y. A.; Ayres, N.; McCormick, C. L. Kinetics and Molecular Weight Control of the Polymerization of Acrylamide via RAFT. *Macromolecules* **2004**, *37* (24), 8941–8950.

(106) Stenzel, M. H.; Cummins, L.; Roberts, G. E.; Davis, T. P.; Vana, P.; Barner-Kowollik, C. Xanthate Mediated Living Polymerization of Vinyl Acetate: A Systematic Variation in MADIX/RAFT Agent Structure. *Macromolecular Chemistry and Physics* **2003,** *204* (9), 1160-1168.

(107) Lu, D.; Xiao, C.; Sun, F. Controlled Grafting of Poly(Vinyl Acetate) onto Starch via RAFT Polymerization. *Journal of Applied Polymer Science* **2012**, *124* (4), 3450–3455.

(108) Lu, D. R.; Xiao, C. M.; Xu, S. J.; Ye, Y. F. Tailor-Made Starch-Based Conjugates Containing Well-Defined Poly(Vinyl Acetate) and Its Derivative Poly(Vinyl Alcohol). *Express Polymer Letters* **2011**, *5* (6), 535–544.

(109) Ran, J.; Wu, L.; Zhang, Z.; Xu, T. Atom Transfer Radical Polymerization (ATRP): A Versatile and Forceful Tool for Functional Membranes. *Progress in Polymer Science* **2014**, *39* (1), 124–144.

(110) Liu, P.; Su, Z. Surface-Initiated Atom Transfer Radical Polymerization (SI-ATRP) of n-Butyl Acrylate from Starch Granules. *Carbohydrate Polymers* **2005**, *62* (2), 159–163.

(111) Moghaddam, P. N.; Fareghi, A. R.; Entezami, A. A.; Mehr, M. A. G. Synthesis of Biodegradable Thermoplastic Copolymers Based on Starch by Atom Transfer Radical Polymerization (ATRP): Monolayer Chain Growth on Starch. *Starch - Stärke* **2013**, *65*

(3–4), 210–218.

(112) Avval, M. E.; Moghaddam, P. N.; Fareghi, A. R. Modification of Starch by Graft Copolymerization: A Drug Delivery System Tested for Cephalexin Antibiotic. *Starch - Stärke* **2013**, *65* (7–8), 572–583.

(113) Nurmi, L.; Holappa, S.; Mikkonen, H.; Seppälä, J. Controlled Grafting of Acetylated Starch by Atom Transfer Radical Polymerization of MMA. *European Polymer Journal* **2007**, *43* (4), 1372–1382.

(114) Bansal, A.; Ray, S. S.; Chatterjee, A. K. Expanded Corn Starch a Novel Material as Macroinitiator/Solid Support in SI and AGET ATRP: GMA Polymerization. *Journal of Polymer Research* **2015**, *22* (2), 1–10.

(115) Fan, Y.; Boulif, N.; Picchioni, F. Thermo-Responsive Starch-g-(PAM-Co-PNIPAM): Controlled Synthesis and Effect of Molecular Components on Solution Rheology. *Polymers* **2018**, *10* (1), 92-104.

(116) Wu, J.; Jiang, X.; Zhang, L.; Cheng, Z.; Zhu, X. Iron-Mediated Homogeneous Icar ATRP of Methyl Methacrylate under Ppm Level Organometallic Catalyst Iron(III) Acetylacetonate. *Polymers* **2016**, *8* (2), 1–13.

(117) Cazotti, J. C.; Fritz, A. T.; Garcia-Valdez, O.; Smeets, N. M. B.; Dubé, M. A.; Cunningham, M. F. Graft Modification of Starch Nanoparticles Using Nitroxide-Mediated Polymerization and the Grafting from Approach. *Carbohydrate Polymers* **2020**, *21* (11), 4492-4501 *228*.

(118) Cazotti, J. C.; Fritz, A. T.; Garcia-Valdez, O.; Smeets, N. M. B.; Dubé, M. A.; Cunningham, M. F. Grafting from Starch Nanoparticles with Synthetic Polymers via Nitroxide-Mediated Polymerization. *Macromolecular Rapid Communications* **2019**, *40* (10), 1800834.

(119) Mujtaba, M.; Morsi, R. E.; Kerch, G.; Elsabee, M. Z.; Kaya, M.; Labidi, J.; Khawar, K. M. Current Advancements in Chitosan-Based Film Production for Food Technology; A Review. *International Journal of Biological Macromolecules* **2019**, *121*, 889–904.

(120) Muzzarelli, R. A. A. Chapter 3 - Chtin Chemistry. Chitin **1977**, 87–154.

(121) Xu, Y.; Gallert, C.; Winter, J. Chitin Purification from Shrimp Wastes by Microbial Deproteination and Decalcification. *Applied Microbiology and Biotechnology* **2008**, *79* (4), 687–697.

(122) Yaghobi, N.; Hormozi, F. Multistage Deacetylation of Chitin: Kinetics Study. *Carbohydrate Polymers* **2010**, *81* (4), 892–896.

(123) Kubota, N.; Eguchi, Y. Facile Preparation of Water-Soluble N-Acetylated Chitosan and Molecular Weight Dependence of Its Water-Solubility. *Polymer Journal* **1997**, *29* (2), 123–127.

(124) Clark, G. L.; Smith, A. F. X-Ray Diffraction Studies of Chitin, Chitosan, and Derivatives. The *Journal of Physical Chemistry* **1936**, *40* (7), 863–879.

(125) Ogawa, K.; Yui, T.; Okuyama, K. Three D Structures of Chitosan. *International Journal of Biological Macromolecules* **2004**, *34* (1–2), 1–8.

(126) Feng, F.; Liu, Y.; Zhao, B.; Hu, K. Characterization of Half N-Acetylated Chitosan Powders and Films. *Procedia Engineering* **2012**; *27*, 718–732.

(127) Nishimura, S. I.; Kohgo, O.; Kurita, K.; Kuzuhara, H. Chemospecific Manipulations of a Rigid Polysaccharide: Syntheses of Novel Chitosan Derivatives with Excellent Solubility in Common Organic Solvents by Regioselective Chemical Modifications. *Macromolecules* **1991**, *24* (17), 4745–4748.

(128) Rinaudo, M.; Pavlov, G.; Desbrières, J. Influence of Acetic Acid Concentration on the Solubilization of Chitosan. *Polymer* **1999**, *40* (25), 7029–7032.

(129) Mourya, V. K.; Inamdar, N. N. Chitosan-Modifications and Applications: Opportunities Galore. *Reactive and Functional Polymers* **2008**, *68* (6), 1013–1051.

(130) Zong, Z.; Kimura, Y.; Takahashi, M.; Yamane, H. Characterization of Chemical and Solid State Structures of Acylated Chitosans. *Polymer* **2000**, *41* (3), 899–906.

(131) Garcia-Valdez, O.; Champagne, P.; Cunningham, M. F. Graft Modification of Natural Polysaccharides via Reversible Deactivation Radical Polymerization. *Progress in Polymer Science* **2018**, *76*, 151–173.

(132) Kim, K. W.; Thomas, R. L.; Lee, C.; Park, H. J. Antimicrobial Activity of Native Chitosan, Degraded Chitosan, and O-Carboxymethylated Chitosan. *Journal of Food Protection* **2003**, *66* (8), 1495–1498.

(133) Bigogno, R. G.; Rodríguez, R. J. S.; Abreu, M. de F. Quaternized Chitosan for Ecological Treatment of Bauxite Mining Effluents. *Journal of Polymers and the.*

Environment **2018**, *26* (11), 4169–4175.

(134) Bobu, E.; Raluca, N.; Lupei, M.; Ciolacu, F. L.; Desbrières, J. Synthesis and Characterization of N-Alkyl Chitosan for Papermaking Applications. *Cellulose Chemistry and Technology 2***011,** *45* (9), 619-625.

(135) Naggi, A. M.; Torri, G.; Compagnoni, T.; Casu, B. Synthesis and Physico-Chemical Properties of the Polyampholyte Chitosan 6-Sulfate. *Chitin in Nature and Technology*; **1986**, 371–377.

(136) Holme, K. R.; Perlin, A. S. Chitosan N-Sulfate. A Water-Soluble Polyelectrolyte. *Carbohydrate Research* **1997**, *302* (1-2), 7-12.

(137) Jenkins, D. W.; Hudson, S. M. Review of Vinyl Graft Copolymerization Featuring Recent Advances toward Controlled Radical-Based Reactions and Illustrated with Chitin/Chitosan Trunk Polymers. *Chemical Reviews* **2001**, *101*, 3245–3273.

(138) Pourjavadi, A.; Mahdavinia, G. R.; Zohuriaan-Mehr, M. J.; Omidian, H. Modified Chitosan. I. Optimized Cerium Ammonium Nitrate-Induced Synthesis of Chitosan-Graft-Polyacrylonitrile. *Journal of Applied Polymer Science* **2003**, *88* (8), 2048–2054.

(139) Tiwari, A.; Singh, V. Synthesis and Characterization of Electrical Conducting Chitosan-Graft-Polyaniline. *Express Polymer Letters* **2007**, *1* (5), 308–317.

(140) Tiwari, A.; Gong, S. Electrochemical Detection of a Breast Cancer Susceptible Gene Using CDNA Immobilized Chitosan-Co-Polyaniline Electrode. *Talanta* **2009**, *77* (3), 1217–1222.

(141) Casimiro, M. H.; Botelho, M. L.; Leal, J. P.; Gil, M. H. Study on Chemical, UV and Gamma Radiation-Induced Grafting of 2-Hydroxyethyl Methacrylate onto Chitosan. *Radiation Physics and Chemistry* **2005**, *72* (6), 731–735.

(142) Lagos, A.; Reyes, J. Grafting onto Chitosan. I. Graft Copolymerization of Methyl Methacrylate onto Chitosan with Fenton's Reagent (Fe^{2+}–H_2O_2) as a Redox Initiator. *Journal of Polymer Science Part A: Polymer Chemistry* **1988**, *26* (4), 985–991.

(143) Hua, D.; Tang, J.; Cheng, J.; Deng, W.; Zhu, X. A Novel Method of Controlled Grafting Modification of Chitosan via RAFT Polymerization Using Chitosan-RAFT Agent. *Carbohydrate Polymers* **2008**, *73* (1), 98–104.

(144) El Tahlawy, K.; Hudson, S. M. Synthesis of a Well-Defined Chitosan Graft Poly(Methoxy Polyethyleneglycol Methacrylate) by Atom Transfer Radical Polymerization Polymerization. *Journal of Applied Polymer Science* **2003**, *89* (4), 901–912.

(145) Li, N.; Bai, R.; Liu, C. Enhanced and Selective Adsorption of Mercury Ions on Chitosan Beads Grafted with Polyacrylamide via Surface-Initiated Atom Transfer Radical Polymerization. *Langmuir* **2005**, *21* (25), 11780–11787.

(146) Liu, P.; Su, Z. Surface-Initiated Atom Transfer Radical Polymerization (SI-ATRP) of Styrene from Chitosan Particles. *Material Letters* **2006**, *60* (9–10), 1137–1139.

(147) García-Valdez, O.; Champagne-Hartley, R.; Saldívar-Guerra, E.; Champagne, P.; Cunningham, M. F. Modification of Chitosan with Polystyrene and Poly(*n*-Butyl

Acrylate) via Nitroxide-Mediated Polymerization and Grafting from Approach in Homogeneous Media. *Polymer Chemistry* **2015**, *6* (15), 2827–2836.

(148) Kulbokaite, R.; Ciuta, G.; Netopilik, M.; Makuska, R. N-PEG'ylation of Chitosan via "Click Chemistry" Reactions. *Reactive and Functional Polymers* **2009**, *69* (10), 771–778.

(149) Gandhi, A.; Paul, A.; Sen, S. O.; Sen, K. K. Studies on Thermoresponsive Polymers: Phase Behaviour, Drug Delivery and Biomedical Applications. *Asian Journal of Pharmaceutical Sciences* **2015**, *10* (2), 99–107.

(150) Somcynsky, T. The Lower Critical Solution Temperature (LCST) of Non-polar Polymer Solutions: An Introduction. *Polymer Engineering and Science* **1982**, *22* (2), 58–63.

(151) Zhao, C.; Dolmans, L.; Zhu, X. X. Thermoresponsive Behavior of Poly(Acrylic Acid-Co-Acrylonitrile) with a UCST. *Macromolecules* **2019**, *52* (12), 4441-4446.

(152) Lutz, J. F.; Akdemir, Ö.; Hoth, A. Point by Point Comparison of Two Thermosensitive Polymers Exhibiting a Similar LCST: Is the Age of Poly(NIPAM) Over? *Journal of the American Chemical Society* **2006**, *128* (40), 13046–13047.

(153) Plate, N. A.; Lebedeva, T. L.; Valuev, L. I. Lower Critical Solution Temperature in Aqueous Solutions of N-Alkyl-Substituted Polyacrylamides. *Polymer Journal* **1999**, *31* (1), 21–27.

(154) Lessard, D. G.; Ousalem, M.; Zhu, X. X. Effect of the Molecular Weight on the Lower Critical Solution Temperature of Poly(*N*,*N*-Diethylacrylamide) in Aqueous Solutions.

Canadian Journal of Chemistry **2001**, *79* (12), 1870–1874.

(155) Du, H.; Wickramasinghe, R.; Qian, X. Effects of Salt on the Lower Critical Solution Temperature of Poly (N-Isopropylacrylamide). The *Journal of Physical Chemistry B* **2010**, *114* (49), 16594–16604.

(156) Furyk, S.; Zhang, Y.; Ortiz-Acosta, D.; Cremer, P. S.; Bergbreiter, D. E. Effects of End Group Polarity and Molecular Weight on the Lower Critical Solution Temperature of Poly(N-Isopropylacrylamide). *Journal of Polymer Science Part A: Polymer Chemistry* **2006**, *44* (4), 1492–1501.

(157) Xia, Y.; Burke, N. A. D.; Stöver, H. D. H. End Group Effect on the Thermal Response of Narrow-Disperse Poly(N-Isopropylacrylamide) Prepared by Atom Transfer Radical Polymerization. *Macromolecules* **2006**, *39* (6), 2275–2283.

(158) Patel, T.; Ghosh, G.; Yusa, S. ichi; Bahadur, P. Solution Behavior of Poly(n-Isopropylacrylamide) in Water: Effect of Additives. *Journal of Dispersion Science and Technology* **2011**, *32* (8), 1111-1118.

(159) Cooperstein, M. A.; Canavan, H. E. Assessment of Cytotoxicity of (N-Isopropyl Acrylamide) and Poly(N-Isopropyl Acrylamide)-Coated Surfaces. *Biointerphases* **2013**, *8* (1), 1–12.

(160) Haq, M. A.; Su, Y.; Wang, D. Mechanical Properties of PNIPAM Based Hydrogels: A Review. *Materials Science and Engineering C* **2017**, *70*, 842–855.

(161) Vancoillie, G.; Frank, D.; Hoogenboom, R. Thermoresponsive Poly(Oligo Ethylene

Glycol Acrylates). *Progress in Polymer Science* **2014**, *39* (6), 1074–1095.

(162) Becer, C. R.; Hahn, S.; Fijten, M. W. M.; Thijs, H. M. L.; Hoogenboom, R.; Schubert, U. S. Libraries of Methacrylic Acid and Oligo(Ethylene Glycol) Methacrylate Copolymers with LCST Behavior. *Journal of Polymer Science Part A: Polymer Chemistry* **2008**, *46* (21), 7138–7147.

(163) Roy, D.; Brooks, W. L. A.; Sumerlin, B. S. New Directions in Thermoresponsive Polymers. *Chemical Society Reviews* **2013**, *42* (17), 7214–7243.

(164) Okuyama, Y.; Yoshida, R.; Sakai, K.; Okano, T.; Sakurai, Y. Swelling Controlled Zero Order and Sigmoidal Drug Release from Thermo-Responsive Poly(N-Isopropylacrylamide-Co-Butyl Methacrylate) Hydrogel. *Journal of Biomaterials Science, Polymer Edition* **1993**, *4* (5), 545–556.

(165) Coughlan, D. C.; Corrigan, O. I. Drug-Polymer Interactions and Their Effect on Thermoresponsive Poly(N-Isopropylacrylamide) Drug Delivery Systems. *International Journal of Pharmaceutics* **2006**, *313* (1–2), 163–174.

(166) Jones, D. S.; Lorimer, C. P.; McCoy, C. P.; Gorman, S. P. Characterization of the Physicochemical, Antimicrobial, and Drug Release Properties of Thermoresponsive Hydrogel Copolymers Designed for Medical Device Applications. *Journal of Biomedical Materials Research - Part B: Applied Biomaterials* **2008**, *85* (2), 417–426.

(167) Chung, J. E.; Yokoyama, M.; Yamato, M.; Aoyagi, T.; Sakurai, Y.; Okano, T. Thermo-Responsive Drug Delivery from Polymeric Micelles Constructed Using Block

Copolymers of Poly(N-Isopropylacrylamide) and Poly(Butylmethacrylate). *Journal of Controlled Release* **1999**, *62* (1–2), 115–127.

(168) Qasim, M.; Baipaywad, P.; Udomluck, N.; Na, D.; Park, H. Enhanced Therapeutic Efficacy of Lipophilic Amphotericin B against Candida Albicans with Amphiphilic Poly(N-Isopropylacrylamide) Nanogels. *Macromolecular Research* **2014**.

(169) Liu, H.; Wang, S. Poly(N-Isopropylacrylamide)-Based Thermo-Responsive Surfaces with Controllable Cell Adhesion. *Science China Chemistry* **2014**, *57* (4), 552–557.

(170) Ashraf, S.; Park, H. K.; Park, H.; Lee, S. H. Snapshot of Phase Transition in Thermoresponsive Hydrogel PNIPAM: Role in Drug Delivery and Tissue Engineering. *Macromolecular Research* **2016,** *24* (4), 297–304.

(171) Lutz, J. F. Polymerization of Oligo(Ethylene Glycol) (Meth)Acrylates: Toward New Generations of Smart Biocompatible Materials. *Journal of Polymer Science Part A: Polymer Chemistry* **2008**, *46* (11), 3459–3470.

(172) Zhu, H.; Geng, Q.; Chen, W.; Zhu, Y.; Chen, J.; Du, J. Antibacterial High-Genus Polymer Vesicle as an "Armed" Drug Carrier. *Journal of Materials Chemistry B* **2013**, *1* (40), 5496–5504.

(173) Huang, Y.; Sun, Y.; Wang, Q. Encapsulation and in Vitro Release of Erythromycin Using Biopolymer Micelle. *Cellular and Molecular Biology* **2015**, *61* (7), 60–64.

(174) Yang, B.; Duhamel, J. Extraction of Oil from Oil Sands Using Thermoresponsive Polymeric Surfactants. *ACS Applied Materials & Interfaces* **2015**, *7* (10), 5879–5889.

(175) Fundueanu, G.; Constantin, M.; Ascenzi, P.; Simionescu, B. C. An Intelligent Multicompartmental System Based on Thermo-Sensitive Starch Microspheres for Temperature-Controlled Release of Drugs. *Biomedical Microdevices* **2010**, *12* (4), 693–704.

(176) Zheng, B.; Karski, M.; Taylor, S. D. Thermoresponsive Hydroxybutylated Starch Nanoparticles. *Carbohydrate Polymers* **2019**, *209*, 145–151.

(177) Dai, M.; Liu, Y.; Ju, B.; Tian, Y. Preparation of Thermoresponsive Alginate/Starch Ether Composite Hydrogel and Its Application to the Removal of Cu(II) from Aqueous Solution. *Bioresource Technology* **2019**, *294*.

(178) Crompton, K. E.; Goud, J. D.; Bellamkonda, R. V.; Gengenbach, T. R.; Finkelstein, D. I.; Horne, M. K.; Forsythe, J. S. Polylysine-Functionalised Thermoresponsive Chitosan Hydrogel for Neural Tissue Engineering. *Biomaterials* **2007**, *28* (3), 441–449.

(179) Chen, J. P.; Cheng, T. H. Thermo-Responsive Chitosan-Graft-Poly(N-Isopropylacrylamide) Injectable Hydrogel for Cultivation of Chondrocytes and Meniscus Cells. *Macromolecular Bioscience* **2006**, *6* (12), 1026–1039.

(180) Chen, J. P.; Kuo, C. Y.; Lee, W. L. Thermo-Responsive Wound Dressings by Grafting Chitosan and Poly(N-Isopropylacrylamide) to Plasma-Induced Graft Polymerization Modified Non-Woven Fabrics. *Applied Surface Science* **2012**, *262*, 95–101.

(181) Miguel, S. P.; Ribeiro, M. P.; Brancal, H.; Coutinho, P.; Correia, I. J. Thermoresponsive Chitosan-Agarose Hydrogel for Skin Regeneration. *Carbohydrate Polymers* **2014**, *111*,

366–373.

(182) Ren, K.; Du, H.; Yang, Z.; Tian, Z.; Zhang, X.; Yang, W.; Chen, J. Separation and Sequential Recovery of Tetracycline and Cu(II) from Water Using Reusable Thermoresponsive Chitosan-Based Flocculant. *ACS Applied Materials & Interfaces* **2017**, *9* (11), 10266–10275.

Chapter 2

(1) Li, J. Y.; Yeh, A. I. Relationships between Thermal, Rheological Characteristics and Swelling Power for Various Starches. *Journal of Food Engineering* **2001**, *50* (3), 141–148.

(2) Ellis, R. P.; Cochrane, M. P.; Dale, M. F. B.; Duffus, C. M.; Lynn, A.; Morrison, I. M.; Prentice, R. D. M.; Swanston, J. S.; Tiller, S. A. Starch Production and Industrial Use. *Journal of the Science of Food and Agriculture* **1998**, *77* (3), 289–311.

(3) Masina, N.; Choonara, Y. E.; Kumar, P.; du Toit, L. C.; Govender, M.; Indermun, S.; Pillay, V. A Review of the Chemical Modification Techniques of Starch. *Carbohydrate Polymers* **2017**, *157*, 1226–1236.

(4) Wang, S.; Copeland, L. Molecular Disassembly of Starch Granules during Gelatinization and Its Effect on Starch Digestibility: A Review. *Food and Function* **2013**, *4* (11), 1564–1580.

(5) Shin, J. Y.; Jones, N.; Lee, D. I.; Fleming, P. D.; Joyce, M. K.; DeJong, R.; Bloembergen,

S. Rheological Properties of Starch Latex Dispersions and Starch Latex-Containing Coating Colors. *Conference and Trade Show* **2012**, *1*, 382–406.

(6) Bloembergen, S.; McLennan, I.; Lee, D. I.; Van Leeuwen, J. Paper Binder Performance with Biobased Nanoparticles. *Paper360* **2008**, *3* (8), 46–48.

(7) Li, L. Characterization of Polysaccharides in Starch Using Fluorescence Techniques, Ph.D. Thesis, University of Waterloo, **2020**.

(8) Saeki, S.; Kuwahara, N.; Nakata, M.; Kaneko, M. Upper and Lower Critical Solution Temperatures in Poly (Ethylene Glycol) Solutions. *Polymer (Guildf).* **1976**, *17* (8), 685–689.

(9) Haq, M. A.; Su, Y.; Wang, D. Mechanical Properties of PNIPAM Based Hydrogels: A Review. *Materials Science and Engineering C* **2017**, *70*, 842–855.

(10) Hu, Z.; Cai, T.; Chi, C. Thermoresponsive Oligo(Ethylene Glycol)-Methacrylate- Based Polymers and Microgels. *Soft Matter* **2010**, *6* (10), 2115–2123.

(11) Pak, F.; Farajollahi, A.; Movafaghi, A.; Naseri, A. Influencing Factors on Reproducibility and Stability of MRI NIPAM Polymer Gel Dosimeter. *BioImpacts* **2013**, *3* (4), 163–168.

(12) Lutz, J. F.; Akdemir, Ö.; Hoth, A. Point by Point Comparison of Two Thermosensitive Polymers Exhibiting a Similar LCST: Is the Age of Poly(NIPAM) Over? *Journal of the American Chemical Society* **2006**, *128* (40), 13046–13047.

(13) Góis, J. R.; Popov, A. V.; Guliashvili, T.; Serra, A. C.; Coelho, J. F. J. Synthesis of Functionalized Poly(Vinyl Acetate) Mediated by Alkyne-Terminated RAFT Agents. *RSC*

Advances **2015**, *5* (111), 91225–91234.

(14) Keddie, D. J.; Moad, G.; Rizzardo, E.; Thang, S. H. RAFT Agent Design and Synthesis. *Macromolecules* **2012**, *45* (13), 5321–5342.

(15) Schluter, A. D., Hawker, Craig J. and Sakamoto, J. *Synthesis of Polymers: New Structures and Methods. John Wiley & Sons* **2016**.

(16) Gottlieb, H. E.; Kotlyar, V.; Nudelman, A. NMR Chemical Shifts of Common Laboratory Solvents as Trace Impurities. *Journal of Organic Chemistry.* **1997**, *62* (21), 7512–7515.

(17) Weeldenburg, J. G. The Action of Sodium Hydroxide on Carbon Disulphide. *Recueil des Travaux Chimiques des Pays-Bas* **1928**, *47* (6), 496–512.

(18) Fahmy, B. Y. A.; Fadl, M. H. On Emulsion Xanthation of Cellulose . II . Aspects of the reaction mechanis m and acceleration of cellulose emulsion xanthation by inclusion or occlusion with CS_2 in fibers. *Svensk Papperstidning* **1964**, *67* (7), 279–285.

(19) Tomasik, P.; Schilling, C. H. Chemical Modification of Starch. *Advances in Carbohydrate Chemistry and. Biochemistry* **2004**, *59*, 175–403.

(20) Vancoillie, G.; Frank, D.; Hoogenboom, R. Thermoresponsive Poly(Oligo Ethylene Glycol Acrylates). *Progress in Polymer Science* **2014**, *39* (6), 1074–1095.

(21) Kulik, A. S.; De Costa, J. R. C.; Haverkamp, J. Water Organization and Molecular Mobility in Maize Starch Investigated by Two-Dimensional Solid-State NMR. *Journal of Agricultural and Food Chemistry* **1994**, *42* (12), 2803–2807.

(22) Moad, G.; Rizzardo, E.; Thang, S. H. End-Functional Polymers, Thiocarbonylthio Group

Removal/Transformation and Reversible Addition-Fragmentation-Chain Transfer (RAFT) Polymerization. *Polymer International* **2011**, *60* (1), 9–25.

(23) Jesson, C. P.; Pearce, C. M.; Simon, H.; Werner, A.; Cunningham, V. J.; Lovett, J. R.; Smallridge, M. J.; Warren, N. J.; Armes, S. P. H_2O_2 Enables Convenient Removal of RAFT End-Groups from Block Copolymer Nano-Objects Prepared via Polymerization-Induced Self- Assembly in Water. *Macromolecules* **2017**, *50* (1), 182–191.

(24) Pfukwa, R.; Pound, G.; Klumperman, B. Facile End Group Modification of Raft Made Polymers, by Radical Exchange with Hydrogen Peroxide. *Polymer Preprints* **2008**, *49* (2), 117–118.

(25) Yang, B.; Duhamel, J. Extraction of Oil from Oil Sands Using Thermoresponsive Polymeric Surfactants. *ACS Applied Materials & Interfaces* **2015**, *7* (10), 5879–5889.

(26) Somcynsky, T. The Lower Critical Solution Temperature (LCST) of Non-polar Polymer Solutions: An Introduction. *Polymer Engineering and Science* **1982**, *22* (2), 58–63.

(27) Du, H.; Wickramasinghe, R.; Qian, X. Effects of Salt on the Lower Critical Solution Temperature of Poly (N-Isopropylacrylamide). *Journal of Physical Chemistry B* **2010**, *114* (49), 16594–16604.

(28) Lessard, D. G.; Ousalem, M.; Zhu, X. X. Effect of the Molecular Weight on the Lower Critical Solution Temperature of Poly(*N*,*N*-Diethylacrylamide) in Aqueous Solutions. *Canadian Journal of Chemistry* **2001**, *79* (12), 1870–1874.

(29) Akimoto, J.; Ito, Y. Thermoresponsive Biodegradable Polymeric Materials for

Biomedical Application. *Sustainibility & Green Polymer Chemistry: Green Products and Processes* **2020**, *1*, 159–172.

Chapter 3

(1) Tenenbaum, D. J. Oils Sands Development: A Health Risk Worth Taking? *Environmental Health Perspectives* **2009**, *117* (4), A150-A156

(2) Masliyah, J.; Zhou, Z. J.; Xu, Z.; Czarnecki, J.; Hamza, H. Understanding Water-Based Bitumen Extraction from Athabasca Oil Sands. *The Canadian Journal of Chemical Engineering* **2008**, *82* (4), 628–654.

(3) Takamura, K. Microscopic Structure of Athabasca Oil Sand. *The Canadian Journal of Chemical Engineering* **1982**, *60* (4), 538-545.

(4) Speight, J. G. The Chemistry and Technology of Petroleum. *CRC Press* **2006**.

(5) Czarnecki, J.; Radoev, B.; Schramm, L. L.; Slavchev, R. On the Nature of Athabasca Oil Sands. *Advances in Colloid and Interface Science* **2005**, *114*, 53–60.

(6) Rao, F.; Liu, Q. Froth Treatment in Athabasca Oil Sands Bitumen Recovery Process: A Review. *Energy and Fuels* **2013**, *27* (12), 7199–7207.

(7) Miller, J. D.; Misra, M. Hot Water Process Development for Utah Tar Sands. *Fuel Processing Technology* **1982**, *6* (1), 27–59.

(8) Choung, J.; Walker, J.; Xu, Z.; Masliyah, J. Effect of Temperature on the Stability of

Froth Formed in the Recycle Process Water of Oil Sands Extraction. *The Canadian Journal of Chemical Engineering* **2008**, *82* (4), 801–806.

(9) Flury, C.; Afacan, A.; Tamiz Bakhtiari, M.; Sjoblom, J.; Xu, Z. Effect of Caustic Type on Bitumen Extraction from Canadian Oil Sands. *Energy & Fuels* **2014**, *28* (1), 431–438.

(10) Kotlyar, L. S.; Deslandes, Y.; Sparks, B. D.; Kodama, H.; Schutte, R. Characterization of Colloidal Solids from Athabasca Fine Tails. *Clays and Clay Minerals* **1993**, *41* (3), 341–345.

(11) Lo, C. C.; Brownlee, B. G.; Bunce, N. J. Mass Spectrometric and Toxicological Assays of Athabasca Oil Sands Naphthenic Acids. *Water Research* **2006**, *40* (4), 655–664.

(12) Long, Y.; Dabros, T.; Hamza, H. Stability and Settling Characteristics of Solvent-Diluted Bitumen Emulsions. *Fuel* **2002**, *81* (15), 1945–1952.

(13) Yang, B.; Duhamel, J. Extraction of Oil from Oil Sands Using Thermoresponsive Polymeric Surfactants. *ACS Applied Materials & Interfaces* **2015**, *7* (10), 5879–5889.

(14) Zhang, Q. Thermoresponsive Starch Nanoparticles for Use in the Extraction of Oil from Oil Sands. M.Sc. Thesis, University of Waterloo, **2018**.

(15) Aslam, M. I.; Verma, R. K.; Roy, R.; Roy, S. P. Effect of Poly (N-IsoPropylAcrylamide) "PNIPAM" on Hepatic Cells of Swiss Albino Mice, Mus Musculus. *International Journal of Applied Sciences and Biotechnology* **2013**, *1* (4), 208–213.

(16) Zhou, Z. A.; Li, H.; Chow, R.; Adeyinka, O. B.; Xu, Z.; Masliyah, J. Impact of Fine Solids on Mined Athabasca Oil Sands Extraction II. Effect of Fine Solids with Different Surface

Wettability on Bitumen Recovery. *The Canadian Journal of Chemical Engineering* **2017**, *95* (1), 120–126.

(17) Luque de Castro, M. D.; Priego-Capote, F. Soxhlet Extraction: Past and Present Panacea. *Journal of Chromatography A* **2010**, *1217* (16), 2383–2389.

(18) Sthle, L.; Wold, S. Analysis of Variance (ANOVA). *Chemometrics and Intelligent Laboratory Systems* **1989**, 259–272.

(19) Kunz, W.; Henle, J.; Ninham, B. W. About the Science of the Effect of Salts. *Current Opinion in Colloid & Interface Science* **2004**, *9* (1–2), 19–37.

(20) Du, H.; Wickramasinghe, R.; Qian, X. Effects of Salt on the Lower Critical Solution Temperature of Poly (N-Isopropylacrylamide). *Journal of Physical Chemistry B* **2010**, *114* (49), 16594–16604.

(21) Zheng, B. Synthesis and Characterization of Thermoresponsive Starch Nanoparticles, M.Sc. Thesis, University of Waterloo, **2016**.

(22) Rocha, J. A.; Baydak, E. N.; Yarranton, H. W.; Sztukowski, D. M.; Ali-Marcano, V.; Gong, L.; Shi, C.; Zeng, H. Role of Aqueous Phase Chemistry, Interfacial Film Properties, and Surface Coverage in Stabilizing Water-in-Bitumen Emulsions. *Energy and Fuels* **2016**, *30* (7), 5240–5252.

(23) Leung, S. S. C.; MacKinnon, M. D.; Smith, R. E. H. Aquatic Reclamation in the Athabasca, Canada, Oil Sands: Naphthenate and Salt Effects on Phytoplankton Communities. *Environmental Toxicology and Chemistry* **2001**, *20* (7), 1532–1543.

(24) Palmgren, C.; Edmunds, N. High Temperature Naptha to Replace Steam in the SAGD Process. *SPE International Heavy Oil Symposium. OnePetro* **1995**, 475–485.

Chapter 4

(1) Kant, R. Textile Dyeing Industry an Environmental Hazard. *Natural Sciences* **2012**, *4* (1), 22–26.

(2) Robinson, T.; McMullan, G.; Marchant, R.; Nigam, P. Remediation of Dyes in Textile Effluent: A Critical Review on Current Treatment Technologies with a Proposed Alternative. *Bioresource Technology* **2001**, *77* (3), 247–255.

(3) Punzi, M.; Mattiasson, B.; Jonstrup, M. Treatment of Synthetic Textile Wastewater by Homogeneous and Heterogeneous Photo-Fenton Oxidation. *Journal of Photochemistry and Photobiology A: Chemistry* **2012**, *248*, 30–35.

(4) Hassaan, M. A.; Nemr, A. El. Health and Environmental Impacts of Dyes: Mini Review. *American Journal of Environmental Science and Engineering* **2017**, *1* (3), 64–67.

(5) Sarayu, K.; Sandhya, S. Current Technologies for Biological Treatment of Textile Wastewater-A Review. *Applied Biochemistry and Biotechnology* **2012**, *167* (3), 645–661.

(6) Pérez, M.; Torrades, F.; Domènech, X.; Peral, J. Fenton and Photo-Fenton Oxidation of Textile Effluents. *Water Research* **2002**, *36* (11), 2703–2710.

(7) Holkar, C. R.; Jadhav, A. J.; Pinjari, D. V.; Mahamuni, N. M.; Pandit, A. B. A Critical Review on Textile Wastewater Treatments: Possible Approaches. *Journal of*

Environmental Management **2016**, *182*, 351–366.

(8) Wang, J. L.; Xu, L. J. Advanced Oxidation Processes for Wastewater Treatment: Formation of Hydroxyl Radical and Application. *Critical Reviews in Environmental Science and Technology* **2012**, *42* (3), 251–325.

(9) Zhu, Y.; Zhu, R.; Xi, Y.; Zhu, J.; Zhu, G.; He, H. Strategies for Enhancing the Heterogeneous Fenton Catalytic Reactivity: A Review. *Applied Catalysis B: Environmental* **2019**, *255,* 117739–117755.

(10) Munoz, M.; de Pedro, Z. M.; Casas, J. A.; Rodriguez, J. J. Preparation of Magnetite-Based Catalysts and Their Application in Heterogeneous Fenton Oxidation - A Review. *Applied Catalysis B: Environmental* **2015**, *176–177*, 249–265.

(11) Pliego, G.; Zazo, J. A.; Garcia-Muñoz, P.; Munoz, M.; Casas, J. A.; Rodriguez, J. J. Trends in the Intensification of the Fenton Process for Wastewater Treatment: An Overview. *Critical Reviews in Environmental Science and Technology* **2015**, *45* (24), 2611–2692.

(12) Zhang, M. hui; Dong, H.; Zhao, L.; Wang, D. xi; Meng, D. A Review on Fenton Process for Organic Wastewater Treatment Based on Optimization Perspective. *Science of the Total Environment* **2019**, *670*, 110–121.

(13) Karthikeyan, S.; Titus, A.; Gnanamani, A.; Mandal, A. B.; Sekaran, G. Treatment of Textile Wastewater by Homogeneous and Heterogeneous Fenton Oxidation Processes. *Desalination* **2011**, *281* (1), 438–445.

(14) Clarizia, L.; Russo, D.; Di Somma, I.; Marotta, R.; Andreozzi, R. Homogeneous Photo-Fenton Processes at near Neutral pH: A Review. *Applied Catalysis B: Environmental* **2017**, *209*, 358–371.

(15) Gligorovski, S.; Strekowski, R.; Barbati, S.; Vione, D. Environmental Implications of Hydroxyl Radicals (•OH). *Chemical Reviews* **2015**, *115* (24), 13051-13092.

(16) Xue, W.; Huang, D.; Zeng, G.; Wan, J.; Zhang, C.; Xu, R.; Cheng, M.; Deng, R. Nanoscale Zero-Valent Iron Coated with Rhamnolipid as an Effective Stabilizer for Immobilization of Cd and Pb in River Sediments. *Journal of Hazardous Materials* **2018**, *341*, 381–389.

(17) Jain, B.; Singh, A. K.; Kim, H.; Lichtfouse, E.; Sharma, V. K. Treatment of Organic Pollutants by Homogeneous and Heterogeneous Fenton Reaction Processes. *Environmental Chemistry Letters* **2018**, *16* (3), 947-967.

(18) Su, L.; Xiong, Y.; Wu, M.; Duan, Z.; Zhang, Z.; Xie, W.; Zhu, D.; Luo, Y.; He, X. From Starch to Magnetic Porous Fe_2O_3@C: A Promising Peroxidase-Mimicking Heterogeneous Biocatalyst for Degradation of Organic Dye. *Starch - Stärke* **2018**, *70* (5–6), 1700221

(19) Zobel, H. F. Molecules to Granules: A Comprehensive Starch Review. *Starch - Stärke* **1988**, *40* (2), 44–50.

(20) El Qada, E. N.; Allen, S. J.; Walker, G. M. Adsorption of Methylene Blue onto Activated Carbon Produced from Steam Activated Bituminous Coal: A Study of Equilibrium

Adsorption Isotherm. *Chemical Engineering Journal* **2006**, *124* (1–3), 103–110.

(21) Tang, M.; Wang, D.; Hou, Y.; Buchili, P.; Sun, L. Preparation, Characterization, Bioavailability in Vitro and in Vivo of Tea Polysaccharides-Iron Complex. *European Food Research and Technology* **2013**, *236* (2), 341–350.

(22) Krenkova, J.; Foret, F. Iron Oxide Nanoparticle Coating of Organic Polymer-Based Monolithic Columns for Phosphopeptide Enrichment. *Journal of Separation Science* **2011**, *34* (16–17), 2106–2112.

(23) Pitarresi, G.; Tripodo, G.; Cavallaro, G.; Palumbo, F. S.; Giammona, G. Inulin-Iron Complexes: A Potential Treatment of Iron Deficiency Anaemia. *European Journal of Pharmaceutics and Biopharmaceutics* **2008**, *68* (2), 267–276.

(24) Baalousha, M.; Manciulea, A.; Cumberland, S.; Kendall, K.; Lead, J. R. Aggregation and Surface Properties of Iron Oxide Nanoparticles: Influence of PH and Natural Organic Matter. *Environmental Toxicology and Chemistry* **2008**, *27* (9), 1875–1882.

(25) Soshnikova, Y. M.; Roman, S. G.; Chebotareva, N. A.; Baum, O. I.; Obrezkova, M. V.; Gillis, R. B.; Harding, S. E.; Sobol, E. N.; Lunin, V. V. Starch-Modified Magnetite Nanoparticles for Impregnation into Cartilage. *Journal of Nanoparticle Research.* **2013**, *15* (11), 1-10.

(26) Pereira, J. H. O. S.; Queirós, D. B.; Reis, A. C.; Nunes, O. C.; Borges, M. T.; Boaventura, R. A. R.; Vilar, V. J. P. Process Enhancement at near Neutral pH of a Homogeneous Photo-Fenton Reaction Using Ferricarboxylate Complexes: Application to

Oxytetracycline Degradation. *Chemical Engineering Journal.* **2014**, *253*, 217–228

(27) Roudi, A. M.; Chelliapan, S.; Mohtar, W. H. M. W.; Kamyab, H. Prediction and Optimization of the Fenton Process for the Treatment of Landfill Leachate Using an Artificial Neural Network. *Water* **2018**, *10* (5), 595.

(28) Tengrui, L.; Al-Harbawi, A.; Jun, Z.; Bo, L. M. The Effect and Its Influence Factors of the Fenton Process on the Old Landfill Leachate. *Journal of Applied Sciences* **2007**, *7* (5), 724–727.

(29) Wang, X.; Zhang, L. Kinetic Study of Hydroxyl Radical Formation in a Continuous Hydroxyl Generation System. *RSC Advances* **2018**, *8* (71), 40632–40638.

(30) Watts, R. J.; Foget, M. K.; Kong, S. H.; Teel, A. L. Hydrogen Peroxide Decomposition in Model Subsurface Systems. *Journal of Hazardous Materials B* **1999**, *69* (2), 229–243.

(31) Mierzwa, J. C.; Rodrigues, R.; Teixeira, A. C. S. C. UV-Hydrogen Peroxide Processes. *Advanced Oxidation Processes for Wastewater Treatment: Emerging Green Chemical Technology* **2018,** 13–48.

(32) El Haddad, M. E.; Regti, A.; Laamari, M. R.; Mamouni, R.; Saffaj, N. Use of Fenton Reagent as Advanced Oxidative Process for Removing Textile Dyes from Aqueous Solutions. *Journal of Materials and Environmental Science* **2014**, *5* (3), 667–674.

(33) Parovuori, P.; Hamunen, A.; Forssell, P.; Autio, K.; Poutanen, K. Oxidation of Potato Starch by Hydrogen Peroxide. *Starch - Stärke* **1995**, *47* (1), 19–23.

(34) Zhou, G.; Fang, F.; Chen, Z.; He, Y.; Sun, H.; Shi, H. Facile Synthesis of Paper Mill

Sludge-Derived Heterogeneous Catalyst for the Fenton-like Degradation of Methylene Blue. *Catalysis Communications* **2015**, *62*, 71–74.

(35) Silver, J.; Morrison, I. E. G.; Rees, L. V. C. A Mössbauer Spectroscopic Study of Frozen Solutions of $FeCl_3$ - Phenols. *Inorganic and Nuclear Chemistry Letters* **1979**, *15* (11–12), 433–436.

Chapter 5

(1) Knaul, J. Z.; Bui, V. T.; Creber, K. A. M.; Kasaai, M. R. Characterization of Deacetylated Chitosan and Chitosan Molecular Weight Review. *Canadian Journal of Chemistry* **1998**, *76* (11), 1699–1706.

(2) Mujtaba, M.; Morsi, R. E.; Kerch, G.; Elsabee, M. Z.; Kaya, M.; Labidi, J.; Khawar, K. M. Current Advancements in Chitosan-Based Film Production for Food Technology; A Review *International Journal of Biological Macromolecules* 2**019**, *121*, 889–904.

(3) Ravi Kumar, M. N. V. A Review of Chitin and Chitosan Applications. *Reactive and Functional Polymers* **2000**, *46* (1), 1–27.

(4) Hamilton, V.; Yuan, Y.; Rigney, D. A.; Puckett, A. D.; Ong, J. L.; Yang, Y.; Elder, S. H.; Bumgardner, J. D. Characterization of Chitosan Films and Effects on Fibroblast Cell Attachment and Proliferation *Journal of Materials Science: Materials in Medicine* **2006**; *17* (12), 1373–1381.

(5) Mori, T.; Okumura, M.; Matsuura, M.; Ueno, K.; Tokura, S.; Okamoto, Y.; Minami, S.;

Fujinaga, T. Effects of Chitin and Its Derivatives on the Proliferation and Cytokine Production of Fibroblasts in Vitro *Biomaterials* **1997**, *18* (13), 947–951.

(6) Bumgardner, J. D.; Wiser, R.; Gerard, P. D.; Bergin, P.; Chestnutt, B.; Marini, M.; Ramsey, V.; Elder, S. H.; Gilbert, J. A. Chitosan: Potential Use as a Bioactive Coating for Orthopaedic and Craniofacial/Dental Implants. *Journal of Biomaterials Science, Polymer Edition* **2003**, *14* (5), 423–438.

(7) Liu, X. F.; Guan, Y. L.; Yang, D. Z.; Li, Z.; Yao, K. De. Antibacterial Action of Chitosan and Carboxymethylated Chitosan. *Journal of Applied Polymer Science* **2001**, *79* (7), 1324–1335.

(8) Deng, H.; Dai, F.; Ma, G.; Zhang, X. Theranostic Gold Nanomicelles Made from Biocompatible Comb-like Polymers for Thermochemotherapy and Multifunctional Imaging with Rapid Clearance. *Advanced Materials* **2015**, *27* (24), 3645–3653.

(9) Schneider, C. A.; Rasband, W. S.; Eliceiri, K. W. NIH Image to ImageJ: 25 Years of Image Analysis. *Nature Methods* **2012**, *9* (7), 671–675.

(10) Pegoretti, A.; Dorigato, A.; Brugnara, M.; Penati, A. Contact Angle Measurements as a Tool to Investigate the Filler-Matrix Interactions in Polyurethane-Clay Nanocomposites from Blocked Prepolymer. *European Polymer Journal* **2008**, *44* (6), 1662–1672.

(11) Moad, G.; Rizzardo, E.; Thang, S. H. Living Radical Polymerization by the RAFT Process. *Australian Journal of Chemistry* **2005**, *58* (6), 379–410.

(12) Liu, G.; Qiu, Q.; Shen, W.; An, Z. Aqueous Dispersion Polymerization of 2-Methoxyethyl

Acrylate for the Synthesis of Biocompatible Nanoparticles Using a Hydrophilic RAFT Polymer and a Redox Initiator. *Macromolecules* **2011**, *44* (13), 5237–5245.

(13) Tang, J.; Hua, D.; Cheng, J.; Jiang, J.; Zhu, X. Synthesis and Properties of Temperature-Responsive Chitosan by Controlled Free Radical Polymerization with Chitosan-RAFT Agent. *International Journal of Biological Macromolecules* **2008**, *43* (4), 383–389.

(14) Schott, H. Further Comments on the Existence of Spherical Micelles. *Journal of Pharmaceutical Sciences* **1973**, *62* (1), 162–166.

(15) Minh, N. C.; Nguyen, V. H.; Schwarz, S.; Stevens, W. F.; Trung, T. S. Preparation of Water Soluble Hydrochloric Chitosan from Low Molecular Weight Chitosan in the Solid State. *International Journal of Biological Macromolecules* **2019**, *121*, 718–726.

(16) Aljbour, N. D.; Beg, M. D. H.; Gimbun, J. Acid Hydrolysis of Chitosan to Oligomers Using Hydrochloric Acid. *Chemical Engineering & Technology* **2019,** *42* (9), 1741–1746.

(17) Varum, K. M.; Ottoy, M. H.; Smidsrod, O. Acid Hydrolysis of Chitosans. *Carbohydrate Polymers* **2001**, *46* (1), 89–98.

(18) Jiang, J.; Pan, X.; Cao, J.; Jiang, J.; Hua, D.; Zhu, X. Synthesis and Property of Chitosan Graft Copolymer by RAFT Polymerization with Tosylic Acid-Chitosan Complex. *International Journal of Biological Macromolecules* **2012**, *50* (3), 586–590.

(19) Pandey, V. K.; Upadhyay, S. N.; Niranjan, K.; Mishra, P. K. Antimicrobial Biodegradable Chitosan-Based Composite Nano-Layers for Food Packaging. *International Journal of Biological Macromolecules* **2020**, *157*, 212–219.

(20) Yang, B.; Duhamel, J. Extraction of Oil from Oil Sands Using Thermoresponsive Polymeric Surfactants. *ACS Applied Materials & Interfaces* **2015**, *7* (10), 5879–5889.

(21) Conzatti, G.; Ayadi, F.; Cavalie, S.; Carrère, N.; Tourrette, A. Thermosensitive PNIPAM Grafted Alginate/Chitosan PEC. *Applied Surface Science* **2019**, *467–468*, 940–948.

(22) Plunkett, K. N.; Zhu, X.; Moore, J. S.; Leckband, D. E. PNIPAM Chain Collapse Depends on the Molecular Weight and Grafting Density. *Langmuir* **2006**, *22* (9), 4259–4266.

(23) Barrère, F.; Mahmood, T. A.; de Groot, K.; van Blitterswijk, C. A. Advanced Biomaterials for Skeletal Tissue Regeneration: Instructive and Smart Functions. *Materials Science and Engineering R: Reports* **2008**, *59* (1), 38–71.

(24) Taciak, B.; Białasek, M.; Braniewska, A.; Sas, Z.; Sawicka, P.; Kiraga, Ł.; Rygiel, T.; Król, M. Evaluation of Phenotypic and Functional Stability of RAW 264.7 Cell Line through Serial Passages. *PLoS One* **2018**, *13* (6), e0198943.

(25) Kuriyama, T.; Fukuma, Y.; Imashiro, C.; Kabayama, K.; Kurashina, Y.; Takemura, K. Detachment of RAW264.7 Macrophages from a Culture Dish Using Ultrasound Excited by a Langevin Transducer. *Journal of Bioscience and Bioengineering* **2021**, *131* (3), 320–325.

(26) Zan, Q.; Wang, C.; Dong, L.; Cheng, P.; Tian, J. Effect of Surface Roughness of Chitosan-Based Microspheres on Cell Adhesion. *Applied Surface Science* **2008**, *255* (2), 401–403.

(27) Lasocka, I.; Szulc-Dąbrowska, L.; Skibniewski, M.; Skibniewska, E.; Gregorczyk-Zboroch, K.; Pasternak, I.; Kalbacova, M. H. Cytocompatibility of Graphene Monolayer

and Its Impact on Focal Cell Adhesion, Mitochondrial Morphology and Activity in Balb/3t3 Fibroblasts. *Materials* **2021**, *14* (3), 1–16.

(28) Zhu, A. P.; Fang, N. Adhesion Dynamics, Morphology, and Organization of 3T3 Fibroblast on Chitosan and Its Derivative: The Effect of O-Carboxymethylation. *Biomacromolecules* **2005**, *6* (5), 2607–2614.

(29) Wu, M. F.; Stachon, T.; Seitz, B.; Langenbucher, A.; Szentmáry, N. Effect of Human Autologous Serum and Fetal Bovine Serum on Human Corneal Epithelial Cell Viability, Migration and Proliferation in Vitro. *International Journal of Ophthalmology* **2017**, *10* (6), 908–913.

(30) Benhabbour, S. R.; Sheardown, H.; Adronov, A. Cell Adhesion and Proliferation on Hydrophilic Dendritically Modified Surfaces. *Biomaterials* **2008**, *29* (31), 4177–4186.

(31) Chen, L.; Li, S. G.; Xiao, F.; Zhang, A. H.; Yao, K. De. Preparation of Thermoresponsive Chitosan Copolymer and Its Cytocompatibility and Detachability. *Chemical Journal of Chinese Universities* **2008**, *29* (5), 1061–1064.

(32) Freier, T.; Koh, H. S.; Kazazian, K.; Shoichet, M. S. Controlling Cell Adhesion and Degradation of Chitosan Films by N-Acetylation. *Biomaterials* **2005**, *26* (29), 5872-5878.

(33) Hayman, E. G.; Pierschbacher, M. D.; Suzuki, S.; Ruoslahti, E. Vitronectin-A Major Cell Attachment-Promoting Protein in Fetal Bovine Serum. *Experimental Cell Research* **1985**, *160* (2), 245–258.

Chapter 6

(1) Lu, D.; Xiao, C.; Sun, F. Controlled Grafting of Poly(Vinyl Acetate) onto Starch via RAFT Polymerization. *Journal of Applied Polymer Science* **2012**, *124* (4), 3450–3455.

(2) Lu, D. R.; Xiao, C. M.; Xu, S. J.; Ye, Y. F. Tailor-Made Starch-Based Conjugates Containing Well-Defined Poly(Vinyl Acetate) and Its Derivative Poly(Vinyl Alcohol). *Express Polymer Letters* **2011**, *5* (6), 535–544.

(3) Roth, P. J.; Davis, T. P.; Lowe, A. B. Comparison between the LCST and UCST Transitions of Double Thermoresponsive Diblock Copolymers: Insights into the Behavior of POEGMA in Alcohols. *Macromolecules* **2012**, *45* (7), 3221–3230.

(4) Yang, B.; Duhamel, J. Extraction of Oil from Oil Sands Using Thermoresponsive Polymeric Surfactants. *ACS Applied Materials & Interfaces* **2015**, *7* (10), 5879–5889.

(5) Lutz, J. F.; Akdemir, Ö.; Hoth, A. Point by Point Comparison of Two Thermosensitive Polymers Exhibiting a Similar LCST: Is the Age of Poly(NIPAM) Over? *Journal of the American Chemical Society* **2006**, *128* (40), 13046–13047.

(6) Takamura, K. Microscopic Structure of Athabasca Oil Sand. *The Canadian Journal of Chemical Engineering* **1982,** *60* (4), 538-545.

(7) Rocha, J. A.; Baydak, E. N.; Yarranton, H. W.; Sztukowski, D. M.; Ali-Marcano, V.; Gong, L.; Shi, C.; Zeng, H. Role of Aqueous Phase Chemistry, Interfacial Film Properties, and Surface Coverage in Stabilizing Water-in-Bitumen Emulsions. *Energy and Fuels* **2016**, *30* (7), 5240–5252.

(8) Rao, F.; Liu, Q. Froth Treatment in Athabasca Oil Sands Bitumen Recovery Process: A Review. *Energy and Fuels* **2013**, *27* (12), 7199–7207.

(9) Zhang, M. hui; Dong, H.; Zhao, L.; Wang, D. xi; Meng, D. A Review on Fenton Process for Organic Wastewater Treatment Based on Optimization Perspective. *Science of the Total Environment* **2019**, *670*, 110–121.

(10) Clarizia, L.; Russo, D.; Di Somma, I.; Marotta, R.; Andreozzi, R. Homogeneous Photo-Fenton Processes at near Neutral PH: A Review. *Applied Catalysis B: Environmental* **2017**, *209*, 358–371.

(11) Gligorovski, S.; Strekowski, R.; Barbati, S.; Vione, D. Environmental Implications of Hydroxyl Radicals (•OH). *Chemical Reviews* **2015**.

(12) Xue, W.; Huang, D.; Zeng, G.; Wan, J.; Zhang, C.; Xu, R.; Cheng, M.; Deng, R. Nanoscale Zero-Valent Iron Coated with Rhamnolipid as an Effective Stabilizer for Immobilization of Cd and Pb in River Sediments. *Journal of Hazardous Materials* **2018**, *341*, 381–389.

(13) Duarte, F.; Madeira, L. M. Fenton- and Photo-Fenton-like Degradation of a Textile Dye by Heterogeneous Processes with Fe/ZSM-5 Zeolite. *Separation Science and Technology* **2010**, *45* (11), 1512–1520.

(14) Herney-Ramirez, J.; Vicente, M. A.; Madeira, L. M. Heterogeneous Photo-Fenton Oxidation with Pillared Clay-Based Catalysts for Wastewater Treatment: A Review. *Applied Catalysis B: Environmental* **2010**, *98* (1-2), 10–26.

(15) Lima Santos Klienchen Dalari, B.; Lisboa Giroletti, C.; Dalri-Cecato, L.; Gonzaga Domingos, D.; Nagel Hassemer, M. E. Application of Heterogeneous Photo-Fenton Process Using Chitosan Beads for Textile Wastewater Treatment. *Journal of Environmental Chemical Engineering* **2020**, *8* (4), 103893.

(16) González-Bahamón, L. F.; Mazille, F.; Benítez, L. N.; Pulgarín, C. Photo-Fenton Degradation of Resorcinol Mediated by Catalysts Based on Iron Species Supported on Polymers. *Journal of Photochemistry and Photobiology A: Chemistry* **2011**, *217* (1), 201–206.

(17) Zhou, G.; Fang, F.; Chen, Z.; He, Y.; Sun, H.; Shi, H. Facile Synthesis of Paper Mill Sludge-Derived Heterogeneous Catalyst for the Fenton-like Degradation of Methylene Blue. *Catalysis Communications* **2015**, *62*, 71–74.

(18) Hua, D.; Tang, J.; Cheng, J.; Deng, W.; Zhu, X. A Novel Method of Controlled Grafting Modification of Chitosan via RAFT Polymerization Using Chitosan-RAFT Agent. *Carbohydrate Polymers* **2008**, *73* (1), 98–104.

(19) Solimando, X.; Champagne, P.; Cunningham, M. F. Synthesis of Biohybrid Particles by Modification of Chitosan Beads via RAFT Polymerization in Dispersed Media. *Macromolecular Reaction Engineering* **2020**, *14* (6).

(20) Schott, H. Further Comments on the Existence of Spherical Micelles. *Journal of Pharmaceutical Sciences* **1973**, *62* (1), 162–166.

(21) Kato, A.; Kan, K.; Ajiro, H.; Akashi, M. Development of a Rapid in Vitro Tissue

Deadhesion System Using the Thermoresponsive Sol-Gel Transition of Hydroxybutyl Chitosan. *Journal of Biomaterials Science, Polymer Edition* **2017**, *28* (10–12), 958–973.

(22) Nie, P.; He, X.; Chen, L. Temperature-Sensitive Chitosan Membranes as a Substrate for Cell Adhesion and Cell Sheet Detachment. *Polymers for Advanced Technologies* **2012**, *23* (3), 447–453.

(23) Hayman, E. G.; Pierschbacher, M. D.; Suzuki, S.; Ruoslahti, E. Vitronectin-A Major Cell Attachment-Promoting Protein in Fetal Bovine Serum. *Experimental Cell Research* **1985**, *160* (2), 245–258.

(24) Zan, Q.; Wang, C.; Dong, L.; Cheng, P.; Tian, J. Effect of Surface Roughness of Chitosan-Based Microspheres on Cell Adhesion. *Applied Surface Sciences* **2008**, *255* (2), 401–403.

(25) Yue, M.; Chian, K. S. Advances in Engineering Fluid Mechanics: Multiphase Reactor and Polymerization System Hydrodynamics. *Elsevier* **1996**.

(26) Zheng, B.; Taylor, S. D. Thermoresponsive Starch for the Flocculation of Oil Sands Mature Fine Tailings. *Environmetal Science and Technology* **2020**, *54* (21), 13981–13991.

(27) Li, H.; Zhou, J.; Chow, R.; Adegoroye, A.; Najafi, A. S. Enhancing Treatment and Geotechnical Stability of Oil Sands Fine Tailings Using Thermo-Sensitive Poly(*n*-Isopropyl Acrylamide). *The Canadian Journal of Chemical Engineering* **2015**, *93* (10), 1780–1786.

(28) Xiao, Z. X.; Wu, G. Y.; Li, Z. H.; Zhang, G. B.; Hao, Y. L.; Wang, Y. Y. Silicon-Glass

Wafer Bonding with Silicon Hydrophilic Fusion Bonding Technology. *Sensors and Actuators* **1999**, *72* (1), 46–48.

(29) Murray, C. A.; Dutcher, J. R. Effect of Changes in Relative and Temperature on Ultrathin Chitosan Films. *Biomacromolecules* **2006**, *7* (12), 3460–3465.

(30) Kuhn, D. M.; Balkis, M.; Chandra, J.; Mukherjee, P. K.; Ghannoum, M. A. Uses and Limitations of the XTT Assay in Studies of Candida Growth and Metabolism. *Journal of Clinical Microbiology* **2003**, *41* (1), 506–508.

(31) Campling, B. G.; Pym, J.; Galbraith, P. R.; Cole, S. P. C. Use of the Mtt Assay for Rapid Determination of Chemosensitivity of Human Leukemic Blast Cells. *Leukemia Research* **1988**, *12* (10), 823–831.

(32) Schneider, D. A.; Gourse, R. L. Relationship between Growth Rate and ATP Concentration in Escherichia Coli: A Bioassay for Available Cellular ATP. *The Journal of Biological Chemistry* **2004**, *279* (9), 8262–8268.

(33) Pollard, P. C.; Moriarty, D. J. W. Validity of the Tritiated Thymidine Method for Estimating Bacterial Growth Rates: Measurement of Isotope Dilution during DNA Synthesis. *Applied and Environmental Microbiology* **1984**, *48* (6), 1076–1083.

(34) Findlay, S. E. G.; Meyer, J. L.; Edwards, R. T. Measuring Bacterial Production via Rate of Incorporation of [3H]Thymidine into DNA. *Journal of Microbiological Methods* **1984**, *2* (2), 57–72.

Appendices

Appendix A-1: Conversion of MEO_2MA Monomer as a Function of Time

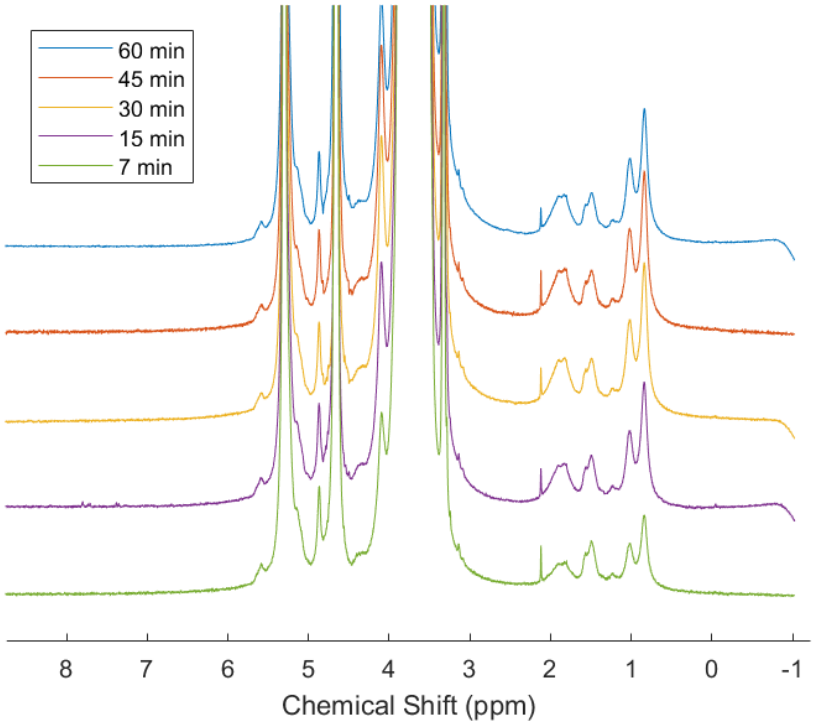

Figure A1-1: ^1H NMR spectra for SNP-g-$PMEO_2MA$ samples removed at different times.

Appendix B-1: ANOVA Test

The ANalysis Of VAriance, or ANOVA test, is commonly used in statistics to determine whether several groups of data are statistically different from each other. In this section, the detailed algorithm for the ANOVA test will be discussed.

Consider N individual data entries separated into k groups. The number of data entries in group 1, group 2, …, and group k are defined as n_1, n_2, ..., and n_k, respectively. The data contained in group j will be denoted as X_{1j}, X_{2j}, …, and $X_{(n_k)j}$. The null hypothesis in the ANOVA test is that there is no difference between the mean of these groups.

To perform the ANOVA test, a value called the Sum of Squares (SS) within the groups needs to be calculated as follows

$$SS\ within\ group = \sum_{j=1}^{k}(\sum_{i=1}^{n_j}(X_{ij} - \bar{X}_j)^2)$$

where $\bar{X}_j$ is the mean of the data in group j. The SS within a group indicates the variation in the data within each data group. The degree of freedom (df) for the SS within a group is calculated as:

$$df_{within\ group} = N - k$$

Then, values named the SS between the groups and the degrees of freedom for the SS between the groups are calculated as

$$SS_{between\ groups} = \sum_{j=1}^{k}(\bar{X}_j - \bar{X})^2$$

$$df_{betwen\ groups} = k - 1$$

where $\bar{X}$ is the mean for all the data. The SS between the groups is an indicator of the variation of the data among each of the data groups.

After these numbers were evaluated, a *F statistic* is calculated as follows:

$$F\ statistic = \frac{SS_{between\ group}/df_{between\ group}}{SS_{within\ group}/df_{within\ group}}$$

The F statistic value is crucial for the ANOVA test. If the *F statistic* value is low, it indicates that there is little variation for the data within the same group, while the data variations across different groups are large. Conversely, a large *F statistic* value indicates that there is much variation for the data within the same group, and that the data variations across different groups are relatively small.

A critical value for the test statistics, *F critical*, can be found in an F statistics table, commonly available in statistics textbooks. The *F statistic* table provides an *F critical* value for a given a numerator degree freedom, a denominator degree of freedom, and a confidence interval p. The $df_{between\ group}$ is used as the numerator degree of freedom, and $df_{within\ group}$ is used as the denominator degree of freedom. If the computed *F statistic* is greater than *F critical*, the null hypothesis is rejected and the data in different groups are significantly different from each other. The confidence interval p measures the degree of certainly with which the null hypothesis can be rejected. If the *F statistic* computed is greater than *F critical* for $p < 0.05$, the null hypothesis can be rejected with 95% confidence. This means that there is a 95% probability that the rejection

of the null hypothesis is correct, and that the data in different groups are truly different from each other.

Conventionally, the results of ANOVA tests are reported in a table similar to Table B1-1.

Table B1-1. Reporting the results of the ANOVA test.

Source of Variation	***SS***	***df***	***MS***	***F***	***P-value***	***F crit***
Between Groups	$SS_{between\ group}$	$df_{between\ group}$	$\frac{SS_{between\ group}}{df_{betwen\ group}}$	*F*	*p*	*F-critical*
Within Groups	$SS_{within\ group}$	$df_{within\ group}$	$\frac{SS_{within\ group}}{df_{within\ group}}$			
Total	$SS_{between\ group} + SS_{within\ group}$	$df_{between\ group} + df_{within\ group}$				

The ANOVA results for bitumen extraction are summarized in Table B1-2 below. The much larger *F statistic* (50) in comparison with the critical F value (6) for a confidence interval $p < 0.01$ shows that the amount of toluene used had a very significant influence on the extraction efficiency at a 99% confidence level.

Table B1-2: ANOVA test results for bitumen extraction at the different toluene concentrations reported in Table 3-2

ANOVA: Single Factor	**SS**	**dF**	**Mean SMS**	**F**	**p-value**	**F crit**
Source of Variation	1804	3	601	50	9.35E-08	6
Between Groups	167	14	12			
	1970	17				